



THE LARGE-SCALE MAGNETIC FIELDS OF  
PLANET-HOSTING SOLAR-TYPE STARS

A Thesis Submitted by

Matthew W. Mengel, M.Phil.,  
G.D.Inf.Tech, B.Inf.Tech.

For the Award of

Doctor of Philosophy

2017

# Abstract

STELLAR MAGNETIC FIELDS AND their associated phenomena influence stellar behaviour and evolution, and potentially have significant impacts on any surrounding planetary system. However, the nature of star-planet interactions is unclear, especially the potential impact on a star of a closely orbiting massive planet with a powerful magnetic field.

This thesis presents a spectropolarimetric survey of the large-scale magnetic fields of planet-hosting solar-type stars. While little evidence is found for a systematic difference in the magnetic field characteristics of planet-hosting stars compared with the population of solar-type stars, a small positive correlation is indicated between the magnitude of the tidal effects of the planet on the star and the magnetic field strength. Nevertheless, further spectropolarimetric observations of hot Jupiter hosting systems are required to confirm this tentative relationship.

For the particular case of a moderately active star with a thin convective zone and a closely orbiting hot Jupiter ( $\tau$  Boötis) presented here, a remarkably rapid magnetic cycle with a period of  $\sim 240$  d is discovered. For stars with shallow convective envelopes, this is an unusual occurrence and suggests a possible role for planetary tidal or magnetic interaction with the star's convective zone and magnetic dynamo. More observations are required to verify this possible star-planet interaction and to extend the work to other similar systems as they come to light from exoplanet surveys.

# Certification of Thesis

This Thesis is the work of Matthew W. Mengel except where otherwise acknowledged, with the majority of the authorship of the papers presented as a Thesis by Publication undertaken by the Student. The work is original and has not previously been submitted for any other award, except where acknowledged.

Student and supervisors signatures of endorsement are held at USQ.

Associate Professor Stephen C. Marsden  
Principal Supervisor

Professor Bradley D. Carter  
Associate Supervisor

Doctor Rim Fares  
Associate Supervisor

# List of Contributions from Publication

## Co-authors

This section details contributions by the various authors for each of the papers presented in this thesis by publication.

Chapter 2, [Mengel et al. \(2017b\)](#):

Mengel, M. W., Marsden, S. C., Carter, B. D., Horner, J., King, R., Fares, R., Jeffers, S. V., Petit, P., Vidotto, A. A., & Morin, J. (2017b). A BCoolest survey of the magnetic fields of planet-hosting solar-type stars. *MNRAS*, 465(3), 2734–2747

Author	Percent Contribution	Tasks Performed
M. W. Mengel	85	Performed target selection, analysis, interpretation, wrote all drafts of paper, conception of project.
S. C. Marsden	}15	Conception of BCoolest project, steering committee of BCoolest collaboration long term observing project, suggested edits to manuscript, conception of project, confidence intervals in statistical analysis
B. D. Carter		
R. Fares		
J. Horner		
R. King		
P. Petit		
S. V. Jeffers		
A. A. Vidotto		
J. Morin		

Chapter 3, Mengel et al. (2016):

Mengel, M. W., Fares, R., Marsden, S. C., Carter, B. D., Jeffers, S. V., Petit, P., Donati, J.-F., & Folsom, C. P. (2016). The evolving magnetic topology of  $\tau$  Boötis. *MNRAS*, 459(4), 4325–4342

Author	Percent Contribution	Tasks Performed
M. W. Mengel	80	Performed analysis, interpretation, wrote all drafts of paper.
R. Fares	} 20	Conception of BCool project, steering committee of BCool collaboration long term observing project, suggested edits to manuscript, conception of project, provided access to code
S. C. Marsden		
B. D. Carter		
S. V. Jeffers		
P. Petit		
J.-F. Donati		
C. Folsom		

Chapter 4, Mengel et al. (2017a):

Mengel, M. W., Jeffers, S. V., Moutou, C., Marsden, S. C., Fares, R., & Carter, B. D. (2017a). A rapid magnetic cycle on  $\tau$  Boötis. in preparation

Author	Percent Contribution	Tasks Performed
M. W. Mengel	85	Conception of project, performed analysis, interpretation, wrote all drafts of paper.
S. V. Jeffers	} 15	Conception of project, data acquisition, interpretation, suggested edits to manuscript
C. Moutou		
S. C. Marsden		
R. Fares		
B. D. Carter		

The following papers to which co-author contributions were made by M. W. Mengel during the period of Candidacy, but not germane to the main thesis and narrative are presented in Appendices A-C.

Nicholson, B. A., Vidotto, A. A., Mengel, M., Brookshaw, L., Carter, B., Petit, P., Marsden, S. C., Jeffers, S. V., & Fares, R. (2016). Temporal variability of the wind from the star  $\tau$  Boötis. *MNRAS*, 459(2), 1907–1915

Wittenmyer, R. A., Johnson, J. A., Butler, R. P., Horner, J., Wang, L., Robertson, P., Jones, M. I., Jenkins, J. S., Brahm, R., Tinney, C. G., Mengel, M. W., & Clark, J. (2016). The Pan-Pacific Planet Search. IV. Two Super-Jupiters in a 3:5 Resonance Orbiting the Giant Star HD 33844. *Ap. J.*, 818, 35

Wittenmyer, R. A., Horner, J., Mengel, M. W., Butler, R. P., Wright, D. J., Tinney, C. G., Carter, B. D., Jones, H. R. A., Anglada-Escudé, G., Bailey, J., & O’Toole, S. J. (2017). The Anglo-Australian Planet Search. XXV. A Candidate Massive Saturn Analog Orbiting HD 30177. *A. J.*, 153, 167

# Acknowledgments

I WOULD LIKE TO OFFER MY SINCERE thanks and acknowledgements to many people and organizations for allowing me to complete this thesis.

Firstly, I would like to acknowledge the Australian Department of Education for the financial support provided via the Australian Postgraduate Awards scheme. Additional funding was made available by the University of Southern Queensland via a Strategic Research Fund provided to the Astrophysics Group for the STARWINDS project. This research was also supported by an Australian Government Research Training Program (RTP) Scholarship.

Data for the project was provided by the BCool Collaboration, Dr. Rim Fares, Dr. Sandra Jeffers, and Dr. Claire Moutou. This data was collected using the HARPS South instrument at the European Southern Observatory, La Silla, Chile; the NARVAL instrument located at the Téléscope Bernard Lyot (TBL) at the Observatoire Midi-Pyrenees, France; and the ESPaDOnS instrument at the Canada-France-Hawaii Telescope (CFHT) located at the Mauna Kea Observatory in Hawaii. TBL/NARVAL are operated by the Institut National des Sciences de l'Univers of the Centre National de la Recherche Scientifique of France. CFHT/ESPaDOnS is operated by the National Research Council of Canada, the Institut National des Sciences de l'Univers of the Centre National de la Recherche Scientifique of France, and the Univer-

sity of Hawaii.

Thanks to the co-authors and colleagues on my papers who provided comments, feedback, access to computer code: Dr. Jonathan Horner, Dr. Rachel King, Dr. Carolyn Brown, Dr. Ian Waite, Dr. Sandra Jeffers, Dr. Pascal Petit, Dr. Aline Vidotto, Dr. Julien Morin, Dr. Jean-Francois Donati and Dr. Colin Folsom. Additional thanks to fellow students Belinda Nicholson, Dr. Victor See and Jack Soutter for their comments and assistance.

Special thanks, of course to my team of supervisors, mentors and co-authors - Associate Professor Stephen Marsden, Professor Brad Carter and Dr. Rim Fares. I could not have completed this journey without their guidance and support.

Finally, my enduring thanks to my family and friends in supporting me throughout my study. I left a career of twenty years to pursue this work, and everyone has been nothing but supportive. Thank you all for making this possible.

# Contents

ABSTRACT	i
CERTIFICATION OF THESIS	ii
LIST OF CONTRIBUTIONS FROM PUBLICATION CO-AUTHORS	iii
ACKNOWLEDGMENTS	vi
TABLE OF CONTENTS	viii
LIST OF FIGURES	xii
LIST OF TABLES	xiv
I INTRODUCTION	I
I.1 The Solar Magnetic Field . . . . .	3
I.1.1 The Solar Dynamo . . . . .	5
I.1.1.1 Differential Rotation: the $\omega$ Effect . . . . .	7
I.1.1.2 Convection and Coriolis: the $\alpha$ Effect . . . . .	7
I.1.2 Solar Cycles . . . . .	8
I.2 Stellar Magnetic Fields . . . . .	10

1.3	Detecting and Modelling Stellar Magnetic Fields . . . . .	11
1.3.1	Detecting Magnetic Fields . . . . .	11
1.3.2	Observational Procedure for Generating Stokes Parameters . . . . .	15
1.3.3	Zeeman Doppler Imaging . . . . .	16
1.3.3.1	Radiative Transfer in the Presence of a Magnetic Field . . . . .	21
1.3.3.2	Limitations of ZDI . . . . .	25
1.3.4	Differential Rotation . . . . .	26
1.4	Stellar Magnetic Fields and Exoplanets . . . . .	27
1.5	Longitudinal Magnetic Field . . . . .	29
1.6	Chromospheric Activity Cycles . . . . .	30
1.7	The Magnetic Fields of Solar-Type Stars . . . . .	31
1.7.1	Magnetic Cycles . . . . .	32
1.7.2	Star-Planet Interaction . . . . .	33
1.8	Research Questions . . . . .	35
1.8.1	To what extent does the presence of a planetary system systematically affect the large-scale magnetic fields of their host solar-type stars, if at all? . . . . .	35
1.8.2	How does the presence of the hot Jupiter $\tau$ Boötis b affect the large-scale magnetic field of the host star in the particular case of $\tau$ Boötis? . . . . .	36
2	A BCOOL SURVEY OF THE MAGNETIC FIELDS OF PLANET HOSTING STARS . . . . .	37
2.1	Mengel et al. (2017b) “A BCOol Survey of the magnetic fields of planet-hosting solar-type stars” . . . . .	38
2.2	Summary of Results . . . . .	53

3	THE EVOLVING MAGNETIC FIELD OF THE PLANET-HOSTING SOLAR-TYPE STAR $\tau$ BOÖTIS	54
3.1	Mengel et al. (2016) “The evolving magnetic topology of $\tau$ Boötis” . . . . .	55
3.2	Summary of Results . . . . .	74
4	A RAPID LARGE-SCALE MAGNETIC CYCLE ON $\tau$ BOÖTIS	75
4.1	Mengel et al. (2017a) “A rapid large-scale magnetic cycle on $\tau$ Boötis” . . . . .	76
4.2	Observations of $\tau$ Boötis January and February 2017 . . . . .	96
4.2.1	Discussion of January-February 2017 Observations of $\tau$ Boötis . . . . .	98
4.3	Summary of Results . . . . .	99
5	DISCUSSION AND CONCLUSIONS	100
5.1	The Magnetic Fields of Planet-Hosting Solar-Type Stars . . . . .	100
5.2	The Magnetic Cycle of $\tau$ Boötis . . . . .	101
5.3	The Confirmation of an Extremely Rapid Magnetic Cycle on $\tau$ Boötis . . . . .	102
5.4	Conclusions . . . . .	103
5.5	The Future . . . . .	104
	REFERENCES	106
	APPENDIX A TEMPORAL VARIATION OF THE WIND FROM THE STAR $\tau$ BOÖTIS	118
A.1	Nicholson et al. (2016) “Temporal variation of the wind from the star $\tau$ Boötis” . . . . .	118

APPENDIX B	THE PAN-PACIFIC PLANET SEARCH. IV. TWO SUPER-JUPITERS IN	
	A 3:5 RESONANCE ORBITING THE GIANT STAR HD 33844	128
B.1	Wittenmyer et al. (2016b) The Pan-Pacific Planet Search. IV.	
	Two Super-Jupiters in a 3:5 Resonance Orbiting the Giant Star	
	HD 33844 . . . . .	128
APPENDIX C	THE ANGLO-AUSTRALIAN PLANET SEARCH XXV: A CANDIDATE	
	MASSIVE SATURN ANALOG ORBITING HD 30177	137
C.1	Wittenmyer et al. (2017) The Anglo-Australian Planet Search	
	XXV: A Candidate Massive Saturn Analog Orbiting HD 30177	137

# List of Figures

(Excluding publications included in Chapters 2-4)

1.1	Butterfly Diagram from D. H. Hathaway, NASA Marshall Flight Center . . . . .	4
1.2	The Solar interior from Kelvinsong CC-BY-SA 3.0 . . . . .	6
1.3	The Solar Dynamo from M. Dikpati, National Center for Atmospheric Research . . . . .	8
1.4	International sunspot number over time from Royal Observatory of Belgium . . . . .	9
1.5	Total Solar Irradiance over Schwabe cycle from G. Kopp, University of Colorado . . . . .	9
1.6	Zeeman splitting and polarisation of components from Reiners (2010) . . . . .	12
1.7	Schematic of combinations of polarisation states . . . . .	13
1.8	Mean LSD profile of $\tau$ Boötis (09 May 2014) . . . . .	14
1.9	Principles of Zeeman Doppler Imaging . . . . .	17
1.10	Magnetic field components recovered by Zeeman Doppler Imaging . . . . .	19

1.11	Change in Stokes $V$ profile for azimuthal field component crossing visible disk . . . . .	20
1.12	Change in Stokes $V$ profile for radial field component crossing visible disk . . . . .	21
1.13	Stokes $V$ profiles for $\tau$ Boötis December 2013 . . . . .	23
1.14	Magnetic maps for $\tau$ Boötis December 2013 . . . . .	23
1.15	Differential for $\tau$ Boötis December 2013 . . . . .	28
1.16	Bandpasses for Ca II H&K and continuum used to calculate S-indices from Wright et al. (2004) . . . . .	31
1.17	X-ray images of HD 1756 from Maggio et al. (2015) showing potential SPI . . . . .	34
4.1	Stokes $V$ profiles for $\tau$ Boötis February 2017 . . . . .	97
4.2	Magnetic topology of $\tau$ Boötis 14-21 February 2017 . . . . .	97
4.3	Longitudinal Magnetic Field and S-index of $\tau$ Boötis . . . . .	98

# List of Tables

(Excluding publications included in Chapters 2-4)

1.1	Journal of observations of $\tau$ Boötis, December 2013 . . . . .	22
4.1	Journal of observations of $\tau$ Boötis, January-February 2017 . . . . .	96

*I suppose when you do it correctly, a good introduction  
and a good outro makes the song feel like it's coming out of  
something and then evolving into something.*

Bruce Springsteen

# 1

## Introduction

OUR UNDERSTANDING OF THE PHYSICAL origins and evolution of stellar magnetic fields remains far from complete. Even for the Earth's nearest stellar neighbour in space, the Sun, many aspects of the dynamo processes responsible for the generation of these magnetic fields are poorly understood. Investigations that aim to understand stellar dynamos more fully are being intensely pursued. Magnetic fields play important roles in a star's evolution, such as in rotational spin-down (Schatzman, 1962) and mass loss, as well as in the formation and evolution of planetary systems, from the influence of magnetic phenomena in planetary formation (Romanova & Lovelace, 2006; Lai et al., 2011) and migration (Kretke et al., 2009) to the impact of stellar winds on planetary atmospheres (Vidotto et al., 2012; Nicholson et al., 2016). These phenomena are poorly constrained by observation. As a single nearby exemplar, stellar dynamo models are heavily based upon studies of the Sun.

To determine if the dynamo of the Sun is unusual or representative of the broader class of solar-type stars, particularly those that host planetary systems, observations of these stars are essential. Conversely, the behaviour of the magnetic field and dynamo processes of stars other than the Sun may inform the understanding of the model of the Solar dynamo.

As profoundly as stellar magnetic activity influences its surrounding planetary system, it is also possible that planetary systems may affect stellar activity, especially in the case of hot Jupiters - massive planets orbiting the parent star in extremely close orbits. These influences may include magnetic reconnection between the stellar and planetary magnetic field (Lanza, 2012), or anomalies on the stellar surface due to magnetic or tidal influences (Cuntz et al., 2000; Shkolnik et al., 2005; Pagano et al., 2009).

In summary, an investigation of the magnetic fields of solar-type stars with planetary systems will provide the means to understand the underlying processes that generate these fields. In addition, understanding the magnetic fields of solar-type stars forms a basis for further investigating the environment inhabited by planets and the reciprocal influences between stellar magnetic fields and orbiting planetary bodies.

The techniques of Zeeman Doppler Imaging (ZDI) have been used for some time to investigate the large-scale magnetic fields of stars, including solar-type stars (see review Donati & Landstreet, 2009); some of which are known to host planetary systems (such as Fares et al., 2013).

However, the ability to investigate stellar magnetic and activity cycles is constrained by the long-term nature of these cycles. One of the previously observed targets  $\tau$  Boötis has exhibited magnetic polarity reversals every  $\sim 360$  d, and a tentative magnetic cycle of  $\sim 720$  d (Fares et al., 2009, 2013). In 2016, Boro Saikia et al. (2016) showed evidence for the first solar-type star (61 Cyg A) to display a magnetic cycle with solar-like variations in its magnetic topology in phase with its chromospheric activity cycle. As in the Sun, the nature of these magnetic cycles provide a means of inferring the underlying dynamo process that produce the stellar magnetic field. Access to historical and new observations of  $\tau$  Boötis from the BCool<sup>1</sup> magnetic survey of solar-type stars

---

<sup>1</sup> website: <http://bcool.ast.obs-mip.fr/>; wiki: <https://bcool.irap.omp.eu/>

(Marsden et al., 2014) will allow for the investigation of possible magnetic cycles and the nature of the star-planet interaction tentatively suggested by Walker et al. (2008).

In addition, utilising telescope resources of the BCool collaboration, a survey of planet-hosting solar-type stars can be undertaken, to measure the magnetic activity of these planet hosts, to discover new targets for long-term investigation and mapping of the large-scale magnetic field and to determine the frequency of detectable magnetic activity of stars that have planetary systems. Further investigation of these planetary systems will provide valuable information as to whether solar-type dynamos are the predominant type of dynamo in stars of a similar evolutionary stage to that of the Sun.

As the magnetic fields of stars are a primary driver of phenomena that impact the space surrounding them, the choice of stars that host planetary systems allows for an investigation of the impact the magnetic phenomena may have on the planets in the system. Magnetic cycles created by the dynamo processes will periodically change the “space weather” of the surrounding environment. As such, understanding the dynamo, the magnetic field it produces and the impact this has on the surrounding space provides a means of understanding not only the star being studied, but the generalised model describing the Sun and the solar system.

## 1.1 THE SOLAR MAGNETIC FIELD

The first detection of a stellar magnetic field was that of the Sun. Hale (1908) inferred that the broadening and splitting of spectral lines in sunspots were due to the Zeeman effect. The solar magnetic field is responsible for significant phenomena that have impacts on the space surrounding our local star; sunspots, flares, coronal mass ejections all influence the environment of the entire solar system.

Additionally, the magnetic field of the Sun has played a major role in the evolution of the Sun itself and its planetary system. Magnetic braking for example, is the phenomenon whereby the Sun’s rotation is slowed by the transfer of angular momentum by the dragging of the magnetic field through the charged particles of the solar wind

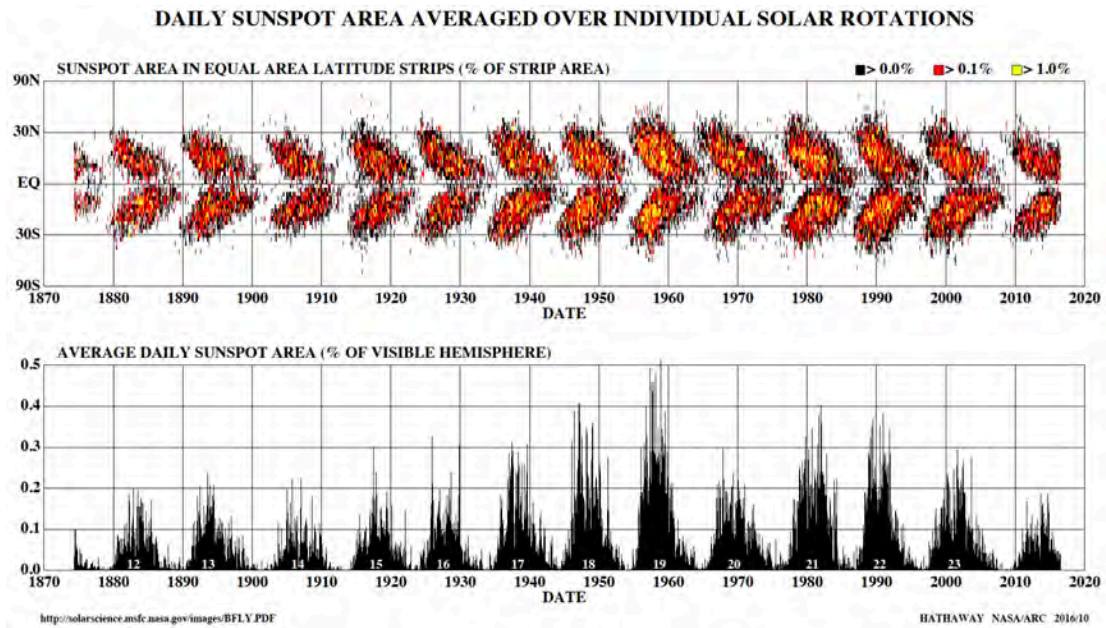


**Figure 1.1:** Solar butterfly (upper) and sunspot coverage (lower) diagrams from 1874 until 2004. The butterfly diagram (above) shows how sunspot locations migrate towards the equator during the 11-year solar cycle. The lower diagram shows how the coverage of the solar disc changes over the same cyclical period. Diagram from D.H. Hathaway, NASA Marshall Flight Center. (<http://solarscience.msfc.nasa.gov/images/bfly.pdf>; retrieved 16 February 2017.)

(Schatzman, 1962) or through a protoplanetary disc (Matt et al., 2012). Further, Muto et al. (2008) suggests that magnetic fields of young stars may impact the migration of planets, and indeed the magnetic field may contribute to the mechanisms of planetary formation (Kretke et al., 2009).

As other planetary systems are discovered, the interaction of the solar magnetic field with those of planetary bodies and the impact that “space weather” may have on the habitability of planets such as Earth has become an important area of study. Cycles of solar activity, such as the 11-year sunspot cycle first noted by Heinrich Schwabe in 1843 and illustrated by Maunder (1904) in his famous “butterfly diagram” (Fig. 1.1) have climatic impacts on the planets of the solar system.

### 1.1.1 THE SOLAR DYNAMO

While stars of different types exhibit magnetic fields, the Sun has a magnetic field that is dynamic and cyclically regenerated. In contrast to so-called “fossil” magnetic fields found in a percentage of more massive stars (e.g. Moss, 2001), which are frozen in place and decay slowly over time, the magnetic field of the Sun must be sustained by dynamo processes.

The Sun is a main-sequence G2 dwarf, and we can broadly define stars with a similar internal structure to the Sun as “solar-type” stars. Stars with masses between  $\sim 0.3M_{\odot}$  and  $\sim 1.3M_{\odot}$  exhibit three interior regions (Fig. 1.2). First, the core where thermonuclear reactions take place converting hydrogen into heavier elements. Second, the radiative zone where the density and pressure fall below that where thermonuclear reactions can be sustained, and where energy from the core is absorbed and re-emitted in random directions. And, finally, the convective zone where the stellar material becomes opaque to radiation and the trapped heat from the lower layers drives a convective process transferring this heat from the stellar interior to the surface. Below  $\sim 0.3M_{\odot}$ , stars are fully convective, while above  $\sim 1.3M_{\odot}$ , stars lack a convective zone.

As the convective zone is fluid in nature, the equator of the Sun and other solar-type stars rotates more quickly than the poles, a phenomenon that is known as differential rotation. This differential rotation is maintained through the convective envelope, but disappears at the interface between the convective and radiative zone, the latter rotating as a solid body (Thompson et al., 2003).

A moving electrically charged fluid (such as the ionised plasma of the Sun) will generate a magnetic field, and this is the basis of the dynamo process. Since the 1950s, the rotational shearing within the convective envelope and helical or cyclonic motions of convective flows have been considered to be the major components of the solar dynamo (Parker, 1955, 1977), turning the kinetic energy into magnetic energy via magnetohydrodynamic processes, sustaining and regenerating the magnetic field over time. The Babcock model (Babcock, 1961; Leighton, 1969) first described the cycle of poloidal and toroidal magnetic field conversion that is broadly accepted and discussed

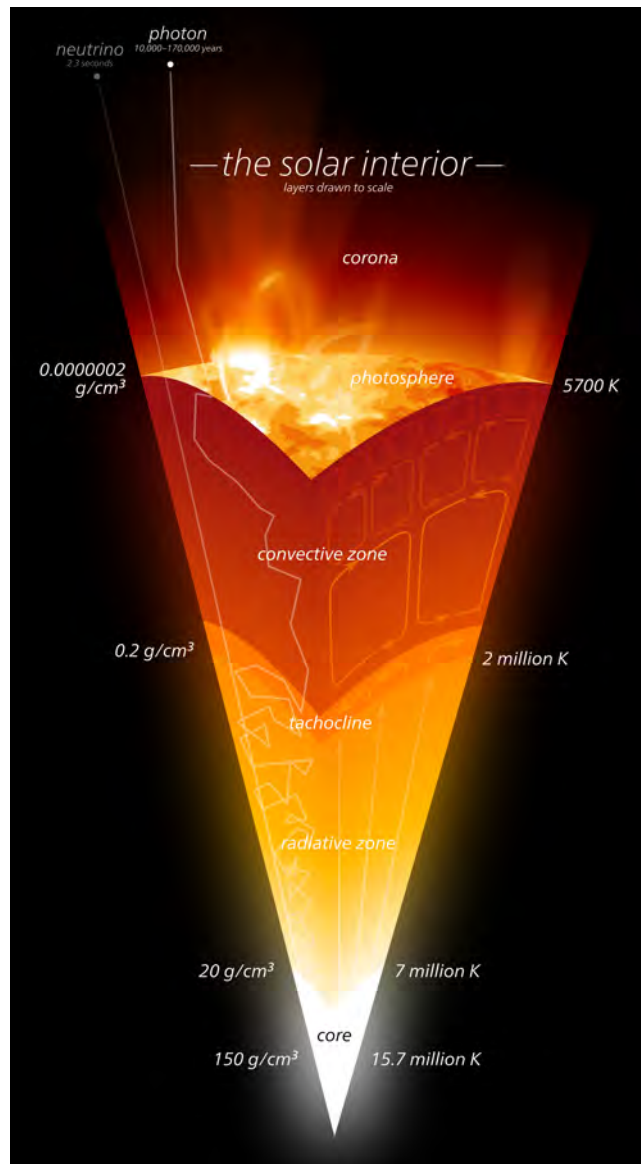


**Figure 1.2:** The Solar interior. Note how the temperature and density decrease with distance from the centre of the Sun. (By Kelvinsong (Own work) [CC BY-SA 3.0 (<http://creativecommons.org/licenses/by-sa/3.0>)], via Wikimedia Commons [https://upload.wikimedia.org/wikipedia/commons/4/43/The\\_solar\\_interior.svg](https://upload.wikimedia.org/wikipedia/commons/4/43/The_solar_interior.svg))

below, albeit with refinements, such as Dikpati & Charbonneau (1999) and Schrijver & Zwaan (2000).

#### 1.1.1.1 DIFFERENTIAL ROTATION: THE $\omega$ EFFECT

If we assume the solar magnetic field to be in an initial state of being a poloidal dipolar field (Fig. 1.3a), the differential rotation of the star will wrap the magnetic field around the Sun, converting the initial poloidal field into a toroidal field (Fig. 1.3a,b). This process is known as the  $\omega$  effect. The presence of a magnetic field in a plasma reduces the local density, and the regions of strong toroidal magnetic field begin to rise towards the stellar surface where the field erupts as a sunspot pair.

It was initially thought that this effect took place either on the stellar surface, or throughout the convective zone. However, the consensus now is that the primary location for the generation of the toroidal field is the tachocline - the interface between the convective and radiative zones. The tachocline is capable of storing the magnetic field and the rotational shear is extremely strong, resulting in magnetic fields strong enough to survive being disrupted by the turbulent convection of the convective envelope (Tobias, 2002).

#### 1.1.1.2 CONVECTION AND CORIOLIS: THE $\alpha$ EFFECT

As the toroidal magnetic field rises toward the surface, Coriolis forces and convective action twists the field in a systematic way dependent upon latitude (Fig. 1.3c). This is termed the  $\alpha$  effect. The twisting of the  $\alpha$  effect makes sunspot groups obey Joy's law, where the leading sunspot in a bipolar pair is at a lower latitude (in the northern hemisphere) than the trailing one (Hale et al., 1919). As the fields producing the sunspots decay, they are swept toward the pole by the meridional flow (Fig. 1.3d) with the following (higher latitude) polarities reconnecting with the pole and other regions connecting with other active regions. Eventually, the active regions nearest the equator in opposite hemispheres reconnect. These reconnected loops now have a poloidal component that is in the correct direction for the next part of the magnetic cycle (Fig. 1.3e,f).

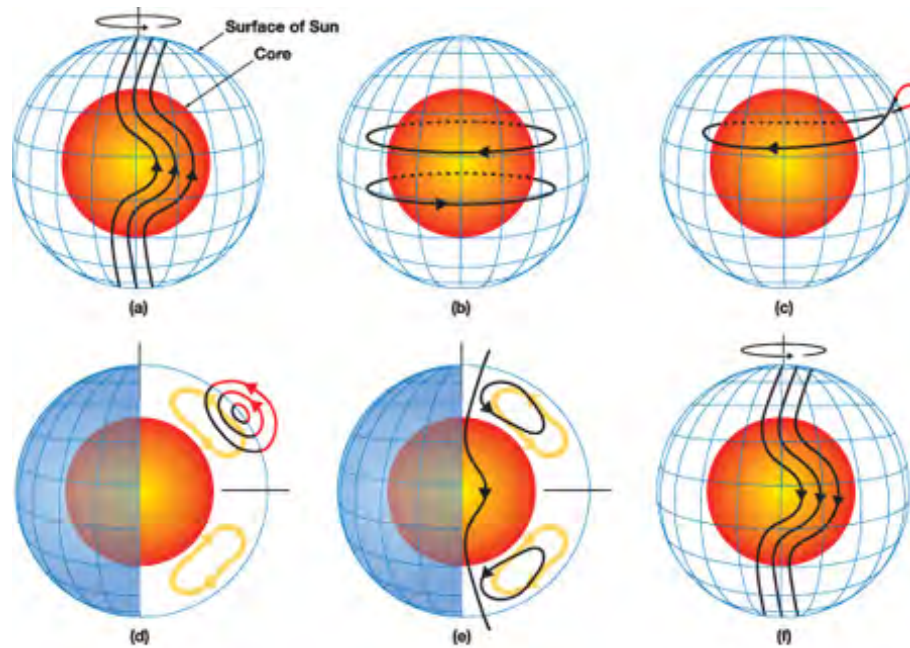
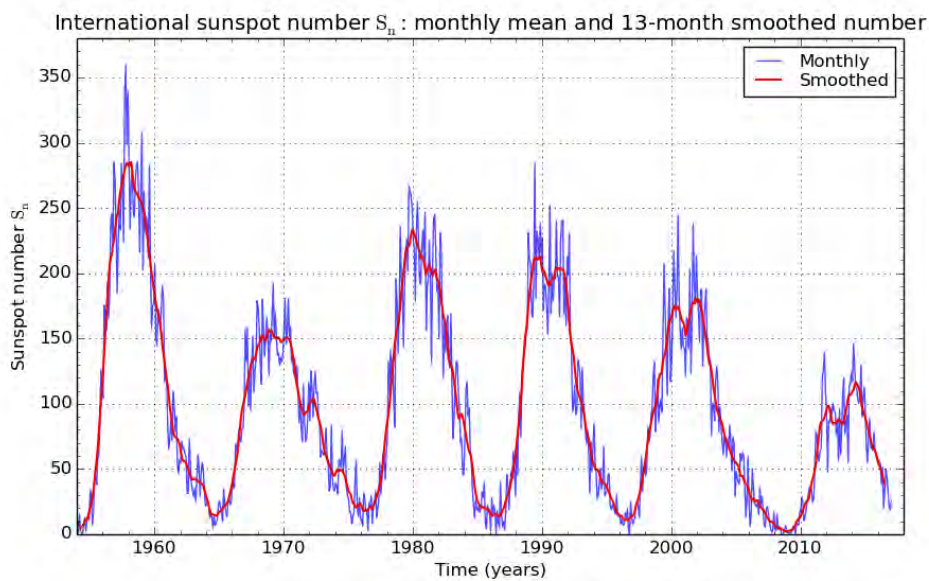


**Figure 1.3:** The solar dynamo and the recycling of magnetic fields. The convective zone is shown in white, the radiative zone in orange. Due to differential rotation, the poloidal magnetic field (a) is wrapped into a toroidal field (b). The toroidal field rises to the surface, twisting and emerging as sunspots (c). Magnetic flux emerges and spreads outward as the spots decay. Panels (d) and (e) show the meridional flow (yellow) carrying the surface magnetic flux toward the poles. This reverses the polar field and the process starts over (f). (Illustration by Mausumi Dikpati, National Center for Atmospheric Research; <http://www.ucar.edu/communications/quarterly/spring06/images/dikpati.jpg>; Retrieved 05 October 2014)

### 1.1.2 SOLAR CYCLES

As noted previously, the Sun exhibits cyclic activity. Most well-known is the 11-year sunspot cycle (Fig. 1.1, Fig. 1.4), also known as the Schwabe cycle. The number of sunspots observed on the solar disc rises and falls over the cycle. Hale (1908) determined that sunspots were magnetic phenomena and also noted (Hale et al., 1919) that the polarity of the sunspot pairs reverses from cycle to cycle. Sunspots are magnetic phenomena; hence the sunspot cycle is indicative of the magnetic activity of the Sun. As Hathaway (2010) summarises in his review paper of the solar cycle, the sunspot number is correlated with other measures of solar activity, including total solar irradiance (TSI, Fig. 1.5), 10.7 cm solar flux (the peak wavelength of solar radio emission), flare and coronal mass ejection activity.



SILSO graphics (<http://sidc.be/silso>) Royal Observatory of Belgium 2017 February 1

**Figure 1.4:** Monthly and smoothed sunspot number over the preceding six Schwabe cycles. Diagram from World Data Center for the production, preservation and dissemination of the international sunspot number, Royal Observatory of Belgium. (<http://www.sidc.be/silso/monthlyssnplot>; retrieved 16 February 2017; SILSO data/image, Royal Observatory of Belgium, Brussels)

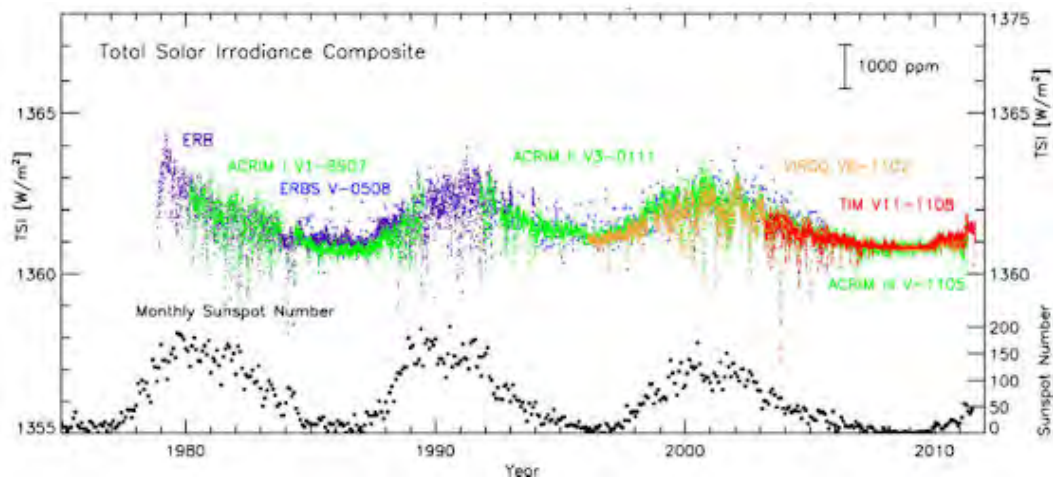


**Figure 1.5:** Total Solar Irradiance (TSI) and sunspot number showing the correlation between the two. Diagram from G. Kopp, University of Colorado. ([http://science.nasa.gov/science-news/science-at-nasa/2013/08jan\\_sunclimate/](http://science.nasa.gov/science-news/science-at-nasa/2013/08jan_sunclimate/); retrieved 05 October 2014.)

In addition to the strong 11-year cycle, there are other magnetic or activity cycles, described by [Hathaway \(2010\)](#) as “weak quasi-periodicities” on longer time-scales such as the 7- or 8-Schwabe-cycle Gleissberg cycle ([Gleissberg, 1939](#)) and on shorter time-scales such as a 154-day period in gamma ray flare activity ([Rieger et al., 1984](#)).

It is clear that the Sun exhibits cyclic activity that is reflective of its underlying physical and dynamo processes. Thus the investigation of whether similar cycles are observed in other stars will also give an insight into their dynamo processes.

## 1.2 STELLAR MAGNETIC FIELDS

Given that the Sun exhibits magnetic activity, it was suspected that other stars would also be magnetically active. [Babcock \(1947\)](#) made the first detection of a Zeeman effect and hence a magnetic field on the chemically peculiar star 78 Vir. Subsequently, using different techniques, magnetic fields have been detected on stars of various masses, temperatures and evolutionary status. The discovery of pulsars ([Bell & Hewish, 1967](#)) was quickly followed by the realization that these objects were neutron stars with very strong magnetic fields ([Pacini, 1967](#)). Strong magnetic fields were then discovered on a white dwarf (Grw+70°8247) by [Kemp et al. \(1970\)](#). The first direct detection of magnetic fields on stars considered to be solar-type was by [Robinson et al. \(1980\)](#);  $\xi$  Boo A (G8V) and 70 Oph A (K0).

Since these first discoveries, magnetic fields have been discovered on numerous stars across the HR diagram. Of these, several stars similar in structure to the Sun have been repeatedly observed over many years, examining the surface magnetic topologies and if and how they evolve over time. These first well-studied stars include AB Dor, LQ Hya and HR 1099 (e.g. [Donati & Cameron, 1997](#); [Cameron & Donati, 2002](#); [Donati et al., 2003](#)). These initial observations began to provide insights into the processes which generate magnetic fields in solar-type stars.

[Donati & Landstreet \(2009\)](#) note that low-mass stars all show magnetic fields and activities (e.g. flares, prominences, winds and activity cycles) most likely indicating that these magnetic fields are the result of dynamo processes due to the interaction of

rotation and convection. Amongst stars of higher masses, only a very small proportion exhibit magnetic activity, but these fields appear to be simpler and less variable than those of lower-mass stars, likely indicating a different origin such as fossil fields.

Most mature stars considered solar-type exhibit low or moderate activity and phenomena similar to that seen on the Sun. Thus it has been logical to assume that the interface dynamo thought to be active in the Sun would be analogous to that found in solar-type stars of a similar evolutionary stage. Studies of solar-type stars other than the Sun have confirmed that while conventional theories of dynamo processes present the most likely models, observations show divergence from typical solar magnetic behaviour (e.g. toroidal fields at the stellar surface). These observations may indicate that a distributed dynamo shaped by near-surface shear (Donati & Cameron, 1997; Donati et al., 2003) may be at play, especially in stars with rapid rotation or shallow convective envelopes, or both.

The study of the magnetic fields of stars at different evolutionary stages can give an insight into the evolution of the Sun's dynamo, while the study of solar-type stars, in general, may give clues as to more general theories of stellar dynamos.

### 1.3 DETECTING AND MODELLING STELLAR MAGNETIC FIELDS

#### 1.3.1 DETECTING MAGNETIC FIELDS

In the presence of a magnetic field, spectral lines are observed to broaden or split (the Zeeman effect). While high-precision spectroscopy alone may resolve this effect, examining the polarisation of light emitted in the presence of the magnetic field reveals the orientation of the field (see Fig 1.6). When encountering a magnetic field parallel to the line-of-sight, two symmetric oppositely polarised  $\sigma$ -components and a central linearly-polarised  $\pi$ -component are produced. A magnetic field orthogonal to the line-of-sight results in the  $\sigma$  components being linearly polarised perpendicular to the magnetic field and the  $\pi$ -component being linearly polarised parallel to the magnetic field. In astronomy, the polarisation parameters are expressed in terms of the Stokes parameters (McMaster, 1961; Collett, 2005);  $I$  being a measure of the total in-

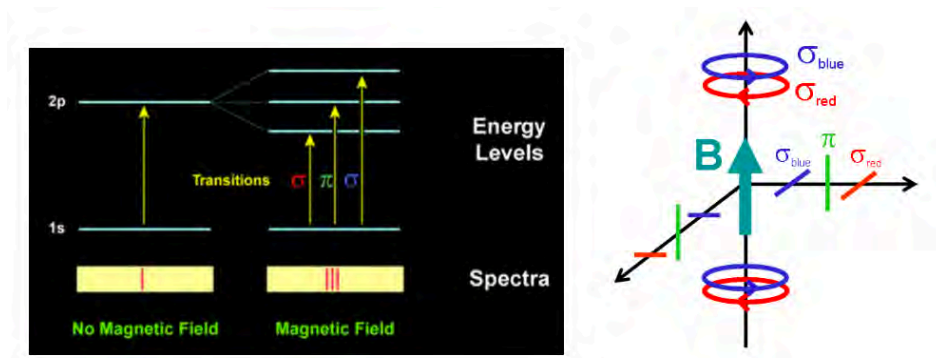


**Figure 1.6:** Simplified diagram showing Zeeman splitting (left panel) and the effect of viewing angle relative to magnetic field direction (right panel). When the magnetic field is parallel to the line-of-sight,  $\sigma$ -components are circularly polarised. When the magnetic field is orthogonal to line-of-sight,  $\sigma$  components being linearly polarised perpendicular to the magnetic field and the  $\pi$ -component parallel to the magnetic field. Reproduced from [Reiners \(2010, Fig. 1\)](#).

tensity,  $Q$  and  $U$  representing the linearly polarised components and  $V$  representing the circularly-polarised component. As shown in Fig. 1.7, Stokes  $Q$  is the difference in intensity of light polarised along two orthogonal axes, Stokes  $U$  is similar to Stokes  $Q$ , with the axes rotated 45 degrees relative to those in  $Q$ . Stokes  $V$  is the difference between the intensity of the left- and right-hand circular polarised light.

Usually, only the Stokes  $V$  parameter is used in investigations of magnetic fields, as the linearly polarised components tend to cancel more completely than the circularly polarised ([Wade et al., 2000](#)) components and are thus generally too small to be detected. [Stenflo \(2013\)](#) additionally shows that for the weak field case (where  $B \lesssim 0.5$  kG), Stokes  $Q$  and  $U$  are proportional to the second derivative of the Stokes  $I$  profile, while Stokes  $V$  is proportional to the first derivative of Stokes  $I$ . Thus, while Stokes  $V$  scales linearly with the line-of-sight component of the magnetic field, the linear polarisation (comprised of the Stokes  $Q$  and  $U$ ) scales with the square of the transverse magnetic field. This results in intrinsically smaller signatures in Stokes  $Q$  and  $U$  compared to Stokes  $V$ , given the same magnetic field strength in the relevant component. [Stenflo \(2013\)](#) also shows that due to the non-linear relationship with the underlying magnetic field strength, noise is a more serious problem for the linear polarisation components than for the circular component. Recently the first cool star to

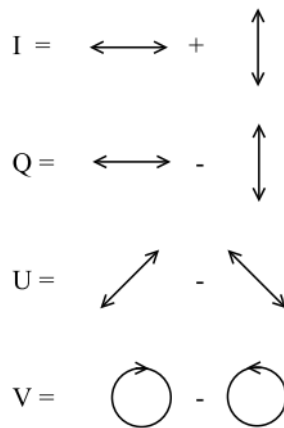


**Figure 1.7:** Schematic of the combination of polarisation states to produce the Stokes parameters.

be imaged using all Stokes parameters was achieved (Rosén et al., 2013, 2014) for the very active giant star II Peg. As technology and techniques improve, further stars may be imaged using all four Stokes parameters.

The Stokes parameters can be measured directly using the technique of spectropolarimetry, where a polarimeter is attached to a high-resolution spectrograph. By using an échelle spectrograph, it is possible to measure the Zeeman signatures of many hundreds or thousands of lines in the spectrum. Typically the Zeeman signatures are extremely small; of the order of 0.1% of the amplitude of the unpolarised continuum. Donati et al. (1997) indicates that the relative noise levels for the Stokes  $V$  profile must be of the order of  $10^{-4}$  in order to make an unambiguous detection of the magnetic field. Achieving this is not possible utilising a single spectral line within a given spectrum unless the star is extremely bright. Donati et al. (1997) developed a cross-correlation method called Least-Squares Deconvolution (LSD), which is used to derive an average Zeeman signature (e.g. Fig. 1.8) from all medium and high-intensity spectral lines (including duplicate lines in échelle order overlaps). Using LSD achieves a multiplex gain of up to 30 times in signal-to-noise for solar-type stars.

Figure 1.8 illustrates an example of an LSD profile calculated from a spectrum from the star  $\tau$  Boötis collected using the NARVAL instrument at Telescope Bernard Lyot

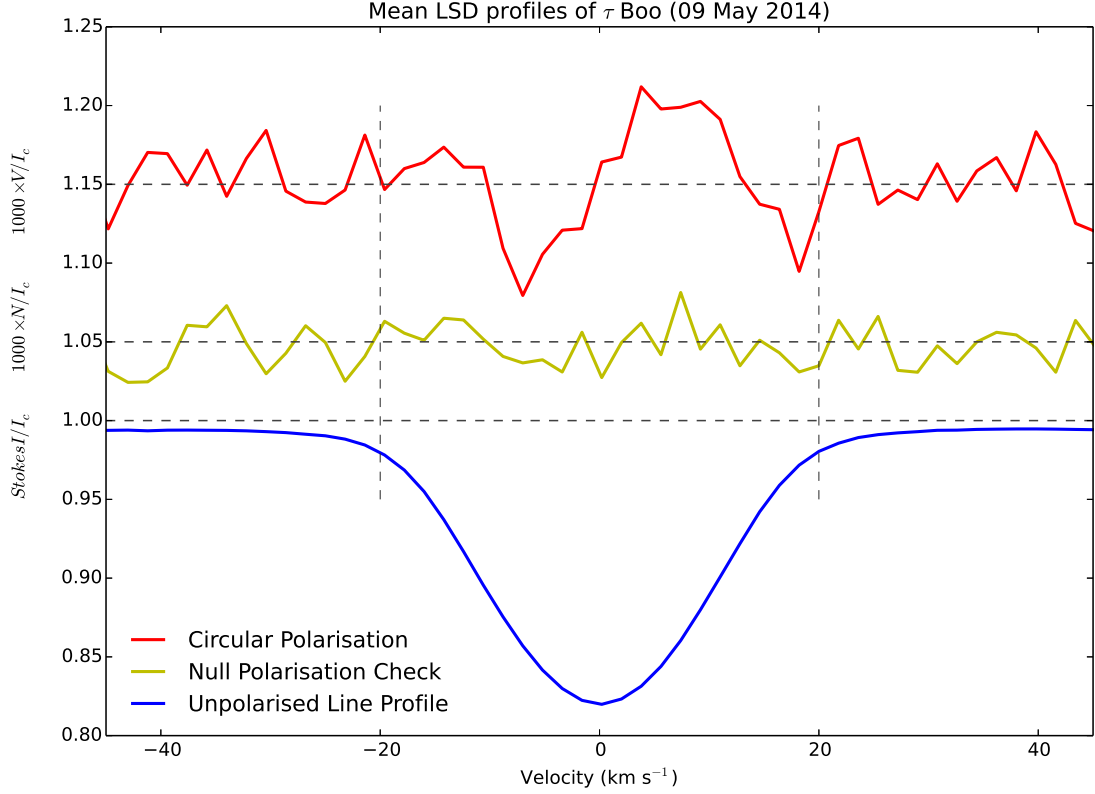


**Figure 1.8:** Circular polarisation (red line), null polarisation check (yellow line) and unpolarised line profile (blue line). The circular polarisation and null checks are expanded by 1000 and shifted for graphical purposes. These profiles are derived from NARVAL data for the star  $\tau$  Boötis. A Zeeman signature is detected with no signal in the null polarisation check in the line profile velocity interval from equation 1.1 (vertical dashed lines). From current work by the author.

(TBL) at Pic du Midi. In this case, a Zeeman signature indicating a magnetic detection is found as shown by the variation in the Stokes  $V$  profile. The three profiles shown are the Stokes  $V$  (in red), Stokes  $I$  (blue) and a null polarisation profile ( $N$ , in yellow; used to check for spurious signals; see Sec. 1.3.2 for more information). For a Zeeman signature to be considered a magnetic detection, the signal must be present in  $V$  but not  $N$ , and it must be located within the line profile velocity interval corresponding to:

$$(v_{rad} - v \sin i) < v < (v_{rad} + v \sin i) \quad (\text{I.I})$$

where  $v_{rad}$  is the radial velocity of the star (in Fig. 1.8,  $v_{rad}$  has been corrected to zero)

and  $v \sin i$  is the line-of-sight projected equatorial rotation velocity.

### 1.3.2 OBSERVATIONAL PROCEDURE FOR GENERATING STOKES PARAMETERS

Observations are obtained using the polarimetric mode of a spectropolarimeter such as NARVAL (attached to the T telescope Bernard Lyot located at Observatoire du Pic du Midi) or ESPaDOnS (at the Canada-France Hawaii Telescope). NARVAL is a clone of ESPaDOnS, and as such is described here for explanatory purposes. NARVAL is composed of a bench mounted high resolution spectrograph and a Cassegrain-mounted polarimetry module. The spectrograph has an optical wavelength coverage of 370 to 1000 nm, and a resolution of  $\sim 65000$  with a pixel size of  $2.6 \text{ km s}^{-1}$ .

The polarimetric module performs polarimetry over the entire spectral range using a series of three Fresnel rhombs. The light is then split into two beams containing opposite polarisation states. These two beams are fed via individual fibres to the spectrograph, allowing the simultaneous capture of both polarisation states and further allowing the unpolarised Stokes  $I$  and circularly-polarised Stokes  $V$  spectra to be determined from each observation. Further information on NARVAL can be found in [Auri ere \(2003\)](#).

Each Stokes  $V$  observation consists of a sequence of four individual exposures. Effectively, this results in eight individual spectra; four left-hand and four right-hand circularly polarised. As described by [Petit et al. \(2003\)](#), the polarisation states in the fibre pair described above are alternated during the sequence to help eliminate instrumental effects; the first and fourth exposures have one arrangement of polarisation states whilst the second and third have the opposite arrangement. Adding all eight spectra yields the unpolarised Stokes  $I$  (intensity) spectrum. The polarised Stokes  $V$  spectrum is obtained as per [Donati et al. \(1997, Eqs. 1, 2\)](#):

$$\frac{V}{I} = \frac{R_V - 1}{R_V + 1} \quad (1.2)$$

where

$$R_V^4 = \frac{i_{1,\perp}/i_{1,\parallel}}{i_{2,\perp}/i_{2,\parallel}} \frac{i_{4,\perp}/i_{4,\parallel}}{i_{3,\perp}/i_{3,\parallel}} \quad (1.3)$$

and  $i_{k,\perp}$  and  $i_{k,\parallel}$  are the two polarised spectra in each exposure,  $k$ .

By destructively adding the spectra, a null polarisation spectrum,  $N$ , can be obtained (Donati et al., 1997, Eqs. 1, 3):

$$\frac{N}{I} = \frac{R_N - 1}{R_N + 1} \quad (1.4)$$

where

$$R_N^4 = \frac{i_{1,\perp}/i_{1,\parallel}}{i_{4,\perp}/i_{4,\parallel}} \frac{i_{2,\perp}/i_{2,\parallel}}{i_{3,\perp}/i_{3,\parallel}} \quad (1.5)$$

As described in Bagnulo et al. (2009), a significant signal (i.e. deviation from zero) in the  $N$  spectrum may be indicative of a spurious polarisation signal in the Stokes  $V$  profile.

### 1.3.3 ZEEMAN DOPPLER IMAGING

Once a magnetic field is detected, a process called Zeeman Doppler Imaging or ZDI (Brown et al., 1991; Donati et al., 1997) is applied to a time sequence of observations over the stellar rotation period to reconstruct the surface magnetic topology of the star. Zeeman Doppler Imaging uses the same principles as Doppler Imaging (Vogt et al., 1987), utilising the Stokes  $V$  parameter rather than Stokes  $I$ . The code used in this work was developed by Brown et al. (1991) and Donati et al. (1997), which implements the Skilling & Bryan (1984) algorithm for maximum entropy reconstruction. The maximum entropy reconstruction generates tomographic maps that contain the minimum information (magnetic features) required to produce the observed Stokes  $V$  LSD profiles within the noise level of the data.

Figures 1.9-1.12 illustrate the basic principles of ZDI (Semel, 1989; Brown et al., 1991; Donati et al., 1997, 2003). The visible disc of the star can be divided into regions

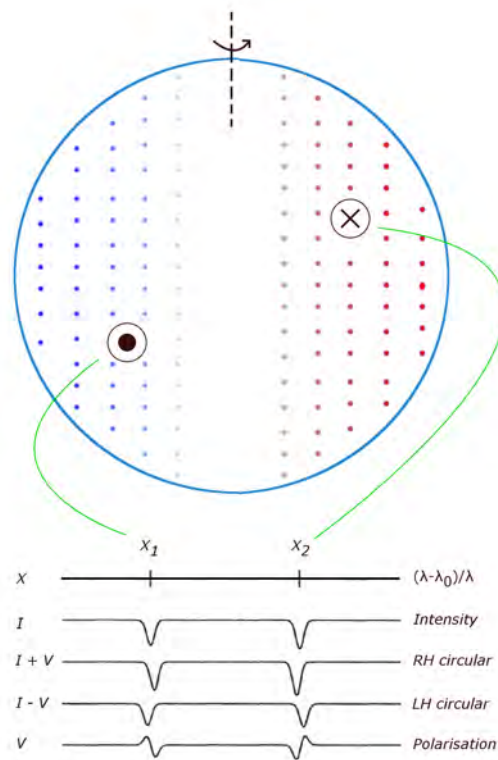


**Figure 1.9:** Principles of Zeeman Doppler Imaging. Two arbitrary magnetic regions of opposite polarity are present on the stellar disc. The disc is separated into areas of equal radial velocity; the blue approaching the observer, red receding from the observer. The contributions to the stellar spectral line from each of the spots appear at  $X_1$  and  $X_2$ , separated by Doppler shift in the wavelength domain. The intensity profile is  $I$ . Each magnetic field induces small opposite wavelengths shifts of the corresponding absorption profile in the right- and left-hand circularly polarised spectra ( $I + V$  and  $I - V$  respectively, where  $V$  is the circular polarisation Stokes parameter). The difference between the profiles  $I + V$  and  $I - V$  results in  $V$ , which has a characteristic shape based on the location of the magnetic regions on the surface of the star. Image adapted from [Carter et al. \(1996\)](#)

of equal rotational velocity. Spectral lines are broadened by the Doppler effect, and zones of equal velocity contribute to the spectral lines at a position according to their Doppler shifted wavelength.

A region of magnetic activity will result in polarised light, and by observing in left- and right-hand circularly polarised light, information on the orientation and intensity of the localised magnetic field can be derived.

The orientation and location of the magnetic lines (radial, azimuthal or meridional - see Fig. 1.10) can be inferred as regions transit the stellar disc. Azimuthal field com-

ponents that are aligned with lines of latitude will reverse sign as they transit the line-of-sight and appear more intense near the stellar limb as their orientation aligns with the observer and can almost disappear from view while crossing the centre of the disc (Fig. 1.11). Radial field lines remain constant in sign and appear most intense as they cross the line-of-sight, aligned with the observer (Fig. 1.12). Meridional field components are more difficult to detect unambiguously as they can appear to be radial in nature depending upon the inclination of the star and the line-of-sight relative to the observer. Donati & Brown (1997) conclude that crosstalk between radial and meridional components is evident at both high inclination angles and low with the directionality of the crosstalk reversed between these cases.

Knowing where peak and minimum intensities of features occur, the longitude of the types of features can be inferred. Similarly, the maximum Doppler shift exhibited by a feature is an indication of its latitude - features that are at higher latitudes (i.e. closer to the pole) will always remain closer to the axis of rotation, meaning that their peak Doppler shift will be less than features closer to the equator. Indeed, depending upon the inclination of the star, features at polar latitudes may remain constantly visible.

Utilising a series of Stokes  $V$  profiles from observations at different phases of the star's rotation, the topology which will generate the best fit to the observed profiles is produced using tomographic techniques. As the problem of determining the best fit is ill-posed, the aforementioned maximum entropy technique is used to choose the simplest configuration consistent with the observations.

The initial implementation of code by Donati et al. (1997) calculated individual pixels for the magnetic images; however the current implementation as described in Donati et al. (2006) reconstructs the field topology as a spherical-harmonic decomposition and applies the maximum entropy method. The Donati et al. (2006) method produces three maps of the stellar surface, one for each of the three components of the magnetic field- radial, meridional and azimuthal (Fig. 1.10, Eqs 1.6,1.7,1.8).

A significant advantage of utilizing the spherical harmonic decomposition method that is now common in ZDI codes, such as those described by Donati et al. (2006) and

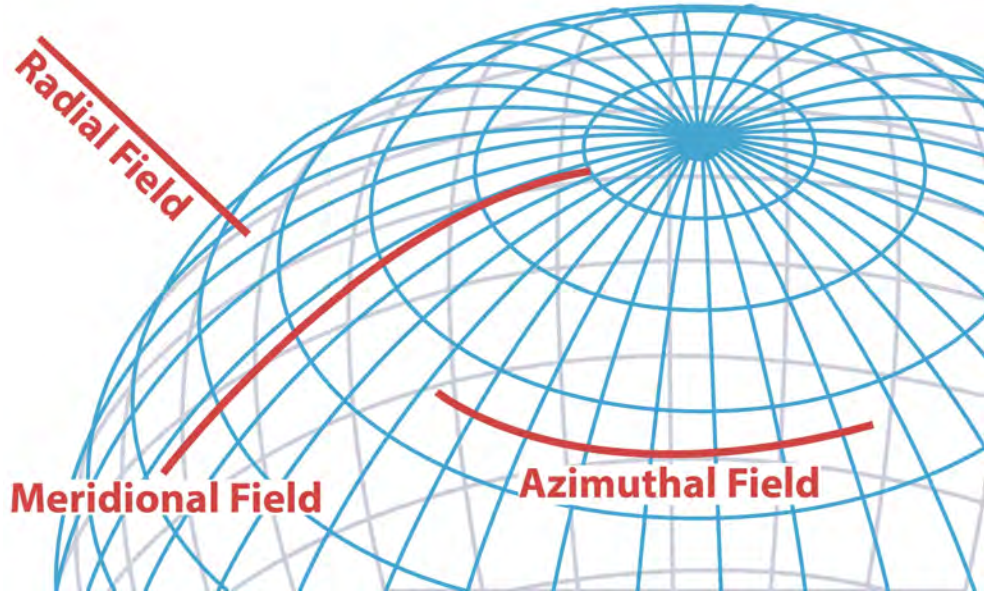


**Figure 1.10:** Zeeman Doppler Imaging reconstructs the three field components of the large-scale magnetic field: radial perpendicular to the stellar surface, azimuthal along the parallels and meridional along the stellar meridians. Image by the author.

Kochukhov et al. (2014), is that the field topology can be quantitatively characterised. The general form of the harmonics, implemented by Donati et al. (2006) as the sum of a potential (poloidal) and non-potential (toroidal) component is expressed by

$$B_r(\vartheta, \phi) = - \sum_{l,m} \alpha_{l,m} Y_{l,m}(\vartheta, \phi) \quad (1.6)$$

$$B_m(\vartheta, \phi) = - \sum_{l,m} [\beta_{l,m} Z_{l,m}(\vartheta, \phi) + \gamma_{l,m} X_{l,m}(\vartheta, \phi)] \quad (1.7)$$

$$B_a(\vartheta, \phi) = - \sum_{l,m} [\beta_{l,m} X_{l,m}(\vartheta, \phi) - \gamma_{l,m} Z_{l,m}(\vartheta, \phi)] \quad (1.8)$$

where  $Y_{l,m}(\vartheta, \phi)$ ,  $Z_{l,m}(\vartheta, \phi)$  and  $X_{l,m}(\vartheta, \phi)$  are spherical-harmonic functions of degree  $l$ , order  $m$  and their derivative with respect to latitude  $\vartheta$  and longitude  $\phi$  (see Donati et al., 2006). The complex coefficient  $\alpha_{l,m}$  characterises the radial field (which

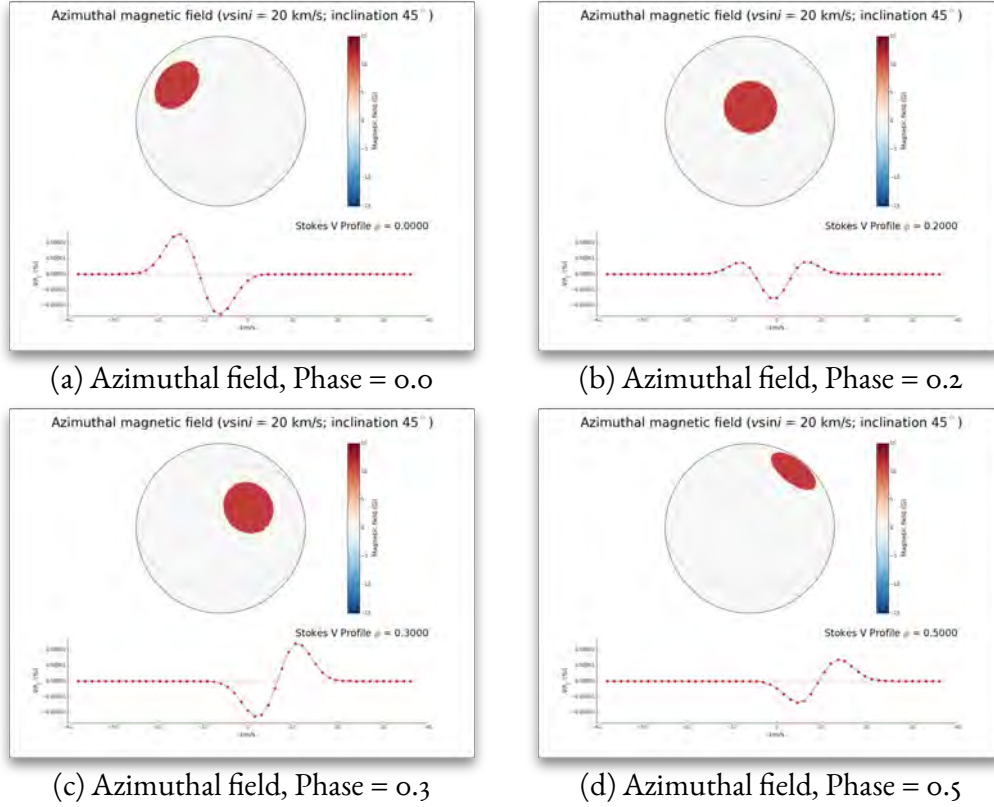


**Figure 1.11:** For an idealised region of azimuthal magnetic field, the Stokes  $V$  signature intensifies when it is closest to the limb of the visible disk. The sign reverses as it crosses the line-of-sight of the observer. This allows the determination of the longitude of the feature. The point in the velocity domain at which the feature reaches a maximum (or disappears) provides information about its latitude. (a)-(d) show the star at rotational phases 0.0, 0.2, 0.3 and 0.5 respectively (top panels) and the idealised Stokes  $V$  profiles (lower panels). A larger animation from which this plot is derived is included in the additional material accompanying the electronic version of this thesis.

is the vertical component of the poloidal, or potential, field).  $\beta_{l,m}$  characterises the horizontal component of the potential field. Finally,  $\gamma_{l,m}$  characterises the toroidal, or non-potential field. The use of spherical harmonics provides a straightforward method to calculate the relative amount of energy, for example in toroidal and poloidal field, or the degree of axisymmetry of the field.

For example, eleven observations of  $\tau$  Boötis were made in December 2013 (see Table 1.1) using the NARVAL instrument at TBL. As  $\tau$  Boötis has a closely orbiting hot Jupiter, the spectra were corrected for variations in radial velocity due to the orbital motion of the planet. The LSD profiles for the Stokes  $V$  parameter were produced

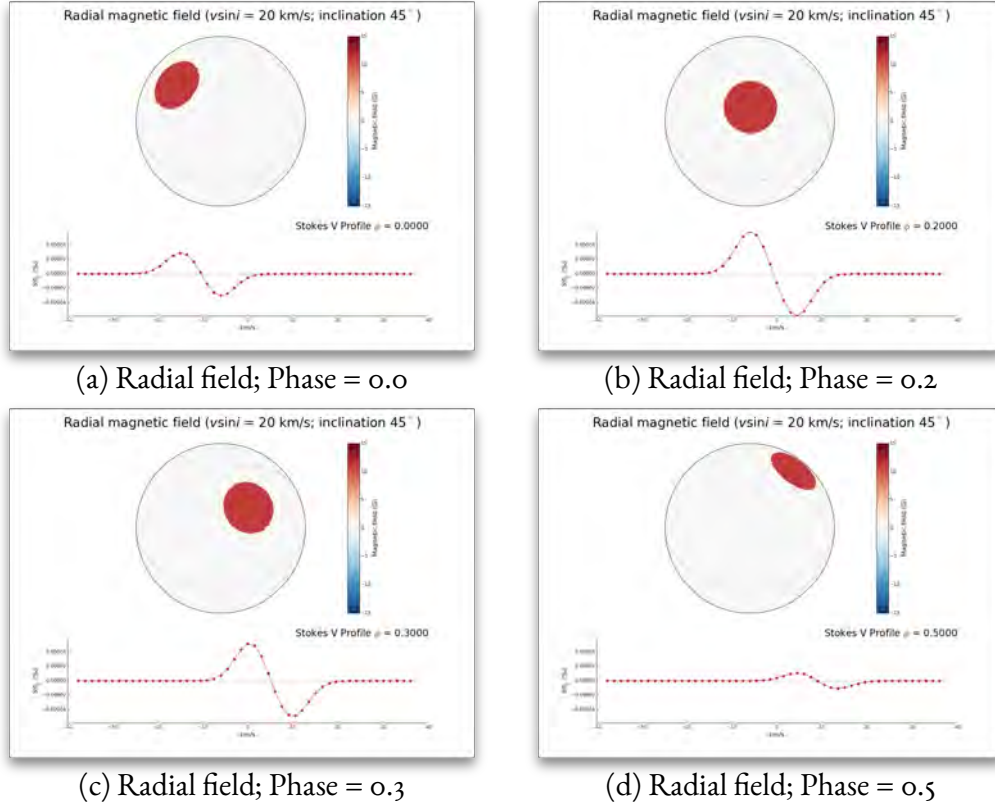


**Figure 1.12:** For an idealised region of radial magnetic field, the Stokes  $V$  signature intensifies as it crosses the line of sight and remains the same sign throughout its transit. This allows the determination of the longitude of the feature. The point in the velocity domain at which the feature reaches a minimum (or disappears) provides information about its latitude. (a)-(d) show the star at rotational phases 0.0, 0.2, 0.3 and 0.5 respectively (top panels) and the idealised Stokes  $V$  profiles (lower panels). A larger animation from which this plot is derived is included in the additional material accompanying the electronic version of this thesis.

and are shown in Figure 1.13. The red lines indicate the actual Stokes  $V$  profiles from the observations, while the black lines show the profiles from the reconstructed maps.

Figure 1.14 illustrates the corresponding set of maps generated by the Zeeman Doppler Imaging process for each magnetic component - radial, azimuthal and meridional.

### 1.3.3.1 RADIATIVE TRANSFER IN THE PRESENCE OF A MAGNETIC FIELD

Fundamental to the understanding of the production of stellar spectra is the concept of radiative transfer. For a plane-parallel atmosphere, the radiative transfer equation

**Table 1.1:** Journal of observations of  $\tau$  Boötis, December 2013 from the NARVAL instrument at TBL. Columns list the UT date, the heliocentric Julian date (at mid-exposure), the UT time (at mid-exposure), the exposure time, the peak signal-to-noise ratio (SNR) of each observation around 700 nm, the rotational cycle from the ephemeris, the rotational phase (0.0 being approximately the centre of the observing run), the radial velocity (RV) associated with each exposure, and whether a magnetic signature is detected (D), marginally detected (M) or is below the detection threshold (N). From work by the author, incorporated into the paper presented in Chapter 2.

Date	HJD (245 5000+)	UT (h:m:s)	$T_{exp}$ (s)	SNR	Cycle	$\phi_{rot}$	RV (km s <sup>-1</sup> )	Detection
04-Dec-2013	1630.73709	05:46:20	4 × 600	1408	959.936	-3.064	-16.822	N
05-Dec-2013	1631.72401	05:27:25	4 × 600	1318	960.234	-2.766	-16.164	D
06-Dec-2013	1632.73127	05:37:48	4 × 600	1280	960.538	-2.462	-16.735	N
07-Dec-2013	1633.71947	05:20:42	4 × 600	1202	960.837	-2.164	-16.993	M
08-Dec-2013	1634.71910	05:20:05	4 × 600	1484	961.138	-1.862	-16.268	D
09-Dec-2013	1635.74031	05:50:32	4 × 600	1479	961.447	-1.553	-16.444	D
11-Dec-2013	1637.72461	05:27:44	4 × 600	1259	962.046	-0.954	-16.520	M
12-Dec-2013	1638.71993	05:20:54	4 × 600	1546	962.346	-0.654	-16.257	D
13-Dec-2013	1639.73536	05:43:02	4 × 600	1505	962.653	-0.347	-17.022	D
15-Dec-2013	1641.72308	05:25:09	4 × 600	1381	963.253	0.253	-16.116	N
17-Dec-2013	1643.75082	06:04:53	4 × 600	1483	963.865	0.865	-16.923	D
21-Dec-2013	1647.73550	05:42:25	4 × 600	1447	965.068	2.068	-16.403	N

is usually expressed as

$$\cos \vartheta \frac{dI_\nu}{d\tau_\nu} = I_\nu - S_\nu \quad (\text{I.9})$$

where  $dI_\nu$  is the change in intensity of light at a given wavelength,  $\nu$ ,  $\tau_\nu$  is the optical depth.  $S_\nu$ , the source function, is the ratio of the emission coefficient of the gas to the absorption coefficient. Finally,  $\vartheta$  is the angle between the line-of sight and the radial direction of the light from the centre of the star. As the optical depth depends on opacity, this equation 1.9 is often expressed in terms of the optical depth based on continuum opacity ( $\tau_\nu^c$ ) and the line-to-continuum opacity,  $\eta_\nu$ :

$$\cos \vartheta \frac{dI_\nu}{d\tau_\nu^c} = I_\nu(1 + \eta_\nu) - S_\nu(1 + \eta_\nu) \quad (\text{I.10})$$

If local thermal equilibrium is assumed, then  $S_\nu$  becomes equivalent to the Planck function  $B_\nu(T)$ .

In the presence of a magnetic field, the radiative transfer equation can be expressed

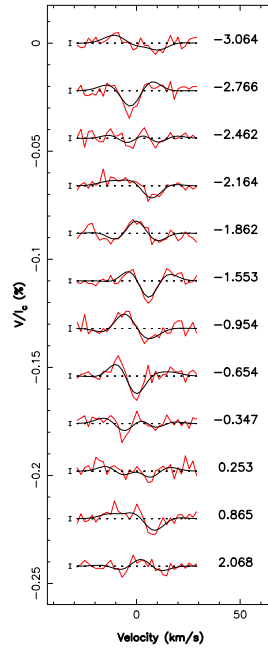


**Figure 1.13:** Stokes  $V$  parameters for  $\tau$  Boötis from December 2013. The observed profiles are shown in red, while synthetic profiles are shown in black. On the left of each profile we show a  $\pm 1\sigma$  error bar. The rotational cycle of each observation is indicated on the right of each profile. From current work by the author.

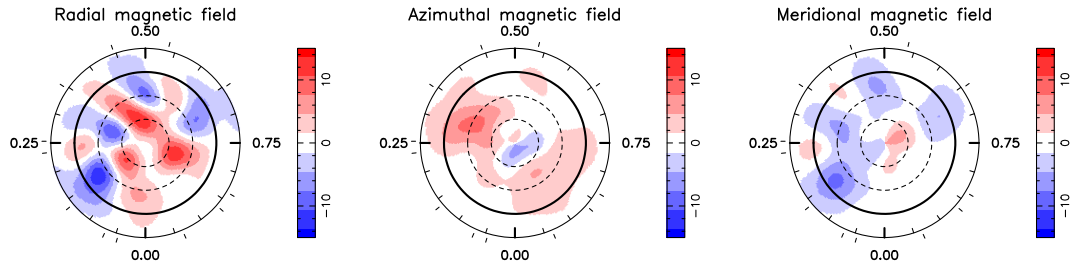


**Figure 1.14:** Magnetic maps for  $\tau$  Boötis from December 2013. The star is shown in flattened polar projection down to a latitude of  $-30^\circ$ . The equator is depicted as a bold circle and parallels as dashed circles. The radial ticks around each plot indicate rotational phases of observations. From current work by the author.

in terms of the four coupled equations for the Stokes parameters ( $I$ ,  $V$ ,  $U$ ,  $Q$ ) as in Landi Degl'Innocenti (1976). Following Rees et al. (1989), Folsom (2013) presents the

following formulation in terms of the Stokes vector,  $\mathbf{I}$

$$\mathbf{I} = \begin{pmatrix} I \\ Q \\ U \\ V \end{pmatrix} \quad (1.11)$$

such that

$$\cos \vartheta \frac{d\mathbf{I}}{d\tau_\nu^c} = \mathbf{K}\mathbf{I} - \mathbf{j} \quad (1.12)$$

where  $\mathbf{K}$ , the total absorption matrix is

$$\mathbf{K} = \mathbf{I} + \eta_\nu \Phi \quad (1.13)$$

$\mathbf{I}$  is the  $4 \times 4$  identity matrix and  $\eta_\nu$  is the line-to-continuum opacity.  $\mathbf{j}$  is the emission vector. Assuming, LTE,  $\mathbf{j}$  takes the form

$$\mathbf{j} = B_\nu(T)\mathbf{e}_o + \eta_\nu B_\nu(T)\Phi\mathbf{e}_o \quad (1.14)$$

where  $\mathbf{e}_o = (1, 0, 0, 0)^T$  and  $B_\nu(T)$  is the Planck function. The matrix  $\Phi$  contains coefficients for absorption ( $\phi$ ) and anomalous dispersion ( $\phi'$ ):

$$\Phi = \begin{pmatrix} \phi_I & \phi_Q & \phi_U & \phi_V \\ \phi_Q & \phi_I & \phi'_V & -\phi'_U \\ \phi_U & -\phi'_V & \phi_I & \phi'_Q \\ \phi_V & \phi'_U & -\phi'_Q & \phi_I \end{pmatrix} \quad (1.15)$$

The definitions of the coefficients are not reproduced here, but can be found in [Rees et al. \(1989, Eq. 7\)](#). Rewriting this formulation in the same form as equation 1.10, the radiative transfer equation in the presence of a magnetic field can be this expressed as

$$\cos \vartheta \frac{d\mathbf{I}}{d\tau_\nu^c} = (\mathbf{I} + \eta_\nu \Phi)\mathbf{I} - (\mathbf{I} + \eta_\nu \Phi)\mathbf{e}_o B_\nu(T) \quad (1.16)$$

There are various methods for solving the radiative transfer equations, and these methods have been implemented in ZDI codes. The code described by [Piskunov & Kochukhov \(2002\)](#) implemented the Diagonal Element Lambda Operator (DELO) method described by [Rees et al. \(1989\)](#). [Donati et al. \(2017\)](#) utilises a new version of the [Donati et al. \(1997, 2006\)](#) code which utilises the Unno-Rachkovsky solution to the problem ([Unno, 1956](#); [Rachkovsky, 1962](#); [Landi Degl’Innocenti & Landolfi, 2004](#)). [Kochukhov & Wade \(2016\)](#) also describe a version of code that implements the Unno-Rachkovsky method. Implementing solutions to the equations of radiative transfer is computationally intensive, and add many more parameters to the reconstructed models that are difficult to constrain (C. P. Folsom, personal communication).

The code utilised in this work, described in [Donati et al. \(1997\)](#), approximates the local line profile as a Gaussian function for the Stokes  $I$ , then uses the weak fields approximation for the local emergent line profile in Stokes  $V$  (see paper presented in Chapter 4). This has not been without criticism (e.g [L. Rosén & O. Kochukhov, 2012](#)). However, given the number of weakly-constrained input parameters to the models (stellar inclination, differential rotation), a computationally efficient method, while less realistic, allows for the exploration of these parameter spaces. A Gaussian line profile provides a reasonable approximation to the radiative transfer solution for cool stars.

### 1.3.3.2 LIMITATIONS OF ZDI

ZDI has inherent limitations due to the method and observational constraints. ZDI and conventional Doppler Imaging are mathematically ill-posed problems, and consequently much discussion regarding the reliability of the techniques exists ([Rice, 1991](#); [Wehlau & Rice, 1993](#); [Rice & Strassmeier, 2000](#)). Codes such as that described in [Donati et al. \(2006\)](#) and [Kochukhov et al. \(2014\)](#) implement regularisation methods such as maximum entropy or Tikhonov regularisation respectively to generate a unique solution for a given set of observations and stellar parameters. Given the significant number of free parameters, and uncertainties in many of these, it is true that the uniqueness of the field reconstruction is only valid with reference to the assumed in-

puts.

When it comes to the use of Stokes  $V$ , [L. Rosén & O. Kochukhov \(2012\)](#) contend that only using Stokes  $V$  to reconstruct the magnetic field without simultaneously using Stokes  $I$  results in an underestimate of the magnetic field strengths. [Kochukhov & Wade \(2016\)](#) also show that neglecting Stokes  $Q$  and  $U$  can result in somewhat different field topologies than using Stokes  $V$  alone or  $V$  and  $I$ . [Kochukhov & Wade \(2016\)](#) also argue that for slowly-rotating stars with complex non-dipolar fields, Stokes  $V$ -only solutions are insufficient to reliably reconstruct the magnetic field without unwarranted assumptions. However, given the difficulty in detecting Stokes  $Q$  and  $U$  due to being much more sensitive to cancellation effects than Stokes  $V$ , Stokes  $V$  remains the most useful and widespread observational data, until new techniques or instruments become available.

A key aspect of ZDI is that the technique is most useful for examining the large-scale field. Small-scale features on the stellar surface will be subject to cancellation effects, and thus will not be detected in the polarisation signal. This underestimates the actual amount of magnetic energy in the stellar magnetic field. Nevertheless, ZDI of the Sun, treated as a star located at some distance, has shown that ZDI can reconstruct the large-scale field reliably ([Fares et al., 2017](#), in preparation).

These limitations surrounding ZDI are well-known and discussed. Uncertainties in the reconstructions may certainly have implications for other work, such as wind modelling and theoretical work regarding dynamo processes. While the limitations of ZDI are acknowledged here, as a technique it is the most useful and powerful way to observe stellar magnetic fields.

#### 1.3.4 DIFFERENTIAL ROTATION

It has been known since the time of Galileo that the Sun exhibits differential rotation, the phenomenon where the equatorial regions rotate faster than the poles. Doppler and Zeeman Doppler Imaging present a method of measuring the differential rotation of magnetically active stars. Given that the rotational shear is one of the ingredients in the generation of stellar magnetic fields ([Parker, 1955, 1977](#)) measurement of differ-

ential rotation may give insights into the stellar dynamo.

As described in [Petit et al. \(2002\)](#), [Donati et al. \(2003\)](#) and [Morin et al. \(2008\)](#), we assume a solar-like differential rotation law:

$$\Omega(\vartheta) = \Omega_{eq} - d\Omega \sin^2 \vartheta \quad (1.17)$$

where  $\Omega(\vartheta)$  is the rotation rate of the star at latitude  $\vartheta$ ,  $\Omega_{eq}$  is the rotation rate at the equator of the star, and  $d\Omega$  is the rotational shear between the equator and the poles.  $\Omega(\vartheta)$ ,  $\Omega_{eq}$ , and  $d\Omega$  are measured in  $\text{rad d}^{-1}$ .

We construct a ZDI image containing a given information content for each pair of  $(\Omega_{eq}, d\Omega)$  and choose the pair of parameters which produces the best fit to the data (i.e. the minimal reduced  $\chi^2$ ). The resulting plot, for example, as in [Figure 1.15](#) shows  $\chi_r^2$  as a function of the free parameters  $\Omega_{eq}$  and  $d\Omega$  for  $\tau$  Boötis in December 2013. 1-, 2- and 3- $\sigma$  contours around the minimum value is shown. Fitting a paraboloid to the data allows us to calculate the most likely parameters and determine the confidence for that measurement.

For more rapid rotators, an alternate technique to determine differential rotation is the Fourier transform method of ([Reiners & Schmitt, 2003](#)). The quotient of the first two zeros of the Fourier transform of an averaged Stokes  $I$  profile ( $q_2/q_1$ ) may be used to derive  $\alpha (d\Omega/\Omega_{eq})$ . This method is sensitive to the resolution of the spectrum used, and breaks down at low values of  $v \sin i$  ( $\lesssim 10 \text{ km s}^{-1}$ ).

#### 1.4 STELLAR MAGNETIC FIELDS AND EXOPLANETS

Planets orbiting solar-type stars other than the Sun were first discovered in the 1990s ([Mayor & Queloz, 1995](#); [Butler & Marcy, 1996](#); [Marcy & Butler, 1996](#)) using precise measurements in the variation of the stellar radial velocity. In other words, the presence of the planets was inferred by the gravitational effects on the motion of the parent star due to the planetary orbits. Since then, utilising several different methods, planetary systems have been discovered around many hundreds of stars (for current lists

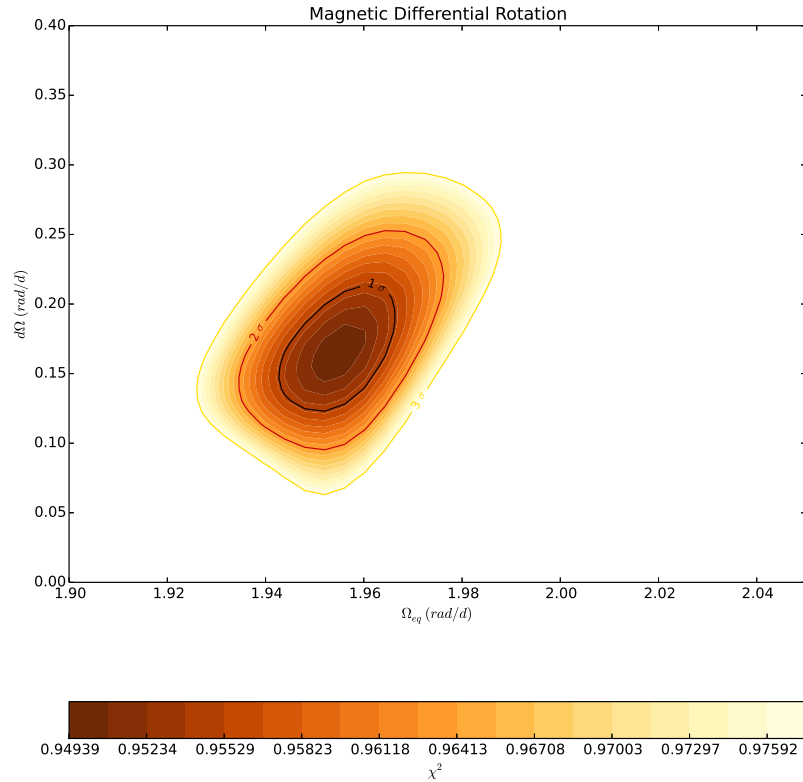


**Figure 1.15:** Differential rotation for  $\tau$  Boötis from December 2013.  $\chi_r^2$  is shown as a function of  $\Omega_{eq}$  and  $d\Omega$ . The contours show 1-, 2- and 3- $\sigma$  confidence levels that the minimum  $\chi_r^2$  is located within the paraboloid. From current work by the author.

and parameters of planetary systems, see e.g. the Extrasolar Planets Encyclopaedia<sup>2</sup>).

As mentioned previously, the stellar magnetic field plays a role in the formation and evolution of planetary systems and the migration of planets within the system. Once a planetary system stabilises, the magnetic activity generated by the magnetic field of the star can have profound impacts on the planets in the system.

In our own solar system, the solar wind erodes planetary atmospheres, especially those with weak or absent magnetic fields such as Mars whose atmosphere has been depleted by this erosion (Barabash et al., 2007). Similar effects are expected in other planetary systems (Zuluaga et al., 2016), especially those with planets orbiting close-in to the parent star (Johansson et al., 2011).

<sup>2</sup><http://exoplanet.eu>

Other more violent magnetic phenomena such as flares and coronal mass ejections may also have serious effects on planetary habitability by bathing the planets in radiation and accelerating the loss of atmospheric components.

The potential impact of “space weather” events on our technological civilisation are serious enough that the US National Weather Service and National Oceanographic and Atmospheric Administration maintain warning systems<sup>3</sup>. Thus the effect of solar magnetic activity and its impacts on the solar system are well studied. The study of similar effects in other planetary systems has the potential to give insights into the evolution of stellar magnetic fields and activity and the potential effects on planetary systems other than our own (e.g Vidotto et al., 2012; Nicholson et al., 2016).

### 1.5 LONGITUDINAL MAGNETIC FIELD

While ZDI requires many observations over time, it is possible to perform a single spectropolarimetric observation and calculate the longitudinal magnetic field,  $B_l$ .  $B_l$ , measured in G, can be derived using a single Stokes  $V$  and corresponding Stokes  $I$  observation (as shown in Fig. 1.8). Essentially the first moment of the Stokes  $V$  profile (Donati & Landstreet, 2009), the longitudinal field may be considered an integration of the magnetic field over the visible surface of the star. As such, it is susceptible to cancellation effects, so a single observation may give an erroneously low value of  $B_l$ .

$B_l$  can be calculated (Mathys, 1989; Donati et al., 1997), for a given velocity ( $v$ , in  $\text{km s}^{-1}$ ) space:

$$B_l = -2.14 \times 10^{11} \frac{\int vV(v)dv}{\lambda_0 g_0 c \int [I_c - I(v)]dv} \quad (1.18)$$

where  $B_l$  is in gauss, and  $\lambda_0$  and  $g_0$  are the average line (from LSD) central wavelength, and mean Landé factor respectively. The velocity space is defined to be inside the stellar lines as defined by the rotationally broadened Stokes  $I$  profile.

While susceptible to the aforementioned cancellation effect, calculating  $B_l$  provides

---

<sup>3</sup><http://www.swpc.noaa.gov>; Retrieved 06 October 2014

a measurement of the strength of a stellar magnetic field, and how it varies over time. It is also useful for determining viable targets for ZDI.

## 1.6 CHROMOSPHERIC ACTIVITY CYCLES

It has been long known that solar chromospheric emissions in the Ca II bands vary with the sunspot cycle (Adams & Nicholson, 1933; Wilson, 1968, 1978). Consequently, measurements of calcium emission have become one of the most commonly used proxies for magnetic activity. The BCool survey of solar-type stars (Marsden et al., 2014) showed that chromospheric activity is correlated with the maximum measured longitudinal magnetic field (see Section 1.5).

The Mt. Wilson survey (Wilson, 1978; Baliunas et al., 1998) was the first large long-term program of observations to search for magnetic activity cycles on stars other than the Sun via the use of the Ca II proxy. The Mt. Wilson survey calculates a value known as the S-index measure of activity, and work utilising other spectrographs usually produce an index calibrated to match the Mt Wilson values for standard stars. Following the example of Wright et al. (2004) and Marsden et al. (2014), the S-index is calculated as:

$$\text{S-index} = \text{Ca}_{\text{HK}}\text{-index} = \frac{aF_H + bF_K}{cF_{R_{\text{HK}}} + dF_{V_{\text{HK}}}} + e \quad (1.19)$$

where  $F_H$  and  $F_K$  are the fluxes in a  $2.18\text{\AA}$  triangular bandpasses centred on the cores of the Ca II H & K lines,  $F_{V_{\text{HK}}}$  and  $F_{R_{\text{HK}}}$  are rectangular  $20\text{\AA}$  bandpasses centred on the continuum at  $3901.07\text{\AA}$  and  $4001.07\text{\AA}$ . These bandpasses are shown in Figure 1.16 [reproduced from Wright et al. (2004, Fig. 1)]. The coefficients  $a$  through  $e$  are calculated for a particular spectrograph such that the S-index for stars observed in common with the Mt. Wilson survey are the same.

Observations have shown that many stars exhibit chromospheric activity cycles, and Boro Saikia et al. (2016) for the first time demonstrated a magnetic cycle for the K5 dwarf 61 Cyg A that, like the Sun, followed the chromospheric cycle. Given that for mature solar-type stars, the chromospheric cycles observed are on the order of years

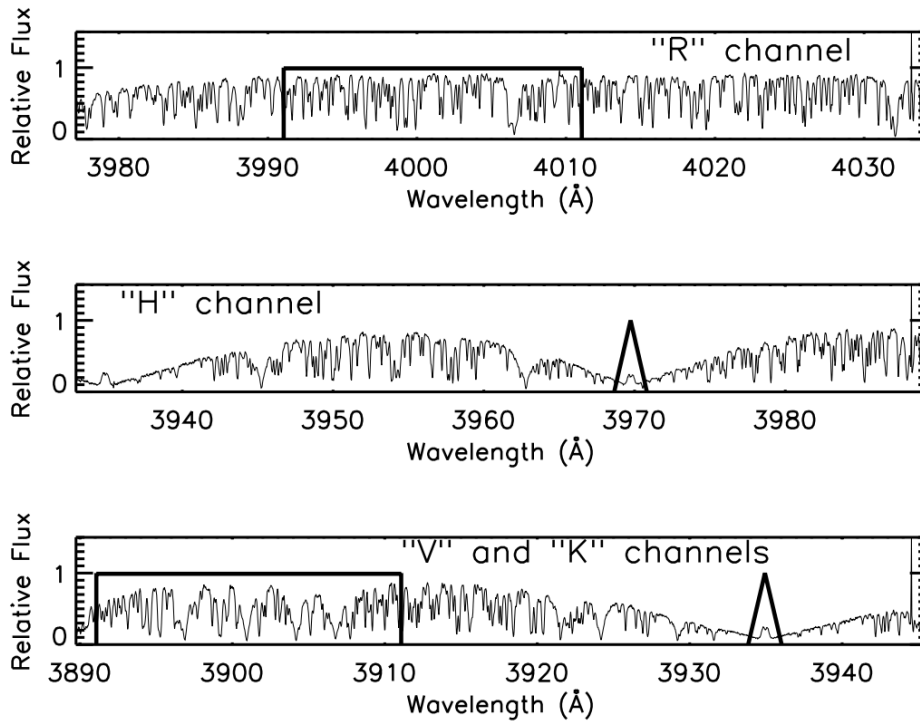


Figure 1.16: R,V,H and K bandpasses used in Equation 1.19 to calculate the S-index, a measure of chromospheric activity. Reproduced from Wright et al. (2004, Fig. 1).

long, this makes observing magnetic cycles on older stars time consuming and challenging.

### 1.7 THE MAGNETIC FIELDS OF SOLAR-TYPE STARS

Magnetic fields have been discovered on many solar-type stars. A snapshot survey of the longitudinal magnetic field of 170 F, G and K stars (Marsden et al., 2014) detected a magnetic field on 67 stars (~39%) of the sample (although it is thought that all solar-type stars should host some level of magnetic activity). There are several clear relationships between the maximum measured value of the magnetic field strength (i.e. the maximum value of  $|B_l|$ ) for a star and its various stellar parameters and activity proxies. In particular, increasing maximum  $|B_l|$  is correlated with the rotation rate, and anti-correlated with age. Magnetic fields are also more frequently detected

on K and G stars than on F stars, perhaps indicating that the convection zone depth is related to the magnetic field strength. [Marsden et al. \(2014\)](#) also shows that the longitudinal magnetic field strength correlates with chromospheric emission (Ca II H&K, Ca Infrared Triplet, etc.).

Many stars have been mapped using ZDI, and some broad trends are apparent in the magnetic field topologies. Rapidly rotating stars exhibit dominant toroidal fields, while as stars age and spin down, their magnetic field becomes predominantly poloidal ([Petit et al., 2008](#)). [See et al. \(2016\)](#) also indicate that the poloidal field components are generally (although not always) more axisymmetric for slower rotators.

### 1.7.1 MAGNETIC CYCLES

Given that magnetic field strength is correlated with chromospheric activity ([Marsden et al., 2014](#)), it would be logical to suggest that stars that exhibit chromospheric activity cycles may have magnetic cycles, where the field strength rises and falls. Additionally, in the Sun the magnetic field topology also changes during the activity cycle. Significantly, the magnetic field becomes less dominantly dipolar as the chromospheric activity increases ([Sanderson et al., 2003](#); [DeRosa et al., 2012](#)). At each minimum of chromospheric activity, the global solar magnetic field undergoes a polarity reversal ([Hathaway, 2010](#)).

Such polarity reversals have been noted on other stars using repeated spectropolarimetric observations (e.g [Donati et al., 2003, 2008](#); [Fares et al., 2009](#); [Petit et al., 2009](#); [Morgenthaler et al., 2011](#); [Fares et al., 2013](#); [Rosén et al., 2016](#); [Boro Saikia et al., 2016](#)). This evidence may be indicative of magnetic cycles. However, very few stars that exhibit chromospheric cycles have been observed with enough frequency over long enough time frames to confirm whether they, in fact, are exhibiting magnetic cycles (whether or not coincident with chromospheric cycles) rather than chaotic variation. One exception is the K<sub>5</sub> dwarf 61 Cyg A ([Boro Saikia et al., 2016](#)). This star is the first found to exhibit reversals of the global polarity and magnetic field topology changes that mimic the behaviour of the solar magnetic cycle. Indeed, the magnetic cycle also follows the chromospheric activity cycle of the star.

Thus far, the only two solar-type stars to exhibit magnetic cycles that follow the chromospheric cycle, the Sun and 61 Cyg A, both have relatively large convective zones. Stars with shallower convective zones have generally exhibited little evidence of cycles. For example, [Jeffers et al. \(2011\)](#) shows that HD 171488, a rapidly-rotating G0 dwarf did not exhibit polarity reversals, suggesting that distributed, rather than traditional solar-type dynamo processes may be present. [Morgenthaler et al. \(2011\)](#) observed polarity reversals on the G0 dwarf HD 78366, perhaps indicative of a magnetic cycle (although with only three observations, it is difficult to determine whether the activity is indeed cyclic). In contrast, [Schröder et al. \(2013\)](#) asserts that there are no cyclic main sequence stars in the Mt. Wilson chromospheric activity survey “much above” one solar mass. A notable exception is the F7 dwarf  $\tau$  Boötis, which seems to exhibit regular polarity reversals ([Fares et al., 2009, 2013](#)).

Due to the length of cycles, which in the case of the Sun and 61 Cyg A are many years in length, determining the nature of magnetic cycles is challenging. Further spectropolarimetric observations of different types of solar-type stars with different ages, stellar parameters and periods of chromospheric cycles are required to see if and, if so how cycles become established. In particular, this type of work provides proxies for studying the development over time of the solar dynamo.

### 1.7.2 STAR-PLANET INTERACTION

Magnetic phenomena generated by stars can have significant impacts on the surrounding environment. Stellar winds can physically strip planetary atmospheres, while X-ray and ultraviolet absorption contribute to heating in planetary atmospheres, resulting in mass loss through photo-evaporation ([Fossati et al., 2010](#); [Lopez & Fortney, 2013](#); [Poppenhaeger et al., 2013](#)). Thus this form of star-planet interaction (SPI) impacts planetary formation and the long-term evolution of planetary atmospheres ([Penz & Micela, 2008](#)).

SPI may potentially progress in the alternate direction, where the presence of a planet or planets may affect the magnetic activity of the star ([Wolk et al., 2015](#)). The primary mechanisms whereby this may occur is either via magnetic reconnection ([Cuntz](#)

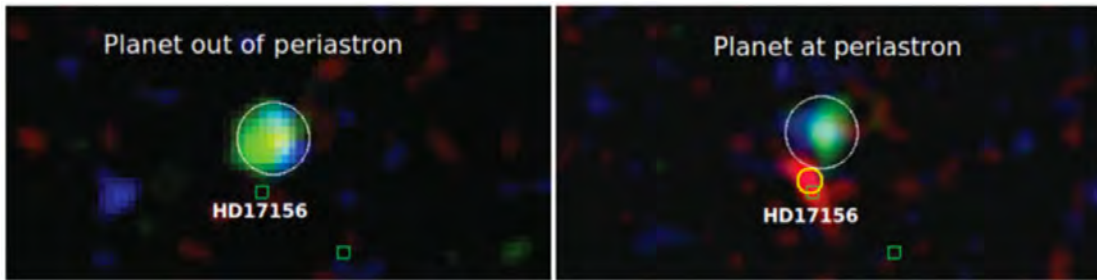


**Figure 1.17:** X-ray images of HD 17156 taken away from planetary periastron (left panel) and near the periastron (right panel). Colours represent photon energy (red = 0.3-1.0 keV, green = 1.0-2.5 keV, blue=2.5-5.0 keV). This image from [Maggio et al. \(2015, Fig. 1\)](#) is proposed to show an example of star-planet interaction. Note that the planet is in an eccentric orbit, allowing for the comparison of potential interaction at different orbital distances between planet and star.

[et al., 2000](#)) or tidal interactions ([Saar et al., 2004](#)). [Wolk et al. \(2015\)](#) summarises three particular cases of SPI. In the case of HD 189733, flare activity is seen hours after an eclipse involving HD 189733b. [Pillitteri et al. \(2014\)](#); [Wolk et al. \(2015\)](#) posit that the flare activity is caused primarily by the tidal interaction between the planet and the star.

In the second example, [Pillitteri et al. \(2014\)](#); [Wolk et al. \(2015\)](#) propose that tidal interaction with the thin convective envelope of the F6 dwarf WASP-18 interferes with the dynamo process of the host star, resulting in the star being “X-ray dark” with very low magnetic activity. WASP-18b is a very massive planet ( $\sim 10M_{Jupiter}$ ) orbiting the host star in only 22 h.

Finally, in the HD 17156 system, the Jupiter-mass planet is on an eccentric orbit. [Maggio et al. \(2015\)](#) show X-ray activity only when the planet is closest to the star (see Figure 1.17). [Maggio et al. \(2015\)](#) propose that this behaviour may be due to magnetic reconnection or by tidal stripping of material from the stellar surface.

In two of the three cases, the planetary systems are described by [Wolk et al. \(2015\)](#) as extreme, or edge cases. WASP-18b is very massive, and in HD 17156, the planet is in an eccentric orbit. However, the final case from [Wolk et al. \(2015\)](#) is described as a more conventional hot-Jupiter system. These examples bring in to focus the difficulties in detecting SPI. Tidal effects are more likely to be present on systems with close-in and

more massive planets. Magnetic reconnection is more likely where the planet is orbiting more closely to the star. Additionally, the magnetic topology of both the planet and star will play a role in SPI. A statistical analysis by [Miller et al. \(2015\)](#) shows that for FGK stars, there is an apparent increase in X-ray luminosity with interaction strength ( $M_p/a^2$ , where  $M_p$  is the planetary mass, and  $a$  is the semi-major axis of the planetary orbit). However, this is driven by a small group of extreme systems, and no relationship was found for coronal activity and interaction strength.

Detection of SPI using spectropolarimetric techniques would require a targeted search of planet-hosting stars, with a focus on hot Jupiter systems. Significant selection biases limit the scope of such an investigation. Most notable is the fact that active stars are usually excluded from planetary surveys, as stellar activity can mimic the behaviour indicative of the presence of planet(s). As Stokes  $V$  signatures are so small, especially in older stars, this means that any spectropolarimetric signal due to SPI will be difficult to disentangle from the intrinsic magnetic activity of the star.

## 1.8 RESEARCH QUESTIONS

In this thesis, two broad questions are addressed.

### 1.8.1 TO WHAT EXTENT DOES THE PRESENCE OF A PLANETARY SYSTEM SYSTEMATICALLY AFFECT THE LARGE-SCALE MAGNETIC FIELDS OF THEIR HOST SOLAR-TYPE STARS, IF AT ALL?

This general case is addressed in Chapter 2. The paper [Mengel et al. \(2017b\)](#) describes a spectropolarimetric survey of planet-hosting solar-type stars. The relationships between the magnetic field of the planet hosts and other stellar parameters are compared to the relationships determined for the population of solar-type stars ([Marsden et al., 2014](#)) to establish if there are any apparent differences. Additionally, for the planet-hosting stars, an analysis is undertaken to see if there is any relationship apparent between the magnetic field and the relative tidal interaction of the star and planet.

### 1.8.2 HOW DOES THE PRESENCE OF THE HOT JUPITER $\tau$ BOÖTIS B AFFECT THE LARGE-SCALE MAGNETIC FIELD OF THE HOST STAR IN THE PARTICULAR CASE OF $\tau$ BOÖTIS?

In Chapters 3 and 4, the papers [Mengel et al. \(2016\)](#) and [Mengel et al. \(2017a\)](#) examine the chromospheric cycle of  $\tau$  Boötis and examines the evolution of the star's magnetic topology over time. [Donati et al. \(2008\)](#) and [Fares et al. \(2009, 2013\)](#) show that  $\tau$  Boötis undergoes reversals of its large-scale radial magnetic field, and tentative cycles have been predicted. In [Mengel et al. \(2016\)](#) (Chapter 3), the reversals from the previous authors were confirmed, however intriguing results lead to a prediction that the star undergoes a more rapid cycle than previously expected. This prediction is examined further in [Mengel et al. \(2017a\)](#) (Chapter 4). As  $\tau$  Boötis is an F-type star with a shallow convective zone, and to date, other stars of this type generally do not seem to exhibit cycles, we attempt to detect any interaction between star and planet that may explain this phenomenon.

*Quand vous allez à la recherche de miel vous devez vous attendre à être piqué par les abeilles.*

Joseph Joubert

# 2

## A BCool Survey of the Magnetic Fields of Planet Hosting Stars

THE FIRST STEP IN INVESTIGATING THE magnetic fields of planet-hosting solar-type stars was to perform a survey of such stars to determine (a) if the magnetic fields of these stars are detectable with the telescopes and equipment available, and (b) if there is any relationship between the magnetic field strength of these stars and the presence or otherwise of a planetary system. Marsden et al. (2014) and the BCool collaboration performed such a snapshot survey for solar-type stars in general. Drawing on this resource, and identifying more targets with planetary systems, this survey was carried out and the results analysed in the following paper, “A BCool Survey of the magnetic fields of planet-hosting solar-type stars” (Mengel et al., 2017b).

For the purposes of this study, a “solar-type” star is defined using the ranges of stellar

parameters similar to those used in Marsden et al. (2014), and are described in Mengel et al. (2017b). The stars have convective zones, yet are not fully convective, and are F, G, and K dwarfs for the most part (although some subgiants are present in the BCool sample). It should also be stated for clarity, that the sample of planet-hosting stars are stars for which the presence of a planet has been confirmed. Thus it is possible that stars considered in the Marsden et al. (2014) sample to be non-planet-hosts *may* potentially host planets. Consequently, future observations of the BCool sample stars may result in the discovery of planets yet unknown. This would thus compel a re-analysis of the results found here.

Snapshot surveys of this type rely on measuring the longitudinal magnetic field of the star ( $B_l$ ). The longitudinal magnetic field is the integration of the line-of-sight magnetic field taken across the visible disc of the star (see section 1.5). While this can have some limitations (due to cancellation effects, as described in the paper), the snapshot survey provides a first filter for which stars may be candidate targets for ZDI mapping and long-term monitoring.

The relationship between star-planet tidal interaction and the magnetic field strength was examined to see if there are any signs of star-planet magnetic interaction. Finally, the sample of planet-hosting stars was compared to the sample of solar-type stars from Marsden et al. (2014) to see if there were any statistical differences due to the presence of a planetary system.

## 2.1 MENGEL ET AL. (2017B) “A BCool SURVEY OF THE MAGNETIC FIELDS OF PLANET-HOSTING SOLAR-TYPE STARS”

The published paper Mengel et al. (2017b), “A BCool Survey of the magnetic fields of planet-hosting solar-type stars” follows.



## A BCoolest survey of the magnetic fields of planet-hosting solar-type stars

M. W. Mengel,<sup>1</sup>★ S. C. Marsden,<sup>1</sup> B. D. Carter,<sup>1</sup> J. Horner,<sup>1</sup> R. King,<sup>1</sup> R. Fares,<sup>2</sup>  
S. V. Jeffers,<sup>3</sup> P. Petit,<sup>4,5</sup> A. A. Vidotto,<sup>6</sup> J. Morin<sup>7</sup> and the BCoolest Collaboration

<sup>1</sup>Computational Engineering and Science Research Centre, University of Southern Queensland, Toowoomba, QLD 4350, Australia

<sup>2</sup>INAF – Osservatorio Astrofisico di Catania, Via Santa Sofia, 78, I-95123 Catania, Italy

<sup>3</sup>Institut für Astrophysik, Georg-August-Universität Göttingen, Friedrich-Hund-Platz 1, D-37077 Göttingen, Germany

<sup>4</sup>Université de Toulouse, UPS-OMP, Institut de Recherche en Astrophysique et Planétologie, F-31400 Toulouse, France

<sup>5</sup>CNRS, Institut de Recherche en Astrophysique et Planétologie, 14 Avenue Edouard Belin, F-31400 Toulouse, France

<sup>6</sup>School of Physics, Trinity College Dublin, The University of Dublin, Dublin 2, Ireland

<sup>7</sup>Laboratoire Univers et Particules de Montpellier, Université de Montpellier, CNRS, place Eugène Bataillon, F-34095 Montpellier, France

Accepted 2016 November 11. Received 2016 November 10; in original form 2016 September 28

### ABSTRACT

We present a spectropolarimetric snapshot survey of solar-type planet-hosting stars. In addition to 14 planet-hosting stars observed as part of the BCoolest magnetic snapshot survey, we obtained magnetic observations of a further 19 planet-hosting solar-type stars in order to see if the presence of close-in planets had an effect on the measured surface magnetic field ( $|B_{\ell}|$ ). Our results indicate that the magnetic activity of this sample is congruent with that of the overall BCoolest sample. The effects of the planetary systems on the magnetic activity of the parent star, if any, are too subtle to detect compared to the intrinsic dispersion and correlations with rotation, age and stellar activity proxies in our sample. Four of the 19 newly observed stars, two of which are subgiants, have unambiguously detected magnetic fields and are future targets for Zeeman–Doppler mapping.

**Key words:** line: profiles – techniques: polarimetric – stars: activity – stars: magnetic field – planetary systems.

## 1 INTRODUCTION

### 1.1 The BCoolest spectropolarimetric survey

The BCoolest spectropolarimetric survey (Marsden et al. 2014) has the objective of observing a large sample of solar-type stars with  $V \lesssim 9$ , attempting to detect their magnetic fields. This serves a two-fold purpose. First, the survey sets out to determine if there is any correlation between the large-scale stellar magnetic field and various stellar parameters. Secondly, the characterization of the magnetic fields of the targeted stars allows for the selection of optimal or interesting targets for further study, such as long-term monitoring and mapping of their magnetic-field topology in order to observe and characterize their magnetic cycles.

Marsden et al. (2014) published spectropolarimetric snapshots of 170 solar-type stars, and reported that the strength of the large-scale magnetic field declines as a function of age and with reduced rotation. Additionally, they found that the mean surface magnetic field detected was higher for K-dwarfs compared to G-dwarfs and F-dwarfs. Marsden et al. (2014) do note this higher field for K-dwarfs may be due to selection biases, although this observation would also be consistent with even stronger fields seen on M-dwarfs

(e.g. Morin et al. 2008). At the most fundamental level, this work adds 19 additional solar-type stars to the BCoolest sample.

In this work, we also aim to examine whether the presence of a planetary system or the nature of the planets in that system correlates with the large-scale magnetic field of the host star. Such correlation would potentially be indicative of star–planet interaction (SPI).

### 1.2 Star–planet interaction

Host stars profoundly influence their surrounding planetary environment. The transfer of angular momentum, stellar winds and magnetic fields play roles in planetary formation, migration and evolution (Horner & Jones 2010). Additionally, stellar winds in cool stars, which are influenced by the variation in stellar magnetic fields, affect the planetary environment and can interact strongly with planetary atmospheres (See et al. 2015; Strugarek et al. 2015; Vidotto et al. 2015). Understanding the magnetic field of host stars allows us to more fully investigate and understand the planetary environment around them, and by extension, examine the habitability of potential Earth-like planets.

Tidal and magnetic interaction between host stars and their planets, especially large close-in ‘hot Jupiters’, has been of considerable interest since the discovery of such planets. Whether such companions result in any change in the magnetic activity of the star remains unanswered. Cuntz, Saar & Musielak (2000), Rubenstein

\* E-mail: matthew.mengel@usq.edu.au

**Table 1.** Planetary parameters of the sample of planet-hosting solar-type stars not previously observed by Marsden et al. (2014). The stellar component's *Hipparcos* number, SPOCS catalogue number and HD number (where applicable) are shown in the first three columns. Column 4 refers to the name by which the planetary components (column 5) are known. The period, projected mass ( $M \sin i$ ) and semimajor axis are shown for each planet. These values are taken from the references listed in the last column; locations where values were unavailable in the literature are denoted by 'X'. Parameters for the systems observed by the BCool survey are shown in Table B1.

Star HIP no.	SPOCS no.	HD no.	Name	Component	Planet(s) Period (d)	$M \sin i$ ( $M_J$ )	Semimajor axis (au)	Refs.
14954	155	19994	94 Cet	b	$537.7 \pm 3.1$	$1.69 \pm 0.26$	$1.428 \pm 0.083$	1
17747	184	23596	HD 23596	b	$1565 \pm 21$	$7.8 \pm 1.1$	$2.83 \pm 0.17$	1
24205 <sup>a</sup>	252	33636	HD 33636	b	$2127.7 \pm 8.2$	$9.28 \pm 0.77$	$3.37 \pm 0.19$	1
25191		290327	HD 290327	b	$2443^{+205}_{-117}$	$2.54^{+0.17}_{-0.14}$	$3.43^{+0.20}_{-0.12}$	2
26381	270	37124	HD 37124	b	$154.46 \pm X$	$0.64 \pm 0.11$	$0.529 \pm 0.031$	1
			HD 37124	c <sup>b</sup>	$2295.00 \pm X$	$0.683 \pm 0.088$	$3.19 \pm 0.18$	1
			HD 37124	d	$843.60 \pm X$	$0.624 \pm 0.063$	$1.639 \pm 0.095$	1
26664		37605	HD 37605	b	$54.23 \pm 0.23$	$2.86 \pm 0.41$	$0.261 \pm 0.015$	1
27253	282	38529	HD 38529	b	$14.3093 \pm 0.0013$	$0.852 \pm 0.074$	$0.1313 \pm 0.0076$	1
			HD 38529	c	$2165 \pm 14$	$13.2 \pm 1.1$	$3.74 \pm 0.22$	1
27384		38801	HD 38801	b	$696.3 \pm 2.7$	$10.7 \pm 0.5$	$1.70 \pm 0.03$	3
28767	293	40979	HD 40979	b	$263.84 \pm 0.71$	$3.83 \pm 0.36$	$0.855 \pm 0.049$	1
29301		42176	KELT2A	b	$4.11379 \pm 0.00001$	$1.524 \pm 0.088$	$0.05504 \pm 0.00086$	4
30057		43691	HD 43691	b	$36.96 \pm 0.02$	$2.49 \pm X$	$0.24 \pm X$	5
32916	324	49674	HD 49674	b	$4.94737 \pm 0.00098$	$0.105 \pm 0.011$	$0.0580 \pm 0.0034$	1
45406		79498	HD 79498	b	$1966.1 \pm 41$	$1.34 \pm 0.07$	$3.13 \pm 0.08$	6
64457	556	114783	HD 114783	b	$496.9 \pm 2.3$	$1.034 \pm 0.089$	$1.169 \pm 0.068$	1
95740	841	183263	HD 183263	b	$635.4 \pm 3.9$	$3.82 \pm 0.4$	$1.525 \pm 0.088$	1
96507		185269	HD 185269	b	$6.8399 \pm 0.0013$	$1.03 \pm 0.03$	$0.077 \pm X$	7
98767	870	190360	HD 190360	b	$2891 \pm 85$	$1.55 \pm 0.14$	$3.99 \pm 0.25$	1
			HD 190360	c	$17.100 \pm 0.015$	$0.0587 \pm 0.0078$	$0.1303 \pm 0.0075$	1
101966	901	196885	HD 196885	b	$1326.0 \pm 3.7$	$2.98 \pm 0.05$	$2.6 \pm 0.1$	8
108859	953	209458	HD 209458	b	$3.52474554 \pm 1.8 \times 10^{-7}$	$0.689 \pm 0.057$	$0.0474 \pm 0.0027$	1

References: 1: Butler et al. (2006), 2: Naef et al. (2010), 3: Harakawa et al. (2010), 4: Beatty et al. (2012), 5: da Silva et al. (2007), 6: Robertson et al. (2012), 7: Moutou et al. (2006), 8: Chauvin et al. (2011).

<sup>a</sup> HIP 24205 (HD 33636) at the time of writing is listed in some catalogues of planet-hosting stars; however, Martioli et al. (2010) have determined the mass of the companion to be much too massive to be considered a planet. While perhaps considered as no longer planet-hosting, in the interests of completeness we include it in our analysis.

<sup>b</sup> Butler et al. (2006) indicate that the mass of HD 37124 c is unclear and an alternative interpretation is for a period of 29.3 d,  $M \sin i = 0.170 M_J$  and semimajor axis of 0.170 au, with slightly different values for HD 37124 a and HD 37124 b.

& Schaefer (2000) and Lanza (2009, 2012) variously suggest that close-in planets may spin-up the host star by transfer of angular momentum resulting in higher activity. Activity enhancement may also occur due to magnetic reconnection events between stellar and planetary magnetic fields. Evidence for SPI has been claimed for several stars using a variety of observed phenomena synchronized with the orbital period of the planet, such as photospheric 'hot spots' (Lanza et al. 2011), chromospheric enhancement (Shkolnik et al. 2005, 2008) and X-ray enhancement (Pillitteri et al. 2010).

A statistical assessment of SPI by Miller et al. (2015) shows that no particular correlation exists between proxies for SPI strength and coronal activity. A relationship with solar-type (FGK) stars was found; however, they note that this is only driven by a handful of extreme hot-Jupiter systems. Miller et al. (2015) also investigated whether planetary properties were correlated with UV luminosity or Ca II H&K, and found no significant difference between hot-Jupiter systems and others. This was in contrast to the conclusions drawn from earlier observations by Shkolnik (2013) and Krejčová & Budaj (2012). However, all such studies note that selection effects may skew these results.

Finally, France et al. (2016) present tentative evidence for SPI for close-in, massive planets via an enhancement of the transition region. France et al. (2016) speculate that this may be due to mag-

netospheric interaction, but urge caution due to a small sample size.

## 2 TARGET SELECTION

### 2.1 New targets (not previously observed by BCool)

Targets were chosen from the exoplanet.eu data base<sup>1</sup> (Schneider et al. 2011). The host stars of the planetary systems were chosen to be broadly solar-type with  $T_{\text{eff}}$  between 5100 and 6300 K and  $M_* < 1.5 M_{\odot}$ , on the main sequence or at the subgiant stage. This selection was further constrained by the observational requirements of the NARVAL instrument and the T lescope Bernard Lyot (see Section 3.1). Targets were chosen with magnitude  $V \lesssim 9$  and declination  $\delta$  above  $-10^\circ$ .

Table 1 shows the configurations of the observed planetary systems. There are six stars which host a planet that can be classified as a hot Jupiter (considering the definition of a massive planet with a semimajor axis of less than  $\sim 0.05$  au). Further, three systems contain two or more detected planets.

<sup>1</sup> <http://exoplanet.eu>

**Table 2.** Stellar parameters of the sample of planet-hosting solar-type stars not previously observed by Marsden et al. (2014). The spectral type is taken from SIMBAD (<http://simbad.u-strasbg.fr/simbad/>, Wenger et al. 2000). Column 11 is the radius of the convective zone of the star. Values are found in the references shown in the final column of the table; locations where values were unavailable in the literature are denoted by ‘X’. <sup>SG</sup> indicates the star is a subgiant (see Fig. 1). In column 5, a superscript ‘a’ indicates that a [M/H] value was unavailable and thus an [Fe/H] value was used. Parameters for the systems observed by the BCoolest survey are shown in Table B2.

HIP no.	SPOCS no.	Spec. type	$T_{\text{eff}}$ (K)	$\log(g)$ (cm s <sup>-2</sup> )	[M/H] or [Fe/H] <sup>a</sup>	$\log(\text{Lum})$ ( $L_{\odot}$ )	Age (Gyr)	Mass ( $M_{\odot}$ )	Radius ( $R_{\odot}$ )	Radius <sub>CZ</sub> ( $R_{\odot}$ )	$v \sin i$ (km s <sup>-1</sup> )	Refs.
14954	155	F8.5V	6188 <sup>+44</sup> <sub>-44</sub>	4.17 <sup>+0.03</sup> <sub>-0.08</sub>	+0.17 <sup>+0.03</sup> <sub>-0.03</sub>	+0.574 <sup>+0.035</sup> <sub>-0.035</sub>	2.56 <sup>+0.40</sup> <sub>-0.36</sub>	1.365 <sup>+0.042</sup> <sub>-0.024</sub>	1.75 <sup>+0.06</sup> <sub>-0.16</sub>	0.265 <sup>+0.009</sup> <sub>-0.009</sub>	8.6 <sup>+0.5</sup> <sub>-0.5</sub>	1, 2
17747	184	F8	5904 <sup>+44</sup> <sub>-44</sub>	4.07 <sup>+0.04</sup> <sub>-0.04</sub>	+0.24 <sup>+0.03</sup> <sub>-0.03</sub>	+0.446 <sup>+0.089</sup> <sub>-0.089</sub>	5.68 <sup>+0.48</sup> <sub>-0.36</sub>	1.159 <sup>+0.062</sup> <sub>-0.018</sub>	1.69 <sup>+0.09</sup> <sub>-0.08</sub>	0.472 <sup>+0.035</sup> <sub>-0.030</sub>	4.2 <sup>+0.5</sup> <sub>-0.5</sub>	1, 2
24205	252	G0	5904 <sup>+44</sup> <sub>-44</sub>	4.44 <sup>+0.04</sup> <sub>-0.04</sub>	-0.12 <sup>+0.03</sup> <sub>-0.03</sub>	+0.039 <sup>+0.077</sup> <sub>-0.077</sub>	3.52 <sup>+2.16</sup> <sub>-2.44</sub>	1.017 <sup>+0.032</sup> <sub>-0.032</sub>	1.02 <sup>+0.04</sup> <sub>-0.04</sub>	0.247 <sup>+0.020</sup> <sub>-0.015</sub>	3.1 <sup>+0.5</sup> <sub>-0.5</sub>	1, 2
25191		G0	5552 <sup>+21</sup> <sub>-44</sub>	4.42 <sup>+0.04</sup> <sub>-0.04</sub>	-0.11 <sup>+0.02a</sup> <sub>-0.02</sub>	-0.143 <sup>+X</sup> <sub>-X</sub>	> 3	0.90 <sup>+X</sup> <sub>-X</sub>	1.00 <sup>+0.01</sup> <sub>-0.01</sub>	X	1.4 <sup>+1.0</sup> <sub>-1.0</sub>	3
26381	270	G4IV–V	5500 <sup>+44</sup> <sub>-44</sub>	4.44 <sup>+0.04</sup> <sub>-0.04</sub>	-0.29 <sup>+0.03</sup> <sub>-0.03</sub>	-0.077 <sup>+0.077</sup> <sub>-0.077</sub>	11.7 <sup>+3.1</sup> <sub>-8.4</sub>	0.850 <sup>+0.022</sup> <sub>-0.016</sub>	0.93 <sup>+0.03</sup> <sub>-0.04</sub>	0.277 <sup>+0.011</sup> <sub>-0.018</sub>	1.2 <sup>+0.5</sup> <sub>-0.5</sub>	1, 2
26664 <sup>SG</sup>		K0	5448 <sup>+44</sup> <sub>-44</sub>	4.51 <sup>+0.02</sup> <sub>-0.02</sub>	+0.34 <sup>+0.03a</sup> <sub>-0.03</sub>	+0.590 <sup>+0.058</sup> <sub>-0.058</sub>	7.07 <sup>+X</sup> <sub>-X</sub>	1.000 <sup>+0.050</sup> <sub>-0.050</sub>	0.90 <sup>+0.05</sup> <sub>-0.05</sub>	X	< 1	4, 5
27253 <sup>SG</sup>	282	G8III/IV	5697 <sup>+44</sup> <sub>-44</sub>	3.94 <sup>+0.02</sup> <sub>-0.02</sub>	+0.27 <sup>+0.03</sup> <sub>-0.03</sub>	+0.802 <sup>+0.079</sup> <sub>-0.079</sub>	3.28 <sup>+0.36</sup> <sub>-0.24</sub>	1.477 <sup>+0.040</sup> <sub>-0.052</sub>	2.50 <sup>+0.08</sup> <sub>-0.06</sub>	0.711 <sup>+0.031</sup> <sub>-0.014</sub>	3.9 <sup>+0.5</sup> <sub>-0.5</sub>	1, 2
27384 <sup>SG</sup>		G8IV	5222 <sup>+44</sup> <sub>-44</sub>	3.84 <sup>+0.10</sup> <sub>-0.10</sub>	+0.26 <sup>+0.03a</sup> <sub>-0.03</sub>	+0.659 <sup>+0.043</sup> <sub>-0.047</sub>	4.67 <sup>+2.56</sup> <sub>-2.56</sub>	1.36 <sup>+0.09</sup> <sub>-0.09</sub>	2.53 <sup>+0.13</sup> <sub>-0.13</sub>	X	0.5 <sup>+0.5</sup> <sub>-0.5</sub>	6
28767	293	F8	6089 <sup>+44</sup> <sub>-44</sub>	4.32 <sup>+0.04</sup> <sub>-0.03</sub>	+0.12 <sup>+0.03</sup> <sub>-0.03</sub>	+0.257 <sup>+0.055</sup> <sub>-0.055</sub>	3.56 <sup>+0.68</sup> <sub>-0.80</sub>	1.154 <sup>+0.028</sup> <sub>-0.022</sub>	1.23 <sup>+0.05</sup> <sub>-0.04</sub>	0.273 <sup>+0.020</sup> <sub>-0.018</sub>	7.4 <sup>+0.5</sup> <sub>-0.5</sub>	1, 2
29301		F7V	6148 <sup>+48</sup> <sub>-48</sub>	4.03 <sup>+0.02</sup> <sub>-0.03</sub>	+0.03 <sup>+0.08a</sup> <sub>-0.08</sub>	+0.550 <sup>+X</sup> <sub>-X</sub>	3.97 <sup>+0.01</sup> <sub>-0.01</sub>	1.314 <sup>+0.063</sup> <sub>-0.060</sub>	1.84 <sup>+0.07</sup> <sub>-0.05</sub>	X	9.0 <sup>+2.0</sup> <sub>-2.0</sub>	7, 8
30057		G0	6200 <sup>+40</sup> <sub>-40</sub>	4.28 <sup>+0.13</sup> <sub>-0.13</sub>	+0.28 <sup>+0.05a</sup> <sub>-0.05</sub>	+0.521 <sup>+X</sup> <sub>-X</sub>	2.8 <sup>+0.8</sup> <sub>-0.8</sub>	1.38 <sup>+0.05</sup> <sub>-0.05</sub>	X	X	4.7 <sup>+X</sup> <sub>-X</sub>	8, 9
32916	324	G0	5662 <sup>+44</sup> <sub>-44</sub>	4.51 <sup>+0.03</sup> <sub>-0.03</sub>	+0.22 <sup>+0.03</sup> <sub>-0.03</sub>	-0.089 <sup>+0.094</sup> <sub>-0.094</sub>	X	1.015 <sup>+0.048</sup> <sub>-0.036</sub>	0.95 <sup>+0.04</sup> <sub>-0.04</sub>	0.271 <sup>+0.013</sup> <sub>-0.009</sub>	0.4 <sup>+0.5</sup> <sub>-0.5</sub>	1, 2
45406		G5	5760 <sup>+80</sup> <sub>-80</sub>	4.37 <sup>+0.12</sup> <sub>-0.12</sub>	+0.24 <sup>+0.06a</sup> <sub>-0.06</sub>	X	2.70 <sup>+X</sup> <sub>-X</sub>	1.06 <sup>+X</sup> <sub>-X</sub>	X	X	X	10, 11
64457	556	K1V	5135 <sup>+44</sup> <sub>-44</sub>	4.57 <sup>+0.03</sup> <sub>-0.04</sub>	+0.10 <sup>+0.03</sup> <sub>-0.03</sub>	-0.415 <sup>+0.045</sup> <sub>-0.045</sub>	6.76 <sup>+X</sup> <sub>-X</sub>	0.853 <sup>+0.034</sup> <sub>-0.038</sub>	0.81 <sup>+0.02</sup> <sub>-0.03</sub>	0.255 <sup>+0.020</sup> <sub>-0.010</sub>	0.9 <sup>+0.5</sup> <sub>-0.5</sub>	1, 2
95740	841	G2IV	5936 <sup>+44</sup> <sub>-44</sub>	4.36 <sup>+0.05</sup> <sub>-0.05</sub>	+0.22 <sup>+0.03</sup> <sub>-0.03</sub>	+0.210 <sup>+0.110</sup> <sub>-0.110</sub>	4.52 <sup>+0.76</sup> <sub>-1.12</sub>	1.121 <sup>+0.064</sup> <sub>-0.040</sub>	1.18 <sup>+0.07</sup> <sub>-0.07</sub>	0.304 <sup>+0.026</sup> <sub>-0.023</sub>	1.6 <sup>+0.5</sup> <sub>-0.5</sub>	1, 2
96507		G2V	6059 <sup>+18</sup> <sub>-18</sub>	4.13 <sup>+0.06</sup> <sub>-0.06</sub>	+0.12 <sup>+0.02a</sup> <sub>-0.02</sub>	+0.49 <sup>+0.1</sup> <sub>-0.1</sub>	3.4 <sup>+0.54</sup> <sub>-0.54</sub>	1.33 <sup>+0.07</sup> <sub>-0.07</sub>	1.76 <sup>+0.07</sup> <sub>-0.07</sub>	X	5.5 <sup>+X</sup> <sub>-X</sub>	12, 13
98767	870	G7IV–V	5552 <sup>+44</sup> <sub>-44</sub>	4.31 <sup>+0.03</sup> <sub>-0.03</sub>	+0.19 <sup>+0.03</sup> <sub>-0.03</sub>	+0.050 <sup>+0.022</sup> <sub>-0.022</sub>	13.4 <sup>+X</sup> <sub>-1.84</sub>	0.983 <sup>+0.026</sup> <sub>-0.048</sub>	1.15 <sup>+0.03</sup> <sub>-0.03</sub>	0.397 <sup>+0.008</sup> <sub>-0.022</sub>	2.2 <sup>+0.5</sup> <sub>-0.5</sub>	1, 2
101966	901	F8IV	6185 <sup>+44</sup> <sub>-44</sub>	4.26 <sup>+0.03</sup> <sub>-0.03</sub>	+0.13 <sup>+0.03</sup> <sub>-0.03</sub>	+0.383 <sup>+0.054</sup> <sub>-0.054</sub>	3.12 <sup>+0.36</sup> <sub>-0.4</sub>	1.230 <sup>+0.028</sup> <sub>-0.020</sub>	1.38 <sup>+0.06</sup> <sub>-0.05</sub>	0.270 <sup>+0.020</sup> <sub>-0.019</sub>	7.7 <sup>+0.5</sup> <sub>-0.5</sub>	1, 2
108859	953	G0V	6099 <sup>+44</sup> <sub>-44</sub>	4.39 <sup>+0.04</sup> <sub>-0.04</sub>	+0.02 <sup>+0.03</sup> <sub>-0.03</sub>	+0.197 <sup>+0.095</sup> <sub>-0.095</sub>	2.44 <sup>+1.32</sup> <sub>-1.64</sub>	1.131 <sup>+0.026</sup> <sub>-0.024</sub>	1.14 <sup>+0.05</sup> <sub>-0.05</sub>	0.241 <sup>+0.018</sup> <sub>-0.016</sub>	4.5 <sup>+0.5</sup> <sub>-0.5</sub>	1, 2

References: 1: Valenti & Fischer (2005), 2: Takeda et al. (2007), 3: Naef et al. (2010), 4: Wang et al. (2012), 5: Isaacson & Fischer (2010), 6: Harakawa et al. (2010), 7: Beatty et al. (2012), 8: McDonald, Zijlstra & Boyer (2012), 9: da Silva et al. (2007), 10: Casagrande et al. (2011), 11: Robertson et al. (2012), 12: Moutou et al. (2006), 13: Jofré et al. (2015).

The stellar parameters of the host stars are shown in Table 2. 12 of the 19 targets were included in the Spectroscopic Properties Of Cool Stars (SPOCS; Valenti & Fischer 2005) data base, and thus their parameters were taken from Valenti & Fischer (2005) and Takeda et al. (2007). For the remaining targets, the stellar parameters were sourced from the references listed in the table. Fig. 1 shows the stars in our sample on a Hertzsprung–Russell (HR) diagram superimposed on the stars for the BCoolest sample (Marsden et al. 2014, Fig. 1). Fig. 1 shows that the sample stars in this work are similar in general characteristics to the full BCoolest sample. Three of the stars in our sample are classified as subgiants with the remainder being dwarf stars.

The lower panel of Fig. 1 shows the rotation velocity ( $v \sin i$ ) for our sample against effective temperature, also superimposed on the overall BCoolest sample. As shown, the sample exhibits a decrease in rotation rate with decreasing effective temperature. Our entire sample of planet-hosting stars display  $v \sin i < 10 \text{ km s}^{-1}$ , which we note is at the lower end of the BCoolest sample.

## 2.2 The BCoolest sample

In addition to the survey described above, we extracted the 14 known planet-hosting stars from the BCoolest sample. As the methods used to derive their various parameters are the same as this new work, we did not re-analyse the data. Instead, we use the results from Marsden et al. (2014) in our discussion and conclusions. The planetary and

stellar parameters are shown in Appendix B, as are the magnetic and chromospheric results from Marsden et al. (2014) for these stars.

## 3 OBSERVATIONS AND DATA PROCESSING

### 3.1 Instrument and observational procedure

Observations were obtained using the polarimetric mode of the NARVAL spectropolarimeter (attached to the T el escope Bernard Lyot located at Observatoire du Pic du Midi). NARVAL is composed of a bench-mounted high-resolution spectrograph and a Cassegrain-mounted polarimetry module. The spectrograph has an optical wavelength coverage of 370–1000 nm, and a resolution of  $\sim 65\,000$  with a pixel size of  $2.6 \text{ km s}^{-1}$ .

The polarimetric module performs polarimetry over the entire spectral range using a series of three Fresnel rhombs. The light is then split into two beams containing opposite polarization states. These two beams are fed via individual fibres to the spectrograph, allowing the simultaneous capture of both polarization states and further allowing the unpolarized Stokes  $I$  and circularly polarized Stokes  $V$  spectra to be determined from each observation. Further information on NARVAL can be found in Auri ere (2003).

Each Stokes  $V$  observation consists of a sequence of four individual exposures. Effectively, this results in eight individual spectra; four left-hand and four right-hand circularly polarized. As described by Petit, Donati & the ESPaDOnS Project Team (2003), the

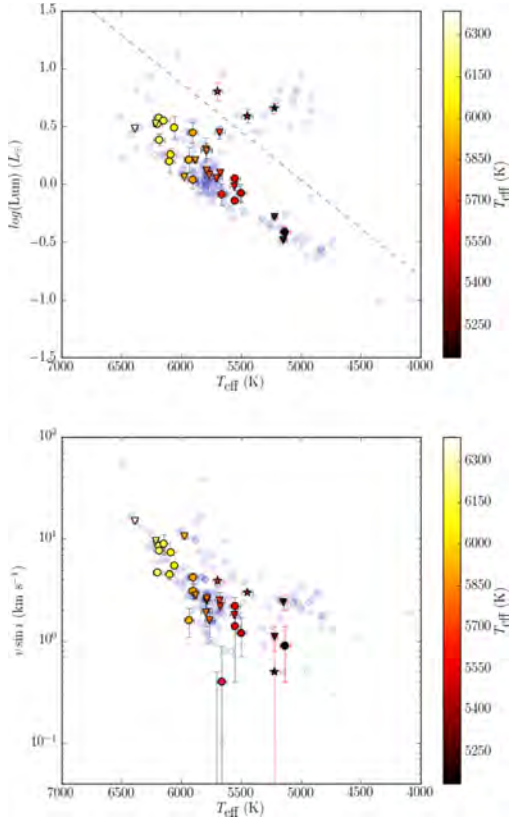


**Figure 1.** HR diagram (upper panel) and  $v \sin i$  versus  $T_{\text{eff}}$  plot (lower panel) for the survey stars (Table 2; circular and star-shaped points) overlaid on the entire BCoolest sample (blue circles; data from Marsden et al. 2014, fig. 1). Planet-hosting stars from the BCoolest survey (Table B2) are shown as inverted triangles. Points with red error bars are magnetic detections, and the colour of the data points represents the effective temperature. Five-pointed star-shaped data points indicate subgiants and circles represent dwarfs with the dashed line dividing these two categories (note inverted triangles from the BCoolest survey are all dwarfs; no planet-hosts in the BCoolest sample were subgiants). This dashed dividing line is in the same position as Marsden et al. (2014, fig. 1).

polarization states in the fibre pair described above are alternated during the sequence to help eliminate instrumental effects; the first and fourth exposures have one arrangement of polarization states, whilst the second and third have the opposite arrangement. Adding all eight spectra yields the unpolarized Stokes  $I$  (intensity) spectrum. The polarized Stokes  $V$  spectrum is obtained as per Donati et al. (1997, equations 1 and 2):

$$\frac{V}{I} = \frac{R_V - 1}{R_V + 1}, \quad (1)$$

where

$$R_V^k = \frac{i_{1,\perp}/i_{1,\parallel}}{i_{2,\perp}/i_{2,\parallel}} \frac{i_{4,\perp}/i_{4,\parallel}}{i_{3,\perp}/i_{3,\parallel}} \quad (2)$$

and  $i_{k,\perp}$  and  $i_{k,\parallel}$  are the two polarized spectra in each exposure,  $k$ .

**Table 3.** Journal of observations showing the object, date and time of the observation, and the exposure time used. As explained in Section 3.1, a Stokes  $V$  observation consists of a sequence of four exposures, hence the nomenclature used here.

HIP no.	HJD 2450000+	Date	UT hh:mm:ss	$T_{\text{exp}}$ (s)
14954	7033.33090	2015-01-10	19:53:06	4 × 900
17747	6958.50071	2014-10-27	23:53:43	4 × 900
24205	6926.67026	2014-09-26	04:02:50	4 × 900
25191	7034.43181	2015-01-11	22:15:20	4 × 900
26381	6957.55553	2014-10-27	01:14:29	4 × 900
26664	6962.64066	2014-11-01	03:17:03	4 × 900
27253	6982.58476	2014-11-21	01:55:21	4 × 900
27384	6960.64135	2014-10-30	03:19:08	4 × 900
28767	6927.68776	2014-09-27	04:27:50	4 × 900
29301	6994.63288	2014-12-03	03:04:50	4 × 900
30057	6994.71807	2014-12-03	05:08:10	4 × 900
32916	6959.64396	2014-10-29	03:23:27	4 × 900
45406	6995.69091	2014-12-04	04:31:58	4 × 900
64457	7030.70798	2015-01-08	04:59:21	4 × 900
	7032.69851	2015-01-10	04:45:26	4 × 900
95740	6995.28708	2014-12-03	18:58:48	4 × 900
96507	6982.30247	2014-11-20	19:18:19	4 × 900
98767	6982.35222	2014-11-20	20:29:11	4 × 900
101966	6984.27534	2014-11-22	18:38:31	4 × 900
108859	6957.33207	2014-10-26	19:53:29	4 × 900

By destructively adding the spectra, a null polarization spectrum,  $N$ , can be obtained (Donati et al. 1997, equations 1 and 3):

$$\frac{N}{I} = \frac{R_N - 1}{R_N + 1}, \quad (3)$$

where

$$R_N^k = \frac{i_{1,\perp}/i_{1,\parallel}}{i_{4,\perp}/i_{4,\parallel}} \frac{i_{2,\perp}/i_{2,\parallel}}{i_{3,\perp}/i_{3,\parallel}}. \quad (4)$$

As described in Bagnulo et al. (2009), a significant signal (i.e. deviation from zero) in the  $N$  spectrum may be indicative of a spurious polarization signal.

### 3.2 Spectropolarimetric observations

All observations were made using NARVAL at Télescope Bernard Lyot between 2014 September and 2015 January. Each star was observed once, except for HIP 64457, which was observed twice. Each observation consisted of a spectropolarimetric sequence of four 900 s exposures. The journal of observations is shown in Table 3.

### 3.3 Data processing

Observations were automatically reduced by a pipeline process utilizing the LIBRE-ESPRIT package. LIBRE-ESPRIT is based on the ESPRIT software (Donati et al. 1997). The reduced Stokes  $I$  and Stokes  $V$  spectra were produced using  $1.8 \text{ km s}^{-1}$  pixel resolution.

### 3.4 Least-squares deconvolution

Zeeman signatures are typically very small and usually the S/N in a reduced spectrum is insufficient for a detection in a single line (Donati, Semel & Rees 1992). Least-squares deconvolution (LSD) is a multiline technique which extracts Stokes  $I$  and Stokes  $V$  information from each individual spectral line in the reduced

**Table 4.** Stellar parameters used to generate line masks for use in LSD. From Marsden et al. (2014, table 2).

Parameter	Units	Range	Step size
$T_{\text{eff}}$	K	4000–6500	250
$\log(g)$	$\text{cm s}^{-2}$	3.5–4.5	0.5
$\log(\text{M}/\text{H})$		−0.2 to +0.2	0.2

**Table 5.** Normalization parameters used to produce LSD profiles, following Marsden et al. (2014, table 4).  $d_0$  = line central depth,  $\lambda_0$  = line central wavelength and  $g_0$  = line Landé factor.

$T_{\text{eff}}(\text{K})$	$d_0$	$\lambda_0(\text{nm})$	$g_0$
4000	0.55	650.0	1.22
4250	0.55	640.0	1.22
4500	0.55	630.0	1.22
4750	0.55	620.0	1.22
5000	0.54	610.0	1.22
5250	0.54	600.0	1.22
5500	0.53	590.0	1.22
5750	0.52	580.0	1.22
6000	0.51	570.0	1.22
6250	0.50	570.0	1.21
6500	0.49	560.0	1.21

spectrum and determines an average profile with a higher S/N than for each individual line (Donati, Semel & Rees 1992; Kochukhov, Makaganiuk & Piskunov 2010).

Marsden et al. (2014) computed a set of line masks for use in LSD for the BCool sample using the Vienna Atomic Line Database (VALD;<sup>2</sup> Kupka et al. 2000). These masks are derived from stellar atmospheric and spectral synthesis models using the stellar parameters  $T_{\text{eff}}$ ,  $\log(g)$  and  $\log(\text{M}/\text{H})$  [or  $\log(\text{Fe}/\text{H})$  if  $\log(\text{M}/\text{H})$  is unavailable or unknown]. For consistency, these same masks were used in this work, and the range of parameters and step size used is shown in Table 4. For more details on the creation of the set of line masks, see Marsden et al. (2014, section 3.3).

For each target, the appropriate line mask was chosen, and LSD profiles for Stokes  $I$  and Stokes  $V$  were created with a resolved element of  $1.8 \text{ km s}^{-1}$ . Depending on the stellar parameters of the star in our sample, the number of lines used in the LSD process varies from  $\sim 7000$  to  $\sim 14000$ .

As in Marsden et al. (2014), the weighting of the spectral lines was adjusted such that the mean weights of the Stokes  $V$  and Stokes  $I$  profiles were close to unity. We use the equations given by Marsden et al. (2014, equations 3–5) for calculating mean weights, and the same normalization parameters ( $d_0$  = line central depth,  $\lambda_0$  = line central wavelength,  $g_0$  = line Landé factor), varied for each 250 K step in effective temperature. The normalization parameters are additionally used in the calculation of the longitudinal magnetic field (Section 3.5) and are reproduced in Table 5.

### 3.5 The longitudinal magnetic field

The mean longitudinal magnetic field,  $B_\ell$  (or given as  $\langle B_z \rangle$  in some publications) is the line-of-sight component of the stellar magnetic field integrated over the visible disc of the star.  $B_\ell$  can be obtained from the Stokes  $I$  and Stokes  $V$  LSD profiles. From Donati et al.

<sup>2</sup> <http://vald.astro.univie.ac.at/~vald3/php/vald.php>

(1997) and Mathys (1989), for the given velocity ( $v$ , in  $\text{km s}^{-1}$ ) space

$$B_\ell = -2.14 \times 10^{11} \frac{\int v V(v) dv}{\lambda_0 g_0 c \int [I_c - I(v)] dv}, \quad (5)$$

where  $B_\ell$  is in gauss, and  $\lambda_0$  and  $g_0$  are given in Table 5.  $c$  is the speed of light in  $\text{km s}^{-1}$  and  $I_c$  is the continuum level of the Stokes  $I$  LSD profile and is normalized to 1. The error in  $B_\ell$  ( $B_{\text{err}}$ ) is calculated by propagating the uncertainties in the reduction pipeline through equation (5). As mentioned by Marsden et al. (2014) and discussed in depth by Shorlin et al. (2002, section 5), the uncertainty depends upon the S/N of the observation, the number of lines used to produce the Stokes  $V$  profile, and the depth and width of the average line. The line depth and width scale linearly with  $v \sin i$ .

An additional uncertainty in  $B_\ell$  is introduced by the choice of the velocity domain used to integrate equation (5). A narrow velocity domain potentially excludes polarized signals, while a domain which is too wide potentially introduces spurious signals due to the noise in the Stokes  $V$  spectrum. For consistency with the measurement of  $B_\ell$  of the BCool sample, the method outlined by Marsden et al. (2014) was used.  $B_\ell$  was calculated using a range of velocity domains, following which, the domain for which the ratio of  $|B_\ell|/B_{\text{err}}$  was maximized was chosen.

For each observation, the value of  $B_\ell$  was calculated for the null profile ( $N_\ell$ ) over the same velocity domain used for the Stokes  $V$  profile. A value of  $|N_\ell|$  which is close to zero is indicative that the magnetic-field measurement is unaffected by spurious polarization signals. This is indeed the case for the majority of our sample. Where  $|N_\ell|$  departs significantly from zero, and is large relative to  $|B_\ell|$ , the measurement must be considered carefully. The values of  $B_\ell$  and  $N_\ell$  for each observation, and the velocity domain used for the calculations are presented in Table 6.

### 3.6 Magnetic detection

Donati et al. (1992) and Donati et al. (1997) describe a method of determining whether a magnetic field is ‘detected’ on a star using the Stokes  $V$  profile. That is, a probability is calculated as to whether the variations in the Stokes  $V$  LSD profile are likely due to the presence of a magnetic field rather than from noise.

Reduced  $\chi^2$  statistics are calculated for the Stokes  $V$  and  $N$  profiles, inside and outside the spectral lines as defined by the position of the unpolarized Stokes  $I$  profile in velocity space. From these values a false alarm probability (FAP) is determined. An unambiguous (or definite) detection is defined as having  $\text{FAP} < 10^{-5}$  (corresponding to a  $\chi^2$  probability greater than 99.999 per cent). A marginal detection is defined as having  $10^{-5} < \text{FAP} < 10^{-3}$  ( $\chi^2$  probability between 99.999 and 99.9 per cent). It is to be noted that there are no marginal detections in our sample.  $\text{FAP} > 10^{-3}$  is classified as a non-detection.

For each observation, the FAP and the classification as a definite detection (D) or non-detection (N) is shown in Table 6. It should be noted that irrespective of the detection state, values for  $B_\ell$  and  $N_\ell$  are shown. The probability function used to determine the FAP takes into account the Stokes  $V$  and  $N$  both inside and outside the spectral lines, whereas the values of  $N_\ell$  and  $B_\ell$  are calculated only over a velocity domain containing the spectral lines. Thus, detections depend on the FAP rather than absolute longitudinal field values. In general, for non-detections (N),  $B_\ell$  will be of the same order as  $N_\ell$ , i.e. the probability is that the measured  $B_\ell$  is due to noise in the Stokes  $V$  LSD profile rather than magnetic activity. The exception in our sample is HIP 28767 (see Table 6 and Appendix A3), which

**Table 6.** Results from the analysis of the Stokes  $V$  LSD profiles of the stars not observed by Marsden et al. (2014). Column 3 provides the date of the observation (in the case of HIP 64457 two observations were obtained). Column 4 shows the radial velocity for the star (see Fig. 2); for comparison, column 5 shows the radial velocity measured by Nidever et al. (2002) or in two cases from Valenti & Fischer (2005) indicated by  $^{VF}$ . Columns 6 and 7 show the signal-to-noise of the Stokes  $V$  profile and the number of lines used in the LSD process, respectively. Column 8 indicates if the magnetic field was unambiguously detected (D) or not (N); note, we have no marginal detections, represented by M in Marsden et al. (2014, table 3). Column 9 shows the false alarm probability calculated for the detection in column 8. Columns 10 and 11 indicate the velocity range used to calculate  $B_\ell$  (column 12) and  $N_\ell$  (column 13) using equation (5).

HIP no.	Obs. no.	HJD +2450000	RV (this work) (km s $^{-1}$ )	RV (Nidever) (km s $^{-1}$ )	SNR $_{LSD}$	Lines used	Detection	FAP	Velocity range (km s $^{-1}$ )	$B_\ell$ (G)	$N_\ell$ (G)
14954	1	7033.33090	+19.64	+19.331	60 048	11 101	N	$5.320 \times 10^{-1}$	+9 +31	$+0.4 \pm 0.3$	$0.0 \pm 0.3$
17747	1	6958.50071	-9.97	-10.6 $^{VF}$	18 483	10 602	N	$9.967 \times 10^{-1}$	-25 +5	$+1.2 \pm 1.1$	$+1.5 \pm 1.1$
24205	1	6926.67026	+5.74	+5.714	16 164	7584	N	$2.109 \times 10^{-1}$	+0 +13	$+1.3 \pm 0.4$	$+0.3 \pm 0.4$
25191	1	7034.43181	+29.54	-	6046	9392	N	$4.518 \times 10^{-1}$	+18 +41	$-2.3 \pm 1.9$	$+1.9 \pm 1.9$
26381	1	6957.55553	-22.93	-23.076	12 834	9365	N	$6.022 \times 10^{-1}$	-34 -13	$-1.3 \pm 1.2$	$+2.3 \pm 1.2$
26664	1	6962.64066	-21.85	-	11 787	12 097	N	$1.245 \times 10^{-1}$	-27 -16	$-1.5 \pm 0.5$	$+0.3 \pm 0.5$
27253	1	6982.58476	+30.44	+30.210	28 583	12 803	D	$2.509 \times 10^{-9}$	+23 +38	$+1.7 \pm 0.3$	$+0.0 \pm 0.3$
27384	1	6960.64135	-25.29	-	13 887	13 918	D	$1.332 \times 10^{-15}$	-31 -20	$+3.4 \pm 0.4$	$-0.1 \pm 0.4$
28767	1	6927.68776	+32.85	+32.542	20 086	10 062	D	$1.448 \times 10^{-9}$	+14 +52	$+4.5 \pm 1.4$	$+3.5 \pm 1.4$
29301	1	6994.63288	-47.25	-	8003	8309	N	$4.801 \times 10^{-1}$	-59 -36	$-2.7 \pm 1.7$	$+1.0 \pm 1.7$
30057	1	6994.71807	-28.98	-	12 649	9147	N	$9.741 \times 10^{-1}$	-36 -22	$+0.5 \pm 0.6$	$-0.5 \pm 0.6$
32916	1	6959.64396	+12.18	+12.045	14 420	11 084	N	$3.266 \times 10^{-2}$	+5 +18	$+0.9 \pm 0.5$	$-0.9 \pm 0.5$
45406	1	6995.69091	+20.08	-	14 833	11 058	N	$9.316 \times 10^{-1}$	+9 +32	$-1.5 \pm 1.0$	$+2.1 \pm 1.0$
64457	1	7030.70798	-11.80	-12.012	17 873	13 110	D	$6.762 \times 10^{-7}$	-18 -5	$+2.5 \pm 0.4$	$-0.5 \pm 0.4$
	2	7032.69851	-11.75	-12.012	21 789	13 048	D	$5.749 \times 10^{-13}$	-18 -5	$+2.4 \pm 0.3$	$-0.6 \pm 0.3$
95740	1	6995.28708	-50.16	-54.9 $^{VF}$	9290	10 006	N	$1.839 \times 10^{-1}$	-58 -41	$+3.0 \pm 0.9$	$+0.6 \pm 0.9$
96507	1	6982.30247	+0.82	-	14 747	10 618	N	$5.742 \times 10^{-1}$	-7 +9	$+0.7 \pm 0.7$	$+0.9 \pm 0.7$
98767	1	6982.35222	-45.08	-45.308	25 620	12 051	N	$9.512 \times 10^{-1}$	-50 -40	$-0.2 \pm 0.2$	$+0.3 \pm 0.2$
101966	1	6984.27534	-30.80	-30.189	14 961	9143	N	$9.940 \times 10^{-1}$	-45 -16	$+1.7 \pm 1.23$	$-0.3 \pm 1.3$
108859	1	6957.33207	-14.56	-14.759	11 851	7164	N	$4.666 \times 10^{-1}$	-23 -5	$-0.9 \pm 0.8$	$-0.6 \pm 0.8$

has a value of  $N_\ell$  close to the calculated  $B_\ell$ , but a very low FAP (i.e. similar values of  $N_\ell$  and  $B_\ell$  do not necessarily preclude a detection).

### 3.7 Radial velocities

The radial velocities of the host stars of the planetary systems were determined in this work (Table 6) and compared, where available, to those calculated by Nidever et al. (2002). A Pseudovoigt profile was fitted to the Stokes  $I$  LSD profile of each observation, with the centroid of the Pseudovoigt considered to be the radial velocity (e.g. Fig. 2). The long-term radial-velocity stability of NARVAL is  $30 \text{ m s}^{-1}$  (Moutou et al. 2007).

While our values are generally close to those previously published, it must be noted that since our sample stars host planetary systems, there will be intrinsic variation in the radial velocity of the host star due to the gravitational influence of the planets. Thus, differences, potentially of significant magnitude, are to be expected depending upon the specific time of observation and the orbital configurations. Hence, the values are presented as indicative only, and for completeness with the BCool sample.

### 3.8 Stellar activity proxies

As for the BCool sample, various measures of stellar activity were calculated for each target in our sample. In addition to the Ca II H&K S-index (Wright et al. 2004), Ca II infrared triplet (IRT) and H $\alpha$  indices were derived.

#### 3.8.1 Ca II H&K emission (S-index)

Following the methodology of Wright et al. (2004), Marsden et al. (2014) determined for NARVAL the coefficients  $a$ ,  $b$ ,  $c$ ,  $d$  and  $e$  (see

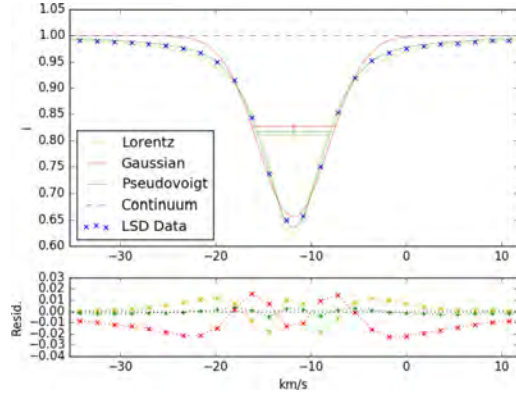


**Figure 2.** Determining the radial velocity of HIP 64457 (HD 114783). The data from the unpolarized Stokes  $I$  LSD profile are shown by the blue crosses. Gaussian (red), Lorentz (yellow) and Pseudovoigt (green) profiles are fitted to the LSD profile data (upper panel). Residuals from each fit are shown in the lower panel. The centroid of the Pseudovoigt fitted profile is taken as the radial velocity of the star.

Table 7) of the equation

$$S\text{-index} = \frac{aF_H + bF_K}{cF_{RHK} + dF_{VHK}} + e, \quad (6)$$

where  $F_H$  and  $F_K$  are the fluxes in  $2.18 \text{ \AA}$  triangular bandpasses centred on the cores of the Ca II H&K lines and  $F_{RHK}$  and  $F_{VHK}$  are the fluxes in two rectangular  $20 \text{ \AA}$  bandpasses centred on the continuum either side of the HK lines at  $3901.07$  and  $4001.07 \text{ \AA}$ , respectively.

**Table 7.** Table of coefficients for equation (6) as calculated by Marsden et al. (2014) for the NARVAL instrument.

Coefficient	NARVAL
<i>a</i>	12.873
<i>b</i>	2.502
<i>c</i>	8.877
<i>d</i>	4.271
<i>e</i>	$1.183 \times 10^{-3}$

For each reduced unpolarized spectrum of each star, overlapping orders were removed. Equation (6) was then applied to the remaining spectrum, generating the Ca II H&K S-indices for each spectrum. As per Marsden et al. (2014), the sample standard deviation of the S-indices for each star was calculated as an empirical measure of the uncertainty. The mean and standard deviation values for each star are shown in Table 8.

### 3.8.2 Derived chromospheric parameters

The S-indices were then used to derive various chromospheric parameters for each star, all of which are shown in Table 8.  $\text{Log}(R'_{\text{HK}})$  was derived using Wright et al. (2004, equations 9–12), using *Hipparcos*  $B - V$  values. Using the further formulations from Wright et al. (2004, equations 13–15),  $\log(P_{\text{rot}}/\tau)$  ( $\log(\text{Rossby number})$ ), the chromospheric period and chromospheric age for each target were calculated.

### 3.8.3 $H\alpha$ emission

The  $H\alpha$ -index was determined for each unpolarized reduced spectrum using the equation

$$H\alpha\text{-index} = \frac{F_{H\alpha}}{F_{V_{H\alpha}} + F_{R_{H\alpha}}}, \quad (7)$$

where  $F_{H\alpha}$  is the flux from a 3.6 Å rectangular bandpass centred on the  $H\alpha$  line (6562.85 Å), and  $F_{V_{H\alpha}}$  and  $F_{R_{H\alpha}}$  are the fluxes in 2.2 Å rectangular bandpasses located on the continuum either side of the  $H\alpha$  line centred at 6558.85 and 6567.30 Å. These bandpasses are defined by Gizis, Reid & Hawley (2002, table 3).

As for the S-index, the sample standard deviation of the  $H\alpha$ -indices for each star was calculated as an empirical measure of the uncertainty. The mean and standard deviation of the  $H\alpha$ -index for each star are shown in Table 8.

### 3.8.4 Ca II IRT emission

The activity index for the Ca II IRT ( $\text{Ca}_{\text{IRT}}$ -index) was calculated from each unpolarized reduced spectrum using the equation (Petit et al. 2013, equation 1)

$$\text{Ca}_{\text{IRT}}\text{-index} = \frac{F_{8498} + F_{8542} + F_{8662}}{F_{V_{\text{IRT}}} + F_{R_{\text{IRT}}}}, \quad (8)$$

where  $F_{8498}$ ,  $F_{8542}$  and  $F_{8662}$  are the integrated fluxes of three 2 Å rectangular bandpasses centred on the corresponding Ca II IRT lines (located at 8498.02, 8542.09 and 8662.14 Å), while  $F_{V_{\text{IRT}}}$  and  $F_{R_{\text{IRT}}}$  are the fluxes in 5 Å rectangular bandpasses located on the continuum either side of the Ca II triplet at 8475.8 and 8704.9 Å. The mean

**Table 8.** Chromospheric activity of the stars not observed by Marsden et al. (2014).  $B - V$  and  $V$  values are from *Hipparcos*. Where Wright et al. (2004) have calculated an S-index, it is shown in column 4. Chromospheric ages, periods and  $\log(P_{\text{rot}}/\tau)$  have been determined using the equations presented in Wright et al. (2004). As noted in the text, sample standard deviations are used as an indication of various errors. Note that HIP 64457<sup>a</sup> has two sequences of observations (eight exposures) compared with all other targets (four exposures).

HIP no.	$B - V$ ( <i>Hipparcos</i> )	$V$	S-index Wright.	S-index (this work)	$\log(R'_{\text{HK}})$	Chromospheric age (Gyr)	Chromospheric period (d)	$\text{Ca}_{\text{IRT}}$ -index	$H\alpha$ -index	$\log(P_{\text{rot}}/\tau)$
14954	0.575	5.07	0.173	$0.1569 \pm 0.0003$	$-4.99^{+0.00}_{-0.04}$	$5.404^{+0.051}_{-0.044}$	$16.1^{+0.0}_{-0.1}$	$0.7411 \pm 0.0011$	$0.3057 \pm 0.0001$	$+0.320^{+0.001}_{-0.001}$
17747	0.634	7.25	0.150	$0.1451 \pm 0.0004$	$-5.10^{+0.00}_{-0.01}$	$7.814^{+0.132}_{-0.079}$	$25.4^{+0.1}_{-0.1}$	$0.7561 \pm 0.0008$	$0.3106 \pm 0.0001$	$+0.361^{+0.002}_{-0.001}$
24205	0.588	7.00	0.180	$0.1773 \pm 0.0011$	$-4.87^{+0.01}_{-0.00}$	$3.515^{+0.049}_{-0.105}$	$15.5^{+0.1}_{-0.2}$	$0.8209 \pm 0.0009$	$0.3146 \pm 0.0002$	$+0.266^{+0.002}_{-0.004}$
25191	0.761	8.99	–	$0.1558 \pm 0.0085$	$-5.05^{+0.05}_{-0.07}$	$6.777^{+1.622}_{-1.069}$	$39.4^{+2.4}_{-1.6}$	$0.8139 \pm 0.0031$	$0.3307 \pm 0.0019$	$+0.344^{+0.026}_{-0.018}$
26381	0.667	7.68	0.179	$0.1881 \pm 0.0016$	$-4.86^{+0.01}_{-0.01}$	$3.314^{+0.078}_{-0.078}$	$23.5^{+0.2}_{-0.2}$	$0.8462 \pm 0.0007$	$0.3292 \pm 0.0006$	$+0.257^{+0.004}_{-0.004}$
26664	0.827	8.67	–	$0.1866 \pm 0.0049$	$-4.94^{+0.02}_{-0.02}$	$4.524^{+0.397}_{-0.253}$	$40.3^{+1.0}_{-0.6}$	$0.7546 \pm 0.0004$	$0.3401 \pm 0.0008$	$+0.299^{+0.010}_{-0.007}$
27253	0.773	5.95	0.174	$0.1750 \pm 0.0005$	$-4.96^{+0.00}_{-0.00}$	$4.854^{+0.056}_{-0.036}$	$37.3^{+0.1}_{-0.1}$	$0.6871 \pm 0.0007$	$0.3231 \pm 0.0001$	$+0.308^{+0.001}_{-0.001}$
27384	0.873	8.26	–	$0.1978 \pm 0.0046$	$-4.93^{+0.01}_{-0.02}$	$4.393^{+0.290}_{-0.240}$	$42.3^{+0.8}_{-0.7}$	$0.7187 \pm 0.0006$	$0.3368 \pm 0.0005$	$+0.296^{+0.008}_{-0.007}$
28767	0.573	6.74	0.234	$0.2543 \pm 0.0003$	$-4.58^{+0.00}_{-0.00}$	$1.249^{+0.002}_{-0.005}$	$7.8^{+0.0}_{-0.0}$	$0.8398 \pm 0.0017$	$0.3138 \pm 0.0002$	$+0.011^{+0.001}_{-0.002}$
29301	0.530	8.68	–	$0.1384 \pm 0.0028$	$-5.13^{+0.04}_{-0.01}$	$8.752^{+0.392}_{-1.088}$	$12.9^{+0.2}_{-0.5}$	$0.7734 \pm 0.0010$	$0.3041 \pm 0.0008$	$+0.375^{+0.006}_{-0.016}$
30057	0.596	8.03	–	$0.1492 \pm 0.0019$	$-5.05^{+0.01}_{-0.02}$	$6.763^{+0.466}_{-0.290}$	$19.6^{+0.3}_{-0.2}$	$0.7451 \pm 0.0006$	$0.3076 \pm 0.0002$	$+0.345^{+0.008}_{-0.005}$
32916	0.729	8.10	0.211	$0.1858 \pm 0.0012$	$-4.90^{+0.01}_{-0.01}$	$3.824^{+0.090}_{-0.076}$	$31.0^{+0.2}_{-0.2}$	$0.7615 \pm 0.0009$	$0.3281 \pm 0.0003$	$+0.278^{+0.003}_{-0.003}$
45406	0.693	8.05	–	$0.1493 \pm 0.0013$	$-5.08^{+0.01}_{-0.01}$	$7.346^{+0.286}_{-0.262}$	$32.6^{+0.3}_{-0.3}$	$0.7730 \pm 0.0009$	$0.3222 \pm 0.0003$	$+0.354^{+0.004}_{-0.004}$
64457 <sup>a</sup>	0.930	7.56	0.215	$0.2033 \pm 0.0032$	$-4.96^{+0.01}_{-0.01}$	$4.896^{+0.207}_{-0.184}$	$45.4^{+0.5}_{-0.5}$	$0.7618 \pm 0.0018$	$0.3528 \pm 0.0007$	$+0.309^{+0.005}_{-0.004}$
95740	0.678	7.86	0.145	$0.1521 \pm 0.0027$	$-5.06^{+0.02}_{-0.02}$	$6.811^{+0.450}_{-0.509}$	$30.1^{+0.5}_{-0.6}$	$0.7634 \pm 0.0007$	$0.3171 \pm 0.0005$	$+0.346^{+0.007}_{-0.008}$
96507	0.606	6.67	–	$0.1286 \pm 0.0009$	$-5.26^{+0.01}_{-0.02}$	$12.638^{+0.559}_{-0.214}$	$25.4^{+0.5}_{-0.2}$	$0.7486 \pm 0.0021$	$0.3110 \pm 0.0001$	$+0.430^{+0.008}_{-0.003}$
98767	0.749	5.73	0.148	$0.1499 \pm 0.0018$	$-5.08^{+0.01}_{-0.01}$	$7.461^{+0.354}_{-0.321}$	$39.2^{+0.5}_{-0.4}$	$0.7657 \pm 0.0019$	$0.3324 \pm 0.0003$	$+0.356^{+0.005}_{-0.005}$
101966	0.559	6.39	0.151	$0.1455 \pm 0.0014$	$-5.07^{+0.01}_{-0.01}$	$7.213^{+0.332}_{-0.334}$	$15.5^{+0.2}_{-0.2}$	$0.7701 \pm 0.0010$	$0.3039 \pm 0.0006$	$+0.352^{+0.005}_{-0.005}$
108859	0.594	7.65	0.154	$0.1558 \pm 0.0085$	$-5.01^{+0.06}_{-0.09}$	$5.831^{+1.886}_{-1.193}$	$18.6^{+1.5}_{-1.0}$	$0.8025 \pm 0.0023$	$0.3112 \pm 0.0003$	$+0.326^{+0.033}_{-0.024}$

and standard deviation of the  $C_{\text{aIRT}}$ -index for each star are shown in Table 8.

## 4 RESULTS AND DISCUSSION

### 4.1 Magnetic detections

Due to the small size of our sample, we did not attempt a comprehensive analysis of detection rates and their correlation with stellar and observational parameters as per Marsden et al. (2014). However, we can make some broad observations relating to the overall BCool sample.

Of the sample of 19 newly observed stars, we obtained magnetic detections with a FAP  $< 10^{-5}$  on four targets. As noted by Marsden et al. (2014), for the BCool sample in general, the detection rates of the magnetic field drop with increasing age, with decreasing  $v \sin i$  and with decreasing activity (i.e. S-index). Given that our sample of planet-hosting stars are generally older than 2 Gyr, are relatively slow rotators *and* have low activity indices, it is to be expected that our overall detection rate will be low. As such, it is unsurprising that it is in fact lower than the overall BCool sample. Using the broad categorization of Marsden et al. (2014, G-stars:  $5000 \leq T_{\text{eff}} \leq 6000$  K; F-Stars:  $T_{\text{eff}} > 6000$  K), we have a 25 per cent detection rate for G-stars (cf. 38 per cent BCool) and 14 per cent for F-stars (cf. 32 per cent BCool).

Higher measured  $B_z$  correlates with a higher S-index, and magnetic detections are more prevalent with higher S-indices ( $\geq 0.18$ ). However, some magnetic detections with lower S-indices are apparent; these exceptions generally have a significantly higher  $\text{SNR}_{\text{LSD}}$ . This correlation is also noted by Marsden et al. (2014).

Even if we consider the additional planet-hosting stars from the BCool survey (Appendix B), our detection rate remains very low (24 per cent of the 33 total stars). Our rate is even lower if the two very young planet-hosts HIP 16537 ( $\epsilon$  Eri;  $0.00^{+0.60}_{-0.00}$  Gyr) and HIP 107350 (HN Peg;  $0.00^{+0.88}_{-0.00}$  Gyr) from the BCool survey are disregarded as outliers, given that high activity (and thus magnetic field) is strongly correlated with young age and rapid rotation.

We find a correlation with S-index. All stars with an S-index greater than  $\sim 0.18$  obtained a detection. Only one star of our 19 new targets, HIP 27253, with an S-index below 0.18 ( $0.1750 \pm 0.0005$ ) produced a detection. This result is consistent with the finding from Marsden et al. (2014) that, as would be expected, increasing S-index is strongly correlated with the rate of detections.

### 4.2 $|B_z|$ Measurements

In Fig. 3, we plot the maximum  $|B_z|$  against  $T_{\text{eff}}$  for the sample of 19 newly observed stars and the BCool planet-hosts superimposed on the entire BCool sample (data from Marsden et al. (2014)). Our results are consistent with the low-activity area of the BCool sample.

In Fig. 4, we similarly overplot our sample and BCool planet-hosts over the entire BCool survey for  $|B_z|$  against  $v \sin i$ . As in Marsden et al. (2014, fig. 13, section 6.3.3), stars above the dashed line are considered to have high values of  $|B_z|$  compared to stars with a similar  $v \sin i$ . We note that only a single star in our new sample (HIP 28767) has a longitudinal magnetic field marginally above this line. It also has, by far, the highest S-index in our sample. Given the correlation of decreasing  $|B_z|$  with increasing age, it is not surprising that almost our entire sample is located below this cut-off line.

Fig. 5 illustrates that once again, the planet-hosting sample of this work is entirely consistent with the BCool survey results. In the upper panel of Fig. 5, we show the magnetic-field strength against

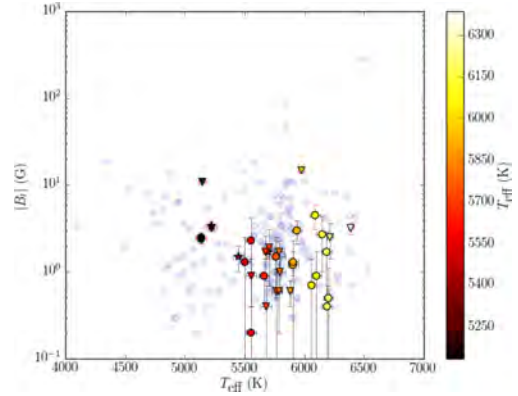


Figure 3. Plot of the maximum measured  $|B_z|$  versus  $T_{\text{eff}}$  for the planet-hosting stars (symbols are as in Fig. 1). The complete BCool sample is shown as blue circles.

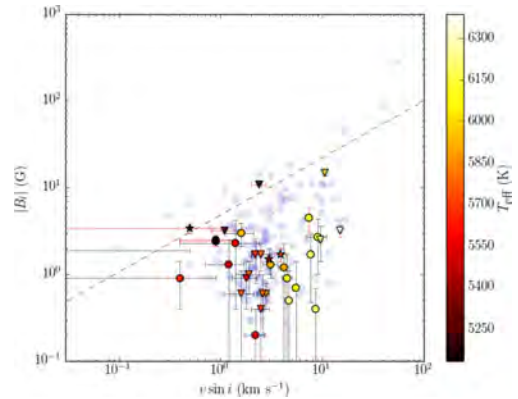
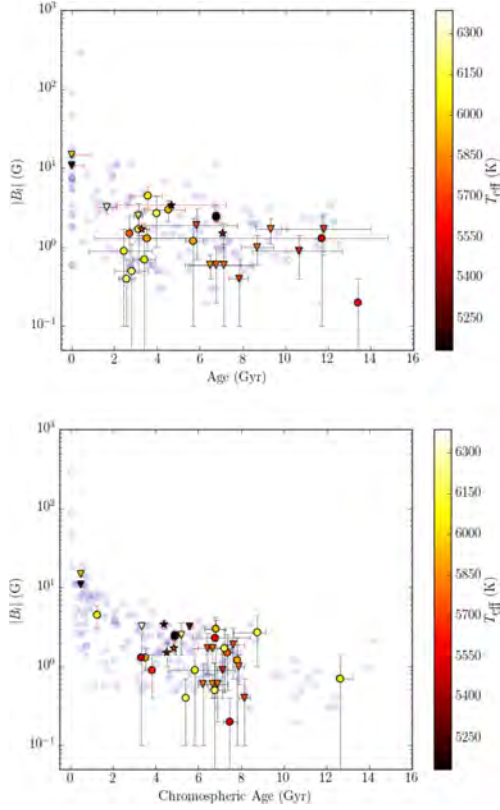


Figure 4. Plot of the maximum measured  $|B_z|$  versus  $v \sin i$  for the planet-hosting stars (symbols are as in Fig. 1). Stars located above the dashed line have significantly higher  $|B_z|$  than others with similar  $v \sin i$ , as per Marsden et al. (2014, section 6.3.3). The complete BCool sample is shown as blue circles.

the published ages of the stars (superimposed on the BCool sample), and in the lower panel, the magnetic field against the chromospheric age we derive. It is clear that our sample has older, evolved stars, and as expected their level of activity is lower than the younger stars which generate the more extreme magnetic fields.

Another general observation consistent with Marsden et al. (2014) is that cooler stars in our sample tend to have higher  $|B_z|$ . However, it should be noted that there are only five K-dwarfs in the combined set of planet-hosting stars.

Chromospheric activity seems to be the most strongly correlated with  $|B_z|$ , as shown in Fig. 6. It should be noted that more active stars are generally excluded from planet-search programmes, given that phenomena generated by stellar activity can mimic the cyclic variations used to detect planets (Saar & Donahue 1997; Saar, Butler & Marcy 1998; Jeffers et al. 2014), additionally biasing the entire sample to less active stars. Much work is currently underway in attempting to disentangle stellar activity signals from those generated from planetary sources (Petit et al. 2015; Feng et al. 2016; Hébrard



**Figure 5.** Plot of maximum measured  $|B_{\ell}|$  versus age (upper panel) and chromospheric age (lower panel; calculated from the equations of Wright et al. 2004 and shown in Table 8) for the planet-hosting stars. Symbols are as in Fig. 1. The complete BCoolest sample is shown as blue circles.

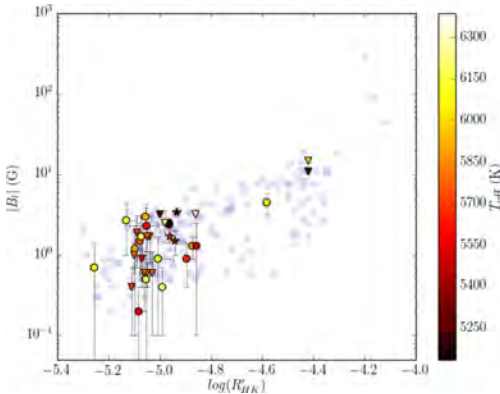


**Figure 6.** Plot of maximum measured  $|B_{\ell}|$  versus  $\log(R'_{\text{HR}})$  (Table 8) for the planet-hosting stars. Symbols are as in Fig. 1. The complete BCoolest sample is shown as blue circles.

et al. 2016; Herrero et al. 2016). This may in future allow for a broadening of the sample set of planet-hosting stars.

### 4.3 Planetary influences

In Fig. 7, we present the configuration of the planetary systems from both our new sample and the BCoolest sample, and their relationship with the activity proxy (S-index) and the magnetic field [ $\log(|B_{\ell}|)$ ]. In both panels, each circle represents a planet, and its centre point on the x-axis represents the semimajor axis of its orbit. In the case of systems with more than one planet, each planet is represented, with all planets in a system having the same y-axis value. The size of the circles is proportional to the planetary mass. In the upper panel, the y-axis represents the magnetic-field strength of the host star, and the colour of the circle its S-index. In the lower panel, the y-axis represents the S-index of the host star and the colour of the circle is  $\log(|B_{\ell}|)$ . Finally, if a magnetic detection occurred for

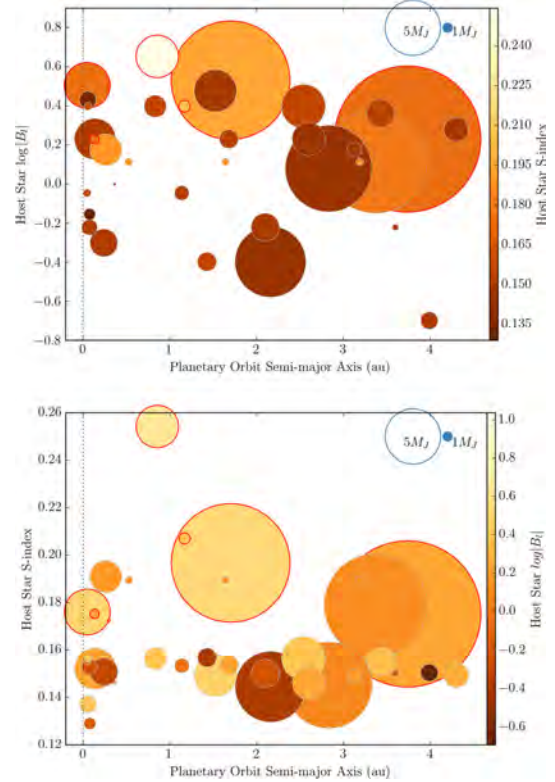


**Figure 7.** S-index and  $\log(|B_{\ell}|)$  shown against the semimajor axis of planetary orbits for the BCoolest planet-hosting stars and the new survey targets. The fill colours of the circles represent  $\log(|B_{\ell}|)$  (upper panel) and S-index (lower panel). The radius of circles are proportional to planetary masses,  $M \sin i$ . Red edges to the circles indicate the host star had a magnetic detection. HIP107350 (HN Peg) and HIP16537 ( $\epsilon$  Eri) are not included on this plot for clarity. HN Peg b has a semimajor axis of  $\sim 790$  au, and  $\epsilon$  Eri has a relatively high S-index (0.5357) compared to the other sample stars; both have magnetic detections and  $\log(|B_{\ell}|)$  much higher than all other stars shown. We find no detectable correlation between mass and orbital distance of the planets in the system and the activity of the star.

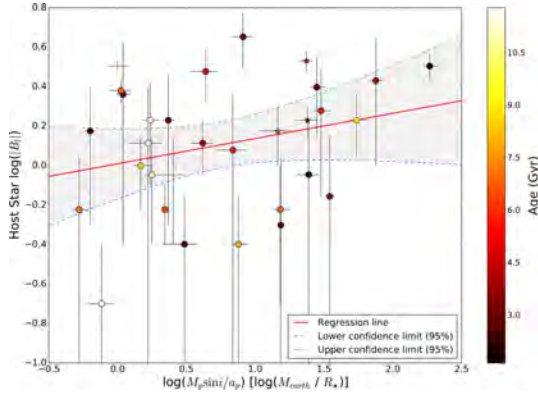


**Figure 8.**  $\log(|B_l|)$  shown against mass ratio for the BCool planet-hosting stars and the new survey targets. Points are coloured according to age. Note there is a very weak positive linear relationship (see regression line). The shaded area represents the 95 per cent confidence interval. Within this confidence interval, the population relationship may be zero. The young, active stars HIP107350 (HN Peg) and HIP16537 ( $\epsilon$  Eri) are not included on this plot for clarity.

a host star, the circle(s) representing its planet(s) are outlined in red. There appears to be no correlation between the magnetic-field strength and the planetary configuration.

There are several planets which would warrant the colloquial appellation of ‘hot Jupiter’, and would therefore seem the most likely candidates for SPI, whether through tidal effects, magnetic interaction, or other posited SPI mechanisms. However, the presence of these planets do not result in any detectable trend towards higher activity or higher measured longitudinal magnetic field. This is consistent with the findings of Miller et al. (2015).

Indeed, investigating potential tidal effects in particular, if we plot  $\log(|B_l|)$  versus the logarithm of the mass ratio (planetary mass divided by the orbital semimajor axis), shown in Fig. 8, there appears to be a weak positive linear relationship. This should be interpreted with some caution, given the very low  $R^2$  value and the 95 per cent confidence interval. This confidence interval provides an estimate of the uncertainty around the proposed relationship, and indicates that the population relationship may be zero. Plotting  $\log(|B_l|)$  against the logarithm of the relative height of the tidal bulge induced on the star –  $h_t$  from Figueira et al. (2016, equation 1) – shows absolutely no correlation (Fig. 9).

It is noted that the sample is small, and while there are some ‘hot Jupiters’, none of them are at the higher end of the mass range, nor are the more massive planets particularly close to the host star. Given the correlations between stellar parameters and the strength of the stellar magnetic field detailed by Marsden et al. (2014), it is clear that any effect of SPI on the global stellar magnetic field or activity proxies measured here, if it exists, is too subtle to detect in our sample. Fares et al. (2013) and Vidotto et al. (2014) came to similar conclusions and called for larger samples. However, the inherent biases in planet-search programmes which exclude active stars makes increasing the sample size and scope difficult. Alternatively, in the absence of a larger sample, increasing the amount of observations of both the set of planet-hosting and non-planet-hosting stars would allow us to analyse the full magnetic variability range for each star and to look for influence on any magnetic cycles.

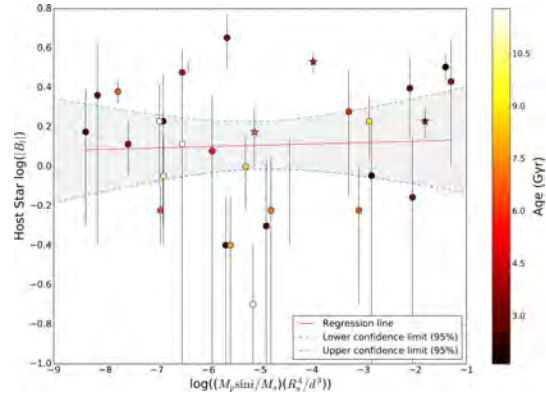


**Figure 9.**  $\log(|B_l|)$  shown against the log of the relative tidal height ( $h_t$ ) for the BCool planet-hosting stars and the new survey targets. Points are coloured according to age. Horizontal error bars have been omitted for clarity. No trend is apparent, although a regression line is shown. The shaded area represents the 95 per cent confidence interval around the regression line. The young, active stars HIP107350 (HN Peg) and HIP16537 ( $\epsilon$  Eri) are not included on this plot for clarity.

## 5 CONCLUSIONS

We have presented an investigation of the large-scale magnetic field of 19 additional solar-type stars for the BCool survey (Marsden et al. 2014). We expanded our sample of planet-hosting stars by adding the previously observed planet-host in the BCool survey. The results we obtain for these stars are congruent with the wider BCool survey. The selection by planet-search surveys of low-activity mature stars biases the sample of stars with discovered planets towards those with higher ages and lower intrinsic activity. Consequently, we obtain a lower rate of magnetic detections, and of lower measures of  $|B_l|$ , the longitudinal magnetic field, than the wider survey of 170 solar-type stars.

While we cannot rule out that the presence of the planets around these host stars has an effect on the host star’s magnetic field, we show that such an effect is too subtle to detect in our sample. A larger sample of planet-hosting solar-type stars may reveal a trend. If a trend exists, there may be a lower limit to the planetary mass and upper limit to the semimajor axis of the planetary orbit for which any SPI becomes apparent using these methods. Further target selection should perhaps focus on massive hot-Jupiter systems to further investigate these limits.

The four planetary systems for which we have made magnetic detections may be candidates for long-term magnetic topology monitoring (see Appendix A). Observation of the magnetic field of the host star may allow for modelling of the space weather environment of its planetary system (Vidotto et al. 2015; Alvarado-Gómez et al. 2016; Nicholson et al. 2016). Also, with these known magnetic fields, it may be possible to determine whether other methods, such as radio observations, may be able to detect magnetic interactions between star and planet, or to at least place limits on the expected signals one may expect from such behaviour (Fares et al. 2010; Vidotto et al. 2012, 2015; See et al. 2015).

## ACKNOWLEDGEMENTS

This work was based on observations obtained with NARVAL at the T el escope Bernard Lyot (TBL). TBL/NARVAL are operated by INSU/CNRS.

SVJ acknowledges research funding by the Deutsche Forschungsgemeinschaft (DFG) under grant SFB 963/1, project A16.

The Strategic Research Funding for the Starwinds project provided by the University of Southern Queensland provides resources to the Astrophysics group within the Computational Engineering and Science Research Centre at USQ (MWM, SCM, BDC). MWM is supported by an Australian Postgraduate Award Scholarship.

This research has made use of NASA's Astrophysics Data System. This research has made use of the SIMBAD data base, operated at CDS, Strasbourg, France. This research has made use of the VizieR catalogue access tool, CDS, Strasbourg, France. This work has made use of the VALD data base, operated at Uppsala University, the Institute of Astronomy RAS in Moscow, and the University of Vienna.

The authors would like to thank Victor See and Colin Folsom for their helpful comments and suggestions on the original manuscript. Further thanks to the BCOOL Collaboration.

## REFERENCES

- Alvarado-Gómez J. D., Hussain G. A. J., Cohen O., Drake J. J., Garraffo C., Grunhut J., Gombosi T. I., 2016, *A&A*, 594, A95
- Aurière M., 2003, in Arnaud J., Meunier N., eds, *EAS Publ. Ser. Vol. 9, Magnetism and Activity of the Sun and Stars*. EDP Sciences, Les Ulis, p. 105
- Bagnulo S., Landolfi M., Landstreet J. D., Landi Degl'Innocenti E., Fossati L., Sterzik M., 2009, *PASP*, 121, 993
- Beatty T. G. et al., 2012, *ApJ*, 756, L39
- Benedict G. F. et al., 2006, *ApJ*, 132, 2206
- Butler R. P. et al., 2006, *ApJ*, 646, 505
- Casagrande L., Schönrich R., Asplund M., Cassisi S., Ramírez I., Meléndez J., Bensby T., Feltzing S., 2011, *A&A*, 530, A138
- Chauvin G., Beust H., Lagrange A.-M., Eggenberger A., 2011, *A&A*, 528, A8
- Cuntz M., Saar S. H., Musielak Z. E., 2000, *ApJ*, 533, L151
- da Silva R. et al., 2007, *A&A*, 473, 323
- Díaz R. F. et al., 2016, *A&A*, 585, A134
- Donati J.-F., Semel M., Rees D. E., 1992, *A&A*, 265, 669
- Donati J.-F., Semel M., Carter B. D., Rees D. E., Cameron A. C., 1997, *MNRAS*, 291, 658
- Fares R. et al., 2010, *MNRAS*, 406, 409
- Fares R., Moutou C., Donati J.-F., Catala C., Shkolnik E. L., Jardine M. M., Cameron A. C., Deleuil M., 2013, *MNRAS*, 435, 1451
- Feng F., Tuomi M., Jones H. R. A., Butler R. P., Vogt S., 2016, *MNRAS*, 461, 2440
- Figueira P. et al., 2016, *A&A*, 592, A143
- France K. et al., 2016, *ApJ*, 820, 89
- Gizis J. E., Reid I. N., Hawley S. L., 2002, *ApJ*, 123, 3356
- Gregory P. C., Fischer D. A., 2010, *MNRAS*, 403, 731
- Harakawa H. et al., 2010, *ApJ*, 715, 550
- Hébrard É. M., Donati J.-F., Delfosse X., Morin J., Moutou C., Boisse I., 2016, *MNRAS*, 461, 1465
- Herrero E., Ribas I., Jordi C., Morales J. C., Perger M., Rosich A., 2016, *A&A*, 131, 1
- Horner J., Jones B., 2010, *Int. J. Astrobiology*, 9, 273
- Isaacson H., Fischer D., 2010, *ApJ*, 725, 875
- Jeffers S. V., Barnes J. R., Jones H. R. A., Reiners A., Pinfield D. J., Marsden S. C., 2014, *MNRAS*, 438, 2717
- Jofré E., Petrucci R., Saffe C., Saker L., Artur de la Villarmosa E., Chavero C., Gómez M., Maas P. J. D., 2015, *A&A*, 574, A50
- Kochukhov O., Makaganiuk V., Piskunov N. E., 2010, *A&A*, 524, A5
- Krejčová T., Budaj J., 2012, *A&A*, 540, A82
- Kupka F. G., Ryabchikova T. A., Piskunov N. E., Stempels H. C., Weiss W. W., 2000, *Balt. Astron.*, 9, 590
- Lanza A. F., 2009, *A&A*, 505, 339
- Lanza A. F., 2012, *A&A*, 544, 23
- Lanza A. F. et al., 2011, *A&A*, 525, A14
- Luhman K. L. et al., 2007, *ApJ*, 654, 570
- McDonald I., Zijlstra A. A., Boyer M. L., 2012, *MNRAS*, 427, 343
- Marsden S. C. et al., 2014, *MNRAS*, 444, 3517
- Martíoli E., McArthur B. E., Benedict G. F., Bean J. L., Harrison T. E., Armstrong A., 2010, *ApJ*, 708, 625
- Mathys G., 1989, *Fundam. Cosm. Phys.*, 13, 143
- Miller B. P., Gallo E., Wright J. T., Pearson E. G., 2015, *ApJ*, 799, 163
- Morin J. et al., 2008, *MNRAS*, 390, 567
- Moutou C. et al., 2006, *A&A*, 458, 327
- Moutou C. et al., 2007, *A&A*, 473, 651
- Naef D. et al., 2010, *A&A*, 523, A15
- Nicholson B. A. et al., 2016, *MNRAS*, 459, 1907
- Nidever D. L., Marcy G. W., Butler R. P., Fischer D. A., Vogt S. S., 2002, *ApJS*, 141, 503
- Petit P., Donati J.-F., the ESPaDOnS Project Team, 2003, in Arnaud J., Meunier N., eds, *EAS Publ. Ser. Vol. 9, Magnetism and Activity of the Sun and Stars*. EDP Sciences, Les Ulis, p. 97
- Petit P., Aurière M., Konstantinova-Antova R., Morgenthaler A., Perrin G., Roudier T., Donati J.-F., 2013, in Rozelot J.-P., Neiner C., eds, *Lecture Notes in Physics Vol. 857, The Environments of the Sun and the Stars*. Springer-Verlag, Berlin, p. 231
- Petit P. et al., 2015, *A&A*, 584, A84
- Pillitteri I., Wolk S. J., Cohen O., Kashyap V., Knutson H., Lisse C. M., Henry G. W., 2010, *ApJ*, 722, 1216
- Quillen A. C., Thorndike S., 2002, *ApJ*, 578, L149
- Robertson P. et al., 2012, *ApJ*, 749, 39
- Rubenstein E. P., Schaefer B. E., 2000, *ApJ*, 529, 1031
- Saar S. H., Donahue R. A., 1997, *ApJ*, 485, 319
- Saar S. H., Butler R. P., Marcy G. W., 1998, *ApJ*, 498, L153
- Schneider J., Dedieu C., Le Sidaner P., Savalle R., Zolotukhin I., 2011, *A&A*, 532, 79
- See V., Jardine M., Fares R., Donati J.-F., Moutou C., 2015, *MNRAS*, 450, 4323
- Shkolnik E. L., 2013, *ApJ*, 766, 9
- Shkolnik E., Walker G. A. H., Bohlender D. A., Gu P. G., Kürster M., 2005, *ApJ*, 622, 1075
- Shkolnik E., Bohlender D. A., Walker G. A. H., Collier Cameron A., 2008, *ApJ*, 676, 628
- Shorlin S. L. S., Wade G. A., Donati J.-F., Landstreet J. D., Petit P., Sigut T. A. A., Strasser S., 2002, *A&A*, 392, 637
- Strugarek A., Brun A. S., Matt S. P., Réville V., 2015, *ApJ*, 815, 111
- Takeda G., Ford E. B., Sills A., Rasio F. A., Fischer D. A., Valenti J. A., 2007, *ApJS*, 168, 297
- Valenti J. A., Fischer D. A., 2005, *ApJS*, 159, 141
- Vidotto A. A., Fares R., Jardine M., Donati J.-F., Opher M., Moutou C., Catala C., Gombosi T. I., 2012, *MNRAS*, 423, 3285
- Vidotto A. A. et al., 2014, *MNRAS*, 441, 2361
- Vidotto A. A., Fares R., Jardine M., Moutou C., Donati J. F., 2015, *MNRAS*, 449, 4117
- Wang S. X. et al., 2012, *ApJ*, 761, 46
- Wenger M. et al., 2000, *A&AS*, 143, 9
- Wright J. T., Marcy G. W., Butler R. P., Vogt S. S., 2004, *ApJS*, 152, 261
- Wright J. T. et al., 2007, *ApJ*, 657, 533

## APPENDIX A: MAGNETIC DETECTIONS

### A1 HIP 27253 (HD 38529)

The star HIP 27253 (G8III/IV;  $T_{\text{eff}} = 5697 \pm 44$  K) is known to host two planets. HD 38529b has a minimum mass  $\sim 0.85M_J$ , and orbits at a distance of  $\sim 0.13$  au, while the much more massive HD 38529c ( $\sim 13M_J$ ) orbits at approximately 3.75 au. HIP 27253 has the lowest S-index of the four stars for which we obtained detections ( $0.1750 \pm 0.0005$ ). It is relatively bright ( $V \sim 6$ ) compared with the

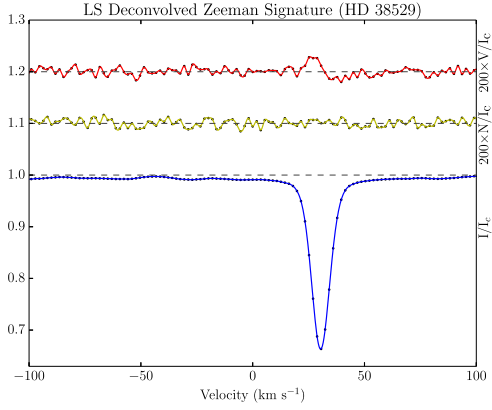


**Figure A1.** Plot of the LSD profiles of HIP 27253 (HD 38529). The upper line (in red) is the Stokes  $V$  profile, expanded 200 times and shifted up by 0.2. The centre line (yellow) represents the LSD null profile also expanded by 200 and shifted up 0.1. The lower line (in blue) shows the Stokes  $I$  (intensity) LSD profile.

remainder of the sample, with over 12 000 lines used in the LSD process, resulting in a relatively high  $\text{SNR}_{\text{LSD}}$  of  $\sim 28\,000$ .

One of the two subgiants for which we obtained a magnetic detection, Takeda et al. (2007) place its age at over 3 Gyr, whilst we derive a chromospheric age of  $\sim 4.8$  Gyr. An older subgiant star with a close Jupiter-mass planet, HIP 27253 would be an interesting target for further investigation. The LSD profile including Stokes  $V$ , Stokes  $I$  and null ( $N$ ) profiles is shown in Fig. A1.

#### A2 HIP 27384 (HD 38801)

HIP 27384 (G8IV;  $T_{\text{eff}} = 5222 \pm 44$  K) is the second of our two subgiants which have a magnetic detection (LSD profiles shown in Fig. A2). A single large planet HD 38801b with a mass of  $\sim 10.7M_J$  orbits the star at 1.7 au. A mature star with age measurements  $>4$  Gyr, HIP 27384 has one of the largest  $|B_\ell|$  measurements in our sample. Its low  $v \sin i \approx 0.5 \text{ m s}^{-1}$  makes tomographic mapping of the surface magnetic field challenging.

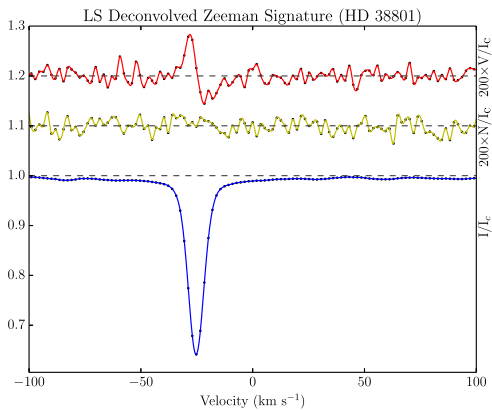


**Figure A2.** Plot of LSD profiles for HIP 27384 (HD 38801). The plot is described in Fig. A1.

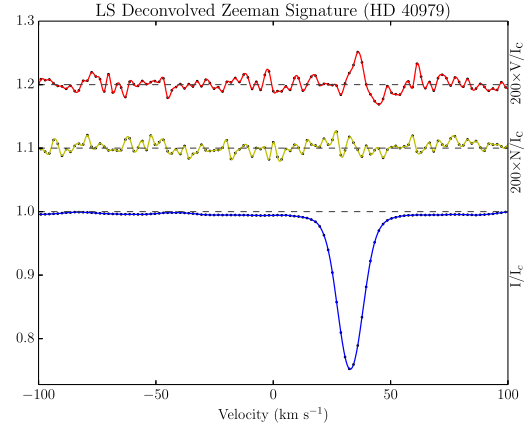


**Figure A3.** Plot of LSD profiles for HIP 28767 (HD 40979). The plot is described in Fig. A1.

#### A3 HIP 28767 (HD 40979)

HIP 28767 (F8;  $T_{\text{eff}} = 6089 \pm 44$  K) has by far the highest S-index of the sample ( $0.2543 \pm 0.0003$ ), and consequently it is not surprising that a magnetic field was detected. A significant field in the null profile ( $|N_\ell|$ ) relative to the size of the measured  $|B_\ell|$  means that follow-up observations may be necessary to confirm the actual level of the longitudinal field with more confidence. The hottest star in our sample to have a detection, HIP 28767 has an  $\sim 3.8M_J$  planet (HD 40979b) orbiting at a distance of  $\sim 0.85$  au. The Stokes  $V$ , Stokes  $I$  and  $N$  profiles for HIP 28767 are shown in Fig. A3.

#### A4 HIP 64457 (HD 114783)

Two observations of HIP 64457 (K1V;  $T_{\text{eff}} = 5135 \pm 44$  K) were taken during the observing period, and the set of LSD profiles from the second observation (taken at  $\approx$  HJD 2457032.7) is shown in Fig. A4. HD 114783b, with a mass approximately that of Jupiter, orbits the star at a distance of  $\sim 1.1$  au. As one of the two stars (the other being HIP 28767; Section A3) with an S-index above 0.2, it was likely to provide a magnetic detection. With a similar

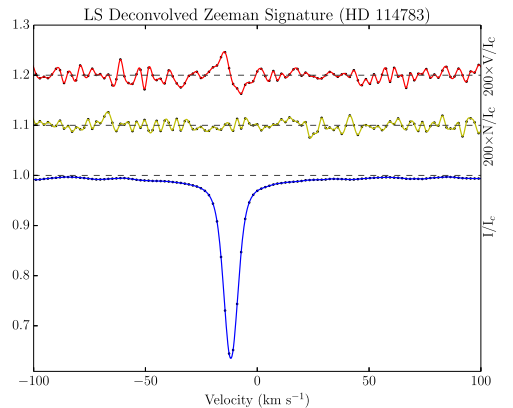


**Figure A4.** Plot of LSD profiles for HIP 64457 (HD 114783). The plot is described in Fig. A1.

temperature and rotation rate, a comparison of the magnetic activity and/or cycles of HIP 64457 and HIP 27384 (Section A2) may provide an insight into any apparent differences or similarities of dynamo between dwarfs and subgiants.

## APPENDIX B: PLANET-HOSTS FROM BCOOL SURVEY

**Table B1.** Planetary parameters of the sample of planet-hosting solar-type stars from the BCOol survey (Marsden et al. 2014), as an extension of Table 1. The stellar component's *Hipparcos* number, SPOCS catalogue number and HD number (where applicable) are shown in the first three columns. Column 4 refers to the name by which the planetary components (column 5) are known. The period, mass ( $M \sin i$ ) and semimajor axis is shown for each planet. These values are from the references listed in the last column.

Star HIP no.	SPOCS no.	HD no.	Name	Component	Planet(s)			Refs.
					Period (d)	$M \sin i$ ( $M_J$ )	Semimajor axis (au)	
1499	13	1461	HD 1461	b	5.771 52 ± 0.000 45	0.0203 ± 0.0019	0.0634 ± 0.0022	1
			HD 1461	c	13.5052 ± 0.0029	0.0176 ± 0.0023	0.1117 ± 0.0039	1
3093	26	3651	54 Psc	b	62.206 ± 0.021	0.227 ± 0.023	0.296 ± 0.017	2
7513	85	9826	$\nu$ And	b	4.617 113 ± 0.000 082	0.687 ± 0.058	0.0595 ± 0.0034	2
			$\nu$ And	c	241.23 ± 0.30	1.98 ± 0.17	0.832 ± 0.048	2
			$\nu$ And	d	1290.1 ± 8.4	3.95 ± 0.33	2.54 ± 0.15	2
8159	97	10697	HD 10697	b	1076.4 ± 2.4	6.38 ± 0.53	2.16 ± 0.12	2
12048	128	16141	HD 16141	b	75.523 ± 0.055	0.260 ± 0.028	0.363 ± 0.021	2
16537 <sup>a</sup>	171	22049	$\epsilon$ Eri	b	2502 ± 10	0.78 ± 0.08	3.39 ± 0.36	3
53721	472	95128	47 Uma	b	1078 <sup>+2</sup> <sub>-3</sub>	2.53 <sup>+0.07</sup> <sub>-0.06</sub>	2.100 <sup>+0.02</sup> <sub>-0.02</sub>	4
			47 Uma	c	2391 <sup>+100</sup> <sub>-87</sub>	0.540 <sup>+0.066</sup> <sub>-0.073</sub>	3.6 <sup>+0.1</sup> <sub>-0.1</sub>	4
			47 Uma	d	14 002 <sup>+4018</sup> <sub>-5095</sub>	1.64 <sup>+0.29</sup> <sub>-0.48</sub>	11.6 <sup>+2.1</sup> <sub>-2.9</sub>	4
67275	577	120136	$\tau$ Boo	b	3.312 463 ± 0.000 014	4.13 ± 0.34	0.0481 ± 0.0028	2
96901	855	186427	16 Cyg B	b	798.5 ± 1.0	1.68 ± 0.15	1.681 ± 0.097	2
100970	894	195019	HD 195019	b	18.201 63 ± 0.000 40	3.70 ± 0.30	0.1388 ± 0.0080	5
107350 <sup>b</sup>	942	206860	HN Peg	b		16.0 ± 9.4	795.0 ± 15.0	6
109378	960	210277	HD 210277	b	442.19 ± 0.50	1.29 ± 0.11	1.138 ± 0.066	2
113357	990	217014	51 Peg	b	4.230 785 ± 0.000 036	0.472 ± 0.039	0.0527 ± 0.0030	2
113421	992	217107	HD 217107	b	7.126 90 ± 0.000 22	1.41 ± 0.12	0.0748 ± 0.0043	2
			HD 217107	c	3200 ± 1000	2.21 ± 0.66	4.3 ± 1.2	2

References: 1: Díaz et al. (2016), 2: Butler et al. (2006), 3: Benedict et al. (2006), 4: Gregory & Fischer (2010), 5: Wright et al. (2007), 6: Luhman et al. (2007).

<sup>a</sup>HIP16537 ( $\epsilon$  Eri) is suspected to host a second planet (Quillen & Thorndike 2002).

<sup>b</sup>The planet orbiting HIP107530 (HN Peg) was discovered by direct imaging, and as a result, its orbital parameters unclear; semimajor axis is therefore taken as the projected separation (Luhman et al. 2007).

**Table B2.** Stellar parameters of the sample of planet-hosting solar-type stars from the BCOol survey (Marsden et al. 2014, table 1), as an extension of Table 2. The spectral type is from SIMBAD (<http://simbad.u-strasbg.fr/simbad/>; Wenger et al. 2000). Column 11 is the radius of the convective zone of the star. Values are found in the references shown in the final column of the table; locations where values were unavailable in the literature, are denoted by 'X'.

HIP no.	SPOCS no.	Spec. type	$T_{\text{eff}}$ (K)	$\log(g)$ ( $\text{cm s}^{-2}$ )	[M/H]	$\log(\text{Lum})$ ( $L_{\odot}$ )	Age (Gyr)	Mass ( $M_{\odot}$ )	Radius ( $R_{\odot}$ )	Radius <sub>CZ</sub> ( $R_{\odot}$ )	$v \sin i$ ( $\text{km s}^{-1}$ )	Refs.
1499	13	G0V	5765 <sup>+44</sup> <sub>-44</sub>	4.37 <sup>+0.03</sup> <sub>-0.03</sub>	+0.16 <sup>+0.03</sup> <sub>-0.03</sub>	+0.078 <sup>+0.041</sup> <sub>-0.041</sub>	7.12 <sup>+1.40</sup> <sub>-1.56</sub>	1.026 <sup>+0.040</sup> <sub>-0.030</sub>	1.11 <sup>+0.04</sup> <sub>-0.04</sub>	0.323 <sup>+0.019</sup> <sub>-0.020</sub>	1.6 <sup>+0.5</sup> <sub>-0.5</sub>	1,2
3093	26	K0V	5221 <sup>+25</sup> <sub>-25</sub>	4.51 <sup>+0.02</sup> <sub>-0.01</sub>	+0.16 <sup>+0.02</sup> <sub>-0.02</sub>	-0.286 <sup>-0.018</sup> <sub>-0.018</sub>	X	0.882 <sup>+0.026</sup> <sub>-0.021</sub>	0.88 <sup>+0.03</sup> <sub>-0.02</sub>	0.296 <sup>+0.006</sup> <sub>-0.009</sub>	1.1 <sup>+0.3</sup> <sub>-0.3</sub>	1,2
7513	85	F9V	6213 <sup>+22</sup> <sub>-22</sub>	4.16 <sup>+0.02</sup> <sub>-0.04</sub>	+0.12 <sup>+0.01</sup> <sub>-0.01</sub>	+0.522 <sup>+0.021</sup> <sub>-0.021</sub>	3.12 <sup>+0.20</sup> <sub>-0.24</sub>	1.310 <sup>+0.021</sup> <sub>-0.014</sub>	1.64 <sup>+0.04</sup> <sub>-0.05</sub>	0.315 <sup>+0.028</sup> <sub>-0.073</sub>	9.6 <sup>+0.3</sup> <sub>-0.3</sub>	1,2
8159	97	G5IV	5680 <sup>+44</sup> <sub>-44</sub>	4.03 <sup>+0.03</sup> <sub>-0.03</sub>	+0.10 <sup>+0.03</sup> <sub>-0.03</sub>	+0.448 <sup>+0.054</sup> <sub>-0.054</sub>	7.84 <sup>+0.40</sup> <sub>-0.48</sub>	1.112 <sup>+0.026</sup> <sub>-0.020</sub>	1.73 <sup>+0.06</sup> <sub>-0.07</sub>	0.568 <sup>+0.038</sup> <sub>-0.032</sub>	2.5 <sup>+0.5</sup> <sub>-0.5</sub>	1,2
12048	128	G5IV	5794 <sup>+44</sup> <sub>-44</sub>	4.19 <sup>+0.04</sup> <sub>-0.04</sub>	+0.09 <sup>+0.03</sup> <sub>-0.03</sub>	+0.30 <sup>+0.10</sup> <sub>-0.10</sub>	8.68 <sup>+0.76</sup> <sub>-0.76</sub>	1.052 <sup>+0.026</sup> <sub>-0.022</sub>	1.39 <sup>+0.07</sup> <sub>-0.07</sub>	0.416 <sup>+0.030</sup> <sub>-0.028</sub>	1.9 <sup>+0.5</sup> <sub>-0.5</sub>	1,2
16537	171	K2Vk:	5146 <sup>+31</sup> <sub>-31</sub>	4.61 <sup>+X</sup> <sub>-0.02</sub>	+0.00 <sup>+0.02</sup> <sub>-0.02</sub>	-0.486 <sup>-0.011</sup> <sub>-0.011</sub>	0.00 <sup>+0.60</sup> <sub>-0.00</sub>	0.856 <sup>+0.006</sup> <sub>-0.008</sub>	0.77 <sup>+0.02</sup> <sub>-0.01</sub>	0.235 <sup>+0.005</sup> <sub>-0.006</sub>	2.4 <sup>+0.4</sup> <sub>-0.4</sub>	1,2
53721	472	G1V	5882 <sup>+16</sup> <sub>-16</sub>	4.31 <sup>+0.03</sup> <sub>-0.04</sub>	+0.02 <sup>+0.01</sup> <sub>-0.01</sub>	+0.206 <sup>+0.021</sup> <sub>-0.021</sub>	6.48 <sup>+1.44</sup> <sub>-1.04</sub>	1.063 <sup>+0.022</sup> <sub>-0.029</sub>	1.24 <sup>+0.04</sup> <sub>-0.04</sub>	0.325 <sup>+0.028</sup> <sub>-0.026</sub>	2.8 <sup>+0.2</sup> <sub>-0.2</sub>	1,2
67275	577	F6IV	6387 <sup>+25</sup> <sub>-25</sub>	4.27 <sup>+0.04</sup> <sub>-0.03</sub>	+0.25 <sup>+0.02</sup> <sub>-0.02</sub>	+0.481 <sup>+0.024</sup> <sub>-0.024</sub>	1.64 <sup>+0.44</sup> <sub>-0.52</sub>	1.341 <sup>+0.054</sup> <sub>-0.039</sub>	1.46 <sup>+0.05</sup> <sub>-0.05</sub>	0.230 <sup>+0.010</sup> <sub>-0.005</sub>	15.0 <sup>+0.3</sup> <sub>-0.3</sub>	1,2
96901	855	G3V	5674 <sup>+17</sup> <sub>-17</sub>	4.30 <sup>+0.04</sup> <sub>-0.02</sub>	+0.02 <sup>+0.01</sup> <sub>-0.01</sub>	+0.095 <sup>+0.024</sup> <sub>-0.024</sub>	11.80 <sup>+2.20</sup> <sub>-2.00</sub>	0.956 <sup>+0.026</sup> <sub>-0.025</sub>	1.17 <sup>+0.04</sup> <sub>-0.03</sub>	0.371 <sup>+0.023</sup> <sub>-0.024</sub>	2.2 <sup>+0.2</sup> <sub>-0.2</sub>	1,2
100970	894	G3IV-V	5788 <sup>+44</sup> <sub>-44</sub>	4.18 <sup>+0.03</sup> <sub>-0.04</sub>	+0.00 <sup>+0.03</sup> <sub>-0.03</sub>	+0.286 <sup>+0.069</sup> <sub>-0.069</sub>	9.32 <sup>+0.76</sup> <sub>-0.72</sub>	1.025 <sup>+0.020</sup> <sub>-0.018</sub>	1.38 <sup>+0.06</sup> <sub>-0.05</sub>	0.413 <sup>+0.026</sup> <sub>-0.028</sub>	2.5 <sup>+0.5</sup> <sub>-0.5</sub>	1,2
107350	942	G0V	5974 <sup>+25</sup> <sub>-25</sub>	4.48 <sup>+0.01</sup> <sub>-0.03</sub>	-0.01 <sup>+0.02</sup> <sub>-0.02</sub>	+0.062 <sup>+0.033</sup> <sub>-0.033</sub>	0.00 <sup>+0.88</sup> <sub>-0.00</sub>	1.103 <sup>+0.012</sup> <sub>-0.016</sub>	1.04 <sup>+0.03</sup> <sub>-0.03</sub>	0.239 <sup>+0.010</sup> <sub>-0.007</sub>	10.6 <sup>+0.3</sup> <sub>-0.3</sub>	1,2
109378	960	G0	5555 <sup>+44</sup> <sub>-44</sub>	4.39 <sup>+0.03</sup> <sub>-0.03</sub>	+0.20 <sup>+0.03</sup> <sub>-0.03</sub>	-0.020 <sup>+0.035</sup> <sub>-0.035</sub>	10.64 <sup>+2.04</sup> <sub>-2.20</sub>	0.986 <sup>+0.038</sup> <sub>-0.052</sub>	1.06 <sup>+0.03</sup> <sub>-0.04</sub>	0.343 <sup>+0.019</sup> <sub>-0.022</sub>	1.8 <sup>+0.5</sup> <sub>-0.5</sub>	1,2
113357	990	G2.5IVa	5787 <sup>+25</sup> <sub>-25</sub>	4.36 <sup>+0.04</sup> <sub>-0.03</sub>	+0.15 <sup>+0.02</sup> <sub>-0.02</sub>	+0.117 <sup>+0.025</sup> <sub>-0.025</sub>	6.76 <sup>+1.64</sup> <sub>-1.48</sub>	1.054 <sup>+0.039</sup> <sub>-0.036</sub>	1.15 <sup>+0.04</sup> <sub>-0.04</sub>	0.327 <sup>+0.058</sup> <sub>-0.024</sub>	2.6 <sup>+0.3</sup> <sub>-0.3</sub>	1,2
113421	992	G8IV	5704 <sup>+44</sup> <sub>-44</sub>	4.42 <sup>+0.04</sup> <sub>-0.03</sub>	+0.27 <sup>+0.03</sup> <sub>-0.03</sub>	+0.050 <sup>+0.031</sup> <sub>-0.031</sub>	5.84 <sup>+1.92</sup> <sub>-2.44</sub>	1.108 <sup>+0.034</sup> <sub>-0.052</sub>	1.08 <sup>+0.04</sup> <sub>-0.03</sub>	0.316 <sup>+0.022</sup> <sub>-0.018</sub>	0.0 <sup>+0.5</sup> <sub>-0.0</sub>	1,2

References: 1: Valenti & Fischer (2005), 2: Takeda et al. (2007).

**Table B3.** Results from the analysis of the Stokes  $V$  LSD profiles of the planet-hosting stars in the BCool sample (Marsden et al. 2014, table 3). Column 3 provides the date of the observation corresponding to the observation number shown in column 2. Column 4 shows the radial velocity for the star determined by Marsden et al. (2014); for comparison, column 5 shows the radial velocity measured by Nidever et al. (2002) (<sup>NS</sup> indicates a non-radial velocity standard star;  $\sigma_{\text{res}} \geq 100 \text{ m s}^{-1}$ ). Columns 6 and 7 show the signal-to-noise of the Stokes  $V$  profile and the number of lines used in the LSD process, respectively. Column 8 indicates is the magnetic field was unambiguously detected (D), marginal (M) or not (N). Stars indicated by superscript ‘a’ have multiple observations and where appropriate the number of definite (D) and marginal (M) detections are shown as fractions of the total number of observations. HIP113357<sup>b</sup> has multiple observations; all non-detections (N). Column 9 shows the false alarm probability calculated for the detection in column 8. Columns 10 and 11 indicate the velocity range used to calculate  $B_\ell$  (column 12) and  $N_\ell$  (column 13) using equation (5).

HIP no.	Obs. no.	Obs. date	RV (this work) (km s <sup>-1</sup> )	RV (Nidever) (km s <sup>-1</sup> )	SNR <sub>LSD</sub>	Lines used	Detection	FAP	Velocity range (km s <sup>-1</sup> )	$B_\ell$ (G)	$N_\ell$ (G)
1499	1	2010 October 19	-10	-10.166	23 795	11 140	N	$6.059 \times 10^{-01}$	-18 -2	-0.6 ± 0.5	-0.6 ± 0.5
3093 <sup>a</sup>	1	2010 August 10	-32.7	-32.961	44 842	13 129	D (22/28)	$0.000 \times 10^{+00}$	-40 -25	-3.2 ± 0.2	-0.1 ± 0.2
7513	1	2006 November 14	-28.3	-28.674	36 749	9872	N	$7.340 \times 10^{-01}$	-49 -9	+2.5 ± 1.1	-0.3 ± 1.1
8159	1	2011 January 27	-45.9	-46.022	31 246	10 271	N	$9.024 \times 10^{-01}$	-54 -38	-0.4 ± 0.3	+0.1 ± 0.3
12048	1	2010 December 18	-50.7	-50.971	22 279	10 271	N	$4.743 \times 10^{-02}$	-58 -45	+1.0 ± 0.4	+0.4 ± 0.4
16537 <sup>a</sup>	1	2007 February 01	16.5	16.332	39 693	11 754	D (52/58) M (3/58)	$0.000 \times 10^{+00}$	11 23	-10.9 ± 0.2	-0.2 ± 0.2
53721	1	2009 December 31	11.5	11.235	37 281	9006	N	$4.988 \times 10^{-01}$	5 18	+0.6 ± 0.2	+0.2 ± 0.2
67275 <sup>a</sup>	1	2013 May 13	-16	-16.542 ± 0.340	75 344	8271	D (3/8) M (2/8)	$6.090 \times 10^{-08}$	-38 5	+3.2 ± 0.5	-0.1 ± 0.5
96901	1	2011 July 17	-27.7	-27.871	35 324	9669	N	$5.381 \times 10^{-01}$	-47 -9	-1.7 ± 0.9	-0.4 ± 0.9
100970	1	2011 June 21	-91.1	-91.582 ± 0.188 <sup>NS</sup>	36 392	10 466	N	$4.175 \times 10^{-01}$	-104 -77	+1.7 ± 0.6	-0.6 ± 0.6
107350 <sup>a</sup>	1	2010 June 21	-16.6	-16.833	21 322	8764	D (68/91) M (7/91)	$0.000 \times 10^{+00}$	-29 -5	+14.8 ± 0.9	+0.0 ± 0.9
109378	1	2010 November 26	-20.7	-20.873	37 867	12 151	N	$4.703 \times 10^{-01}$	-32 -9	-0.9 ± 0.5	+0.2 ± 0.5
113357 <sup>b</sup>	1	2010 December 15	-33.1	-33.225	20 777	11 111	N	$7.351 \times 10^{-01}$	-40 -27	+0.6 ± 0.4	+0.1 ± 0.4
113421	1	2010 October 20	-13.3	-13.399	21 447	11 135	N	$5.690 \times 10^{-01}$	-31 4	-1.9 ± 1.2	-0.5 ± 1.2

**Table B4.** Chromospheric activity of planet-hosting stars in the BCool sample (Marsden et al. 2014, tables 5 and 1).  $B - V$  and  $V$  values are from *Hipparcos*. Where Wright et al. (2004) have calculated an S-index, it is shown in column 4. Chromospheric ages, periods and  $\log(P_{\text{rot}}/\tau)$  have been determined using the equations presented in Wright et al. (2004). Sample standard deviations are used as an indication of various errors.

HIP no.	$B - V$ ( <i>Hipparcos</i> )	$V$	S-index Wright.	S-index (this work)	$\log(R'_{\text{HK}})$	Chromospheric age (Gyr)	Chromospheric period (d)	$\text{Ca}_{\text{IRT}}$ -index	H $\alpha$ -index	$\log(P_{\text{rot}}/\tau)$
1499	0.674	6.47	0.156	0.1567 ± 0.0014	-5.03 <sup>+0.01</sup> <sub>-0.01</sub>	6.214 <sup>+0.221</sup> <sub>-0.215</sub>	29.0 <sup>+0.3</sup> <sub>-0.3</sub>	0.7149 ± 0.0016	0.2908 ± 0.0001	+0.336 <sup>+0.004</sup> <sub>-0.004</sub>
3093	0.850	5.88	0.169	0.1724 ± 0.0007	-5.00 <sup>+0.00</sup> <sub>-0.01</sub>	5.589 <sup>+0.203</sup> <sub>-0.000</sub>	44.0 <sup>+0.4</sup> <sub>-0.0</sub>	0.7065 ± 0.0007	0.3122 ± 0.0002	+0.324 <sup>+0.004</sup> <sub>-0.000</sub>
7513	0.536	4.10	0.146	0.1565 ± 0.0009	-4.98 <sup>+0.01</sup> <sub>-0.00</sub>	5.201 <sup>+0.000</sup> <sub>-0.185</sub>	11.9 <sup>+0.0</sup> <sub>-0.1</sub>	0.7498 ± 0.0014	0.2768 ± 0.0001	+0.316 <sup>+0.000</sup> <sub>-0.004</sub>
8159	0.720	6.27	0.149	0.1445 ± 0.0013	-5.11 <sup>+0.01</sup> <sub>-0.01</sub>	8.151 <sup>+0.269</sup> <sub>-0.263</sub>	36.9 <sup>+0.3</sup> <sub>-0.3</sub>	0.6900 ± 0.0012	0.2889 ± 0.0002	+0.366 <sup>+0.004</sup> <sub>-0.004</sub>
12048	0.670	6.83	0.145	0.1461 ± 0.0019	-5.10 <sup>+0.01</sup> <sub>-0.01</sub>	7.888 <sup>+0.265</sup> <sub>-0.257</sub>	30.3 <sup>+0.3</sup> <sub>-0.3</sub>	0.7067 ± 0.0013	0.2860 ± 0.0003	+0.362 <sup>+0.004</sup> <sub>-0.004</sub>
16537	0.881	3.72	0.447	0.5357 ± 0.0019	-4.42 <sup>+0.00</sup> <sub>-0.00</sub>	0.489 <sup>+0.000</sup> <sub>-0.000</sub>	11.8 <sup>+0.0</sup> <sub>-0.0</sub>	0.8566 ± 0.0017	0.3446 ± 0.0004	-0.262 <sup>+0.000</sup> <sub>-0.000</sub>
53721	0.624	5.03	0.154	0.1501 ± 0.0014	-5.05 <sup>+0.01</sup> <sub>-0.01</sub>	6.662 <sup>+0.233</sup> <sub>-0.227</sub>	23.1 <sup>+0.2</sup> <sub>-0.2</sub>	0.7519 ± 0.0014	0.2838 ± 0.0001	+0.343 <sup>+0.004</sup> <sub>-0.004</sub>
67275	0.508	4.50	0.202	0.1760 ± 0.0001	-4.86 <sup>+0.00</sup> <sub>-0.00</sub>	3.347 <sup>+0.000</sup> <sub>-0.000</sub>	8.2 <sup>+0.0</sup> <sub>-0.0</sub>	0.7431 ± 0.0003	0.2780 ± 0.0001	+0.259 <sup>+0.000</sup> <sub>-0.000</sub>
96901	0.661	6.25	0.148	0.1537 ± 0.0005	-5.04 <sup>+0.00</sup> <sub>-0.00</sub>	6.435 <sup>+0.000</sup> <sub>-0.000</sub>	27.6 <sup>+0.0</sup> <sub>-0.0</sub>	0.7476 ± 0.0009	0.2897 ± 0.0001	+0.340 <sup>+0.000</sup> <sub>-0.000</sub>
100970	0.662	6.87	0.147	0.1521 ± 0.0041	-5.05 <sup>+0.03</sup> <sub>-0.03</sub>	6.662 <sup>+0.717</sup> <sub>-0.662</sub>	28.0 <sup>+0.7</sup> <sub>-0.7</sub>	0.7154 ± 0.0007	0.2870 ± 0.0003	+0.343 <sup>+0.011</sup> <sub>-0.012</sub>
107350	0.587	5.96	-	0.3330 ± 0.0014	-4.42 <sup>+0.00</sup> <sub>-0.00</sub>	0.489 <sup>+0.000</sup> <sub>-0.000</sub>	4.6 <sup>+0.0</sup> <sub>-0.0</sub>	0.9147 ± 0.0005	0.3153 ± 0.0003	-0.262 <sup>+0.000</sup> <sub>-0.000</sub>
109378	0.773	6.54	0.155	0.1534 ± 0.0007	-5.07 <sup>+0.01</sup> <sub>-0.00</sub>	7.134 <sup>+0.000</sup> <sub>-0.239</sub>	41.2 <sup>+0.0</sup> <sub>-0.4</sub>	0.7024 ± 0.0012	0.3000 ± 0.0002	+0.351 <sup>+0.000</sup> <sub>-0.004</sub>
113357	0.666	5.45	0.148	0.1528 ± 0.0021	-5.06 <sup>+0.01</sup> <sub>-0.02</sub>	6.895 <sup>+0.484</sup> <sub>-0.233</sub>	28.7 <sup>+0.5</sup> <sub>-0.3</sub>	0.7154 ± 0.0014	0.2900 ± 0.0002	+0.347 <sup>+0.008</sup> <sub>-0.004</sub>
113421	0.744	6.17	0.15	0.1494 ± 0.0029	-5.09 <sup>+0.02</sup> <sub>-0.02</sub>	7.630 <sup>+0.521</sup> <sub>-0.496</sub>	39.0 <sup>+0.7</sup> <sub>-0.7</sub>	0.6861 ± 0.0006	0.2979 ± 0.0003	+0.359 <sup>+0.008</sup> <sub>-0.008</sub>

This paper has been typeset from a  $\text{\TeX}/\text{\LaTeX}$  file prepared by the author.

## 2.2 SUMMARY OF RESULTS

The overarching result from [Mengel et al. \(2017b\)](#) is that the magnetic fields of confirmed planet-hosting solar-type stars do not seem to behave differently than those of the wider family of solar-type stars. In fact, the magnetic fields are not detected as often, due to the inherent biases involved in selecting planet-hosting stars (older, lower rotational periods, etc.), but otherwise seem to conform to the relationships established by [Marsden et al. \(2014\)](#) and others.

A small correlation between the magnitude of the tidal effect of planets on the host star was found. More observations, especially of hot Jupiter systems are required to determine if this relationship is statistically significant.

While these results are seemingly negative, they are important. In the case of SPI, this work provides signposts as to which types of systems should be targeted for more likely signs of magnetic or tidal interaction. Additionally, it shows that the sample of planet-hosting stars needs to be expanded to younger stars and more extreme systems to find relationships that may be due to planets. These are challenging tasks, and there is much work under way looking to find planets in younger systems.

*L'évolution procède comme un bricoleur qui pendant des millions et des millions d'années, remanierait lentement son oeuvre, la retouchant sans cesse, coupant ici, allongeant là, saisissant toutes les occasions d'ajuster, de transformer, de créer.*

François Jacob

# 3

## The Evolving Magnetic Field of the Planet-Hosting Solar-Type Star $\tau$ Boötis

THE PLANET-HOSTING F7 DWARF  $\tau$  BOÖTIS has been regularly observed with spectropolarimetry since 2007 (Catala et al., 2007), with subsequent observations showing reversals of the large-scale radial magnetic field in a  $\sim 2$  yr cycle (Donati et al., 2008; Fares et al., 2009, 2013). In Mengel et al. (2016), six new epochs of spectropolarimetric observations from 2011 through 2015 were analysed in order to investigate the cycle of the magnetic field of  $\tau$  Boötis.

To observe whether the magnetic activity of  $\tau$  Boötis follows other activity indicators, the chromospheric activity of the star was determined using the Ca II H&K activity proxy. The star was, in the final epoch of observation, at an activity minimum. This permitted a close observation of the evolution of the magnetic field through this

minimum. Given that the Sun reverses its global field polarity after the activity minimum, this is an important point in any magnetic cycle.

$\tau$  Boötis is host to a hot Jupiter, with a mass of approximately  $6M_{Jupiter}$  orbiting at a distance of 0.049 au. The convective envelope of  $\tau$  Boötis is only  $\sim 0.5M_{Jupiter}$  (Fares et al., 2009) and the orbit of the planet is presumed to be synchronised to the stellar rotation. These factors would make  $\tau$  Boötis a prime candidate to investigate for signs of star-planet interaction, which could take the form of magnetic reconnection events or tidal effects from the planet causing changes to the star’s magnetic activity. For example, Fares et al. (2009) speculates that tidal forces from  $\tau$  Boötis b may synchronise the rotation of the convective envelope, enhancing the shear at the tachocline, thus influencing the dynamo process and by extension, the magnetic cycle. While some tentative indications of such interactions have been claimed (e.g. Walker et al., 2008), none have been particularly convincing. Interestingly, other main sequence F stars have not shown magnetic cycles (Jeffers et al., 2011; Schröder et al., 2013), although some have shown reversals, implying that any cycle periods may be long or otherwise not observed. An intriguing possibility is that  $\tau$  Boötis b has either accelerated or stabilised the dynamo process, resulting in a cycle on  $\tau$  Boötis.

### 3.1 MENGEL ET AL. (2016) “THE EVOLVING MAGNETIC TOPOLOGY OF $\tau$ BOÖTIS”

The published paper Mengel et al. (2016), “The evolving magnetic topology of  $\tau$  Boötis” follows.



## The evolving magnetic topology of $\tau$ Boötis

M. W. Mengel,<sup>1</sup>★ R. Fares,<sup>2</sup> S. C. Marsden,<sup>1</sup> B. D. Carter,<sup>1</sup> S. V. Jeffers,<sup>3</sup> P. Petit,<sup>4,5</sup>  
J.-F. Donati,<sup>4,5</sup> C. P. Folsom<sup>6,7</sup> and the BCoOL Collaboration

<sup>1</sup>Computational Engineering and Science Research Centre, University of Southern Queensland, Toowoomba, Qld, Australia

<sup>2</sup>INAF - Osservatorio Astrofisico di Catania, Via Santa Sofia, 78, I-95123 Catania, Italy

<sup>3</sup>Institut für Astrophysik, Georg-August-Universität Göttingen, Friedrich-Hund-Platz 1, D-37077 Göttingen, Germany

<sup>4</sup>Université de Toulouse, UPS-OMP, Institut de Recherche en Astrophysique et Planétologie, F-31400 Toulouse, France

<sup>5</sup>CNRS, Institut de Recherche en Astrophysique et Planétologie, 14 Avenue Edouard Belin, F-31400 Toulouse, France

<sup>6</sup>Université Grenoble Alpes, IPAG, F-38000 Grenoble, France

<sup>7</sup>CNRS, IPAG, F-38000 Grenoble, France

Accepted 2016 April 7. Received 2016 April 5; in original form 2015 November 9

### ABSTRACT

We present six epochs of spectropolarimetric observations of the hot-Jupiter-hosting star  $\tau$  Boötis that extend the exceptional previous multiyear data set of its large-scale magnetic field. Our results confirm that the large-scale magnetic field of  $\tau$  Boötis varies cyclicly, with the observation of two further magnetic reversals; between 2013 December and 2014 May and between 2015 January and March. We also show that the field evolves in a broadly solar-type manner in contrast to other F-type stars. We further present new results which indicate that the chromospheric activity cycle and the magnetic activity cycles are related, which would indicate a very rapid magnetic cycle. As an exemplar of long-term magnetic field evolution,  $\tau$  Boötis and this long-term monitoring campaign presents a unique opportunity for studying stellar magnetic cycles.

**Key words:** magnetic fields – techniques: polarimetric – stars: activity – stars: imaging – stars: individual:  $\tau$  Boo – planetary systems.

### 1 INTRODUCTION

Magnetic fields of planet-hosting stars are of significant interest given the expected role of the magnetic field in both stellar and planetary system evolution.  $\tau$  Boötis (HR 5185, HD 120136, F7V, age  $\sim 1$  Gyr; list of stellar parameters given in Table 1) hosts a hot Jupiter with a mass of  $\sim 6M_{\text{Jupiter}}$  (Brogi et al. 2012; Rodler, Lopez-Morales & Ribas 2012; Borsa et al. 2015) orbiting at 0.049 au in approximately 3.31 d (Butler et al. 1997; Leigh et al. 2003; Borsa et al. 2015) and has been the subject of periodic observation of its magnetic field since 2007. This unique long-term spectropolarimetric observational series of  $\tau$  Boötis has allowed the investigation of the evolution of its magnetic topology over an extended period.

Donati et al. (2008) and Fares et al. (2009, 2013) have observed that  $\tau$  Boötis exhibits a magnetic cycle including polarity reversals occurring roughly on a yearly time-scale. Studies of younger stars which like  $\tau$  Boötis have shallow convective zones (Marsden et al. 2006; Jeffers & Donati 2008; Jeffers et al. 2011), have not shown magnetic cycles; perhaps because the duration of the cycles are longer than the periods of observation or because their cycles are irregular or chaotic. Fares et al. (2009) speculate that the hot Jupiter

with  $M_p \sim 6M_{\text{Jupiter}}$  (compared to the stellar convective envelope with a mass of  $\sim 0.5M_{\text{Jupiter}}$ ) may accelerate the stellar magnetic activity cycle by synchronizing the outer convective envelope of the star (due to tidal interactions) and enhancing the shear at the tachocline.

$\tau$  Boötis has been a target of interest for those searching for star–planet interaction (SPI). Photometric observations from the MOST satellite by Walker et al. (2008) suggested that a persistent active region exists on the star synchronized with the period of the hot Jupiter, but leading the subplanetary longitude by  $\sim 68^\circ$ . The presence of a persistent active region may suggest SPI. Lanza (2012) contends that models rule out that any such ‘hotspots’ are due to magnetic SPI, and therefore if truly related to the planetary period, they must be via some other mechanism. Given that the orbital period of the planet  $\tau$  Boötis b and the star’s rotational period are presumed to be synchronized, observations of the star may not resolve whether or not any rotationally modulated chromospheric features are indicative of SPI or not.

More recently, Borsa et al. (2015) analysed spectra of  $\tau$  Boötis using the HARPS-N spectrograph. Their study suggests that a high-latitude plage was present near one pole of the star. While Borsa et al. (2015) conclude that ‘it is unclear if it is due to SPI or to a corotating active region, or both’, this observation is particularly interesting as it overlaps with one of the epochs presented in this work and is discussed in the conclusion.

\* E-mail: [matthew.mengel@usq.edu.au](mailto:matthew.mengel@usq.edu.au)

**Table 1.** Table of stellar parameters for  $\tau$  Boötis. [References: 1 = Borsa et al. (2015); 2 = Brogi et al. (2012)]

Parameter		Value	Reference
$T_{\text{eff}}$	(K)	$6399 \pm 45$	1
$\log g$	( $\text{cm s}^{-1}$ )	$4.27 \pm 0.06$	1
[Fe/H]		$0.26 \pm 0.03$	1
$v \sin i$	( $\text{km s}^{-1}$ )	$14.27 \pm 0.06$	1
Luminosity	( $L_{\odot}$ )	$3.06 \pm 0.16$	1
Mass	( $M_{\odot}$ )	$1.39 \pm 0.25$	1
Radius	( $R_{\odot}$ )	$1.42 \pm 0.08$	1
Age	(Gyr)	$0.9 \pm 0.5$	1
Inclination	( $^{\circ}$ )	$44.5 \pm 1.5$	2

We present in this paper a new set of epochs to extend the spectropolarimetric study of  $\tau$  Boötis as part of the BCool collaboration<sup>1</sup> on the magnetic fields of cool stars. Radial magnetic maps from previous epochs of observation have been used as boundary conditions for modelling the wind environment around the star (Vidotto et al. 2012). Similarly, work presented here provides these boundary conditions for an ongoing monitoring of the stellar wind of  $\tau$  Boötis (Nicholson et al. 2016).

Investigation of the Ca II H&K stellar activity proxy of the star is shown in Section 3. Modelling of the large-scale magnetic field of the star, including its differential rotation is presented in Section 4. We draw conclusions in Section 5.

## 2 OBSERVATIONS AND DATA PROCESSING

Stokes V spectropolarimetric data of  $\tau$  Boötis were obtained in 2011 May using the HARPS polarimeter (hereafter, referred to as HARPSpol) and in 2013–2015, using the NARVAL high-resolution spectropolarimeter. Each Stokes V spectrum is derived from a sequence of four subexposures taken with the waveplates (HARPSpol)/retarder rhombs (NARVAL) of the polarimeters in different positions (Semel, Donati & Rees 1993; Donati et al. 1997). The phases of the data are derived using the same orbital ephemeris as that used by Catala et al. (2007), Donati et al. (2008) and Fares et al. (2009, 2013):

$$T_0 = \text{HJD } 2453450.984 + 3.31245E, \quad (1)$$

with phase 0.0 denoting the first conjunction (i.e. the planet furthest from the observer).

### 2.1 Observations with HARPSpol

HARPSpol (Piskunov et al. 2011) is located at the ESO 3.6-m telescope at La Silla. HARPSpol has a spectral resolution of around 110 000, with spectral coverage from 380 to 690 nm. In 2011 May, 18 spectra were collected over six nights using HARPSpol, providing good coverage of the complete rotational cycle. The journal of observations from 2011 May is shown in Table B1.

### 2.2 Observations with NARVAL

NARVAL is attached to the 2-m Telescope Bernard Lyot (TBL) at Pic du Midi. A twin of the CFHT ESPaDOnS instrument (Donati 2003), NARVAL has a spectral coverage of 370–1048 nm with a

<sup>1</sup> <http://bcool.ast.obs-mip.fr>

resolution of approximately 65 000. Information on NARVAL can be found in Aurière (2003).

From 2013 April 23 until May 13 (approximately 21 nights), eight observations were taken using NARVAL. The coverage of the stellar cycle was incomplete, with two observations close to  $\phi_{\text{rot}} \sim 0.25$  and the remaining six giving relatively even coverage of  $0.5 < \phi_{\text{rot}} < 1$ . 12 observations were taken using NARVAL from 2013 December 4 until December 21 (17 nights). The coverage of the stellar surface was sparse but relatively complete. 11 observations were taken using NARVAL between 2014 May 4 and May 18 (14 nights). In 2015 January, seven observations were obtained using NARVAL over 12 nights. The journal of observations from 2013 April through 2015 January is shown in Table B2.

Beginning in 2015 March, a further series of observations of  $\tau$  Boötis were obtained. The observations were more sparsely separated and spanned a significant period of time ( $\sim 70$  d,  $\sim 22$  rotations). Given that this period is considered too long for a single Zeeman Doppler Imaging (ZDI) analysis due to potential for feature evolution, this data set was divided into multiple overlapping epochs and analysed separately. Thus, this observational data is presented in its own journal of observations (Table B3).

### 2.3 Data reduction

Data from NARVAL was automatically reduced using the LIBRE-ESPRIT software package. A specifically modified version of LIBRE-ESPRIT was used by J.-F. Donati to reduce the data from HARPSpol. LIBRE-ESPRIT produces Stokes I (unpolarized) and Stokes V (circularly polarized) spectra, in addition to a null (N) spectrum which is used to determine the authenticity of a detected polarization signal (Donati et al. 1997).

#### 2.3.1 Least-squares deconvolution (LSD)

As Zeeman signatures are typically smaller than the noise level within a single spectral line, they are difficult to detect, especially for solar-type stars such as  $\tau$  Boötis. The LSD technique is applied to improve the S/N of the data by combining the information provided by many spectral lines (Donati et al. 1997). The line mask used to perform the deconvolution is the same as described in Donati et al. (2008) and Fares et al. (2009), using a Kurucz model atmosphere with solar abundances, an effective temperature of 6250 K and  $\log g$  of  $4.0 \text{ cm s}^{-1}$ , including most strong lines in the optical domain (central depths  $> \sim 40$  per cent of the local continuum before macroturbulent or rotational broadening) but excluding the strongest, broadest features such as Balmer lines. This results in each deconvolution utilizing 3000–4000 lines, depending on the particular spectral coverage of the instrument.

In the journals of observations (Tables B1–B3), a definite detection (D) in the LSD Stokes V profile is defined as a false alarm probability (*fap*) of less than  $10^{-5}$ . A marginal detection (M) has a false alarm probability greater than  $10^{-5}$  but less than  $10^{-3}$  (Donati et al. 1997).

#### 2.3.2 Radial velocity

Due to the presence of the hot Jupiter in orbit around  $\tau$  Boötis, the radial velocity (RV) of the star varies from observation to observation. The best-fitting semi-amplitude of  $476 \text{ m s}^{-1}$  we derive is close to that found by Butler et al. (1997) and in good agreement with the expected phasing using the orbital ephemeris of (Catala

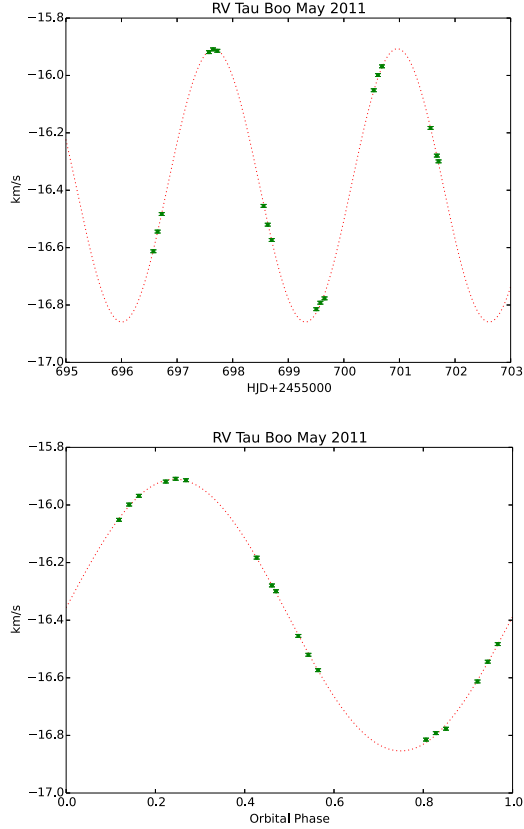


**Figure 1.** Radial velocity of  $\tau$  Boötis, 2011 May derived from HARPSpol data as a function of HJD (upper panel) and as a function of orbital phase (lower panel). The errors in the measurements are  $\sim 5 \text{ m s}^{-1}$ , which is the approximate error for HARPSpol in pure spectroscopic mode (Mayor et al. (2003) and the accompanying HARPS performance summary<sup>2</sup>). The fitted semi-amplitude of  $476 \text{ m s}^{-1}$  is close to that in Butler et al. (1997).

et al. 2007, see Fig. 1 for 2011 May observations). The spectra are automatically corrected by the LIBRE-ESPRIT software for RV variations due to the motion of the Earth. The RV of the star due to the orbital motion of the system is derived by fitting the Stokes I LSD profile of each observation with a Gaussian and determining the centre of the profile. The spectra are then corrected for the RV due to the system's orbital motion.

### 3 Ca II H&K ACTIVITY PROXY

The emission in the cores of the Ca II H&K lines is one of the most widely used proxies for stellar chromospheric activity. The S-index for each observation of  $\tau$  Boötis was calculated using the method

<sup>2</sup> <http://www.eso.org/sci/facilities/lasilla/instruments/harps/inst/performance.html>

**Table 2.** Table of coefficients for equation (2) as calculated by Marsden et al. (2014) for the NARVAL instrument.

Coefficient	NARVAL
$a$	12.873
$b$	2.502
$c$	8.877
$d$	4.271
$e$	$1.183 \times 10^{-3}$

of Wright et al. (2004) and utilizing the coefficients for NARVAL derived by Marsden et al. (2014) for the equation:

$$\text{S-index} = \text{Ca}_{\text{HK}}\text{-index} = \frac{aF_{\text{H}} + bF_{\text{K}}}{cF_{\text{RHK}} + dF_{\text{VHK}}} + e, \quad (2)$$

where  $F_{\text{H}}$  and  $F_{\text{K}}$  are the fluxes in a  $2.18\text{\AA}$  triangular bandpasses centred on the cores of the Ca II H&K lines,  $F_{\text{RHK}}$  and  $F_{\text{VHK}}$  are rectangular  $20\text{\AA}$  bandpasses centred on the continuum at  $3901.07$  and  $4001.07\text{\AA}$  (Wright et al. 2004, fig. 1). These coefficients for the NARVAL instrument are shown in Table 2.

Following the methodology of Marsden et al. (2014), overlapping orders were removed from the reduced spectra of  $\tau$  Boötis and adjusted for the RV for the observation. In addition to the newly observed epochs, all prior observations of  $\tau$  Boötis with the NARVAL instrument were retrieved from the Polarbase<sup>3</sup> (Petit et al. 2014) data base, and we calculated values of the S-index for each normalized individual exposure of  $\tau$  Boötis, making four data points for each spectropolarimetric sequence. These are shown in Fig. 2. As noted in Fares et al. (2009),  $\tau$  Boötis exhibits intrinsic variability through each night and night to night, and this can be observed in the data. Using a least-squares fit of a sinusoid to the unweighted S-index data, we find a longer term variability in chromospheric activity of  $\sim 117$  d. This result corresponds well to the  $\sim 116$  d period reported by Baliunas et al. (1997) and Henry et al. (2000) from the Mount Wilson HK project (Baliunas et al. 1998).

There also appears to be a longer term trend apparent in the data. Baliunas et al. (1997) reports a low-amplitude 11.6 yr activity cycle, however our data set is too short to reliably perform a fit of that duration. In attempting to fit multiple periods, various results converged depending upon initial conditions. There are several fits of equally good quality with different periodicities from approximately  $\sim 300$  d to several thousand days and given the large gaps in the observational records, these periods are uncertain. Further observational epochs taken at shorter intervals are required to accurately characterize the cyclic behaviour of the Ca II H&K activity proxy of  $\tau$  Boötis and if any relationship to other observed cycles exists.

## 4 MAGNETIC MAPPING

### 4.1 Model description

ZDI is used to reconstruct maps of the magnetic topology of  $\tau$  Boötis from the observed Stokes V signatures. The process uses the principles of maximum entropy image reconstruction to produce the configuration of the large-scale magnetic field containing the minimum information required to produce the observed magnetic signatures. The code used is that described in Donati et al. (2006)

<sup>3</sup> <http://polarbase.irap.omp.eu/>

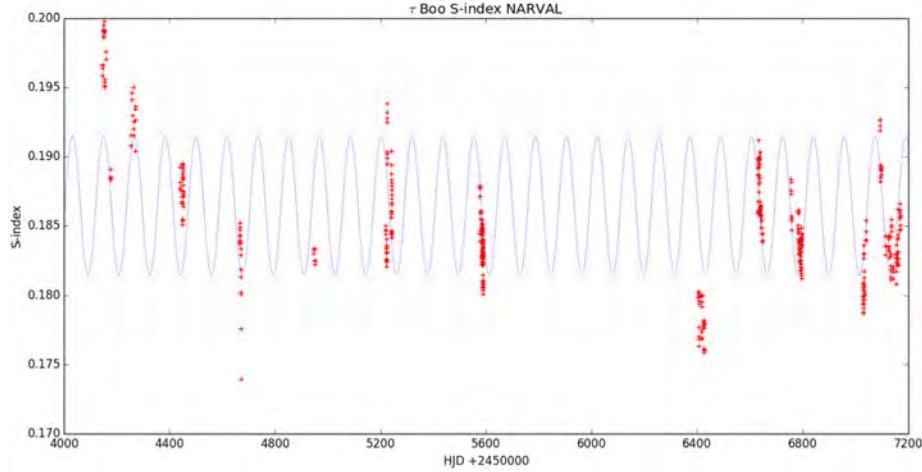


**Figure 2.** Ca II H&K S-indices for  $\tau$  Boötis. NARVAL observations are shown in red. A least-squares fit of a sinusoid to the unweighted data (blue line) yields a period of  $\sim 117$  d, which corresponds closely to the  $\sim 116$  d period reported by Baliunas et al. (1997) and Henry et al. (2000).

wherein spherical-harmonic expansions are used to describe the field configuration with respect to its poloidal and toroidal components. An advantage of this method is that the coefficients of the spherical harmonics can be used to calculate the energy contained in, for example, axisymmetric and non-axisymmetric modes, and to determine relative contributions of dipolar, quadrupolar and higher order components.

The stellar surface is divided into units of similar projected area and the contribution of each unit area to the Stokes V profile (based on field strength, orientation, surface location and motion) is calculated. The process continues iteratively wherein profiles are reconstructed and compared to the observed profiles until a match within the desired error is reached (typically a unit reduced  $\chi^2$ ; i.e.  $\chi_r^2 \sim 1$ ).

The local Stokes I profile is modelled by a Gaussian [full width at half-maximum (FWHM) of  $11 \text{ km s}^{-1}$ ], while the local Stokes V is calculated assuming the weak field approximation (Donati et al. 1997):

$$V \propto g B_{\text{los}} \frac{dI}{d\nu}, \quad (3)$$

where  $B_{\text{los}}$  is the local line-of-sight component of the magnetic field and  $g$  is the mean Landé factor.

## 4.2 Differential rotation

### 4.2.1 Method

When a star is differentially rotating, the signatures produced by magnetic regions will repeat from rotational cycle to rotational cycle but with differences resulting from shifts in the relative location of the regions due to the differential rotation. We consider that the rotation will follow a simplified solar-type law:

$$\Omega(\theta) = \Omega_{\text{eq}} - d\Omega \sin^2 \theta, \quad (4)$$

where  $\Omega(\theta)$  is the rotation rate of the star at latitude  $\theta$  in  $\text{rad d}^{-1}$ ,  $\Omega_{\text{eq}}$  is the rotation rate at the equator and  $d\Omega$  is the rotational shear between the equator and the poles.

Applying the method described by Donati et al. (2000), Petit, Donati & Collier-Cameron (2002), Donati, Cameron & Petit (2003) and Morin et al. (2008), we construct a magnetic image containing a given information content for each pair of  $(\Omega_{\text{eq}}, d\Omega)$  and choose the pair of parameters which produces the best fit to the data (i.e. the smallest  $\chi_r^2$ ). An example for the 2013 December data set is shown in Fig. 3(a). Fig. 3(b) shows how we derive  $\sim 1\sigma$  variation bars as a measure of uncertainty by varying various stellar parameters ( $\sin i \pm 1 \text{ km s}^{-1}$ ; inclination  $\pm 10^\circ$ ; target reconstructed average magnetic field  $B_{\text{mod}} \pm \sim 10$  per cent) and calculating the extreme variations.

Donati et al. (2008) measured the differential rotation of  $\tau$  Boötis utilizing the Stokes V data, equal to  $\Omega_{\text{eq}} = 2.10 \pm 0.04 \text{ rad d}^{-1}$  and  $d\Omega = 0.50 \pm 0.12 \text{ rad d}^{-1}$ . However, subsequent observations have yielded either different values of  $\Omega_{\text{eq}}$  and  $d\Omega$  [e.g. 2008 January,  $d\Omega = 0.28 \pm 0.10$ ; Fares et al. (2009)] or no measurement has been possible (Fares et al. 2013).

### 4.2.2 Results

The 2011 May HARPSpol data produced a well-defined paraboloid, albeit with a larger error compared to other runs. The HARPSpol data are of a lower S/N than that from NARVAL, however, the 2011 May phase coverage is superior to the other runs. The derived parameters of  $\Omega_{\text{eq}} = 2.03^{+0.05}_{-0.05}$  and  $d\Omega = 0.42^{+0.11}_{-0.11} \text{ rad d}^{-1}$  is consistent with those of Donati et al. (2008).

For the NARVAL data from 2013 April/May, we measure a significant error bar. The maps for 2013 April and May show that there are only two observations of the star consistent with phase  $\sim 0.25$  ( $\phi_{\text{rot}}$  of  $-2.749$  and  $+3.262$ ), and these are separated by  $\sim 6$  full rotations ( $\sim 20$  d). Removing these observations results in a smaller error and a lower value of  $d\Omega$ . However, the DR measurement used in our mapping and reported in Table 3 is made with all observations present, hence a much larger error is calculated. The derived parameters for 2013 April/May were  $\Omega_{\text{eq}} = 2.05^{+0.04}_{-0.04}$  and  $d\Omega = 0.38^{+0.18}_{-0.19} \text{ rad d}^{-1}$ .

With a better coverage of the stellar rotational cycle in 2013 December, a clear paraboloid was again generated (Fig. 3a). The

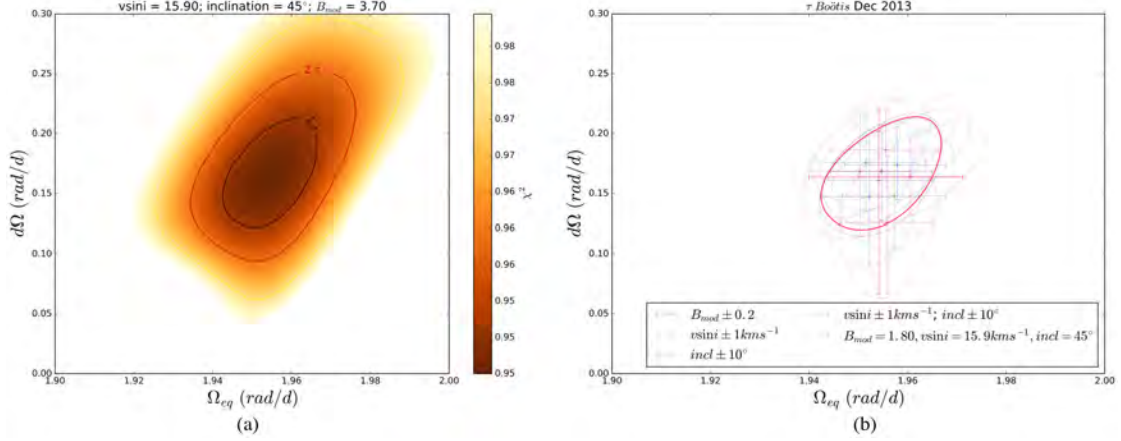


**Figure 3.** Differential rotation of  $\tau$  Boötis for 2013 December. Panel (a) shows the variation of  $\chi_r^2$  as a function of  $\Omega_{\text{eq}}$  and  $d\Omega$  for the selected stellar parameters ( $v \sin i = 15.9 \text{ km s}^{-1}$ , inclination  $45^\circ$ ) and a target  $B_{\text{mod}}$  appropriate for the desired  $\chi_r^2$  used to reconstruct the magnetic maps of this epoch. Panel (b) shows second-order polynomial fits for the  $1\sigma$  threshold paraboloids surrounding the minimum  $\chi_r^2$ , where the red paraboloid corresponds to the plot in panel (a). Other paraboloids represent fits to the corresponding DR calculations varying the target  $B_{\text{mod}}$  ( $\pm \sim 10$  per cent, black),  $v \sin i$  ( $\pm 1 \text{ km s}^{-1}$ ) and stellar inclination ( $\pm 10^\circ$ ) independently (green and blue) and  $v \sin i$  and inclination angle together (magenta). The overall variation bars are used to derive the uncertainty in the measured DR parameters.

**Table 3.** Summary of differential rotation parameters for  $\tau$  Boötis as measured by the  $\chi^2$  minimization method. For comparison, the FT method (Sec. 4.2.4, assuming  $\Omega_{\text{eq}} = 2.00 \text{ rad d}^{-1}$ ) yields  $d\Omega = 0.35 \pm 0.14 \text{ rad d}^{-1}$ . The values presented below are used in the magnetic mapping.

Epoch	$\Omega_{\text{eq}}$ ( $\text{rad d}^{-1}$ )	$d\Omega$ ( $\text{rad d}^{-1}$ )
2011 May	$2.03^{+0.05}_{-0.05}$	$0.42^{+0.11}_{-0.11}$
2013 April/May	$2.05^{+0.04}_{-0.04}$	$0.38^{+0.18}_{-0.19}$
2013 December	$1.95^{+0.01}_{-0.01}$	$0.16^{+0.04}_{-0.04}$
2014 May	$1.99^{+0.01}_{-0.01}$	$0.10^{+0.04}_{-0.04}$
2015 January	$1.98^{+0.03}_{-0.03}$	$0.15^{+0.15}_{-0.16}$

measured differential rotation for 2013 December corresponded to parameters of  $\Omega_{\text{eq}} = 1.95^{+0.01}_{-0.01} \text{ rad d}^{-1}$  and  $d\Omega = 0.16^{+0.04}_{-0.04} \text{ rad d}^{-1}$ .

The data for 2014 May once more produced a clear paraboloid with the parameters  $\Omega_{\text{eq}} = 1.99^{+0.01}_{-0.01} \text{ rad d}^{-1}$  and  $d\Omega = 0.10^{+0.04}_{-0.04} \text{ rad d}^{-1}$ . Finally, the derived parameters for 2015 January were  $\Omega_{\text{eq}} = 1.98^{+0.03}_{-0.03} \text{ rad d}^{-1}$  and  $d\Omega = 0.15^{+0.15}_{-0.16} \text{ rad d}^{-1}$ .

These values are summarized in Table 3.

#### 4.2.3 A discussion of variable differential rotation measurement

Table 3 makes clear that the technique used to determine differential rotation yields a wide variation in  $d\Omega$ , but is consistent with solar-like differential rotation with the equator rotating faster than the poles.  $\Omega_{\text{eq}}$  is much more constrained within a range from  $\sim 1.95$  to  $2.05 \text{ rad d}^{-1}$ , ignoring the error. As simulations performed by Petit et al. (2002) show, factors including the phase coverage and observational cadence can have significant effects on the measured differential rotation parameters.

Notably, apart from the 2011 May HARPSpol observation, at best the observations of  $\tau$  Boötis have had a single observation per night (approximately one  $4 \times 600 \text{ s}$  observation every one-third of

a rotation) over several full stellar rotations. As the technique used to determine differential rotation is a  $\chi^2$ -landscape technique and dependent upon the regular re-observation of features, it is possible that the significant variation in the measured parameters are due to observational biases. The weakness of the field of  $\tau$  Boötis and the difficulty in observing Zeeman signatures on the star potentially exacerbates this effect. Attempting the  $\chi^2$  minimization method with lower values of target  $B_{\text{mod}}$  with various  $\tau$  Boötis data sets, (corresponding to higher  $\chi_r^2$  fits) thus providing less information for the technique produces a systemic decrease in the calculated values of  $\Omega_{\text{eq}}$  and  $d\Omega$ .

This supposition would need to be confirmed by simulations and it should be noted that this does not rule out the existence of small or significant actual variation in differential rotation of magnetic features on  $\tau$  Boötis; simply that we cannot draw any such conclusion from these measurements. A paper is in preparation (Mengel et al.) examining the effect of phase coverage on measuring DR parameters on slow rotating weak-field stars and how we may determine optimal observational cadences and periods for this type of target.

Finally, it is to be noted that varying  $d\Omega$  will slightly distort the shape of the features on the maps but does not appear to have a significant effect in the determination of the general magnetic field properties (Table 6). Consequently to be internally consistent in applying the maximum-entropy, minimum information mapping technique, these measured values for  $d\Omega$  and  $\Omega_{\text{eq}}$  which give the minimum information solution have been utilized in the magnetic mapping in this work.

#### 4.2.4 Stokes I differential rotation – Fourier transform method

An alternative measurement of the differential rotation can be made using the Fourier transform (FT) method described by Reiners & Schmitt (2003).

An averaged Stokes I profile was created from the NARVAL and HARPSpol data for each observational epoch. Using the method of

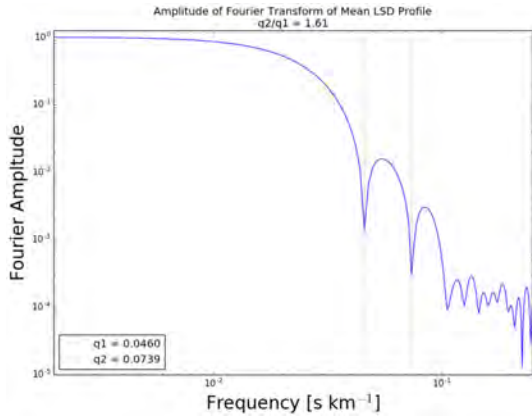


**Figure 4.** Amplitude of the Fourier transform of the averaged LSD Stokes I profile for 2014 May. The first two zeros ( $q_1, q_2$ ) are shown. The ratio  $q_2/q_1$  can be used to derive  $\alpha$  ( $d\Omega/\Omega_{\text{eq}}$ ) as described in the text (Section 4.2.4).

Reiners & Schmitt (2003), we obtained the ratio of the first two zeros of the Fourier-transformed average Stokes I line profile ( $q_2/q_1$ ). An example of this is shown for the 2014 May epoch in Fig. 4. For each epoch, we determined that  $q_2/q_1 = 1.61 \pm 0.07$ . From equation 5 in Reiners & Schmitt (2003), using an inclination angle of  $45^\circ$ , we thus calculate  $\alpha$  ( $d\Omega/\Omega_{\text{eq}}$ ) of  $\approx 0.17$ .

Using the various measured values of  $\Omega_{\text{eq}}$  from Table 3, this produces a value for  $d\Omega$  of between  $0.34$  and  $0.36 \text{ rad d}^{-1}$ , which is in good agreement with the value found by Reiners (2006), Catala et al. (2007), and Borsa et al. (2015) for  $\tau$  Boötis.

It is noted that this technique is quite sensitive to the derived value of  $q_2/q_1$ . Thus using  $q_2/q_1 = 1.61 \pm 0.07$  would yield an uncertainty in  $d\Omega$  of  $0.14 \text{ rad d}^{-1}$ . Again, this uncertainty is in agreement with the measurements of the differential rotation of  $\tau$  Boötis by Reiners (2006).

Yielding a value of  $d\Omega = 0.35 \pm 0.14 \text{ rad d}^{-1}$ , the Fourier transform method is broadly consistent with the values derived by the  $\chi^2$ -landscape method taking into account the errors calculated for both methods. Despite the consistency of the two methods described here, the differential rotation measurement must be viewed with caution due to the uncertainties and assumptions inherent in each method.

### 4.3 Magnetic mapping

#### 4.3.1 Stellar and model parameters

Utilizing the measured differential rotation parameters, a  $\chi^2$  minimization process was used to determine the optimum angle of inclination and  $v \sin i$ . The values derived were close to those used in previously published works (Fares et al. 2009, 2013) so an inclination of  $45^\circ$  and  $v \sin i$  of  $15.9 \text{ km s}^{-1}$  as used in Fares et al. (2013) were chosen and applied to all data sets. (It is noted that this value of  $v \sin i$  varies by  $\sim 10$  per cent from the latest published value shown in Table 1, however, the difference in the models was insignificant using either value, thus we use the derived value for consistency with previous works).

Once the stellar parameters and differential rotation values were chosen, maps were generated for different values of  $\chi_r^2$ .

The reconstructed average magnetic field ( $B_{\text{mod}}$ ) begins to rise significantly with a lower target  $\chi_r^2$  as the process begins fitting inappropriately to the noise inherent in the signatures, this requires the target  $\chi_r^2$  to be chosen with care. This effect is much more pronounced in the HARPSpol data than for the NARVAL data and it would thus be inappropriate to utilize the same  $\chi_r^2$  for the 2011 May data. Thus, a  $\chi_r^2$  was chosen to be  $0.95$  for the NARVAL data, and  $1.10$  for the HARPSpol data. A potential drawback of this is that the comparison of the absolute magnitude of the field strength may no longer be appropriate for the data sets derived from the different instruments or between data sets using the same instrument with significantly different S/N levels and thus target  $\chi_r^2$ .

The spherical harmonic expansions for the reconstructed magnetic models were calculated using  $\ell = 8$  as little improvement was obtained using  $\ell > 8$ , there being near to zero energy in higher order harmonics. This is consistent with previous papers dealing with  $\tau$  Boötis and adequate given there are  $\sim 9$  spatial resolution elements around the equator as per equation (5) (Morin et al. 2010, equation 3).

$$\frac{2\pi v_e \sin i}{\text{FWHM}} = \frac{2\pi(15.9 \text{ km s}^{-1})}{11 \text{ km s}^{-1}} \sim 9 \quad (5)$$

The amount of energy in the various harmonics can be used to describe the configuration of the magnetic field (Donati et al. 2006). These results shown in Table 6 consist of three calculations. First, the amount of the magnetic energy stored in the toroidal component of the field is found from the  $\gamma_{\ell, m}$  term of the complex coefficients of the spherical harmonics. Secondly, the amount of magnetic energy in the poloidal component ( $\alpha_{\ell, m}$  and  $\beta_{\ell, m}$ ) which is axisymmetric (i.e. symmetric about the axis of rotation) is found from the  $\alpha_{\ell, m}$  and  $\beta_{\ell, m}$  coefficients of the spherical harmonics where  $m = 0$ . [Other papers, such as Fares et al. (2009, 2013) use  $m < \ell/2$  rather than  $m = 0$ . We consider  $m = 0$  to be more mathematically correct; however, the difference in practice is quite small so direct comparisons between epochs are possible. Where appropriate, this is noted in the text.] Finally, the amount of magnetic energy in the poloidal component of the magnetic field consisting of dipolar plus quadrupolar components is calculated from  $\alpha_{\ell, m}$  and  $\beta_{\ell, m}$  coefficients where  $\ell \leq 2$ .

As in the differential rotation measurements, an indication of the variation in these values is found by varying the differential rotation measurement by the error found for each epoch (holding inclination and  $v \sin i$  constant), then varying the stellar parameters (inclination  $\pm 10^\circ$ ;  $v \sin i \pm 1.0 \text{ km s}^{-1}$ ) while holding  $d\Omega$  and  $\Omega_{\text{eq}}$  constant. It is noted that the variation of stellar parameters produces variation in field components in a consistent way across the epochs, and the variations, although sometimes large relative to the values, are of the same order of magnitude across the epochs. The amount of toroidal field has the smallest variation due to parameter variation. The amount of energy in axisymmetric and  $\ell \leq 2$  modes in the poloidal field exhibit large variability with chosen stellar parameters, albeit with the dominant parameter affecting this variation being the chosen angle of inclination. Where there is a large uncertainty in the measured ( $d\Omega, \Omega_{\text{eq}}$ ), such as in the 2011 May and 2015 January epochs, the combination of parameters can create significant variation.

As a derived inclination angle for  $\tau$  Boötis which is very close to our chosen value with a low level of uncertainty is known [cf.  $44.5^\circ \pm 1.5^\circ$  (Brogi et al. 2012) versus  $45^\circ$ ], the variation of inclination in our process by  $\pm 10^\circ$  is somewhat conservative and thus our variation values may be overestimated. Consequently, we have a reasonable confidence that epoch-to-epoch changes in

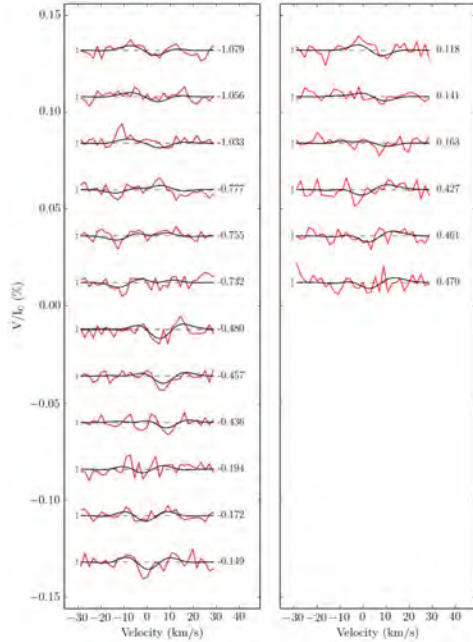


**Figure 5.** Circular polarization profiles of  $\tau$  Boo for HARPSpol observations, 2011 May. The observed profiles are shown in red, while synthetic profiles are shown in black. On the left of each profile, we show a  $\pm 1\sigma$  error bar. The rotational cycle of each observation is indicated on the right of each profile. All images of profile fits such as this are on the same scale across this work.

the field topology are real irrespective of the sometimes large and conservative variation measurements.

As with determining differential rotation, phase coverage must be adequate to successfully reconstruct the features on the stellar surface. Features, and thus energy in the harmonics, may be missed if parts of the stellar surface are not observed. It is noted that the cadence observations of  $\tau$  Boötis in observations after 2011 is lower than previous epochs. Consequently, fewer phases are used in most of the epochs in this work compared to those of Donati et al. (2008) and Fares et al. (2009, 2013). Reconstruction of maps in this work with partial, sampled data sets shows that the latitude information of features and the overall field configurations seem to be conserved, albeit with a reduction in the overall energy seen in the harmonics. These effects for a star with a weak magnetic field was discussed briefly by Fares et al. (2012) and is being further investigated in a forthcoming paper from Mengel et al.

#### 4.3.2 Results – HARPSpol – 2011 May

Fig. 5 shows the observed and reconstructed profiles for 2011 May. Compared to the other epochs presented in this work, the magnetic signature is very small, and the observed profiles (in red) are relatively noisy, thus the reconstructed profiles begin fitting to the noise at a relatively high  $\chi_r^2$ . While HARPSpol has a higher resolution than NARVAL (110 000 cf. 65 000), the spectral coverage is smaller and consequently there are significantly fewer spectral lines to use in LSD. Nevertheless we observe, as per Fares et al. (2009), Fares et al. (2013), and Donati et al. (2008), that a weak magnetic field

is manifest on the surface of  $\tau$  Boötis in the order of 5–10 G. The magnetic topology for 2011 May is shown in Fig. 7, top row. This topology was reconstructed with  $\chi_r^2 = 1.10$ .

The magnetic field has evolved in configuration from the 2011 January observation presented in Fares et al. (2013). The mean field is somewhat weaker at 2.2 G (although as noted before, a direct comparison of the HARPSpol  $B_{\text{mod}}$  may be of limited utility given the differences in the  $\chi_r^2$ ), and the percentage of the toroidal component of the field has remained around the same (from 18 to 20 per cent). In addition, the field configuration has become more complex, with 19 per cent ( $m = 0$ ; value is  $\sim 25$  per cent if using  $m = \ell/2$ ) of the poloidal component in an axisymmetric configuration compared to 37 per cent, and only 26 per cent of the poloidal component contained in modes  $\ell \leq 2$  compared with 35 per cent.

#### 4.3.3 Results – NARVAL – 2013 April/May through 2015 January

Over a period from 2013 April until 2015 January, four epochs of  $\tau$  Boötis were observed using NARVAL at TBL. The reconstructed (black) and observed (red) magnetic profiles for these epochs are shown in Figs 6(a)–(d). In all four epochs, magnetic signatures are clearly observed, and the evolution of the signatures with rotation is clear.

All three sets of maps were reconstructed using the same inclination and  $v \sin i$  parameters and  $\chi_r^2 = 0.95$ . The values of the differential rotation parameters ( $\Omega_{\text{eq}}$ ,  $d\Omega$ ) as derived in Section 4.2 for each epoch were used for each reconstruction.

It is clear from the maps (Fig. 7, second, third, fourth and bottom rows) and from the parameters of the magnetic topology that the large-scale magnetic field on  $\tau$  Boötis evolved significantly over the 18 month period.

Between 2013 April/May and December, the field strength increased, and there was a negligible increase in the percentage of the calculated toroidal component. The amount of poloidal axisymmetry and the amount of field with modes of  $\ell \leq 2$  decreased (Table 6). In short, the field increased slightly in complexity.

Between 2013 December and 2014 May, a significant change occurred with a clear reversal of polarity in the radial field, coincident with a significant decrease in the percentage of the toroidal component (24 per cent to 13 per cent), an increase in the axisymmetric poloidal component (30 per cent to 46 per cent) and a slight increase (40 per cent to 45 per cent) in the amount of the poloidal field with modes of  $\ell \leq 2$ . After the reversal, the field became more poloidal and symmetric.

Between 2014 May and 2015 January as the next polarity reversal (expected between 2015 January and May) approached, the toroidal component of the field once more increased (from 12 per cent to 30 per cent), the axisymmetric component of the poloidal field dropped from 46 per cent to 37 per cent and the percentage of poloidal field in modes  $\ell \leq 2$  decreased slightly from 45 to 41. This represents another increase in the complexity of the field as the radial field reversal approaches.

There have now been three sets of sequential epochs of  $\tau$  Boötis observations which fall between radial field reversals. The latest two epoch pairs (2013 April/May and December; 2014 May and 2015 January) presented in this work show an increase in field strength and complexity between the reversals based on the amount of poloidal axisymmetric modes, modes with  $\ell \leq 2$  and an increase in toroidal field. The other inter-reversal epoch pair (2009 May/2010 January; Fares et al. 2013) of epochs showed an increase in field

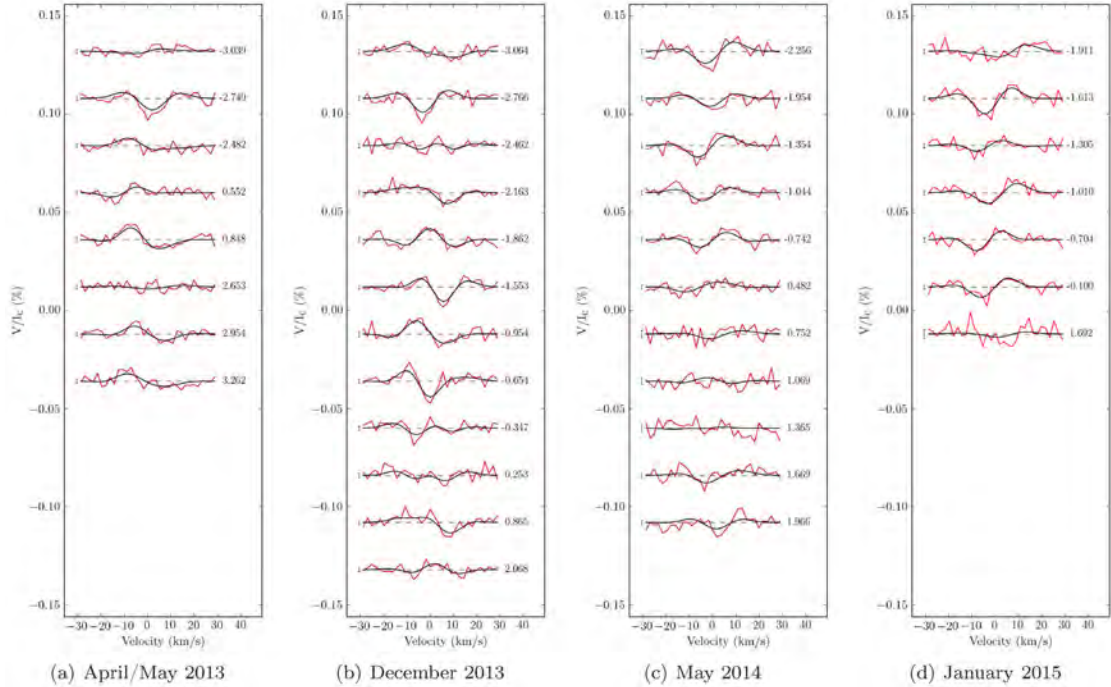


**Figure 6.** Circular polarization profiles of  $\tau$  Boo for NARVAL observations, 2013 April through 2015 January. The observed profiles are shown in red, while synthetic profiles are shown in black. On the left of each profile, we show a  $\pm 1\sigma$  error bar. The rotational cycle of each observation is indicated on the right of each profile.

strength and a decrease in axisymmetry of the poloidal field however the percentage of toroidal field did not increase in that case.

#### 4.3.4 Results – NARVAL – 2015 March–May

Observations of  $\tau$  Boötis from March until 2015 May presented a challenge for mapping as the data were very sparse and spread over 70 d which corresponds to over 20 stellar rotations. This presents a problem due to the potential for feature evolution. In addition, only one or two observations per rotation leaves little information for determining differential rotation using the  $\chi^2$ -landscape technique.

The initial three observations (2015 March 12–17) were widely separated from the rest of the data set. A crude analysis using these three observations confirmed that the expected polarity reversal had occurred, meaning that it had occurred between late January and early March. The long time base of the 2015 March–May observations presented an opportunity to investigate this activity proxy minimum using the available data.

Utilizing a sliding window of approximately eight stellar rotations, the observations from April 2 through May 27 were split into four overlapping data sets (Fig. 8, Table 4) and maps were generated. Individual differential rotation measurements were made for each of the four data sets and the measurements are summarized in Table 5. As can be seen, the  $d\Omega$  values were near solid-body and poorly defined for the first three data sets. This is probably due to insufficient data for the technique (Morgenthaler et al. 2012). For each map,  $\chi_r^2$  of 0.95 was used.

The Stokes V profiles for these data sets are shown in Fig. 9. The maps for the four data sets are shown in Fig. 10 and the resulting field configuration information is presented in Table 7. While the sparseness of the data over this period and other observational biases such as poor S/N may contribute to the lack of features, if accurate, these maps show an intriguing progression through the activity proxy minimum. The observable field strength decreases as the minimum in S-index is passed and increases dramatically as the S-index begins to rise. In all cases, the strength is less than that from the 2015 January epoch prior to the dipole reversal despite being at a higher S-index.

Fig. 8 does show that there are several observations in this epoch that suffer from comparatively poor signal to noise (circles S/N < 1000), where no magnetic signature is detected, which has an effect on the reconstruction. In contrast, the 2015 January data (Fig. 8, data located at  $\sim$  HJD 2457030) where the measured S-indices are lower than the March–May data, apart from the final observation, the data is excellent with S/N above 1386. Apart from the lowest S-index measurement, there are detections; mostly classified as definite. Thus, it may appear at first glance that the variation in the S-index may not correlate with the level of magnetic activity we detect with ZDI due to the effects of varying data quality.

However, if we ignore the 2015 March–May observations with S/N < 1000, a pattern does appear whereas the S-index decreases, the magnetic detections become marginal until finally there is a non-detection. Further, examining all of the observations from the NARVAL epochs presented in this paper (Fig. 11, excluding

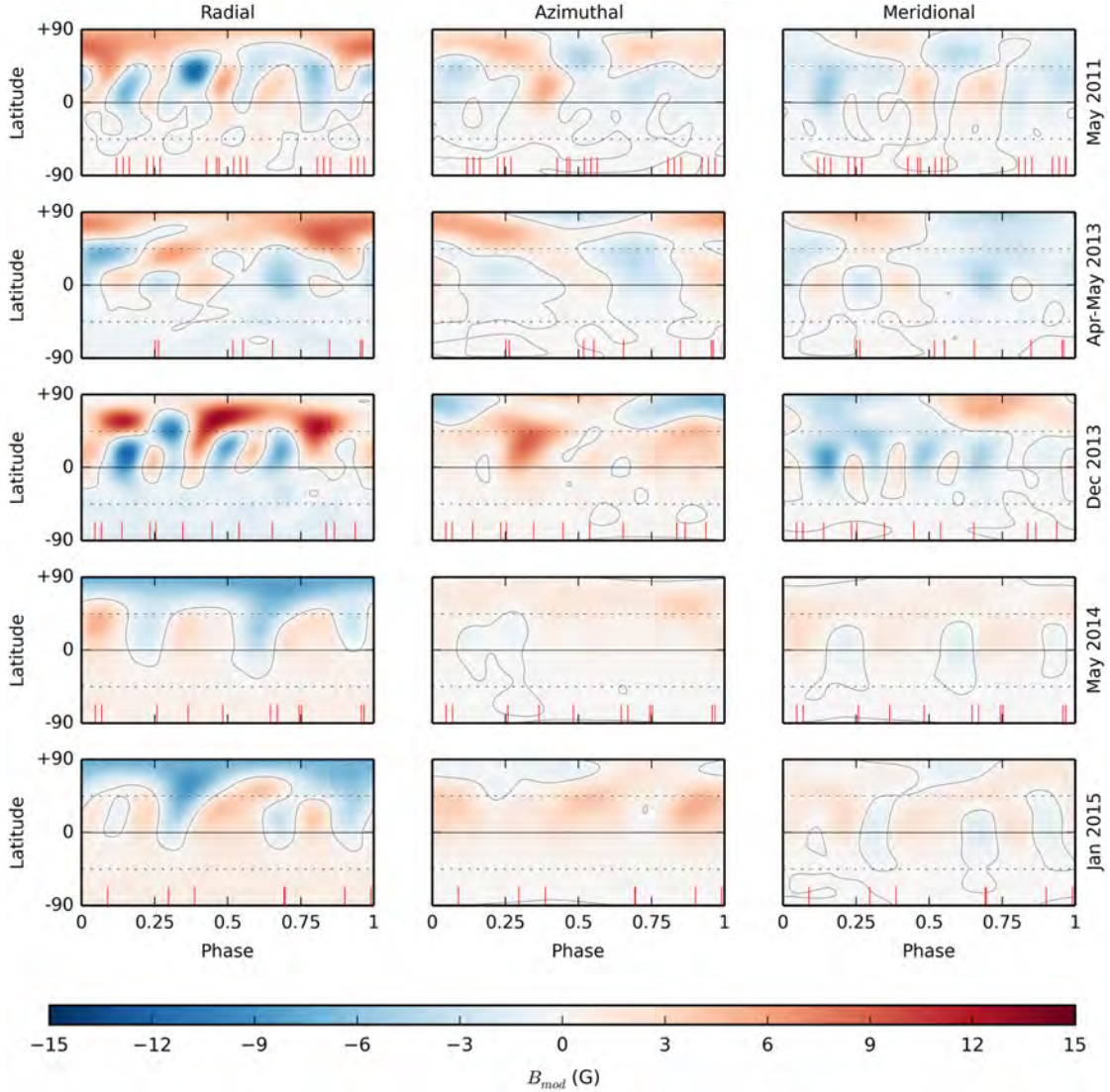


**Figure 7.** Magnetic topology of  $\tau$  Boötis reconstructed from profiles in Fig. 5 and Figs 6(a)–(d). The radial, azimuthal and meridional components of the field (with magnetic field strength labelled in G) are depicted for 2011 May (top), 2013 April and May (second row), 2013 December (third row), 2014 May (fourth row), and 2015 January (bottom row). The contour line indicates where  $B_{\text{mod}}$  is zero. The red ticks along the lower  $x$ -axes indicate the observational phases for each epoch.

$S/N < 1150$  where there is only a single marginal detection), it is clear that as the quality of the data improves, the proportion of marginal detections decreases, while non-detections only appear at lower  $S$ -indices. Hence while the data quality is a factor, it is possible to say that chromospheric activity does exhibit a relationship to the observed magnetic activity of  $\tau$  Boötis.

This may only be within a particular chromospheric activity cycle. Noting that although the  $S$ -indices for 2015 January were universally lower than 2015 March–May, the star’s magnetic field was stronger in January. This may mean that there is a general increase

in magnetic activity as the star’s magnetic cycle proceeds from one reversal to the next, while there is a smaller modulation following the chromospheric activity cycle of which there appear to be  $\sim 3$  per intra-reversal period ( $\sim 117$  d:  $\sim 1$  yr). However, the existing data are not detailed enough to make this statement definitively. Indeed, examining previous epochs and given the uncertainty in exactly when the polarity reversal occurs, it is possible to speculate that the magnetic cycle may correspond to the chromospheric cycle. Three reversals per year would potentially manifest as a yearly reversal due to observational cadences. This is discussed further in Section 5.

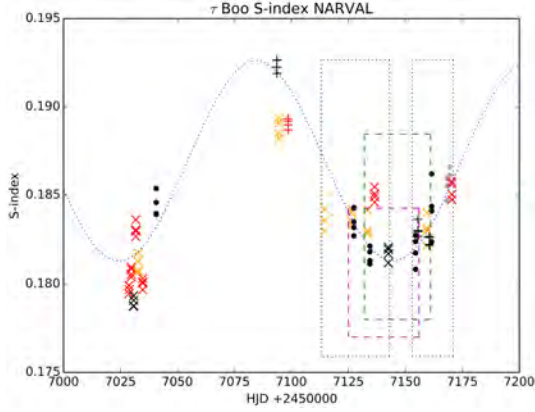


**Figure 8.** Ca II H&K S-indices for  $\tau$  Boötis for January ( $\sim 7030$  HJD+2450000) through 2015 May. NARVAL observations are shown as follows: red = definite detection; orange = marginal detection; black = no detection; grey = incomplete Stokes V sequence. Marker shapes represent S/N near  $\sim 700$  nm in the Stokes V spectrum: circles =  $S/N < 1000$ ; + =  $1000 < S/N < 1300$ ;  $\times$  =  $S/N > 1300$ . A least-squares fit to the unweighted data (blue line) yields a period of  $\sim 120$  d, similar to that reported in Baliunas et al. (1997). The leftmost black dotted rectangle indicates the observations used for the profiles in Fig. 9(a). The magenta and green dashed rectangles correspond to Figs 9(b) and (c), respectively. The rightmost dotted rectangle indicates the observations used for the profiles in Fig. 9(d).

**Table 4.** Use of exposures from 2015 April to May (Table B3) and their use in each map reconstruction. The rotational cycle used for calculating 0.0 (from equation 1) is shown for each map. (\* – observation on May 19 with very poor S/N was not used in the reconstruction).

Obs.	Cycle	Map 1 $\phi_{\text{rot}}$	Map 2 $\phi_{\text{rot}}$	Map 3 $\phi_{\text{rot}}$	Map 4 $\phi_{\text{rot}}$
2015-April-02	1105.992	-4.008			
2015-April-13	1109.586	-0.414	-4.414		
2015-April-14	1109.866	-0.134	-4.134		
2015-April-20	1111.693	1.693	-2.307	-4.307	
2015-April-21	1111.994	1.994	-2.006	-4.006	
2015-April-23	1112.608	2.608	-1.392	-3.392	
2015-April-30	1114.439	4.439	0.439	-1.561	
2015-May-11	1118.047		4.047	2.047	-1.953
2015-May-12	1118.351		4.351	2.351	-1.649
2015-May-16	1119.550			3.550	-0.450
2015-May-17	1119.862			3.862	-0.138
2015-May-19	1120.170				*
2015-May-27	1122.847				2.847
$\phi_{\text{rot}} = 0$ Cycle		1110	1114	1116	1120

**Table 5.** Summary of measured differential rotation parameters for  $\tau$  Boötis for the four maps 2015 March–May. Note the antisolar  $d\Omega$  for the first three epochs, due to poor coverage and/or low detectability of the magnetic field.

Epoch	$\Omega_{\text{eq}}$ ( $\text{rad d}^{-1}$ )	$d\Omega$ ( $\text{rad d}^{-1}$ )
2015 April 02–30	$2.01^{+0.01}_{-0.15}$	$-0.07^{+0.07}_{-0.04}$
2015 May 13–12	$1.88^{+0.15}_{-0.04}$	$-0.12^{+0.13}_{-0.09}$
2015 May 20–17	$1.93^{+0.01}_{-0.01}$	$-0.04^{+0.04}_{-0.03}$
2015 May 12–27	$1.92^{+0.02}_{-0.06}$	$+0.17^{+0.16}_{-0.14}$

The field configuration for 2015 March–May appears to be generally highly symmetrical for the first three data sets, however, there is very little energy in the spherical harmonics to work with during the S-index minimum. It is clear though that after the minimum, there is noticeably more toroidal field evident, and a significant decrease in poloidal axisymmetry and dipolar/quadrupolar modes. This result further suggests that a magnetic activity cycle appears to be coincident with the chromospheric activity cycle.

Given that  $\phi_{\text{rot}} = 0$  is synchronized in each map, it is possible to see features migrating across the star between 2015 March and May, probably due to differential rotation. In addition, in the final two data sets, the emergence of the prominent feature at  $+45^\circ$  near  $\phi_{\text{rot}} = 0.75$  with time is clear. While this may be due to observational effects, it also may be due to increased intensity leading to feature evolution. Notably, maps 1, 3 and 4, all exhibit active regions near  $\phi_{\text{rot}} = 0.75$ . Coincidentally, this is near the active longitude suggested by Shkolnik et al. (2008).

## 5 DISCUSSION AND CONCLUSIONS

The 2015 March–May observational epoch makes clear that  $\tau$  Boötis is near the limit of our ability to apply ZDI. A small magnetic survey of  $\sim 20$  planet hosting stars utilizing NARVAL (Mengel et al., in preparation) and the wider BCool survey (Marsden et al. 2014) finds that fainter stars (these surveys are to  $V \sim 9$ ) with an S-index less than  $\sim 0.2$  usually have magnetic fields too weak to detect.  $\tau$  Boötis is thus unusual in this regard, due to its brightness ( $V \approx 4.5$ ) compared to the wider sample allowing for adequate signal to noise for ZDI. When  $\tau$  Boötis is at the nadir of its chromospheric activity cycle, the magnetic field is on the very limit of where NARVAL can with confidence detect the Zeeman signature.

Despite this limitation, the evolution of the large-scale magnetic field of  $\tau$  Boötis is apparent in the results we present here over two time-scales and (what appear to be) two cyclic periods. Most significantly,  $\tau$  Boötis appears to undergo polarity switches on a regular basis. Fares et al. (2013) notes that the polarity switch appears to be a phenomenon occurring every 360 d, and these latest observations would seem to confirm this hypothesis. The regular reversals appear to occur between January and March in each calendar year. Additionally, magnetic energy appears to rise and fall in a shorter cycle coincident with the S-index of the star.

The evolution of the magnetic field during the period between reversals is illuminating insofar as the behaviour of the large-scale field broadly follows what one would expect in a star such as the Sun. In Fig. 12, the fractional magnetic field for each of the three components at each latitude is shown for these three epochs. Between 2013 April/May and December, the intensity of the radial and azimuthal components increases and the latitude at which the peak intensity is observed decreases towards the equator (Figs 12a and b). After the polarity switch, the radial and azimuthal fields have a relatively lower intensity and their peak intensity is at latitudes close to the pole (Fig. 12c). This cycle then repeats between the two observed radial field reversals (Fig. 13). This pattern of intensifying azimuthal field at lower latitudes approaching a reversal was observed between 2009 May and 2010 January, the only similar set of observations taken between a pair of reversals. It should be noted that with poorer phase coverage, the potential uncertainty in the latitudes of recovered features increases, particularly in the azimuthal and meridional components. This is because with sparser phase coverage, we are less likely to observe either the exact points of entry or exit (or indeed both) of features on the visible stellar surface. The level of this uncertainty is difficult to characterize, thus

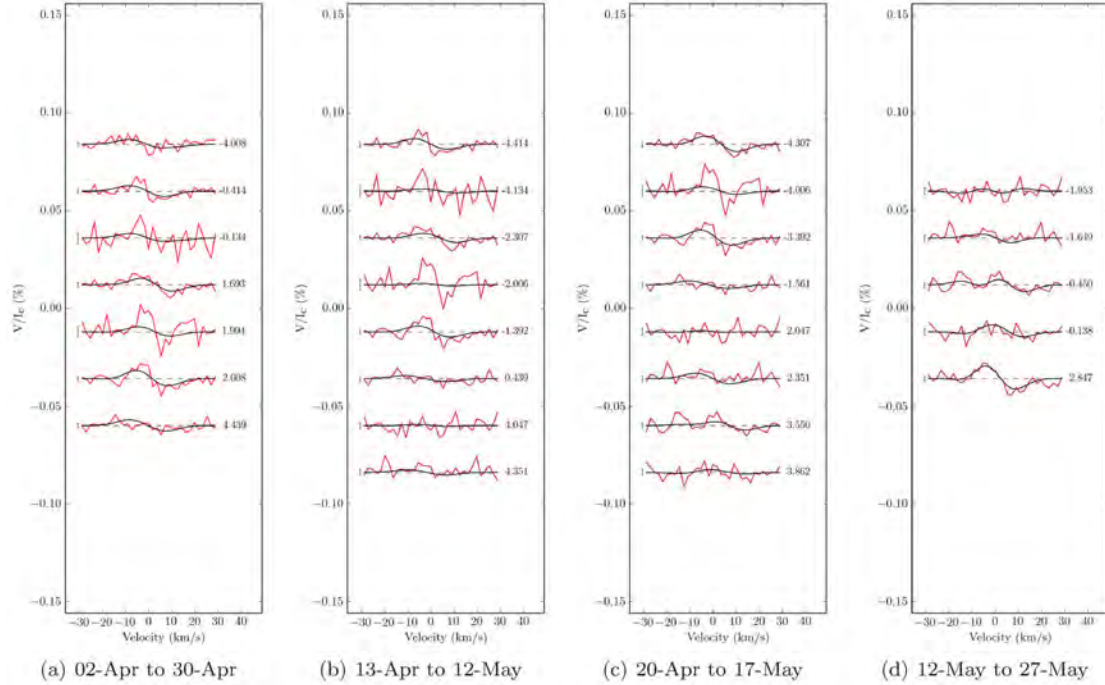


**Figure 9.** Circular polarization profiles of  $\tau$  Boo from NARVAL 2015 April and May. As shown in Table 4, four maps utilizing a ‘sliding window’ of approximately eight rotations were used (apart from the final set of five rotations). The sets overlap and phases are as per Table 4. The observed profiles are shown in red, while synthetic profiles are shown in black. On the left of each profile, we show a  $\pm 1\sigma$  error bar. The rotational cycle of each observation is indicated on the right of each profile.

further observations with higher cadence and denser phase coverage may be required to absolutely confirm the nature of the latitudinal migration of features we propose here.

As a polarity shift approaches, the field also becomes less axisymmetric in the poloidal component and more complex, with slightly less of the poloidal field in modes corresponding to dipolar and quadrupolar components. After the polarity shift occurs, the amount of the toroidal field decreases significantly and the field becomes simpler; more axisymmetric and more strongly dipolar/quadrupolar. [Note that between 2009 May and 2010 January (Fares et al. 2013), the percentage of axisymmetric modes similarly dropped precipitously, however, the complexity of the field decreased slightly differing from the 2013 epochs].

The  $\sim 117$  d period of the  $\text{Ca II H\&K}$  index coupled with a posited  $\sim$ yearly radial field polarity reversal suggests a 3:1 periodic relationship between the cycles. Reversals appear to occur at or near the peak of every third chromospheric cycle. While the sequence of maps by Fares et al. (2009), Fares et al. (2013), Donati et al. (2008) and Catala et al. (2007) indicates that the period of reversal appear to be yearly, this may not necessarily be the case. On the face of it,  $\tau$  Boötis has an approximately 720 d magnetic cycle, which is mostly, but not completely, an analogue of a solar-like cycle. Our results from 2015 March–May show that the timing of the observational epochs for  $\tau$  Boötis may in fact disguise a much faster cycle, such as the 240 d period found by Fares et al. (2013).

Fig. 14 presents the magnetic field configuration information from Tables 6 and 7, also showing the location of the approximate

date of the magnetic polarity reversal. The rapid change in the activity during 2015 March–May would seem to suggest that the magnetic activity cycle is coincident with the chromospheric activity cycle of  $\tau$  Boötis. Were reversals coincident with the peak of the chromospheric activity cycle, the similarity of the 2013–2015 January results would appear to be more related to the similarity their position in the chromospheric cycle more than any intrinsic variation between reversals. Fig. 13 also shows that the decrease in peak fractional latitude (interpreted as solar-like behaviour above) is reversed in the 2015 March–May epoch. This is perhaps due to the strengthening of the polar features in conjunction with the overall magnetic field (Fig. 15), and it would be interesting to see if the peak fractional latitude began to decrease as the chromospheric cycle continued.

Examining previous published results, no reversal between 2008 January and June would appear to settle the matter of a yearly reversal. However, given the large gap in observations between regular observations in 2008 and 2013 and the fact that three times the observational period is not exactly a year, the approximate time of the reversal may have drifted. It is possible two reversals may have occurred in the period between 2008 January and June. Further spectropolarimetric observations of  $\tau$  Boötis during each of the three  $\sim 117$  d chromospheric cycles would be required to confirm the periodicity of the polarity reversal. If the reversals are confirmed to be on a yearly basis, then a mechanism whereby the 3:1 relationship between chromospheric activity and magnetic activity would need to be posited. Magnetohydrodynamic simulations of dynamo and

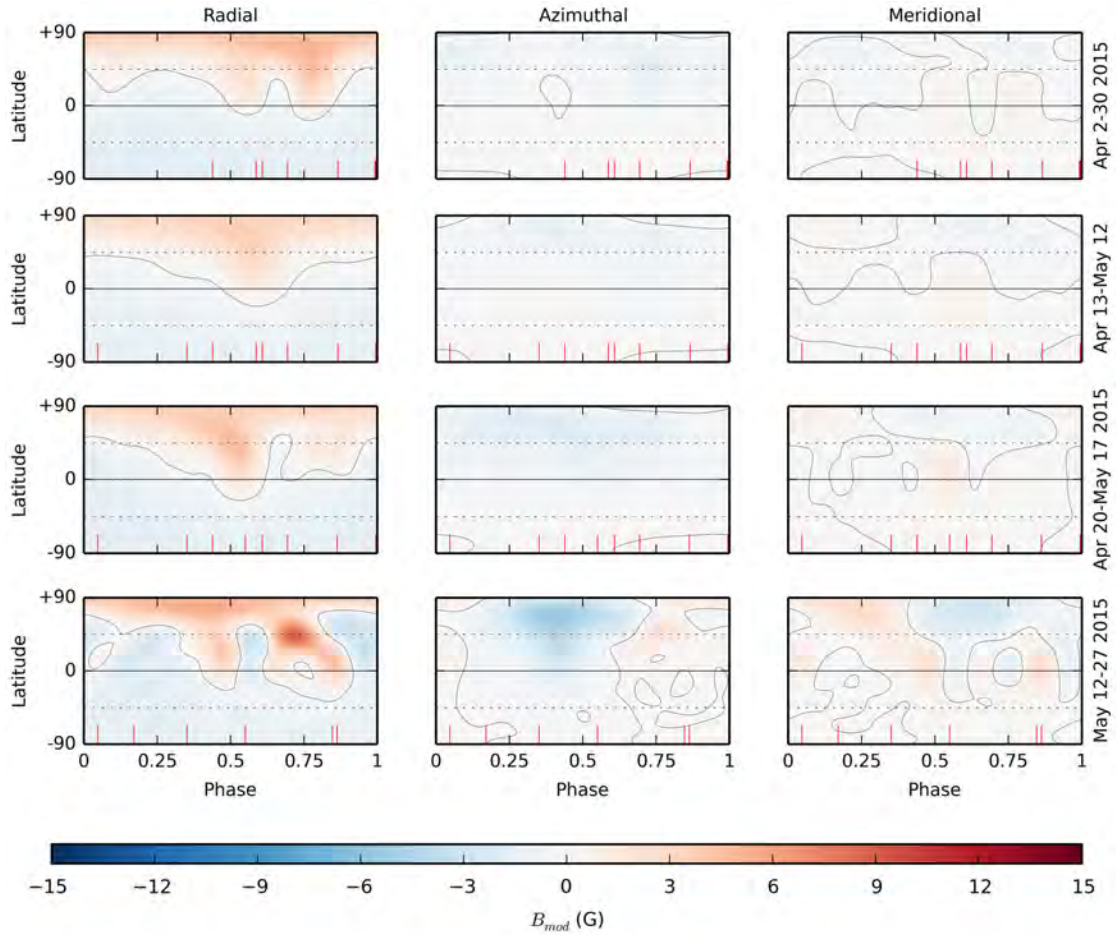


**Figure 10.** Magnetic topology of  $\tau$  Boötis reconstructed from profiles in Fig. 9(a)–(d). The radial, azimuthal and meridional components of the field (with magnetic field strength labelled in G) are depicted. The contour line indicates where  $B_{\text{mod}}$  is zero. The red ticks along the lower x-axes indicate the observational phases for each epoch.

convective processes in F-type stars by Augustson, Brun & Toomre (2013) shows magnetic energy rising and falling regularly with a magnetic reversal occurring on the third such magnetic cycle, thus potentially providing such a mechanism.

Our conclusions about the behaviour of  $\tau$  Boötis should not be significantly altered were the reversal shown to be shorter. As our 2015 March–May observations show, the broad solar-like behaviour of the magnetic field of  $\tau$  Boötis should still be present, simply on a shorter time-scale.

Irrespective of future work on determining the reversal cycle, an observational campaign such as 2015 March–May which spanned the maximum of the chromospheric activity would be very interesting, especially during the period of the magnetic reversal. This would provide insights into the evolution of the magnetic field leading up to, during and following a reversal.

Borsa et al. (2015) performed observations of  $\tau$  Boötis in 2013 April and May which were coincident with the 2013 April and

May epoch presented in this work. Unfortunately, while they observe a plage at high latitude near  $\phi_{\text{rot}} \approx 0.1$ , our observations did not provide any coverage centred on that phase. However, we do see a strong polar/high latitude magnetic feature covering  $\phi_{\text{rot}} \approx 0.85$ – $0.0$ . Given the lack of phase-coincident observations, we cannot confirm or rule out a bright spot observed by Borsa et al. (2015).

While casual observation of the maps we present in this work seem to consistently show a feature present near  $\phi_{\text{rot}} \approx 0.8$ , potentially coincident with the bright spot posited by Walker et al. (2008), analysis of all of the data does not reliably show a persistent active longitude. However, not every data set has coverage of this phase, and those that do may only have one or two observations over several rotations. Thus, we can neither rule out nor confirm if there are magnetic features potentially induced by SPI or other means.

In summary,  $\tau$  Boötis is a prime candidate for further investigation. It exhibits a complex interplay of chromospheric and

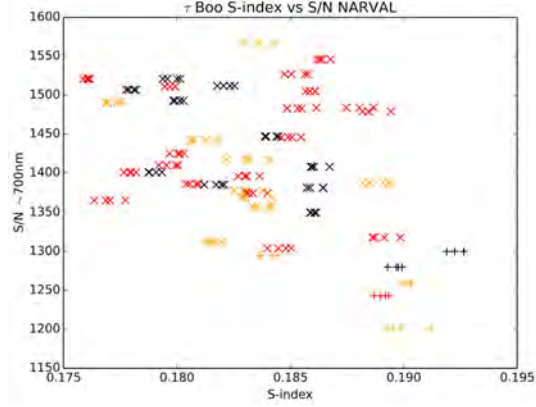


**Figure 11.** Signal to noise measured at  $\sim 700$  nm in the Stokes V spectra plotted against Ca II H&K S-indices for  $\tau$  Boötis for all NARVAL observations presented in this paper. Observations are shown as follows: red = definite detection; orange = marginal detection; black = no detection. Marker shapes represent S/N near  $\sim 700$  nm in the Stokes V profile: + =  $1000 < S/N < 1300$ ; x =  $S/N > 1300$ . There is only one marginal detection below  $S/N \approx 1100$ ; all others are non-detections. These observations are excluded for clarity.

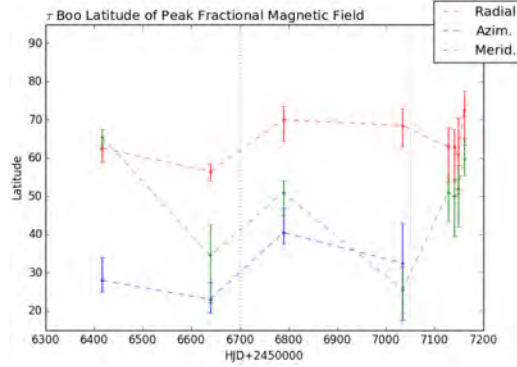


**Figure 13.** Latitude of peak fractional magnetic field components for epochs 2013 April and May–2015 January with variation bars from Fig. 12 and for the 2015 March–May epoch. The black dotted lines indicate a radial field reversal has taken place. Azimuthal field is not included for the 2015 March–May epoch for clarity as the small amount of azimuthal field is spread across a wide area, making the variation bars extremely large.

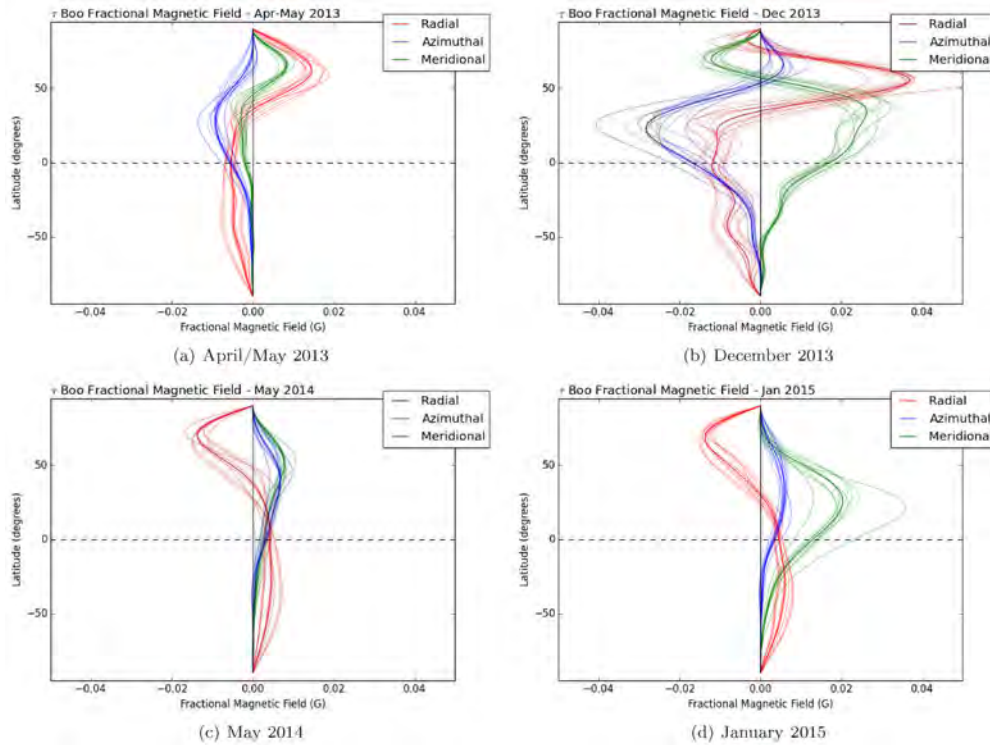


**Figure 12.** Fractional magnetic field by latitude for (a) 2013 April/May, (b) 2013 December, (c) 2014 May, and (d) 2015 January. The radial component is shown in red, azimuthal component in blue, and meridional component in green. Solid dark lines represent the result using the parameters used for mapping (inclination  $45^\circ$ ,  $v \sin i 15.9 \text{ km s}^{-1}$ ). Shaded areas represent varying inclination  $\pm 10^\circ$  and  $v \sin i \pm 1 \text{ km s}^{-1}$ . The reversal in the radial field is evident between 2013 December and 2014. The peak intensity of the field components occur at slightly lower latitudes as the reversal approaches, then revert to higher latitudes after the reversal. It is noted that the above plots assume an annual magnetic field reversal (see further discussion in Section 5).

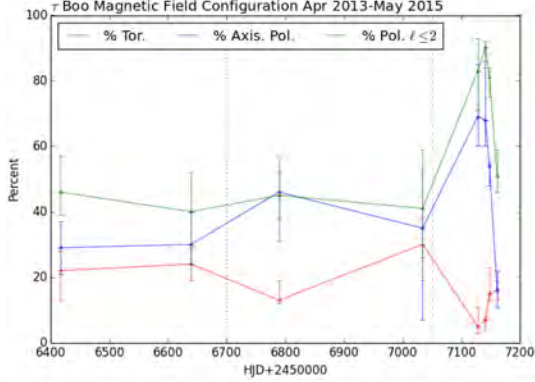


**Figure 14.** Plot of magnetic field topology from Tables 6 and 7. The black dotted lines indicate approximately where a radial field reversal has taken place. The rapid evolution of the measured field components after HJD 2457100 (2015 March–May) is coincident with the chromospheric cycle and suggests the magnetic cycle may be more rapid than the  $\sim 720$  d cycle previously assumed.

magnetic cycles. Whether the hot Jupiter orbiting the star is affecting these cycles is inconclusive, however, further observations may be able to provide more compelling information in the future.

#### ACKNOWLEDGEMENTS

This work was based on observations obtained with HARPSpol (project ID 087.D-0771) at the ESO 3.6-m telescope at La Silla and with NARVAL at the TBL. TBL/NARVAL are operated by

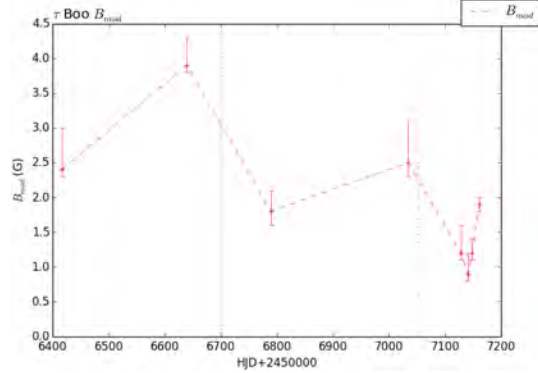


**Figure 15.** Plot of mean magnetic field strength ( $B_{\text{mod}}$ ) from Tables 6 and 7. The black dotted lines indicate approximately where a radial field reversal has taken place.

INSU/CNRS. Previous spectropolarimetric observations of  $\tau$  Boötis were obtained from the Polarbase repository of EsPaDONs and NARVAL observations. In particular, we thank the BCool Collaboration for providing time in their long-term program for ongoing observations of  $\tau$  Boötis.

SVJ acknowledges research funding by the Deutsche Forschungsgemeinschaft (DFG) under grant SFB 963/1, project A16. CPF is supported by the grant ANR 2011 Blanc SIMI5-6 020 01 ‘Toupies: Towards understanding the spin evolution of stars’.

The Strategic Research Funding for the Starwinds project provided by the University of Southern Queensland provides resources to the Astrophysics group within the Computational Engineering

**Table 6.** Summary of magnetic topology evolution of  $\tau$  Boötis 2011–2015. The columns indicated mean magnetic field  $B$ , percentage of magnetic energy in the toroidal component, percentage of the energy contained in the axisymmetric modes of the poloidal component (modes with  $m = 0$ ) and percentage of the energy contained in the modes of  $\ell \leq 2$  of the poloidal component. Variations are based on systematic recalculation based upon varying stellar parameters ( $\Omega_{\text{eq}}$ ,  $d\Omega$ , inclination,  $\sin i$ ) as described in Appendix A.

Epoch	$B$ (G)	per cent toroidal	per cent axisymm. poloidal	per cent $\ell \leq 2$ in poloidal
2011 May	$2.5^{+0.4}_{-0.1}$	$20^{+11}_{-5}$	$19^{+14}_{-6}$	$26^{+17}_{-7}$
2013 April/May	$2.4^{+0.6}_{-0.1}$	$22^{+6}_{-9}$	$29^{+8}_{-8}$	$46^{+11}_{-7}$
2013 December	$3.9^{+0.4}_{-0.1}$	$24^{+6}_{-5}$	$30^{+10}_{-6}$	$40^{+12}_{-11}$
2014 May	$1.8^{+0.3}_{-0.2}$	$13^{+6}_{-1}$	$46^{+6}_{-8}$	$45^{+12}_{-14}$
2015 January	$2.5^{+0.6}_{-0.2}$	$30^{+8}_{-4}$	$35^{+17}_{-28}$	$41^{+18}_{-22}$
2015 March	see Table 7			

**Table 7.** Summary of magnetic topology evolution of  $\tau$  Boötis for the four maps 2014 March–May. The columns indicated mean magnetic field  $B$ , percentage of magnetic energy in the toroidal component, percentage of the energy contained in the axisymmetric modes of the poloidal component (modes with  $m = 0$ ) and percentage of the energy contained in the modes of  $\ell \leq 2$  of the poloidal component. Variations are based on the systematic recalculation based upon varying stellar parameters ( $\Omega_{\text{eq}}$ ,  $d\Omega$ , inclination,  $\sin i$ ) as described in Appendix A.

Epoch	$B$ (G)	per cent toroidal	per cent axisymm. poloidal	per cent $\ell \leq 2$ in poloidal
2015 April 02–30	$1.2^{+0.4}_{-0.1}$	$5^{+6}_{-2}$	$69^{+16}_{-9}$	$83^{+10}_{-12}$
2015 April 13–May 12	$0.9^{+0.3}_{-0.1}$	$7^{+1}_{-3}$	$68^{+18}_{-8}$	$90^{+2}_{-6}$
2015 April 20–May 17	$1.2^{+0.2}_{-0.1}$	$15^{+8}_{-2}$	$54^{+1}_{-6}$	$81^{+3}_{-6}$
2015 May 12–27	$1.9^{+0.1}_{-0.1}$	$16^{+3}_{-3}$	$16^{+6}_{-5}$	$51^{+8}_{-5}$

and Science Research Centre at USQ (MWM, SCM, BDC). MWM is supported by an Australian Postgraduate Award Scholarship.

We thank Claude Catala and Monica Rainer for their assistance in the development of the FT differential code produced by MWM for use in this paper.

Iterative calculations for differential rotation were performed using the University of Southern Queensland High Performance Computing cluster. We thank Richard Young for his assistance in utilizing the HPC resources at USQ.

This research has made use of NASA's Astrophysics Data System.

## REFERENCES

- Augustson K. C., Brun A. S., Toomre J., 2013, *ApJ*, 777, 153
- Aurière M., 2003, in Arnaud J., Meunier N., eds, *EAS Publ. Ser. Vol. 9, Magnetism and Activity of the Sun and Stars*. Cambridge Univ. Press, Cambridge, p. 105
- Baliunas S. L., Henry G. W., Donahue R. A., Fekel F. C., Soon W. H., 1997, *ApJ*, 474, L119
- Baliunas S. L., Donahue R. A., Soon W. H., Henry G. W., 1998, in Donahue R. A., Bookbinder J. A., eds, *ASP Conf. Ser. Vol. 154, Cool Stars, Stellar Systems and the Sun*. Astron. Soc. Pac., San Francisco, p. 153
- Borsa F. et al., 2015, *A&A*, 578, 64
- Broggi M., Snellen I. A. G., de Kok R. J., Albrecht S., Birkby J., de Mooij E. J. W., 2012, *Nature*, 486, 502
- Butler R. P., Marcy G., Williams E., Hauser H., Shirts P., 1997, *ApJ*, 474, L115
- Catala C., Donati J.-F., Shkolnik E., Bohlender D., Alecian E., 2007, *MNRAS*, 374, L42
- Donati J.-F., 2003, in Trujillo-Beuno J., Almeida J. S., eds, *ASP Conf. Ser. Vol. 307, Solar Polarization 3*. Astron. Soc. Pac., San Francisco, p. 41
- Donati J.-F., Semel M., Carter B. D., Rees D. E., Collier Cameron A., 1997, *MNRAS*, 291, 658
- Donati J.-F., Mengel M., Carter B. D., Marsden S., Collier Cameron A., Wichmann R., 2000, *MNRAS*, 316, 699
- Donati J.-F., Cameron A., Petit P., 2003, *MNRAS*, 345, 1187
- Donati J.-F. et al., 2006, *MNRAS*, 370, 629
- Donati J.-F. et al., 2008, *MNRAS*, 385, 1179
- Fares R. et al., 2009, *MNRAS*, 398, 1383
- Fares R. et al., 2012, *MNRAS*, 423, 1006
- Fares R., Moutou C., Donati J.-F., Catala C., Shkolnik E. L., Jardine M. M., Cameron A. C., Deleuil M., 2013, *MNRAS*, 435, 1451
- Henry G. W., Baliunas S. L., Donahue R. A., Fekel F. C., Soon W., 2000, *ApJ*, 531, 415
- Jeffers S. V., Donati J.-F., 2008, *MNRAS*, 390, 635
- Jeffers S. V., Donati J.-F., Alecian E., Marsden S. C., 2011, *MNRAS*, 411, 1301
- Lanza A. F., 2012, *A&A*, 544, AA23
- Leigh C., Cameron A., Horne K., Penny A., James D., 2003, *MNRAS*, 344, 1271
- Marsden S., Donati J.-F., Semel M., Petit P., Carter B., 2006, *MNRAS*, 370, 468
- Marsden S. C. et al., 2014, *MNRAS*, 444, 3517
- Mayor M. et al., 2003, *The Messenger*, 114, 20
- Morgenthaler A. et al., 2012, *A&A*, 540, A138
- Morin J. et al., 2008, *MNRAS*, 384, 77
- Morin J., Donati J.-F., Petit P., Delfosse X., Forveille T., Jardine M. M., 2010, *MNRAS*, 407, 2269
- Nicholson B. A. et al., 2016, *MNRAS*, 459, 1907
- Petit P., Donati J.-F., Collier-Cameron A., 2002, *MNRAS*, 334, 374
- Petit P., Louge T., Théado S., Paletou F., Manset N., Morin J., Marsden S. C., Jeffers S. V., 2014, *PASP*, 126, 469
- Piskunov N. et al., 2011, *The Messenger*, 143, 7
- Reiners A., 2006, *A&A*, 446, 267
- Reiners A., Schmitt J. H. M. M., 2003, *A&A*, 398, 647
- Rodler F., Lopez-Morales M., Ribas I., 2012, *ApJ*, 753, L25
- Semel M., Donati J.-F., Rees D. E., 1993, *A&A*, 278, 231
- Shkolnik E., Bohlender D. A., Walker G. A. H., Collier Cameron A., 2008, *ApJ*, 676, 628
- Vidotto A. A., Fares R., Jardine M., Donati J.-F., Opher M., Moutou C., Catala C., Gombosi T. I., 2012, *MNRAS*, 423, 3285
- Walker G. A. H. et al., 2008, *A&A*, 482, 691
- Wright J. T., Marcy G. W., Butler R. P., Vogt S. S., 2004, *ApJS*, 152, 261

## APPENDIX A: DERIVING VARIATION MEASUREMENTS FOR MAGNETIC FIELD CONFIGURATION

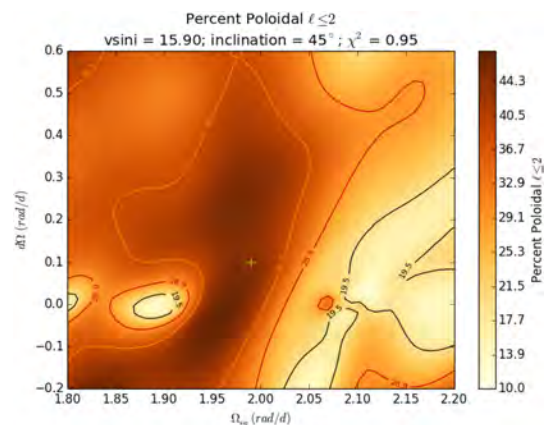
As the energy in the spherical harmonics produced by the ZDI mapping process provide exact values for a given set of modes, a measure of variability of the field configuration values (Tables 6 and 7), due to the uncertainties in the stellar parameters, is desirable. We achieve this by varying the stellar parameters, re-running the mapping process and extracting the various parameters. As variation in  $v \sin i$  and stellar inclination are used in determining the variation of the differential rotation parameters ( $\Omega_{\text{eq}}$ ,  $d\Omega$ ) (see Fig. 3b), we hold each pair of parameters ( $v \sin i$ , inclination) and ( $\Omega_{\text{eq}}$ ,  $d\Omega$ ) constant while varying the others. Otherwise, we generate extreme variations where all parameters are varied to extremes.

Fig. A1 shows a plot of the percentage of poloidal field modes  $\ell \leq 2$  from the 2014 May data set where we vary ( $\Omega_{\text{eq}}$ ,  $d\Omega$ ), holding ( $v \sin i$ , inclination) constant. Taking the  $\sim 1\sigma$  variation in ( $\Omega_{\text{eq}}$ ,  $d\Omega$ ) from the measured value (shown as a yellow cross in Fig. A1; Tables 3 and 5 show variations used) gives us an indication of how the differential rotation measurement affects this field component.

Fig. A2 similarly shows the effect on the measured field component of varying  $v \sin i$  and inclination angle while holding the DR parameters steady at the measured values.

From these measurements, we take the extreme variations from both methods to provide the variations shown in Tables 6 and 7.

It is clear that the dominant parameter for variation of poloidal axisymmetry and dipolar/quadrupolar components is the stellar inclination angle we choose. This is as expected, as errors in the assumed inclination of the star's rotational axis will affect



**Figure A1.** Plot of percentage of poloidal modes  $\ell \leq 2$  varying  $\Omega_{\text{eq}}$  and  $d\Omega$  for the 2014 May data set, using the values of  $v \sin i = 15 \text{ km s}^{-1}$  and inclination of  $45^\circ$ . The yellow cross indicates the measured differential rotation.

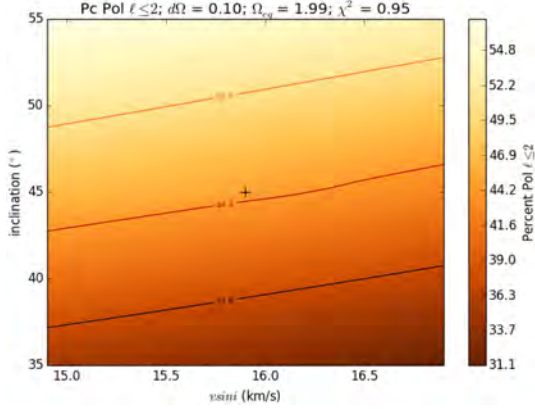


**Figure A2.** Plot of percentage of poloidal modes  $\ell \leq 2$  varying  $v \sin i$  and angle of inclination for the 2014 May data set, using the measured values for differential rotation. The black cross indicates the  $v \sin i$  and inclination chosen for the nominal reconstruction via  $\chi^2$  minimization described in Section 4.

axisymmetry and latitudes of features. As we use a large variation in inclination ( $\pm 10^\circ$ ), our derived variations in these values are systematically larger than those in the percentage of toroidal field and  $B_{\text{mod}}$ .

Extreme changes in  $\Omega_{\text{eq}}$  are significant, but usually, this value is relatively well constrained. Extreme variation in  $d\Omega$  can have an effect on the variation in the toroidal field component, but only if the variation is very large. If variation of  $d\Omega$  is not significantly greater than the  $\sim 1\sigma$  variation in measured value,  $d\Omega$  appears not to have a large effect on the field configuration parameters we derive.

In conclusion, we believe the field configuration parameters we derive are robust and stable, assuming the methodology we use is internally consistent using the derived parameters for  $v \sin i$ , inclination and differential rotation.

## APPENDIX B: JOURNALS OF OBSERVATIONS

**Table B1.** Journal of HARPSpol observations of  $\tau$  Boötis. Columns list the UT date, instrument used, the heliocentric Julian date (at mid-point of the series of four subexposures), the UT time (at mid-point of the series of four subexposures), the exposure time, the peak signal-to-noise ratio (SNR) of each observation (around 583 nm for HARPSpol observations), the rotational cycle from the ephemeris (from equation 1), the rotational phase (0.0 being approximately the centre of the observing run), the radial velocity (RV) associated with each exposure, and whether a magnetic signature is detected (D;  $fap < 10^{-5}$ ), marginally detected (M;  $10^{-3} > fap > 10^{-5}$ ) or is below the detection threshold (N).

Date	Instrument	HJD (245 5000+)	UT (h:m:s)	$T_{\text{exp}}$ (s)	SNR	Cycle	$\phi_{\text{rot}}$	RV ( $\text{km s}^{-1}$ )	Detection
2011-May-15	HARPSpol	696.57356	01:39:37	4 × 600	1081	677.921	−1.079	−16.613	N
2011-May-15	HARPSpol	696.65020	03:29:59	4 × 600	1101	677.945	−1.056	−16.544	N
2011-May-15	HARPSpol	696.72435	05:16:46	4 × 600	1025	677.967	−1.033	−16.483	N
2011-May-16	HARPSpol	697.57360	01:39:44	4 × 600	1074	678.223	−0.777	−15.919	M
2011-May-16	HARPSpol	697.64667	03:24:57	4 × 600	1149	678.245	−0.755	−15.909	N
2011-May-16	HARPSpol	697.72308	05:14:59	4 × 600	1117	678.268	−0.732	−15.914	N
2011-May-17	HARPSpol	698.55641	01:15:01	4 × 600	1052	678.520	−0.480	−16.455	M
2011-May-17	HARPSpol	698.63125	03:02:48	4 × 600	1065	678.543	−0.457	−16.520	N
2011-May-17	HARPSpol	698.70306	04:46:12	4 × 600	1124	678.564	−0.436	−16.574	M
2011-May-17	HARPSpol	699.50424	23:59:57	4 × 600	838	678.806	−0.194	−16.815	N
2011-May-18	HARPSpol	699.57741	01:45:19	4 × 600	1029	678.828	−0.172	−16.792	N
2011-May-18	HARPSpol	699.65246	03:33:24	4 × 600	1069	678.851	−0.149	−16.777	D
2011-May-19	HARPSpol	700.53841	00:49:12	4 × 600	970	679.118	0.118	−16.052	N
2011-May-19	HARPSpol	700.61374	02:37:41	4 × 600	964	679.141	0.141	−15.999	N
2011-May-19	HARPSpol	700.68619	04:22:01	4 × 600	998	679.163	0.163	−15.968	N
2011-May-20	HARPSpol	701.56019	01:20:38	4 × 600	778	679.427	0.427	−16.183	N
2011-May-20	HARPSpol	701.67331	04:03:32	4 × 600	874	679.461	0.461	−16.279	N
2011-May-20	HARPSpol	701.70345	04:46:56	4 × 600	597	679.470	0.470	−16.299	N

**Table B2.** Journal of NARVAL observations up to and including 2015 January of  $\tau$  Boötis. Columns list the UT date, instrument used, the heliocentric Julian date (at mid-point of the series of four subexposures), the UT time (at mid-point of the series of four subexposures), the exposure time, the peak signal-to-noise ratio (SNR) of each observation (at around 700 nm for NARVAL), the rotational cycle from the ephemeris (from equation 1), the rotational phase (0.0 being approximately the centre of the observing run), the radial velocity (RV) associated with each exposure, and whether a magnetic signature is detected (D;  $fap < 10^{-5}$ ), marginally detected (M;  $10^{-3} > fap > 10^{-5}$ ) or is below the detection threshold (N).

Date	Instrument	HJD (245 5000+)	UT (h:m:s)	$T_{\text{exp}}$ (s)	SNR	Cycle	$\phi_{\text{rot}}$	RV ( $\text{km s}^{-1}$ )	Detection
2013-April-23	NARVAL	1405.57009	01:33:59	4 × 600	1493	891.961	-3.040	-16.727	N
2013-April-24	NARVAL	1406.53353	00:41:21	4 × 600	1365	892.251	-2.749	-16.124	D
2013-April-24	NARVAL	1407.41519	21:50:57	4 × 600	1521	892.518	-2.483	-16.631	N
2013-May-04	NARVAL	1417.46698	23:05:45	4 × 600	1491	895.552	0.552	-16.773	M
2013-May-05	NARVAL	1418.44661	22:36:27	4 × 600	1410	895.848	0.848	-16.938	D
2013-May-11	NARVAL	1424.42736	22:08:58	4 × 600	1507	897.653	2.653	-16.998	N
2013-May-12	NARVAL	1425.42272	22:02:19	4 × 600	1401	897.954	2.954	-16.669	D
2013-May-13	NARVAL	1426.44343	22:32:11	4 × 600	1521	898.262	3.262	-16.095	D
2013-December-04	NARVAL	1630.73709	05:46:20	4 × 600	1408	959.936	-3.064	-16.822	N
2013-December-05	NARVAL	1631.72401	05:27:25	4 × 600	1318	960.234	-2.766	-16.164	D
2013-December-06	NARVAL	1632.73127	05:37:48	4 × 600	1280	960.538	-2.462	-16.735	N
2013-December-07	NARVAL	1633.71947	05:20:42	4 × 600	1202	960.837	-2.164	-16.993	M
2013-December-08	NARVAL	1634.71910	05:20:05	4 × 600	1484	961.138	-1.862	-16.268	D
2013-December-09	NARVAL	1635.74031	05:50:32	4 × 600	1479	961.447	-1.553	-16.444	D
2013-December-11	NARVAL	1637.72461	05:27:44	4 × 600	1259	962.046	-0.954	-16.520	M
2013-December-12	NARVAL	1638.71993	05:20:54	4 × 600	1546	962.346	-0.654	-16.257	D
2013-December-13	NARVAL	1639.73536	05:43:02	4 × 600	1505	962.653	-0.347	-17.022	D
2013-December-15	NARVAL	1641.72308	05:25:09	4 × 600	1381	963.253	0.253	-16.116	N
2013-December-17	NARVAL	1643.75082	06:04:53	4 × 600	1483	963.865	0.865	-16.923	D
2013-December-21	NARVAL	1647.73550	05:42:25	4 × 600	1447	965.068	2.068	-16.403	N
2014-May-04	NARVAL	1782.47281	23:14:08	4 × 600	1304	1005.744	-2.256	-17.089	D
2014-May-05	NARVAL	1783.47546	23:17:58	4 × 600	1350	1006.046	-1.954	-16.397	N
2014-May-07	NARVAL	1785.46095	22:57:09	4 × 600	1079	1006.646	-1.354	-16.945	M
2014-May-08	NARVAL	1786.49026	23:39:24	4 × 600	1377	1006.957	-1.044	-16.668	M
2014-May-09	NARVAL	1787.48744	23:35:22	4 × 600	1374	1007.258	-0.742	-16.094	D
2014-May-14	NARVAL	1791.54389	00:56:51	4 × 600	1512	1008.482	0.482	-16.563	N
2014-May-14	NARVAL	1792.43744	22:23:36	4 × 600	954	1008.752	0.752	-17.089	N
2014-May-15	NARVAL	1793.48608	23:33:42	4 × 600	940	1009.069	1.069	-16.438	N
2014-May-16	NARVAL	1794.46699	23:06:15	4 × 600	892	1009.365	1.365	-16.345	N
2014-May-17	NARVAL	1795.47600	23:19:17	4 × 600	1312	1009.669	1.669	-17.048	M
2014-May-18	NARVAL	1796.45889	22:54:42	4 × 600	1295	1009.966	1.966	-16.671	M
2015-January-06	NARVAL	2028.73834	05:44:44	4 × 600	1511	1080.089	-1.911	-16.355	D
2015-January-07	NARVAL	2029.72424	05:24:19	4 × 520	1386	1080.387	-1.614	-16.372	D
2015-January-08	NARVAL	2030.74613	05:55:43	4 × 520	1401	1080.695	-1.305	-17.149	N
2015-January-09	NARVAL	2031.72258	05:21:41	4 × 600	1396	1080.990	-1.010	-16.673	D
2015-January-10	NARVAL	2032.73855	05:44:33	4 × 520	1442	1081.297	-0.704	-16.207	M
2015-January-12	NARVAL	2034.73935	05:45:29	4 × 520	1425	1081.901	-0.100	-16.988	D
2015-January-18	NARVAL	2040.67474	04:11:43	4 × 600	707	1083.692	1.692	-17.178	N

Downloaded from <http://mnras.oxfordjournals.org/> at University of Southern Queensland on August 30, 2016

**Table B3.** Journal of NARVAL observations up to and including March through 2015 May of  $\tau$  Boötis. Columns list the UT date, instrument used, the heliocentric Julian date (at mid-point of the series of four subexposures), the UT time (at mid-point of the series of four subexposures), the exposure time, the peak signal-to-noise ratio (SNR) of each observation (at around 700 nm for NARVAL), the rotational cycle from the ephemeris (from equation 1), the radial velocity (RV) associated with each exposure, and whether a magnetic signature is detected (D;  $fap < 10^{-5}$ ), marginally detected (M;  $10^{-3} > fap > 10^{-5}$ ) or is below the detection threshold (N).

Date	Instrument	HJD (245 5000+)	UT (h:m:s)	$T_{\text{exp}}$ (s)	SNR	Cycle	RV ( $\text{km s}^{-1}$ )	Detection
2015-March-12	NARVAL	2093.60723	02:28:57	$4 \times 600$	1300	1099.672	-17.103	N
2015-March-13	NARVAL	2094.57542	01:43:04	$4 \times 600$	1387	1099.964	-16.769	M
2015-March-17	NARVAL	2098.60339	02:23:04	$4 \times 600$	1243	1101.180	-16.307	D
2015-April-02	NARVAL	2114.54024	00:51:19	$4 \times 600$	1567	1105.992	-16.685	M
2015-April-13	NARVAL	2126.44800	22:38:12	$4 \times 600$	1357	1109.586	-17.002	M
2015-April-14	NARVAL	2127.37286	20:49:59	$4 \times 600$	592	1109.866	-17.016	N
2015-April-20	NARVAL	2133.42700	22:07:56	$4 \times 600$	1369	1111.693	-17.159	M
2015-April-21	NARVAL	2134.42323	22:02:30	$4 \times 600$	590	1111.994	-16.650	N
2015-April-23	NARVAL	2136.45663	22:50:36	$4 \times 600$	1446	1112.608	-17.010	D
2015-April-30	NARVAL	2142.52088	00:23:13	$4 \times 600$	1385	1114.439	-16.554	N
2015-May-11	NARVAL	2154.47299	23:14:38	$4 \times 600$	992	1118.047	-16.542	N
2015-May-12	NARVAL	2155.47975	23:24:25	$4 \times 600$	1043	1118.351	-16.235	N
2015-May-16	NARVAL	2159.45312	22:46:16	$4 \times 600$	1417	1119.550	-16.848	M
2015-May-17	NARVAL	2160.48669	23:34:39	$4 \times 600$	1077	1119.862	-17.049	N
2015-May-19	NARVAL	2161.50449	00:00:21	$4 \times 700$	472	1120.170	-16.243	N
2015-May-27	NARVAL	2170.37187	20:49:57	$4 \times 600$	1527	1122.847	-17.025	D

This paper has been typeset from a  $\text{\LaTeX}$  file prepared by the author.

### 3.2 SUMMARY OF RESULTS

Mengel et al. (2016) clearly demonstrated for the first time that the magnetic field of  $\tau$  Boötis was evolving with the chromospheric activity, just like the Sun. The strength of the magnetic field decreased approaching the minimum and began to increase afterwards. Signs of topological evolution were also observed. This observation strongly suggests that  $\tau$  Boötis has a magnetic cycle.

However, the magnetic reversals were shown to be happening every 360 d or so. This observation contrasts with the chromospheric activity cycle [confirmed by Mengel et al. (2016) to be approximately 117 d, close to that reported by Baliunas et al. (1998)], which is only one-third of the time between reversals. While intriguing and potentially supported by modelling such as Augustson et al. (2013) who presents a model of a 3:1 relationship between chromospheric cycle and reversal, were the dynamo processes solar-type, one would expect a reversal period synchronised with the chromospheric cycle. A close examination of the prior epochs of observation left open the possibility that an observational bias caused by observing  $\tau$  Boötis at predominantly the same time of year resulted in any faster cycle of reversals being missed.

*Das Leben gehört den Lebenden an, und wer lebt, muss  
auf Wechsel gefasst sein.*

Johann Wolfgang von Goethe

# 4

## A Rapid Large-Scale Magnetic Cycle on $\tau$ Boötis

THE OBSERVATIONS OF  $\tau$  BOÖTIS (CHAPTER 3) at the star's activity minimum left open some intriguing questions regarding its magnetic cycle. [Mengel et al. \(2016\)](#) indicates that  $\tau$  Boötis undergoes a magnetic cycle; one that is extremely rapid compared to the Sun. [Boro Saikia et al. \(2016\)](#) published the first confirmation of a truly solar-type magnetic cycle for the star 61 Cyg A, showing that evolved solar-type dwarfs can exhibit such cycles.

As an F-type star,  $\tau$  Boötis would be unique insofar as exhibiting a stable cycle, were it indeed shown to be such. Observations taken at the chromospheric activity maximum would potentially confirm this. Also, observations at different times of the chromospheric activity cycle were needed to confirm if the cycle of polarity reversals

indeed follows the chromospheric cycle (as for the Sun and 61 Cyg A), or whether other dynamo mechanisms are at work to result in a 3:1 relationship between the cycles.

Complimenting the work presented in [Mengel et al. \(2016\)](#), observations were obtained in March 2016 and at the peak of chromospheric activity during June-July 2016, and the analysis is presented in [Mengel et al. \(2017a\)](#). Further observations were made in January and February 2017. Due to the lateness of these observations in the PhD process, these 2017 results are presented separately in Section 4.2.

#### 4.1 [MENGEL ET AL. \(2017A\)](#) “A RAPID LARGE-SCALE MAGNETIC CYCLE ON $\tau$ BOÖTIS”

The prepared manuscript [Mengel et al. \(2017a\)](#), “A rapid large-scale magnetic cycle on  $\tau$  Boötis” follows.

# A rapid large-scale magnetic cycle on $\tau$ Boötis

M. W. Mengel,<sup>1\*</sup> S.V. Jeffers,<sup>2</sup> C. Moutou,<sup>3</sup> S. C. Marsden,<sup>2</sup> R. Fares<sup>4</sup>  
and B. D. Carter<sup>2</sup>

<sup>1</sup>*Computational Engineering and Science Research Centre, University of Southern Queensland, Toowoomba, Qld, Australia*

<sup>2</sup>*Institut für Astrophysik, Georg-August-Universität Göttingen, Friedrich-Hund-Platz 1, 37077 Göttingen, Germany*

<sup>3</sup>*Laboratoire d'Astrophysique de Marseille, Traverse du Siphon, 13013 Marseille, France*

<sup>4</sup>*INAF - Osservatorio Astrofisico di Catania, Via Santa Sofia, 78, I-95123 Catania, Italy*

Accepted 2017 February 00. Received 2017 January 00; in original form 2017 January 00

## ABSTRACT

We present observations that the hot-Jupiter planet hosting star  $\tau$  Boötis exhibits an extremely rapid magnetic activity cycle coincident with its chromospheric activity cycle of  $\sim 120$  d. The large-scale radial magnetic field undergoes regular polarity reversals on this timescale, while the azimuthal component does not. The distribution of poloidal versus toroidal magnetic field shows cyclic variation correlated with chromospheric activity. This is in contrast to most stars with shallow convective envelopes which do not appear to exhibit magnetic cycles. The long-term monitoring of  $\tau$  Boötis has resulted in almost complete spectropolarimetric coverage of its chromospheric activity cycle, which gives insight into the operation of shallow convection zone dynamos.

**Key words:** line: profiles - stars: activity - stars: magnetic fields - techniques: polarimetric - planetary systems.

## 1 INTRODUCTION

It is well-known that the Sun exhibits a 22 yr magnetic cycle, coincident with its activity cycle. When at its activity minimum, the Sun's magnetic field is concentrated at polar latitudes, is symmetrical around the axis of rotation and dipolar components dominate. As the Sun's activity increases, the magnetic field migrates to lower latitudes (Hathaway 2010), and becomes less dominantly dipolar (Sanderson et al. 2003; DeRosa et al. 2012). When the solar magnetic field intensifies after an activity minimum, the polarity of the magnetic field is reversed.

The presence of magnetic cycles on other stars has been inferred by observing known proxies of magnetic activity, such as chromospheric and coronal activity. However, the presence of cyclic activity in these proxies can only show that magnetic field is varying with some regularity; they cannot provide information on the topology or strength of the magnetic field. Zeeman Doppler Imaging (Semel 1989; Donati et al. 1997) can provide information about the geometry of the large-scale magnetic field, allowing for the investigation of any cyclic behaviour of the field's intensity, polarity and geometry.

Using Zeeman Doppler Imaging of the K5 dwarf 61 Cyg A over many epochs spanning 8 yr, for the first time Boro Saikia et al. (2016) were able to demonstrate a star other than the Sun exhibit-

ing a solar-type magnetic cycle in phase with its chromospheric and coronal activity cycles. The study of the K5 dwarf 61 Cyg A revealed that the star exhibits polarity reversals near its activity minima. It also shows a simple dipolar field at the activity minima, becoming more complex as the activity increases towards a maximum.

More generally, long-term Zeeman Doppler Imaging studies of cool stars have revealed rapid variations in large-scale magnetic field topology (Morgenthaler et al. 2012; Jeffers et al. 2014; Boro Saikia et al. 2015), and a few examples of apparently regular polarity reversals (Petit et al. 2009; Morgenthaler et al. 2011; Donati et al. 2008). However, at this stage, only 61 Cyg A is the only star other than the Sun for which we observe a regular cycle which is coincident with the cyclic behaviour of the other activity proxies.

### 1.1 $\tau$ Boötis

$\tau$  Boötis (HR 5185, HD 120136, F7V, age  $\sim 1$  Gyr; list of stellar parameters given in Table 1) hosts a hot Jupiter with a mass of  $\sim 6M_{\text{Jupiter}}$  (Brogi et al. 2012; Rodler et al. 2012; Borsa et al. 2015). As this massive planet orbits its host at a distance of only 0.049 AU in approximately 3.31 days (Butler et al. 1997; Leigh et al. 2003; Borsa et al. 2015), and given that  $\tau$  Boötis has a detectable magnetic field, the system has been of particular interest for those searching for star-planet interactions (SPI). While searches for such SPI has not been fruitful (for example Hallinan

\* E-mail: matthew.mengel@usq.edu.au (MWM)

**Table 1.** Table of stellar parameters for  $\tau$  Boötis. (References: 1 = Borsari et al. (2015); 2 = Brogi et al. (2012))

Parameter		Value	Reference
$T_{\text{eff}}$	(K)	$6399 \pm 45$	1
$\log g$	( $\text{cm s}^{-1}$ )	$4.27 \pm 0.06$	1
[Fe/H]		$0.26 \pm 0.03$	1
$v \sin i$	( $\text{km s}^{-1}$ )	$14.27 \pm 0.06$	1
Luminosity	( $L_{\odot}$ )	$3.06 \pm 0.16$	1
Mass	( $M_{\odot}$ )	$1.39 \pm 0.25$	1
Radius	( $R_{\odot}$ )	$1.42 \pm 0.08$	1
Age	(Gyr)	$0.9 \pm 0.5$	1
Inclination	( $^{\circ}$ )	$44.5 \pm 1.5$	2

et al. (2013) amongst others),  $\tau$  Boötis has been regularly observed with spectropolarimetric techniques since 2007.

Analyses by Catala et al. (2007), Donati et al. (2008), Fares et al. (2009, 2013) and Mengel et al. (2016) have produced over 20 Zeeman Doppler Maps of  $\tau$  Boötis and characterisations of the magnetic topology for each of these observational epochs. The radial field component of  $\tau$  Boötis has been shown to regularly reverse polarity, with an estimated cycle length of  $\sim 2$  yr. However, in addition to the 2 yr cycle, Fares et al. (2009, 2013) suggested that a cycle of  $\sim 240$  d may also exist. Further, in the Mt Wilson survey of Ca II H&K measurements (Duncan et al. 1991; Baliunas et al. 1998), a known proxy for chromospheric activity, Baliunas et al. (1997) and Henry et al. (2000) report a cycle corresponding to a  $\sim 116$  d period for  $\tau$  Boötis. This would be close to a  $\sim 240$  d magnetic cycle, were the behaviour of reversals similar to that of the Sun.

The fact that  $\tau$  Boötis exhibits a regular cycle of any kind is unusual for stars with shallow convective zones (Marsden et al. 2006; Jeffers & Donati 2008; Jeffers et al. 2011). Fares & Donati (2009) speculated whether the presence of the hot Jupiter may play a part in maintaining or accelerating a magnetic cycle on  $\tau$  Boötis.

While Mengel et al. (2016) once again confirmed the periodic reversals, it was also shown that at the chromospheric activity minimum, the magnetic field intensity seemed to drop, and the toroidal component of the field was extremely low compared to measurements at other epochs. The relative amount of toroidal field appeared to increase immediately after the minimum. Based on these results, Mengel et al. (2016) speculated that while the posited 360 d:120 d relationship between the magnetic reversal half-cycle and the chromospheric cycle observed by previous work seemed confirmed, the the majority of observations were taken at times in the chromospheric activity cycle which would produce an observational bias precluding a 1:1 correspondance between the cycles.

Recent work by Schmitt & Mittag (2017), examining chromospheric and coronal activity, also suggests a cyclic behaviour of the chromospheric activity with a period of 120 d. The coronal emission variations also follow such a trend. In this work, using spectropolarimetry, we seek to investigate whether the large-scale magnetic field of  $\tau$  Boötis reverses at a faster rate, coincident with the chromospheric activity cycle. To this end, two epochs of observation were selected, on either side of where a reversal would take place with a rapid cycle. The nature of the geometry changes of the large-scale magnetic field as the chromospheric activity changes was also analysed to see if there were characteristics of a magnetic cycle such as 61 Cyg A present.

In section 3, the chromospheric activity cycle of  $\tau$  Boötis is examined using the Ca II H&K proxy. In section 4, the longitudinal magnetic field of the star and its relationship to the chromospheric activity cycle are examined. Zeeman Doppler Imaging of the large-

scale magnetic field is presented in section 5. The results of analysis of the magnetic field geometry is discussed in section 6, and finally, we summarise our conclusions in section 7.

## 2 OBSERVATIONS AND DATA PROCESSING

### 2.1 Instrument and Observational Procedure

Spectropolarimetric observations of  $\tau$  Boötis were obtained using the NARVAL and ESPaDOnS high-resolution spectropolarimeters. ESPaDOnS is used at the Canada-France-Hawaii Telescope located at the Mauna Kea Observatory, while NARVAL is attached to the T lescope Bernard Lyot, located the the Observatoire du Pic du Midi. ESPaDOnS and NARVAL are twin instruments, each consisting of a bench mounted high-resolution spectrograph, and an associated Cassegrain mounted polarimetry module. Both spectrographs have an optical wavelength coverage of 370 to 1000 nm, and a resolution of  $\sim 65000$  with a pixel size of  $2.6 \text{ km s}^{-1}$ .

Utilising a series of three Fresnel rhombs, the polarimetric modules perform polarimetry over the entire spectral range. Using a Wollaston prism, the light is then split into two beams containing opposite polarisation states which are fed via individual fibres to the spectrograph. This allows the simultaneous capture of both polarisation states and further allowing the unpolarised Stokes  $I$  and circularly-polarised Stokes  $V$  spectra to be determined from each observation.

Each Stokes  $V$  observation consists of a sequence of four individual exposures, resulting in eight individual spectra; four left-hand and four right-hand circularly polarised. As described by Petit et al. (2003), the polarisation states in the fibre pair described above are alternated during the sequence to help eliminate instrumental effects. Adding all eight spectra produces the unpolarised Stokes  $I$  (intensity) spectrum. The polarised Stokes  $V$  spectrum is computed using the equations of Donati et al. (1997, Eqs. 1, 2):

$$\frac{V}{I} = \frac{R_V - 1}{R_V + 1} \quad (1)$$

where

$$R_V^A = \frac{i_{1,\perp}/i_{1,\parallel} \quad i_{4,\perp}/i_{4,\parallel}}{i_{2,\perp}/i_{2,\parallel} \quad i_{3,\perp}/i_{3,\parallel}} \quad (2)$$

and  $i_{k,\perp}$  and  $i_{k,\parallel}$  are the two polarised spectra in each exposure,  $k$ .

By destructively adding the spectra, a null polarisation spectrum,  $N$ , can be obtained (Donati et al. 1997, Eqs. 1, 3):

$$\frac{N}{I} = \frac{R_N - 1}{R_N + 1} \quad (3)$$

where

$$R_N^A = \frac{i_{1,\perp}/i_{1,\parallel} \quad i_{2,\perp}/i_{2,\parallel}}{i_{4,\perp}/i_{4,\parallel} \quad i_{3,\perp}/i_{3,\parallel}} \quad (4)$$

### 2.2 Spectropolarimetric Observations

Observations of  $\tau$  Boötis were obtained in March 2016, to determine whether the polarity of the global dipolar field was as expected, and these were carried out using NARVAL at TBL. Subsequently, regular observations were taken utilising NARVAL at TBL

beginning approximately 75 d later, coincident with the next maximum in chromospheric activity, from early June 2016 until mid-July 2016. The journal of observations for NARVAL is shown in Table A1.

Serendipitously, observations of  $\tau$  Boötis were taken using ESPaDOnS at CFHT from June 9 until June 24 2016 which covered a gap in the TBL observation. The journal of observations for ESPaDOnS is shown in Table A2. Thus coverage of  $\tau$  Boötis spanning approximately fifteen stellar rotations through the chromospheric activity maximum was obtained.

The phases of the data are derived using the same orbital ephemeris as that used by Catala et al. (2007), Donati et al. (2008), Fares et al. (2009, 2013) and Mengel et al. (2016):

$$T_0 = \text{HJD } 2453450.984 + 3.31245E \quad (5)$$

with phase 0.0 denoting the first conjunction (i.e. the planet furthest from the observer). Five maps are reconstructed, and the phase information reflects the offset from the 0.0 phase of each map, positioned near the centre point of each set of observations used in the reconstruction. Note there are 3 observations (July 19, 25 and 26) which are not used in the map reconstructions as they are isolated and separated in time by several rotations from the other observations; including them resulted in the models not converging.

### 2.3 Data Processing

With both instruments, observations were automatically reduced by a pipeline process utilising the LIBRE-ESPRIT package. LIBRE-ESPRIT is based on the ESPRIT software (Donati et al. 1997). The reduced Stokes  $I$  and Stokes  $V$  spectra were produced using  $1.8 \text{ km s}^{-1}$  pixel resolution.

### 2.4 Least Squares Deconvolution

As Zeeman signatures are typically very small (Donati et al. 1992), and as such we apply the multi-line technique of Least Squares Deconvolution (LSD) to improve the S/N of the data (Donati et al. 1992; Kochukhov et al. 2010). The line mask described by Donati et al. (2008) and Fares et al. (2009) and used by Mengel et al. (2016) is also used for the deconvolution in this work. The mask utilises a Kurucz model atmosphere with solar abundances,  $T_{\text{eff}}$  of 6250 K,  $\log(g)$  of  $4.0 \text{ cm s}^{-1}$  and includes most lines in the optical domain with central depths  $>> 40$  per cent of the local continuum before macroturbulent or rotational broadening but excludes the strongest, broadest features such as Balmer lines. Thus each deconvolution can access 3000-4000 lines.

In the journals of observations (tables A1-A2), the final column described whether the magnetic field has been unambiguously detected or not. Donati et al. (1992) and Donati et al. (1997) describe a statistical test to determine if the variability in the Stokes  $V$  profile is likely due to the presence of the magnetic field rather than noise. In Tables A1-A2, a definite detection (D) is defined as a false alarm probability (FAP) of less than  $10^{-5}$ . A marginal detection (M) has a FAP between  $10^{-5}$  and  $10^{-3}$ . A FAP of greater than  $10^{-3}$  is described as a non-detection (N).

### 2.5 Radial Velocities

While the LIBRE-ESPRIT package compensates for radial velocity variation due to the movement of the Earth, it does not correct

for the much larger radial velocity variation due to the presence of the hot Jupiter  $\tau$  Boötis b orbiting its parent star with a period of  $\sim 3.31$  d. The radial velocity due to the orbital motion of the system is determined by finding the centroid of a Pseudovoigt fit to the unpolarized Stokes  $I$  profile. The spectra are then corrected for the radial velocity due to the system's orbital motion. In Tables A1 and A2, the radial velocities derived from each observation are shown. In Appendix B, the period of  $\tau$  Boötis b around the star is shown to be recovered using the observations from ESPaDOnS/CFHT (Table A2).

### 3 STELLAR ACTIVITY PROXY: CA II H & K EMISSION (S-INDEX)

As a prime motivation for this work was to investigate the behaviour of the magnetic field of  $\tau$  Boötis with regard to its chromospheric activity as suggested by Mengel et al. (2016), the Ca II H & K activity proxy was extracted from each spectrum using the method described by Wright et al. (2004). Marsden et al. (2014) determined for NARVAL the coefficients  $a$ ,  $b$ ,  $c$ ,  $d$ , and  $e$  of the equation:

$$\text{S-index} = \frac{aF_H + bF_K}{cF_{RHK} + dF_{VHK}} + e \quad (6)$$

where  $F_H$  and  $F_K$  are the fluxes in  $2.18 \text{ \AA}$  triangular bandpasses centred on the cores of the Ca II H&K lines and  $F_{RHK}$  and  $F_{VHK}$  are the fluxes in two rectangular  $20 \text{ \AA}$  bandpasses centred on the continuum either side of the HK lines at  $4001.07 \text{ \AA}$  and  $3901.07 \text{ \AA}$  respectively. The corresponding coefficients for ESPaDOnS were determined using data obtained for a forthcoming survey by Moutou et al. (in preparation).

As described in Marsden et al. (2014), for each reduced unpolarised spectrum of each star, overlapping orders were removed, and equation 6 applied to the remaining spectrum. The computed S-indices were added to the existing data set described by Mengel et al. (2016, Sec. 3) and plotted in the lower right panel of Figure 1.

Figure 1 shows that during the period of observation in June-July of 2016 (HJD 2457543 onwards), the chromospheric activity reached a maximum before beginning a decline. A Lomb-Scargle (Lomb 1976; Scargle 1982; Zechmeister & Kürster 2009) periodogram (shown in figure 1, upper panel) was computed using the entire data set of S-Indices from Mengel et al. (2016, Sec. 3) and obtained for this work. The peak power of the periodogram was at 117.8 d, and this was used as an initial guess to perform a least-squares fit to the data (shown by the blue line in the lower left panel of figure 1). This confirms that the chromospheric activity of  $\tau$  Boötis follows a cycle of  $\sim 118$  d, corresponding to previously reported periods of  $\sim 116$  d from various sources (Balinas et al. 1997, 1998; Henry et al. 2000; Schmitt & Mittag 2017).

#### 3.1 Rotational Modulation

During the period June 17-24 2016, ESPaDOnS observed  $\tau$  Boötis at regular intervals  $\sim 0.3$  stellar rotations apart for  $\sim 2.2$  complete rotations. Coincidentally, this data was at the peak of the longer-term 118 d variability, allowing a focus of the night-to-night variability. The S-Indices for this well-sampled set of data were analysed using a Lomb-Scargle periodogram (figure 2, lower left panel). The peak power was observed at 3.5 d, with a least-squares best fit to the data corresponding to  $3.5 \pm 0.3$  d (figure 2, lower right). This is

close to orbital period of  $\tau$  Boötis b and rotational period of the star (3.31 d).

#### 4 LONGITUDINAL MAGNETIC FIELD

The longitudinal magnetic field ( $B_\ell$ ) is a measure of the magnetic field integrated over the visible disc of the star, and can be derived from the Stokes  $I$  and  $V$  LSD profiles. As Donati & Landstreet (2009) explains, this gives an indication of the large-scale field strength, but smoothes out smaller-scale features. This is due to cancellation effects when integrating the entire line-of-sight field components.  $B_\ell$  can be calculated (Donati et al. 1997; Mathys 1989), for a given velocity ( $v$ , in  $\text{km s}^{-1}$ ) space:

$$B_\ell = -2.14 \times 10^{11} \frac{\int vV(v)dv}{\lambda_0 g_0 c \int [I_c - I(v)]dv} \quad (7)$$

where  $B_\ell$  is in gauss, and  $\lambda_0$  and  $g_0$  are the average line (from LSD) central wavelength, and mean Landé factor respectively. For  $\tau$  Boötis, we use  $\lambda_0$  of 570 nm and  $g_0$  of 1.21, and the integration was performed across the Stokes  $V$  profile ( $\pm 16 \text{ km s}^{-1}$ ).

The resulting measurements of  $B_\ell$  are shown in figure 3 (upper panel) with the corresponding S-Index plotted in the lower panel. We see a large number of measurements of  $B_\ell$  around 0 G, which is indicative of cancellation effects in the integration. Of note is that during the March 17-21 observations, the values of  $B_\ell$  are dominantly negative, while from June 03 onwards, the strongest values for  $B_\ell$  are positive, indicating that the large-scale global field has likely changed polarity.

Additionally, if the maximum values of the measured  $B_\ell$  are taken to be indicative of the strength of the global field, it is clear that these maxima broadly follow the trend of the S-Index. Given that individual observations are subject to cancellation effects, and especially considering that  $\tau$  Boötis has a very weak global magnetic field this observation should be treated with caution.

##### 4.1 Rotational Modulation

As with the S-Index, we can use the variation in  $B_\ell$  to investigate the rotation of the star. As for the S-Index (section 3.1) the June 17-24 2016 ESPaDOoS observations were used. Figure 2 (upper panels) shows the Lomb-Scargle periodogram for  $|B_\ell|$  and the least-squares fit to the data. The period is the same as for the S-Index, albeit with a larger error bar. It appears that the absolute value of  $B_\ell$  is roughly anti-correlated with the S-Index. As always when discussing  $B_\ell$ , this observation needs to be approached cautiously, however, this could be interpreted as cancellation effects of small-scale structure (spots, etc) responsible for Ca II H&K emission; more small-scale features present on the visible stellar disc result in more likely cancellations.

## 5 MAGNETIC MAPPING

### 5.1 Model Description

Zeeman Doppler Imaging is a tomographic technique used to reconstruct surface magnetic maps from the Stokes  $V$  profiles produced using LSD. As the problem is ill-posed, the simplest magnetic topology compatible with the observed profiles is selected using the principles of maximum entropy. The code used is based

upon that described by Donati et al. (2006). Spherical harmonic expansions describe the magnetic field components, allowing an interpretation of the amount of energy in various modes. For example, the relative amounts of poloidal and toroidal components can be determined, as can relative contributions of dipolar, quadrupolar and higher order components.

The surface of the star is divided into units of similar projected area and the contribution of each unit area to the Stokes  $V$  profile (based on field strength, orientation, surface location and motion) is calculated. The process continues iteratively wherein profiles are reconstructed and compared to the observed profiles until a match within the desired error is reached. The choice of the optimal stopping criteria (usually a reduced  $\chi^2$ ) is important, and in this work we implement a suggested method of determining this criteria proposed by Alvarado-Gómez et al. (2015), described in section 5.3.

We compared two methods of modelling the local Stokes  $I$  profile. Firstly, by a Gaussian [full width at half-maximum (FWHM) of  $11 \text{ km s}^{-1}$ ], and also with a Voigt profile with a similar profile in the core. No significant differences were observed between the methods. The local Stokes  $V$  is calculated assuming the weak field approximation (Donati et al. 1997):

$$V \propto g B_{los} \frac{dI}{dv} \quad (8)$$

where  $B_{los}$  is the local line-of-sight component of the magnetic field and  $g$  is the mean Landé factor.

### 5.2 Differential rotation

In the case that a star is differentially rotating, signatures corresponding to magnetic regions should repeat in each rotational cycle but with differences resulting from shifts in the relative location of the regions due to the differential rotation. It is assumed that rotation will follow a simplified solar-type law:

$$\Omega(\theta) = \Omega_{eq} - d\Omega \sin^2 \theta \quad (9)$$

where  $\Omega(\theta)$  is the rotation rate of the star at latitude  $\theta$  in  $\text{rad d}^{-1}$ ,  $\Omega_{eq}$  is the rotation rate at the equator and  $d\Omega$  is the rotational shear between the equator and the poles.

A commonly used method described by Donati et al. (2000), Petit et al. (2002), Donati et al. (2003), Morin et al. (2008) among others is to construct a ZDI image containing a given information content for each pair of ( $\Omega_{eq}$ ,  $d\Omega$ ) and choose the pair of parameters which produces the best fit to the data (i.e. the minimal reduced  $\chi^2$ ). Using a similar technique, we construct a grid of models for each pair of ( $\Omega_{eq}$ ,  $d\Omega$ ) and determine the parameters which provide the maximum entropy solution for a given target reduced  $\chi^2$  (see Sec. 5.3). This solution provides a target entropy to apply to the  $\chi^2$  minimization technique.

The results for each epoch are summarised in Table 2. These values are used in the ZDI mapping. Note that a differential rotation measurement was not possible for the June 03-08 epoch. In this case, the map was produced with both solid-body rotation and values for  $B_{mean}$  and field components were determined for both solid-body rotation and with a mean ( $\Omega_{eq}$ ,  $d\Omega$ ) from the epochs in this work, generating variation bars for these results.  $\sim 1\sigma$  variation bars are determined for each epoch by systematically varying the stellar parameters ( $v \sin i \pm 1 \text{ km s}^{-1}$ , inclination  $\pm 5^\circ$ ). This process is illustrated for the March 17-21 epoch in Figure C1 (lower panel).

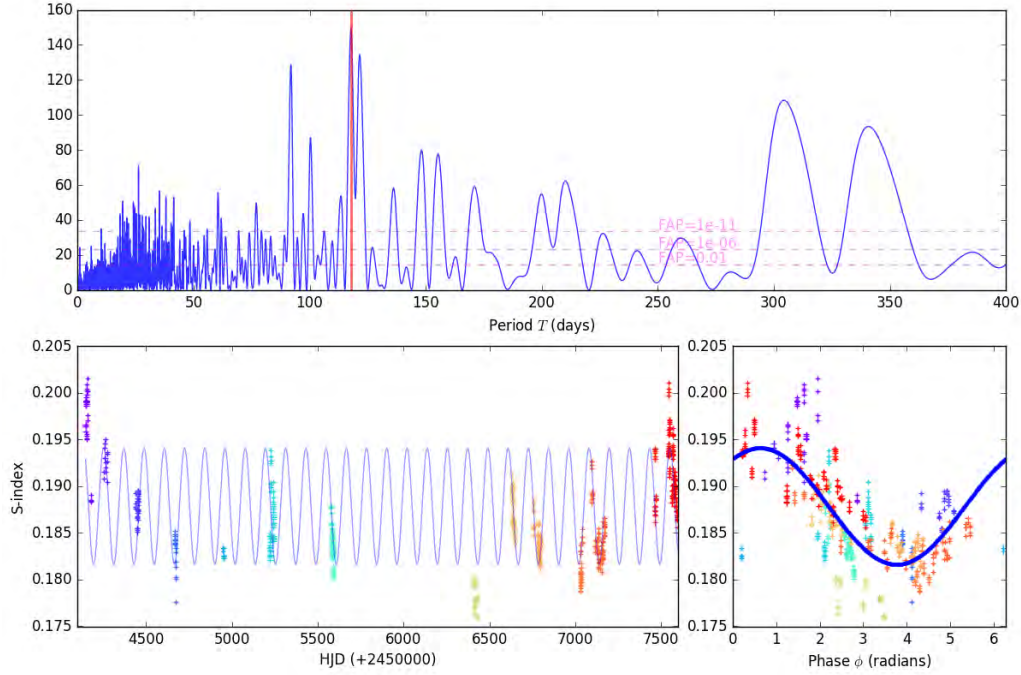


**Figure 1.** Chromospheric activity (S-index) for  $\tau$  Boötis. The upper panel shows a normalised Lomb-Scargle periodogram for the data. The peak power is at approximately 117.8 d, indicated by the vertical red line. A least squares fit of this period is shown in the lower left panel, with the phase folded data in the lower right panel. The colour coding of the data left to right is identical in the lower panels and corresponds to the HJD to indicate the position of the corresponding observations in the panels.

**Table 2.** Summary of differential rotation parameters for  $\tau$  Boötis as measured by method described in Section 5.2 with variation bars produced as explained in Appendix C. Additionally, the target reduced  $\chi^2$  produced using the second-derivative of entropy method (see Sec. 5.3 and Appendix D). The values presented below are used in the magnetic mapping. Note that DR parameters were unable to be determined for the June 03-08 epoch. In the map reconstruction, both solid-body rotation and a mean of the values produced below are used to generate variation bars in the results.

Epoch	$\Omega_{eq}$ rad d <sup>-1</sup>	$d\Omega$ rad d <sup>-1</sup>	Target $\chi_r^2$
2016 March 17-21	$2.02^{+0.07}_{-0.08}$	$0.27^{+0.20}_{-0.23}$	0.65
2016 June 03-08	–	–	0.79
2016 June 09-24	$1.98^{+0.01}_{-0.01}$	$0.05^{+0.07}_{-0.05}$	0.88
2016 June 22-July 03	$2.03^{+0.03}_{-0.05}$	$0.19^{+0.10}_{-0.12}$	0.73
2016 July 05-15	$1.95^{+0.05}_{-0.07}$	$0.33^{+0.15}_{-0.17}$	0.83

### 5.3 Target Reduced $\chi^2$

Alvarado-Gómez et al. (2015, Sec. 6.2) propose a method of determining the optimum reduced  $\chi^2$ , by calculating a point where the growth in entropy of the reconstructed ZDI maps moves into a regime indicative of noise signatures. The entropy,  $S$ , of an image can be estimated by

$$S = - \sum_k P_k \log_2(P_k) \quad (10)$$

where the probability that the difference between adjacent elements ( $P_k$ ) is equal to  $k$ . The total entropy ( $S_T$ ) is given by the sum of values produced by applying equation 10 to the three component maps (radial, azimuthal and meridional):

$$S_T = S_R + S_A + S_M \quad (11)$$

As described by Alvarado-Gómez et al. (2015), for converged solutions, determining the maximum value of the second derivative of  $S_T$  as a function of  $\chi^2$  should describe the optimum target  $\chi^2$ . This was performed for each of the five epochs, and the optimum  $\chi^2$  values determined are shown in Table 2. Plots similar to those produced by Alvarado-Gómez et al. (2015) are shown in Appendix D.

As  $\tau$  Boötis has a very weak magnetic field, as the value of the target  $\chi_r^2$  increases, the amount of field in present in the reconstruction quickly drops to near zero. This results in a relatively small range of converged target  $\chi_r^2$  values. With the  $B_{mean}$  for the optimal  $\chi_r^2$  of the reconstructed maps below  $\sim 3.5$  G, small changes (even of  $\pm 0.1\chi_r^2$ ) can result in variation of  $B_{mean}$  of as much as  $\pm 50\%$ .

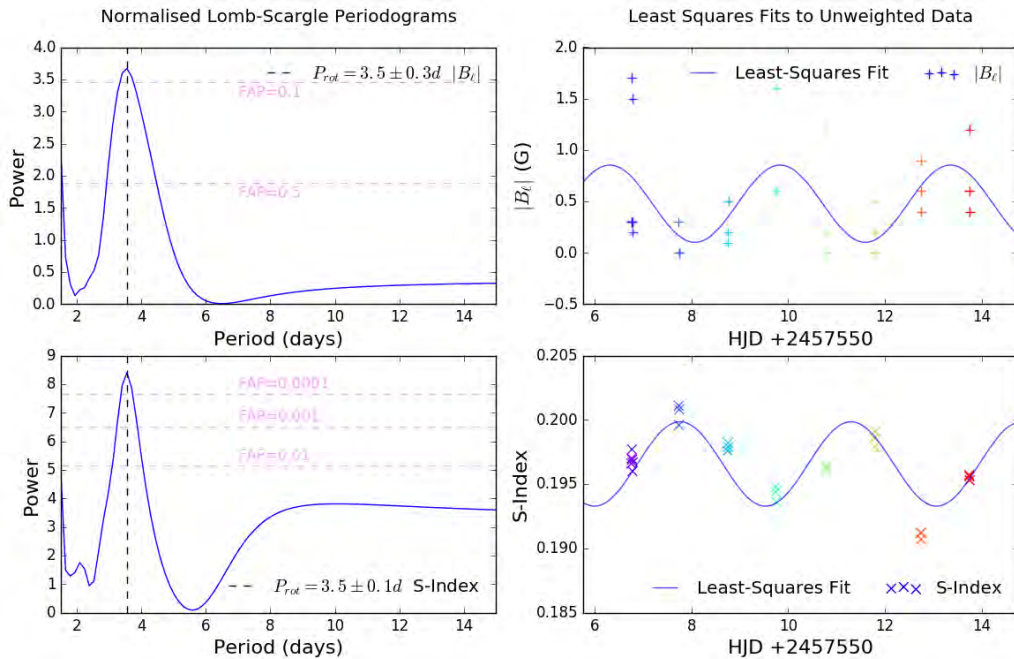


**Figure 2.** Rotational modulation of chromospheric activity (S-index) and longitudinal magnetic field for  $\tau$  Boötis June 17-24 2016. The panels to the left show normalised Lomb-Scargle periodograms for the data ( $|B_\ell|$ , upper left; S-Index, lower left). The peak power for each are shown. Least squares fits of these periods are shown in the panels on the right (error bars for  $|B_\ell|$  are omitted for clarity). The colour coding corresponds to the HJD as a visual aid. It is noted that the absolute value of  $B_\ell$  appears to be at maximum when the S-Index is lower, roughly an anti-correlation albeit not quite in phase. This may be indicative of the effect of small-scale field cancellations. However it should be noted that there are some relatively large changes in  $|B_\ell|$  over very short periods so this observation may need to be treated with caution.

Thus the relative values of  $B_{mean}$  for  $\tau$  Boötis still need to be treated cautiously.

As the target  $\chi^2$  was varied, how this affected the reconstructed field configuration was also observed. Plots showing the percentages of toroidal field, the percentage of axisymmetric poloidal field and the amount of poloidal field in the modes  $l \leq 2$  (dipolar and quadrupolar field) are displayed in Figure D1. It appears that in each case, the amount of toroidal field in the reconstructed harmonics is relatively well constrained. However, this is not always the case for the other parameters, especially in the June 03-08 epoch. While keeping this caveat in mind, the method derived by Alvarado-Gómez et al. (2015) for determining a robust stopping criteria for ZDI reconstruction appears to be applicable to stars with slow rotation and magnetic fields much weaker than the exemplar of HD 1237, whose measured longitudinal magnetic field ( $|B_\ell|$ ) is of the order of 5 times higher than that of  $\tau$  Boötis.

#### 5.4 Stellar and Model Parameters

A maximum-entropy method similar to that used for determining differential rotation parameters (see Sec. 5.2) was used to find optimum values for  $v \sin i$  and the stellar inclination. This process yielded various values, however for each epoch,  $v \sin i$  and inclina-

tion were within the range  $15.9 \pm 1.0 \text{ km s}^{-1}$  and  $45 \pm 5^\circ$  respectively. While this derived  $v \sin i$  is around  $1.6 \text{ km s}^{-1}$  higher than the value published by Borsa et al. (2015), for consistency with previous analyses of  $\tau$  Boötis we use the derived rather than the published value. As Mengel et al. (2016, Appendix A) describes, small variations in  $v \sin i$  have minimal impacts on the reconstructed models (compared to inclination). The target reduced  $\chi^2$  and differential rotation parameters for the ZDI models are shown in Table 2.

Spherical harmonic expansions for the reconstructed magnetic models were calculated using  $\ell = 8$ . For values of  $\ell > 8$ , there is near to zero energy in higher order harmonics. This is consistent with previous investigations of  $\tau$  Boötis by Mengel et al. (2016); Fares et al. (2009, 2013); Donati et al. (2008).

The configuration of the magnetic field reconstructed using these model parameters can be described by investigating amount of energy present in the various harmonics (Donati et al. 2006). The amount of the magnetic energy stored in the toroidal component of the field is found from the  $\gamma_{l,m}$  term of the complex coefficients of the spherical harmonics, and is shown as a percentage of the total energy of the harmonics in column 3 of Table 3. Column 4 of Table 3 contains the percentage of energy in the poloidal component ( $\alpha_{l,m}$  and  $\beta_{l,m}$ ) which is axisymmetric (i.e. symmetric about the axis of rotation), and is found from the  $\alpha_{l,m}$  and  $\beta_{l,m}$  co-

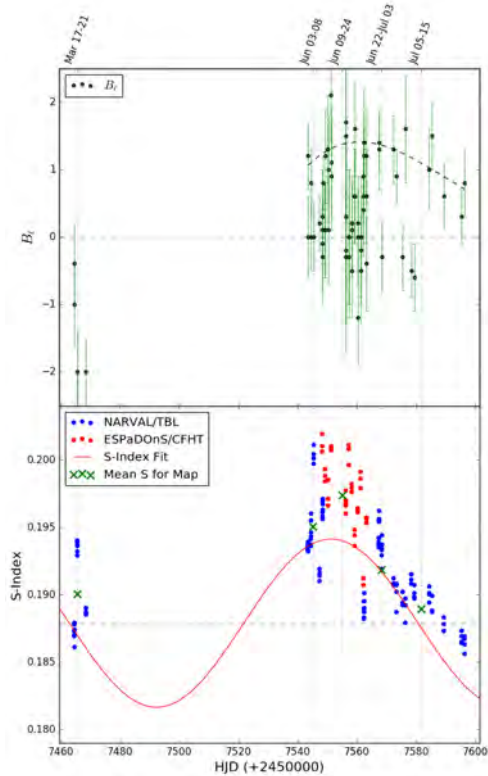


**Figure 3.** Longitudinal magnetic field ( $B_l$ ) of  $\tau$  Boötis over the epochs of observation (upper panel) and corresponding S-Index (lower panel). In the lower panel, the red points indicate observations taken from ESPaDONs, blue from NARVAL. The green cross indicates the mean S-Index for the map generated at that epoch. Note that the dominant polarity has changed from negative for the observations in March 17-21 to positive for the later epochs. Note that cancellation effects lead to numerous results where  $B_l$  is close to zero. However, in the epochs beginning in June, the maximum value of the measured  $B_l$  declines as the S-index declines.

efficients of the spherical harmonics where  $m = 0$ . Finally, column 5 of Table 3 indicates the percentage of the magnetic energy in the poloidal component of the magnetic field consisting of dipolar plus quadrupolar components, calculated from  $\alpha_{\ell,m}$  and  $\beta_{\ell,m}$  coefficients where  $\ell \leq 2$

A measure of the variation in these values is found by varying the differential rotation measurement by the error found for each epoch (holding inclination and  $v \sin i$  constant), then varying the stellar parameters (inclination  $\pm 5^\circ$ ;  $v \sin i \pm 1.0 \text{ km s}^{-1}$ ) while holding  $d\Omega$  and  $\Omega_{eq}$  constant. This is discussed in depth in Appendix C. Additionally, as the chosen target reduced  $\chi^2$  values are very close to the point at which the models do not converge, we also calculated the values of the extreme variations using target  $\chi^2 \pm 0.1$ . This results in quite a large variation in  $B_{mean}$ , as previously discussed. However, with other parameters held steady, some significant varia-

tions in the poloidal components with target  $\chi^2$  were also observed. In contrast, the relative amount of poloidal energy seems relatively well-constrained. This is discussed further in Appendix D.

Mengel et al. (2016, Appendix A) noted that significant variation in the axisymmetric poloidal and  $l \leq 2$  modes was predominantly dependent upon inclination angle. Hence, combining variations in this with target  $\chi^2$  results in some variation bars which are large compared with previously published analyses.

### 5.5 March 2016

Figure 4(a) shows the observed (in red) and reconstructed (in black) Stokes  $V$  profiles from NARVAL for 17-21 March 2016. The reconstructed topology is shown in Figure 5. The previously observed weak magnetic field is once again present. These observations were taken approximately 350 d after the previously observed epoch (Mengel et al. 2016), during which the large-scale dipolar field was positive. In March 2016, the dominant dipolar large-scale field was negative (blue) in the radial map, which is consistent with the observed yearly reversal. The field is mostly poloidal, with a low percentage of toroidal field ( $\sim 17\%$ ). The  $B_{mean}$  is relatively low compared with the other epochs in this work, but of a similar magnitude as the July 05-15 epoch which lies in a similar position in the chromospheric activity cycle (Fig. 3, lower panel).

### 5.6 June-July 2016

During June and July of 2016, a sequence of four maps were produced. The first, third and fourth maps were produced using data from NARVAL with the Stokes  $V$  profiles shown in Figure 4(b)-(d). The second map was produced using data from ESPaDONs, and these Stokes  $V$  profiles are shown in Figure 6. In each case, due to the evolution in features expected over time, each map was limited to approximately 3 stellar rotations with the exception of the ESPaDONs observations, which span  $\sim 4.5$  rotations. In each case, there was regular sampling of the stellar rotational period.

#### 5.6.1 June 03-08: Evidence of Rapid Reversal

The observed and reconstructed Stokes  $V$  profiles from NARVAL for June 03-08 are shown in Figure 4(b), and the reconstructed magnetic maps are shown in Figure 7, top row. It is clear that the global dipolar field is positive in the polar region of the radial map, indicating that the polarity has changed between March and June. This confirms the speculation of Mengel et al. (2016) that the frequency of polarity reversals is very fast (reversal every  $\sim 120$  d, implying a cycle of  $\sim 240$  d) and follows the chromospheric activity cycle. The nature of the reversal, and exactly where it happens is still unclear. As shown in Figure 1, there is a lack of coverage in the post-minimum/pre-maximum part of the cycle, and it is likely that the reversal appears here.

The midpoint of the observation is approaching the maximum of the S-index. The  $B_{mean}$  is higher than the measurement in March, and the amount of toroidal field is at its highest point ( $\sim 45\%$ ) during these observations (Figure 8), and the map of the azimuthal component is more intense than those of the other epochs. Although the percentages of the energy in the axisymmetric poloidal field and in the modes  $l \leq 2$ , are also low relative to the other epochs in this work, it should be noted that these values are poorly constrained (see Fig. D1(b), upper panel) and while it may be tempting to infer that the field is “more complex” than the other epochs in

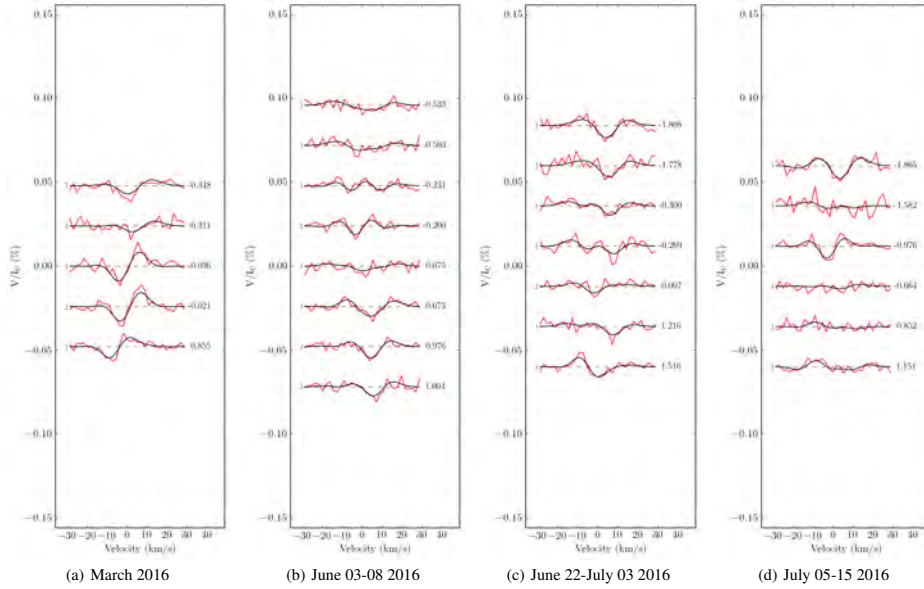


**Figure 4.** Circular polarization profiles of  $\tau$  Boo for NARVAL observations, March 2016 and June-July 2016. The observed profiles are shown in red, while synthetic profiles are shown in black. On the left of each profile we show a  $\pm 1\sigma$  error bar. The rotational cycle of each observation is indicated on the right of each profile. All plots are to the same scale.

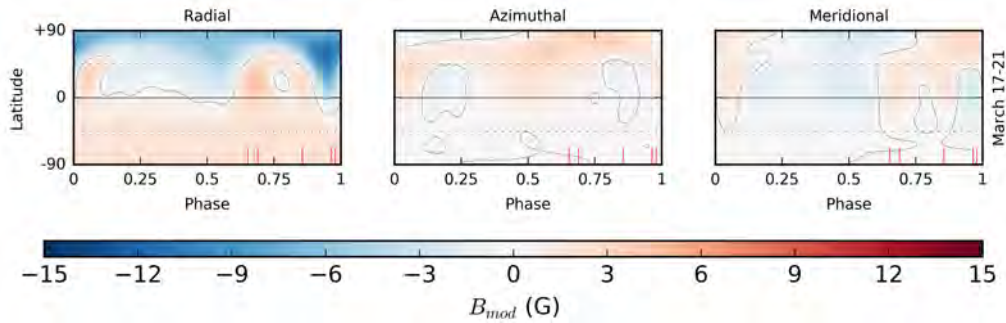


**Figure 5.** Magnetic topology of  $\tau$  Boötis reconstructed from profiles in Fig. 4(a). The radial, azimuthal and meridional components of the field (with magnetic field strength labelled in G) are reconstructed for March 2016. The contour line indicates where  $B_{mod}$  is zero. The red ticks along the lower x-axes indicate the observational phases for each epoch.

this work based on these numbers, this should be tempered with caution.

### 5.6.2 June 09-24: Declining toroidal component

The observed and reconstructed Stokes  $V$  profiles from ESPaDOnS for June 09-24 are shown in Figure 6, and the reconstructed magnetic maps are shown in the second row of Figure 7. With the S-

index reaching its maximum, the mean magnetic field is still relatively high, but there is a marked decline in the percentage of the toroidal field from the previous map. It is visually apparent that there is an increase in the intensity recorded in the radial field map compare to the preceding map, and decrease in the intensity of the azimuthal component. A cautious interpretation may be that the toroidal field is being converted to poloidal by a dynamo process. There is an evolution of the magnetic field features from map to

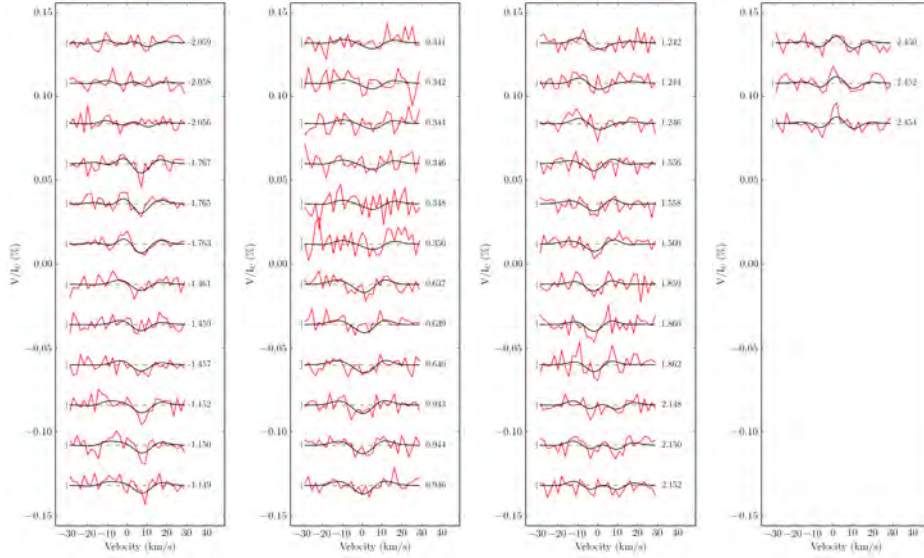


**Figure 6.** Circular polarization profiles of  $\tau$  Boo for ESPaDOnS observations, June 2016. The observed profiles are shown in red, while synthetic profiles are shown in black. On the left of each profile we show a  $\pm 1\sigma$  error bar. The rotational cycle of each observation is indicated on the right of each profile. All plots are to the same scale as Fig. 4.

map, where persistent identifiable regions of large-scale fields are apparent.

### 5.6.3 June 22–July 03: Peak Magnetic Field Intensity

The observed and reconstructed Stokes  $V$  profiles from NARVAL for June 22–July 03 are shown in Figure 4(c), and the reconstructed magnetic maps are shown in Figure 7, third row. Around 15 d after the peak in the chromospheric activity cycle, the highest  $B_{mean}$  of 3.8 G is recorded. While the percentage of the toroidal field is slightly higher than the preceding epoch, it is still significantly lower than the peak value of the toroidal field in the June 03–08 epoch (28% and 45% respectively). As shown in Fig. D1, the percentage of the toroidal field is well constrained in each case.

### 5.6.4 July 05–15: Declining Field Intensity

The observed and reconstructed Stokes  $V$  profiles from NARVAL for July 05–15 are shown in Figure 4(d), and the reconstructed magnetic maps are shown in Figure 7, bottom row. In this final reconstruction, the magnetic field,  $B_{mean}$  has dropped significantly, and is of the same order as that from the March 17–21 epoch (see Fig. 8, upper panel and centre panels), which is in a similar position in the S-Index cycle. The percentage of the toroidal field is also down to 20%. Interestingly, Fig. D1(e) shows that the percentage of toroidal field is very well constrained as a function of the target  $\chi^2_r$ , yet the variation is slightly higher than for the other epochs. This is due to an extreme variation when the inclination,  $v \sin i$  and  $d\Omega$  parameter are at their greatest variation. The standard deviation of the mea-

surement of the percentage of toroidal field is only  $\sim \pm 4\%$ , which is more in line with the variation of the other epochs.

## 6 RESULTS AND DISCUSSION

Figure 8 summarises the results from Table 3 and illustrates two points. Firstly, while noting the caveats regarding the variability of the measure value of the intensity of the magnetic field,  $B_{mean}$  (see section 5.3), we nonetheless can see (Fig. 8, upper panel) the  $B_{mean}$  appears to follow the chromospheric activity cycle (Fig. 8, centre panel). Similarly, the percentage of the toroidal field component (in red, Fig. 8, lower panel) appears to peak near the maximum of the chromospheric activity cycle before declining. Mengel et al. (2016) showed that at the chromospheric activity minimum, the percentage of toroidal field also reached a minimum before beginning to rise again. This is highly suggestive that the magnetic field is converting poloidal field into toroidal field as the chromospheric activity increases from minimum to maximum.

In order to investigate this over a longer timescale, the results for  $B_{mean}$  and percentages of the field components similar to Table 3 from this work and previous published analyses of  $\tau$  Boötis (Mengel et al. 2016; Fares et al. 2013, 2009; Donati et al. 2008) were summarised and plotted, with the dates of observations phase folded as per the S-index cycle in Figure 9. It should be noted that earlier works do not have error estimates for some of these parameters, and differing methodologies for determining stopping criteria, differential rotation and stellar parameters may have been used. Additionally, it seems clear that the large-scale field of  $\tau$  Boötis evolves rapidly, and so long sequences of observations may affect the reconstructed values as the field has changed from the start to

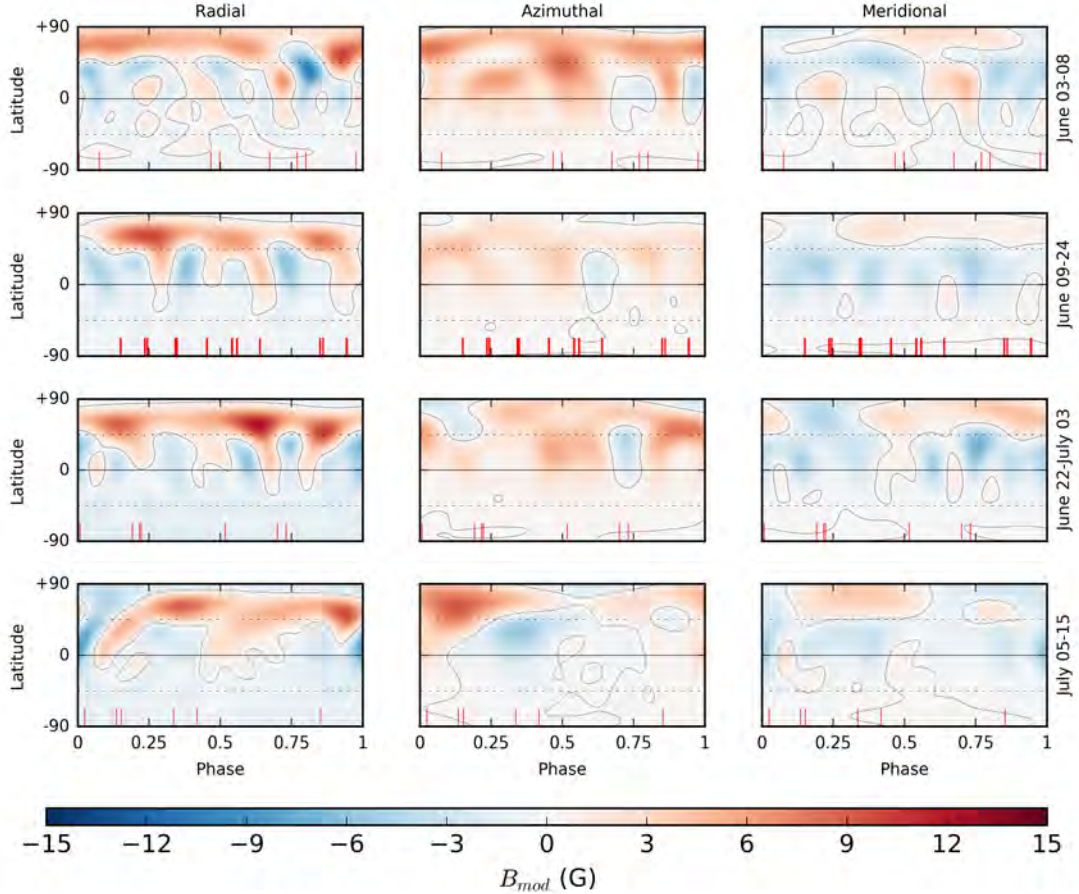


**Figure 7.** Magnetic topology of  $\tau$  Boötis reconstructed from profiles in Fig. 4(b-d) and 6. The radial, azimuthal and meridional components of the field (with magnetic field strength labelled in G) are depicted for June 2016 from TBL/NARVAL (top), June 2016 from CFHT/ESPaDOnS (second row), late June 2016 from TBL/NARVAL (third row), and July 2016 from TBL/NARVAL (bottom row). The contour line indicates where  $B_{mod}$  is zero. The red ticks along the lower x-axes indicate the observational phases for each epoch.

the end of the observational epoch. Our investigations show that in general, the percentage of toroidal field in particular is well-constrained. Values for  $B_{mean}$  should be self-consistent when using a consistent methodology by the authors of the previous works, but should be treated more cautiously. However we have shown that the percentages of axisymmetric poloidal field and the percentage of modes  $l \leq 2$  are not well-constrained in some cases, and indeed this limits these numbers' usefulness in assessing the long-term trend.

In the top panel of Figure 9, the phase-folded S-Index cycle, with a period of 117.8 d is shown, along with the least-squares fit. In the subsequent panels, from the second to the bottom row, are plotted respectively the  $B_{mean}$ , percentage of toroidal field, percentage of poloidal field in modes  $l \leq 2$  and finally the percentage of poloidal field in axisymmetric modes from the references shown

in the key. In the second and third panels, the least-squares fit from the S-index is overlaid on the plot. These two plots clearly show that the magnetic field intensity and the percentage of the magnetic energy in the toroidal component is varying over time with the chromospheric activity cycle.

In the lower two panels dealing with the configuration of the poloidal components, no clear relationship with the chromospheric cycle is apparent. In the work of Mengel et al. (2016) in particular, and in the work presented here (see Fig. 8, lower panel) there are some indications that the percentage of these components may be anti-correlated with the toroidal component and the S-Index (as it is in the cycle exhibited by 61 Cyg A (Boro Saikia et al. 2016)), but the longer-term analysis does not clearly reflect this. Given that these values are not well constrained in some cases, it may

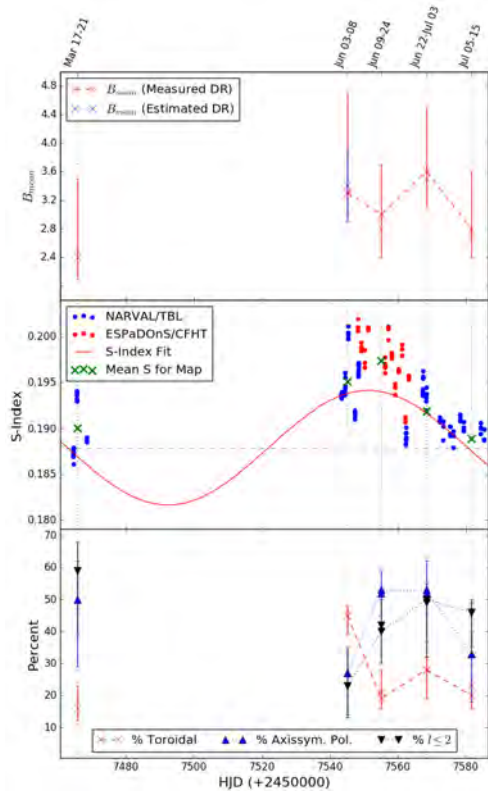


**Figure 8.** Measurements of  $B_{mean}$  (upper panel), and field topology (lower panel) compared to the S-Index (centre panel). It is noted that  $B_{mean}$  generally declines as the S-index declines. Similarly, the percentage of toroidal field decreases as the peak in the S-index is reached. In the four epochs in June and July, the percentages in the measures of poloidal axisymmetry and modes  $l \leq 2$  generally increase, but as explained in the text, these are somewhat poorly constrained.

be necessary to perform an analysis to exclude epochs with poorly constrained results to see if a trend emerges.

The solar-type cycle exhibited by the K5V star 61 Cyg A (Boro Saikia et al. 2016) is characterised by the increasing complexity of the poloidal field as the chromospheric activity increases. 61 Cyg A exhibits very small variation in the amount of toroidal field, with Boro Saikia et al. (2016) showing that only one epoch of observation showed a significant change. It is known that azimuthal rings are present in stars with rapid rotation, and as  $\tau$  Boötis rotates with a period  $\sim$  one tenth that of 61 Cyg A it is likely that this is the reason for this difference. Another significant difference between 61 Cyg A and  $\tau$  Boötis is that the azimuthal component of the reconstructed field does not appear to regularly reverse polarity for  $\tau$  Boötis; only the radial field appear to undergo regular reversals. We note that Morgenthaler et al. (2011) and Petit et al. (2009) observed a similar behaviour for HD 190771 ( $T_{eff} = 5834 \pm 50$  K;

$P_{rot} = 8.8$  d) wherein the radial field reverses, but the azimuthal may not. Given that these rapidly-rotating stars exhibit otherwise cyclic behaviour with respect to radial field reversals, this perhaps may indicate a difference in dynamo mechanisms between the deeply convective K5 dwarf and the hotter, rapidly rotating F and G stars with shallower convective zones. Alternatively, as strong azimuthal components are found in rapidly-rotating stars, but not in slow rotators like 61 Cyg A, it could be speculated that the azimuthal reversals depend upon the total withdrawal of the toroidal component [as described for the Sun by McIntosh et al. (2014)] which is unlikely when this component is relatively strong. This could result in sometimes failed attempted reversals.

The nature of the polarity reversal process in the radial field is still unclear. Spectropolarimetric observations across the missing phases of the chromospheric activity cycle would perhaps answer questions about how the opposite polarity field emerges. The map for the July 05-15 epoch tantalisingly shows a strengthening negative polarity area at around  $\phi = 0$  extending towards the polar region. Maps presented by Fares et al. (2009, 2013) also show small areas of opposite polarity in the polar region.

## 7 CONCLUSIONS

We present here the first example of an F-type star to exhibit a large-scale magnetic cycle coincident with its chromospheric activity cycle. This cycle is extremely rapid. Unlike the Sun and 61 Cyg A, whose magnetic cycles are on the order of years,  $\tau$  Boötis reverses the polarity of its radial field approximately every  $\sim 120$  d.

It cannot be stated that the magnetic cycle of  $\tau$  Boötis is strictly “solar type”, given the uncertainty around the behaviour of the poloidal components, and the fact that the azimuthal component does not regularly reverse polarity. However, these results may provide some guidance to the theoretical underpinning of the nature of the dynamo processes in rapidly-rotating stars with shallow convective envelopes. While star-planet interaction was not investigated in this work, an open question is whether the planet  $\tau$  Boötis b has any effect on the ability of this F-type star to sustain a regular magnetic cycle in contrast to other rapidly rotating stars of this type which seem to exhibit more chaotic behaviour.

We also showed that the absolute value of the longitudinal magnetic field was, on a short timescale, anti-correlated with the S-index of the star. This is suggestive that when many small-scale structures are visible of the stellar surface, the likelihood of cancellation effects increases, with  $B_l$  tending to zero.

$\tau$  Boötis remains a challenging target for spectropolarimetry given its weak magnetic field. Further work to close the gaps in the chromospheric activity cycle may provide further insights into the nature of the magnetic behaviour of this intriguing stellar system.

## ACKNOWLEDGMENTS

This work was based on observations obtained with NARVAL at the Telescope Bernard Lyot (TBL). TBL/NARVAL are operated by the Institut National des Sciences de l’Univers of the Centre National de la Recherche Scientifique of France. This work is also based on observations obtained with ESPaDOnS at the Canada-France-Hawaii Telescope (CFHT) which is operated by the National Research Council of Canada, the Institut National des Sciences de l’Univers of the Centre National de la Recherche Scientifique of

**Table 3.** Summary of magnetic topology evolution of  $\tau$  Boötis for the five maps March through July 2016. The columns indicated mean magnetic field  $B$ , percentage of magnetic energy in the toroidal component, percentage of the energy contained in the axisymmetric modes of the poloidal component (modes with  $m = 0$ ) and percentage of the energy contained in the modes of  $\ell \leq 2$  of the poloidal component. Variations are based on the systematic recalculation based upon varying stellar parameters ( $\Omega_{\text{eq}}$ ,  $d\Omega$ , inclination,  $v \sin i$ ) as described in Appendix C.

Epoch	$B_{\text{mean}}$ (G)	% toroidal	% axisymm. poloidal	% $\ell \leq 2$ in poloidal
2016 March 17-21	$2.4^{+1.1}_{-0.3}$	$16^{+7}_{-4}$	$50^{+12}_{-21}$	$59^{+9}_{-20}$
2016 June 03-08	$3.3^{+1.4}_{-0.3}$	$45^{+3}_{-6}$	$27^{+8}_{-13}$	$23^{+11}_{-10}$
2016 June 09-24	$2.8^{+0.9}_{-0.4}$	$21^{+7}_{-5}$	$52^{+7}_{-7}$	$42^{+8}_{-12}$
2016 June 22-July 03	$3.5^{+1.0}_{-0.4}$	$28^{+4}_{-9}$	$52^{+10}_{-15}$	$49^{+6}_{-17}$
2016 July 05-15	$2.7^{+0.9}_{-0.3}$	$23^{+17}_{-7}$	$33^{+16}_{-15}$	$46^{+4}_{-11}$

France, and the University of Hawaii. This research has made use of NASA's Astrophysics Data System.

The Strategic Research Funding for the Starwinds project provided by the University of Southern Queensland provides resources to the Astrophysics group within the Computational Engineering and Science Research Centre at USQ (MWM, SCM, BDC). MWM is supported by an Australian Postgraduate Award Scholarship. MWM would like to thank Associate Professor Jonti Horner for his comments and feedback on the paper.

## REFERENCES

- Alvarado-Gómez J. D., et al., 2015, *A&A*, 582, A38
- Baliunas S. L., Henry G. W., Donahue R. A., Fekel F. C., Soon W. H., 1997, *ApJ*, 474, L119
- Baliunas S. L., Donahue R. A., Soon W. H., Henry G. W., 1998, in Donahue R. A., Bookbinder J. A., eds, *ASP Conf. Ser. Vol. 154, Cool Stars, Stellar Systems and the Sun*. Astron. Soc. of the Pac., pp 153–172
- Boro Saikia S., Jeffers S. V., Petit P., Marsden S., Morin J., Folsom C. P., 2015, *A&A*, 573, A17
- Boro Saikia S., et al., 2016, *A&A*, 594, A29
- Borsa F., et al., 2015, *A&A*, 578, 64
- Broggi M., Snellen I. A. G., de Kok R. J., Albrecht S., Birkby J., de Mooij E. J. W., 2012, *Nature*, 486, 502
- Butler R. P., Marcy G. W., Williams E., Hauser H., Shirts P., 1997, *ApJ*, 474, L115
- Catala C., Donati J.-F., Shkolnik E., Bohlender D., Alecian E., 2007, *MNRAS*, 374, L42
- DeRosa M. L., Brun A. S., Hoeksema J. T., 2012, *ApJ*, 757, 96
- Donati J.-F., Landstreet J., 2009, *ARA&A*, 47, 333
- Donati J.-F., Semel M., Rees D. E., 1992, *A&A*, 265, 669
- Donati J.-F., Semel M., Carter B. D., Rees D. E., Cameron A. C., 1997, *MNRAS*, 291, 658
- Donati J.-F., Mengel M., Carter B. D., Marsden S., Collier Cameron A., Wichmann R., 2000, *MNRAS*, 316, 699
- Donati J.-F., Collier Cameron A., Petit P., 2003, *MNRAS*, 4, 1187
- Donati J.-F., et al., 2006, *MNRAS*, 370, 629
- Donati J.-F., et al., 2008, *MNRAS*, 385, 1179
- Duncan D. K., et al., 1991, *ApJS*, 76, 383
- Fares R., et al., 2009, *MNRAS*, 398, 1383
- Fares R., Moutou C., Donati J.-F., Catala C., Shkolnik E. L., Jardine M. M., Cameron A. C., Deleuil M., 2013, *MNRAS*, 435, 1451
- Hallinan G., Sirothia S. K., Antonova A., Ishwara-Chandra C. H., Bourke S., Doyle J. G., Hartman J., Golden A., 2013, *ApJ*, 762, 34
- Hathaway D. H., 2010, *Living Reviews in Solar Physics*, 7, 1
- Henry G. W., Baliunas S. L., Donahue R. A., Fekel F. C., Soon W. H., 2000, *ApJ*, 531, 415
- Jeffers S. V., Donati J.-F., 2008, *MNRAS*, 390, 635
- Jeffers S. V., Donati J.-F., Alecian E., Marsden S. C., 2011, *MNRAS*, 411, 1301
- Jeffers S. V., Petit P., Marsden S. C., Morin J., Donati J.-F., Folsom C. P., The BCoolest C., 2014, *A&A*, 569, A79
- Kochukhov O., Makaganiuk V., Piskunov N. E., 2010, *A&A*, 524, A5
- Leigh C., Cameron A., Horne K., Penny A., James D., 2003, *MNRAS*, 344, 1271
- Lomb N. R., 1976, *Ap&SS*, 39, 447
- Marsden S. C., Donati J.-F., Semel M., Petit P., Carter B. D., 2006, *MNRAS*, 370, 468
- Marsden S. C., et al., 2014, *MNRAS*, 444, 3517
- Mathys G., 1989, *Fundamentals Cosmic Phys.*, 13, 143
- McIntosh S. W., et al., 2014, *ApJ*, 792, 12
- Mengel M. W., Fares R., Marsden S. C., Carter B. D., Jeffers S. V., Petit P., Donati J.-F., Folsom C. P., 2016, *MNRAS*, 459, 4325
- Morgenthaler A., Petit P., Morin J., Aurière M., Dintrans B., Konstantinova-Antova R., Marsden S., 2011, *Astronomische Nachrichten*, 332, 866
- Morgenthaler A., et al., 2012, *A&A*, 540, A138
- Morin J., et al., 2008, *MNRAS*, 384, 77
- Petit P., Donati J.-F., Collier-Cameron A., 2002, *MNRAS*, 334, 374
- Petit P., Donati J.-F., the ESPaDOnS Project Team 2003, in Arnaud J., Meunier N., eds, *EAS Pub. Ser. Vol. 9, Magnetism and Activity of the Sun and Stars*. p. 97
- Petit P., Dintrans B., Morgenthaler A., Van Grootel V., Morin J., Lanoux J., Aurière M., Konstantinova-Antova R., 2009, *A&A*, 508, L9
- Rodler F., Lopez-Morales M., Ribas I., 2012, *ApJ*, 753, L25
- Sanderson T. R., Appourchaux T., Hoeksema J. T., Harvey K. L., 2003, *Journal of Geophysical Research: Space Physics*, 108, 1
- Scargle J. D., 1982, *ApJ*, 263, 835
- Schmitt J., Mittag M., in press 2017, *A&A*
- Semel M., 1989, *A&A*, 225, 456
- Wright J. T., Marcy G. W., Butler R. P., Vogt S. S., 2004, *ApJS*, 152, 261
- Zechmeister M., Kürster M., 2009, *A&A*, 496, 577

## APPENDIX A: JOURNALS OF OBSERVATIONS

## APPENDIX B: RADIAL VELOCITY OF $\tau$ BOÖTIS

$\tau$  Boötis b is a planet with a mass of  $\sim 6 M_{\text{Jupiter}}$  orbiting at a distance of  $\sim 0.049$  au. This induces a variation in the observed radial velocity of  $\tau$  Boötis. Fitting a Pseudovoigt profile to the unpolarized Stokes  $I$  profiles derived via LSD, the centroid represents the radial velocity measurement. In Fig. B1, the upper panel shows a Lomb-Scargle periodogram used to determine the period with the peak power, used as an initial estimate of a least-squares fit (shown in the lower left panel). The phase-folded fit is shown in the lower right panel.

Using the data from ESPaDOnS at CFHT, we recover a best-fit period of  $\sim 3.312$  d with a semi-amplitude of  $\sim 461$  km  $s^{-1}$ . These

**Table A1.** Journal of NARVAL observations from March through July 2016 of  $\tau$  Boötis. Columns list the UT date, the heliocentric Julian date (at midpoint of the series of 4 sub-exposures), the UT time (at midpoint of the series of 4 sub-exposures), the exposure time, the peak signal-to-noise ratio (SNR) of each observation (at around 700 nm for NARVAL), the rotational cycle from the ephemeris (from Equation 5), the radial velocity (RV) associated with each exposure, and whether a magnetic signature is detected (D;  $fap < 10^{-5}$ ), marginally detected (M;  $10^{-3} > fap > 10^{-5}$ ) or is below the detection threshold (N). Five epochs are used to create maps. In column 7, the rotational phase ( $\phi_{rot}$ ) is used in the map reconstruction and is calculated from the 0.0 phase of the map, defined to be near the midpoint of the series of observations used for the map. The final 3 observations, indicated with  $\phi_{rot}$  as “-” are not used in the mapping as explained in the text.

Date	HJD (245 5000+)	UT (h:m:s)	$T_{exp}$ (s)	SNR	Cycle	$\phi_{rot}$	RV (km s $^{-1}$ )	Detection
2016-March-17	2464.53781	00:48:35	4 × 600	1122	1211.6524	-0.3476	-17.147	N
2016-March-17	2464.65892	03:42:58	4 × 600	1190	1211.6890	-0.3110	-17.209	N
2016-March-18	2465.57036	01:35:23	4 × 600	1135	1211.9641	-0.0359	-16.897	D
2016-March-18	2465.61821	02:44:17	4 × 600	1189	1211.9786	-0.0214	-16.843	D
2016-March-21	2468.52215	00:25:47	4 × 600	1424	1212.8553	0.8553	-17.124	D
2016-June-03	2543.42188	22:02:33	4 × 600	1150	1235.4667	-0.5333	-16.570	N
2016-June-04	2543.52351	00:28:55	4 × 600	1285	1235.4974	-0.5026	-16.667	N
2016-June-04	2544.42415	22:05:54	4 × 600	1348	1235.7693	-0.2307	-17.122	N
2016-June-05	2544.52457	00:30:31	4 × 600	1355	1235.7996	-0.2004	-17.088	M
2016-June-05	2545.43724	22:24:50	4 × 600	1232	1236.0752	0.0752	-16.421	N
2016-June-07	2547.41791	21:57:11	4 × 600	1493	1236.6731	0.6731	-17.066	D
2016-June-08	2548.42082	22:01:27	4 × 600	1532	1236.9759	0.9759	-16.731	D
2016-June-08	2548.51409	24:15:47	4 × 600	1523	1237.0040	1.0040	-16.647	D
2016-June-22	2562.38504	21:11:18	4 × 600	1083	1241.1915	-1.8085	-16.236	M
2016-June-22	2562.48618	23:36:57	4 × 600	954	1241.2221	-1.7779	-16.209	N
2016-June-27	2567.38125	21:06:22	4 × 600	1436	1242.6998	-0.3002	-17.126	N
2016-June-27	2567.48394	23:34:15	4 × 600	1137	1242.7308	-0.2692	-17.138	M
2016-June-28	2568.39836	21:31:07	4 × 600	1430	1243.0069	0.0069	-16.660	N
2016-July-02	2572.40439	21:40:15	4 × 600	1332	1244.2163	1.2163	-16.232	M
2016-July-03	2573.39881	21:32:19	4 × 600	1426	1244.5165	1.5165	-16.747	D
2016-July-05	2575.44688	22:41:46	4 × 600	1381	1245.1348	-1.8652	-16.342	D
2016-July-06	2576.3847	21:12:21	4 × 600	849	1245.4179	-1.5821	-16.426	N
2016-July-08	2578.39412	21:26:08	4 × 600	1561	1246.0245	-0.9755	-16.604	D
2016-July-09	2579.42697	22:13:34	4 × 600	1421	1246.3363	-0.6637	-16.270	N
2016-July-14	2584.44904	22:45:55	4 × 600	1250	1247.8524	0.8524	-17.138	N
2016-July-15	2585.43962	22:32:28	4 × 600	1385	1248.1515	1.1515	-16.336	N
2016-July-19	2589.37159	20:54:58	4 × 600	1385	1249.3385	-	-16.329	N
2016-July-25	2595.36588	20:47:27	4 × 600	1510	1251.1481	-	-16.341	N
2016-July-26	2596.38525	21:15:28	4 × 600	1345	1251.4559	-	-16.608	N

values are close to the measurements first reported by [Butler et al. \(1997\)](#). The radial velocities derived here are used to correct the LSD profiles such that they have a uniform centre point in velocity space.

#### APPENDIX C: VARIATION BARS FROM DIFFERENTIAL ROTATION AND OTHER PARAMETER VARIATION

In this appendix, we give some insight into the stability of the reconstructed values for the field components described in Table 3. As the energy in the spherical harmonics used in the Zeeman Doppler Imaging models gives no indication of error for a given set of modes, we vary stellar parameters to give some indication of the stability of the results.

Firstly, the variation in the measurement of differential rotation must be determined. Figure C1 shows this process for the June 22-July 03 epoch. For each combination of  $(\Omega_{eq}, d\Omega)$ , with the “optimal” values of  $v \sin i$  and stellar inclination a ZDI model is produced for a given target level of entropy and the resulting reduced  $\chi^2$  for each model determined. In the upper panel of Figure C1,

$\chi_r^2$  is shown as a function of  $(\Omega_{eq}, d\Omega)$ . The best fit solution is located at the minimum  $\chi_r^2$ . In the lower panel of Figure C1, the red paraboloid corresponds to the  $1\sigma$  contour of the upper panel plot. By varying the  $v \sin i \pm 1$  km s $^{-1}$  and the stellar inclination  $\pm 5^\circ$  independently (dashed green) and the  $v \sin i$  and inclination angle together (blue), the maximum extent of the variation is selected as the variation bars for differential rotation.

A similar process of selecting the minimum  $\chi_r^2$  solution can be used to find the best  $v \sin i$  and stellar inclination (albeit without varying other parameters), as shown in Figure C2 for the June 22-July 03 epoch. Each epoch produces a slightly different value for each parameter, but as all are within the variation bars (shown in Figure C2), we select the values used in the main text.

Producing models using the extreme values of  $v \sin i$ , inclination and  $(\Omega_{eq}, d\Omega)$  results in potentially large variation bars. Individually, derived results may be well-constrained, but less so when variations are combined. This is also increased when coupled with varying the target  $\chi_r^2$ , as discussed in Appendix D. Yet another complicating factor is that many of the parameters are linked. The initial  $(\Omega_{eq}, d\Omega)$  values determined are dependent, for example, of the target  $\chi_r^2$ . In turn, the optimum target  $\chi_r^2$  chosen will be affected by

**Table A2.** Journal of ESPaDOnS observations from June 09 to June 24 2016 of  $\tau$  Boötis. Columns list the UT date, the heliocentric Julian date (at midpoint of the series of 4 sub-exposures), the UT time (at midpoint of the series of 4 sub-exposures), the exposure time, the peak signal-to-noise ratio (SNR) of each observation (at around 700 nm for ESPaDOnS), the rotational cycle from the ephemeris (from Equation 5), the radial velocity (RV) associated with each exposure, and whether a magnetic signature is detected (D;  $fap < 10^{-5}$ ), marginally detected (M;  $10^{-3} > fap > 10^{-5}$ ) or is below the detection threshold (N). In column 7, the rotational phase ( $\phi_{rot}$ ) is used in the map reconstruction and is calculated relative to the 0.0 phase of the map, defined to be near the midpoint of the series of observations.

Date	HJD (245 5000+)	UT (h:m:s)	$T_{exp}$ (s)	SNR	Cycle	$\phi_{rot}$	RV ( $\text{km s}^{-1}$ )	Detection
2016-June-09	2548.80866	07:20:00	4 × 90	909	1237.0930	-1.9070	-16.442	N
2016-June-09	2548.81460	07:28:33	4 × 90	891	1237.0948	-1.9052	-16.441	N
2016-June-09	2548.82051	07:37:04	4 × 90	919	1237.0965	-1.9035	-16.437	N
2016-June-10	2549.77840	06:36:31	4 × 90	922	1237.3857	-1.6143	-16.410	N
2016-June-10	2549.78431	06:45:02	4 × 90	918	1237.3875	-1.6125	-16.423	N
2016-June-10	2549.79024	06:53:34	4 × 90	950	1237.3893	-1.6107	-16.420	N
2016-June-11	2550.79110	06:54:54	4 × 90	909	1237.6914	-1.3086	-17.152	N
2016-June-11	2550.79702	07:03:26	4 × 90	832	1237.6932	-1.3068	-17.166	N
2016-June-11	2550.80296	07:11:59	4 × 90	924	1237.6950	-1.3050	-17.158	N
2016-June-12	2551.81323	07:26:51	4 × 90	951	1238.0000	-1.0000	-16.689	M
2016-June-12	2551.81924	07:35:31	4 × 90	936	1238.0018	-0.9982	-16.695	M
2016-June-12	2551.82534	07:44:18	4 × 90	909	1238.0037	-0.9963	-16.687	N
2016-June-17	2556.75776	06:07:28	4 × 90	748	1239.4927	0.4927	-16.706	N
2016-June-17	2556.76370	06:16:00	4 × 90	618	1239.4945	0.4945	-16.691	N
2016-June-17	2556.76963	06:24:33	4 × 90	655	1239.4963	0.4963	-16.707	N
2016-June-17	2556.77598	06:33:42	4 × 90	669	1239.4982	0.4982	-16.708	N
2016-June-17	2556.78191	06:42:15	4 × 90	526	1239.5000	0.5000	-16.696	N
2016-June-17	2556.78785	06:50:47	4 × 90	459	1239.5018	0.5018	-16.696	N
2016-June-18	2557.73939	05:41:06	4 × 90	786	1239.7891	0.7891	-17.182	N
2016-June-18	2557.74533	05:49:39	4 × 90	740	1239.7909	0.7909	-17.172	N
2016-June-18	2557.75126	05:58:12	4 × 90	685	1239.7926	0.7926	-17.161	N
2016-June-19	2558.75171	05:58:57	4 × 90	937	1240.0947	1.0947	-16.438	N
2016-June-19	2558.75764	06:07:30	4 × 90	958	1240.0965	1.0965	-16.424	N
2016-June-19	2558.76358	06:16:03	4 × 90	929	1240.0983	1.0983	-16.441	N
2016-June-20	2559.74426	05:48:20	4 × 90	900	1240.3943	1.3943	-16.419	N
2016-June-20	2559.75018	05:56:51	4 × 90	947	1240.3961	1.3961	-16.428	N
2016-June-20	2559.75611	06:05:24	4 × 90	936	1240.3979	1.3979	-16.438	N
2016-June-21	2560.78485	06:46:52	4 × 90	958	1240.7085	1.7085	-17.150	N
2016-June-21	2560.79078	06:55:25	4 × 90	952	1240.7102	1.7102	-17.147	N
2016-June-21	2560.79672	07:03:58	4 × 90	959	1240.7120	1.7120	-17.150	N
2016-June-22	2561.78515	06:47:25	4 × 90	767	1241.0104	2.0104	-16.693	N
2016-June-22	2561.79108	06:55:57	4 × 90	840	1241.0122	2.0122	-16.690	N
2016-June-22	2561.79701	07:04:30	4 × 90	788	1241.0140	2.0140	-16.692	M
2016-June-23	2562.74468	05:49:14	4 × 90	881	1241.3001	2.3001	-16.279	N
2016-June-23	2562.75060	05:57:46	4 × 90	938	1241.3019	2.3019	-16.298	N
2016-June-23	2562.75652	06:06:18	4 × 90	912	1241.3037	2.3037	-16.303	N
2016-June-24	2563.74629	05:51:39	4 × 90	897	1241.6025	2.6025	-17.008	N
2016-June-24	2563.75221	06:00:11	4 × 90	921	1241.6043	2.6043	-17.005	N
2016-June-24	2563.75813	06:08:42	4 × 90	931	1241.6061	2.6061	-17.007	N

varying the differential rotation parameters. Thus these processes must by necessity be iterative to arrive at stable parameter values. It is likely that the methods used here are relatively conservative, and the variation bars are somewhat conservative.

The effects of varying various parameters individually can be seen in Figures C3 and C4. In each, the various components of the magnetic field geometry from Table 3 are plotted as a function of a pair of parameters used in the models. The location of the optimal values are shown in each plot as a black error bar that indicates the extent of the variations used in the calculating the variation bars in Table 3. As can be seen in Figure C3, which examines  $v \sin i$  and inclination angle, the latter is the dominant factor in the reconstruction, particularly with the poloidal components. In Figure C3, we can also deduce that  $\Omega_{eq}$  is the more significant factor of the two when considering differential rotation. Another thing to note is that in both cases, the value of the percentage of the toroidal component is better constrained than those of the poloidal component.

We believe the field configuration parameters we derive are robust and stable, assuming the methodology we use is internally consistent using the derived parameters for  $v \sin i$  and differential rotation.

#### APPENDIX D: TARGET $\chi^2$ DETERMINATION

Here we examine the effect the selection of the target  $\chi^2$  has on the reconstructed field geometry. In Figure D1, we present the plot of the entropy as a function of  $\chi^2$  and the corresponding first and second derivatives, using the method described by Alvarado-Gómez et al. (2015). As noted in the main text, in contrast to Alvarado-Gómez et al. (2015), the range of target  $\chi^2$  is much smaller, and in some cases, rather than a steady increase in entropy ( $S_T$ ), in some cases, there is a decline before a rise [Fig. D1(c-d)] and in others the entropy varies up and down across the domain of target  $\chi^2$

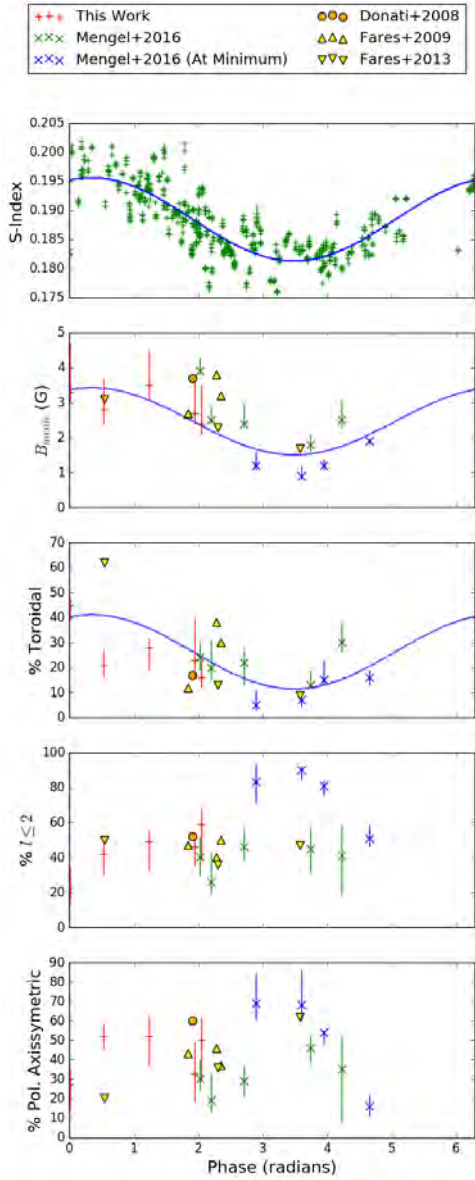


**Figure 9.**  $B_{mean}$  and percentages of energy in various modes of the spherical harmonics compared (lower 4 panels) in relation to the S-index of  $\tau$  Boötis. The symbols correspond to the relevant publication containing these values. Note that prior to Mengel et al. (2016), these published values contained no error or variation bars. In the top 3 panels, the least-squares fit to the period of the S-index cycle is shown. It appears that the  $B_{mean}$  and relative percentage of toroidal component varies with the S-index. However, no particular pattern is evident for the lower two panels.

MNRAS **000**, 1–15 (2017)

[Fig. D1(a)], resulting in a significant scatter in the first and second derivatives. We attribute this to the fact that  $\tau$  Boötis has a very small magnetic field, and thus when there is very little information at the higher target  $\chi_r^2$  values, the entropy behaves somewhat randomly before settling down into a smooth growth. With this caveat, it appears that the method described by Alvarado-Gómez et al. (2015) is robust when applied to  $\tau$  Boötis.

In the upper panels of Figure D1, the plots show the variation of the field geometry values from Table 3, independent of other parameter variation as described in Appendix C. We do not consider  $B_{mean}$  variation here as it is axiomatic that  $B_{mean}$  increases with decreasing target  $\chi_r^2$ . What is immediately apparent is that the percentage of toroidal field in all cases is relatively well-constrained within a small range, usually of  $\sim 10$  percentage points. However in most cases, over the range of target  $\chi_r^2$  the poloidal components do not seem to be particularly well-constrained, varying by as much as 30 percentage point. Additionally, there is no uniformity in the nature of the change, nor does the phase coverage or sampling appear to play a significant part (although given the small sample of epochs, a wider simulation study may show a systematic effect).

Further work on characterising the effects of target  $\chi_r^2$  on modelling would be a useful addition to this useful systematisation of selection of a stopping criteria.

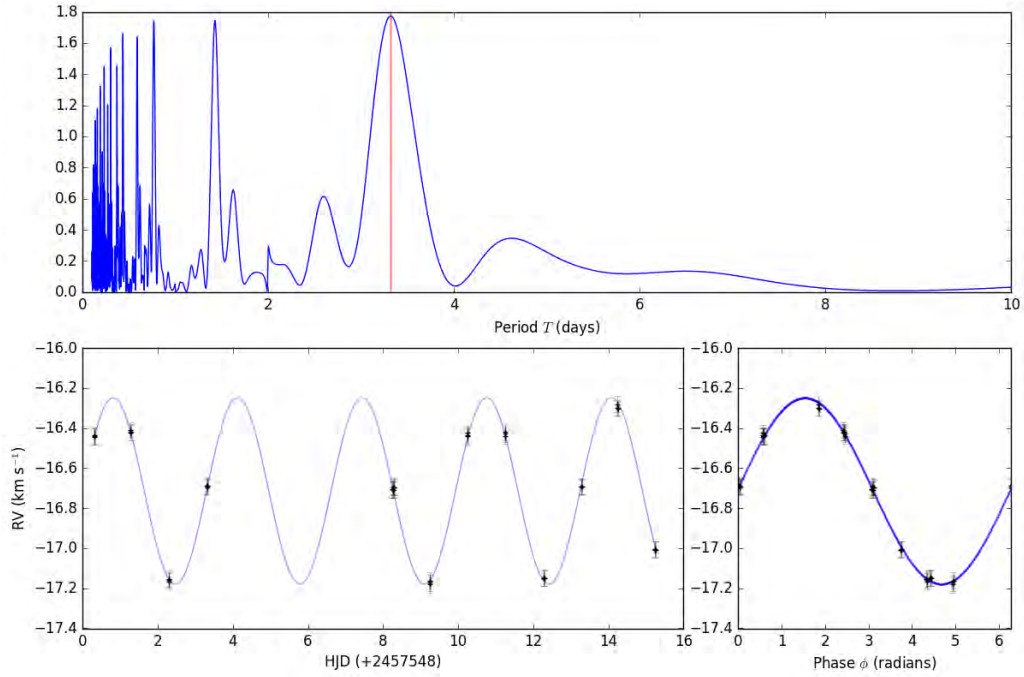


**Figure B1.** Radial velocity of  $\tau$  Boötis used to determine the period of  $\tau$  Boötis b using the data from Table A2. The upper panel is a Lomb-Scargle periodogram, used to estimate the period, with the maximum power indicated by the vertical red line. The lower left panel shows a least-squares fit to the data using the periodogram estimate as initial guess. The lower right figure shows the phase folded data. Error bars in the lower two panels correspond to the long-term radial velocity stability estimate for ESPaDOnS ( $\sim 30 \text{ km s}^{-1}$ ).

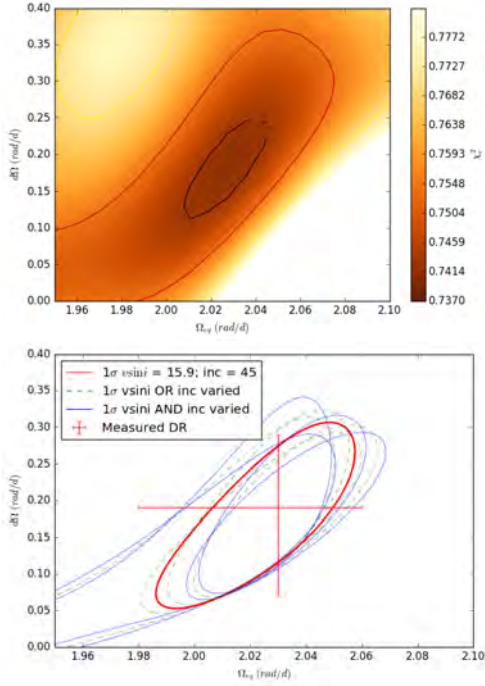


**Figure C1.** Differential rotation determination for June 22-July 03 2016. A Zeeman Doppler map for each combination of the differential rotation parameters ( $\Omega_{eq}, d\Omega$ ) is produced. The upper panel shows the reduced  $\chi^2$  of the produced solution as a function of ( $\Omega_{eq}, d\Omega$ ) for the optimally-selected stellar parameters, in this case  $v \sin i = 15.9 \text{ km s}^{-1}$  and inclination of  $45^\circ$ . The lower panel, shows second-order polynomial fits for the  $1\sigma$  threshold paraboloids surrounding the minimum  $\chi^2$  value, where the red paraboloid corresponds to the plot in the upper panel. Other paraboloids represent fits to the corresponding DR calculations varying the  $v \sin i \pm 1 \text{ km s}^{-1}$  and the stellar inclination  $\pm 5^\circ$  independently (dashed green) and the  $v \sin i$  and inclination angle together (blue). The overall variation bars are used to derive the uncertainty in the measured DR parameters shown in Table 2.

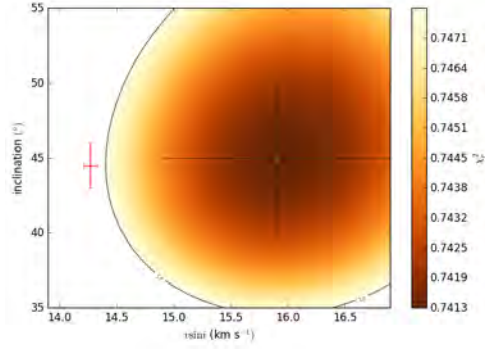


**Figure C2.** Optimal  $v \sin i$  and inclination for June 22-July 03. A Zeeman Doppler map for each combination of the parameters is produced. The plot shows the reduced  $\chi^2$  of the produced solutions as a function of ( $v \sin i, \text{inclination}$ ). The contour shows a  $1\sigma$  threshold surrounding the minimum  $\chi^2$  value. The yellow cross indicates  $v \sin i = 15.9 \text{ km s}^{-1}$  and inclination of  $45^\circ$ , the typical values for these parameters used in this and previous works on  $\tau$  Boötis, and the black error bar indicates the variations used in calculating variation bars for field components. The red cross indicates the published values of  $v \sin i$  and inclination from Table 1.

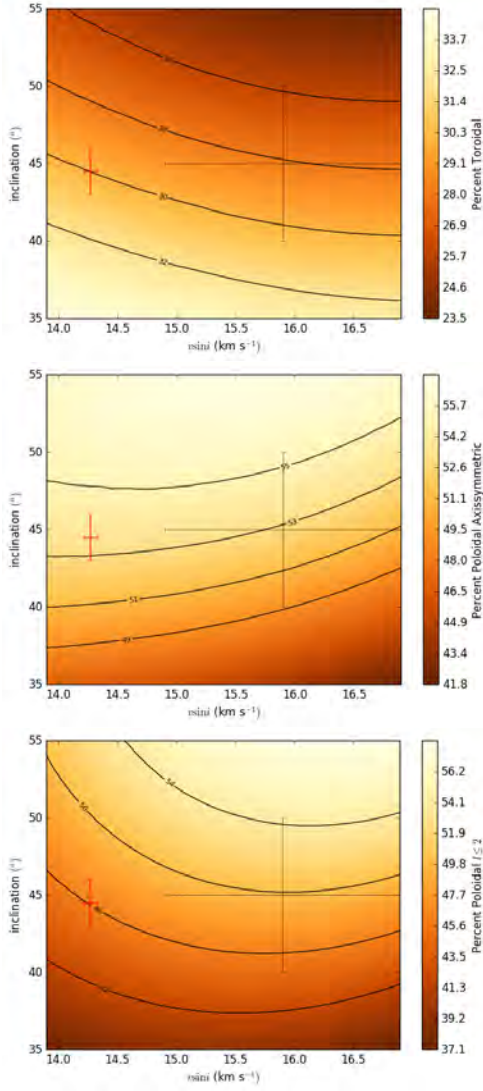


**Figure C3.** Plots indicating the variations in large-scale magnetic field components as a function of  $v \sin i$  and inclination for June 22–July 03. The black error bar indicates the variations used in calculating variation bars for field components, and is centred on  $v \sin i = 15.9 \text{ km s}^{-1}$  and inclination of  $45^\circ$ , the typical values for these parameters used in this and previous works on  $\tau$  Boötis. The red cross indicates the published values of  $v \sin i$  and inclination from Table 1. The plots are from top to bottom, the percentage of toroidal field, the percentage of poloidal field in axisymmetric modes, and finally the percentage of poloidal field in modes  $l \leq 2$ .

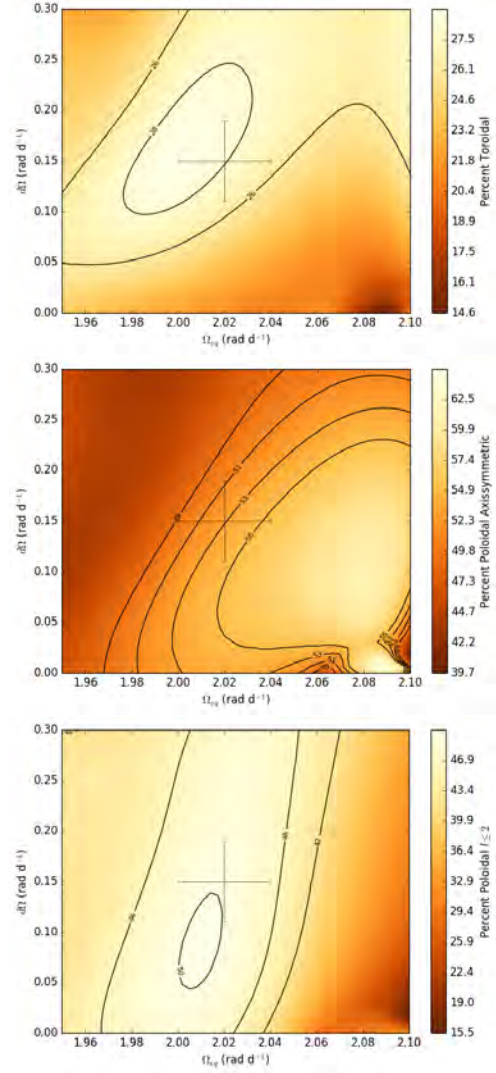


**Figure C4.** Plots indicating the variations in large-scale magnetic field components as a function of  $(\Omega_{\text{eq}}, d\Omega)$  for June 22–July 03. The black error bar indicates the variations used in calculating variation bars for field components, and is centred on the differential rotation measurement for this epoch. The plots are from top to bottom, the percentage of toroidal field, the percentage of poloidal field in axisymmetric modes, and finally the percentage of poloidal field in modes  $l \leq 2$ .

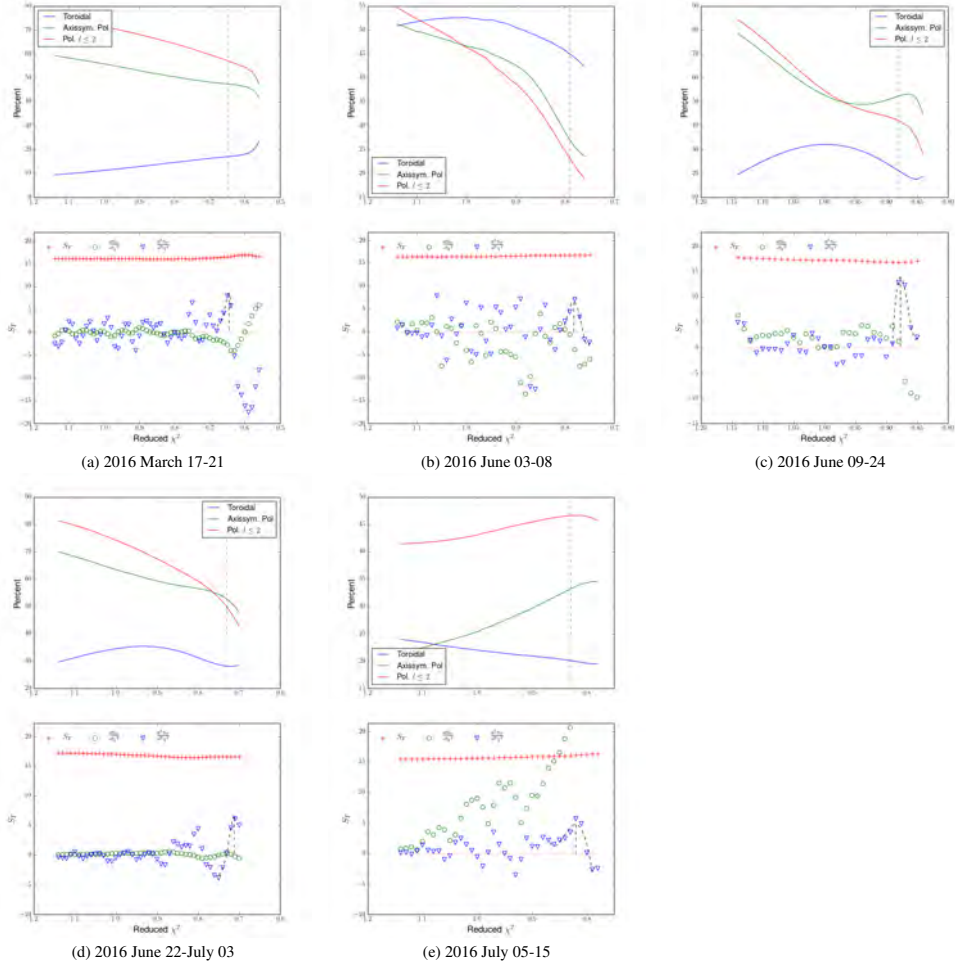


**Figure D1.** Determination of optimal  $\chi^2$  for each map epoch (upper panels, a-e). Red indicates the entropy,  $S_T$ , with green and blue the first and second derivatives respectively (note the first and second derivatives are scaled for clarity - the actual values are not significant, rather the location maximum value of the second derivative is the significant factor). The dashed vertical line shows the maximum second derivative. In the upper panels, the effect of changing  $\chi^2$  on the field components as labelled, and the dashed line showing the optimal  $\chi^2$  from the corresponding lower panel. Note that the percentage of toroidal field (blue) is relatively well constrained, however this is not the case for poloidal axisymmetry or the amount of dipolar+quadrupolar field.

#### 4.2 OBSERVATIONS OF $\tau$ BOÖTIS JANUARY AND FEBRUARY 2017

Further observations of  $\tau$  Boötis were obtained from the NARVAL instrument in January and February 2017. While too late in the PhD for a comprehensive analysis and inclusion in the paper in preparation, preliminary results from these observations are presented here. The journal of observations is shown in Table 4.1. The methods described in Sec. 4.1 (Mengel et al., 2017a, Sec. 5) were applied to produce a Zeeman Doppler Map of  $\tau$  Boötis from this epoch.

Applying the method of determining differential rotation parameters described in Mengel et al. (2017a, Sec. 5 and Appendix C), values for  $\Omega_{eq}$  and  $d\Omega$  of  $1.91_{-0.04}^{+0.04}$  rad d<sup>-1</sup> and  $0.01_{-0.09}^{+0.09}$  rad d<sup>-1</sup> respectively were determined. The method for determining the target  $\chi_r^2$  from Mengel et al. (2017a, Sec. 5 and Appendix D) was used to find the optimum value of 0.78.

The Stokes  $V$  profiles for the period 15 February 2017 through 22 February 2017 are shown in Figure 4.1, with the observed profiles in red, and the reconstructed profiles in black. The observations from 04 January and 06 January were not used in the mapping as they are separated too far from the other observations. The resulting ZDI

**Table 4.1:** Journal of observations of  $\tau$  Boötis January-February 2017 taken using NARVAL at TBL. Columns list the UT date, the heliocentric Julian date (at mid-exposure), the UT time (at mid-exposure), the exposure time, the peak signal-to-noise ratio (SNR) of each observation at around 700 nm, the rotational cycle from the ephemeris, the rotational phase (0.0 being approximately the centre of the observing run), the radial velocity (RV) associated with each exposure, and whether a magnetic signature is detected (D), marginally detected (M) or is below the detection threshold (N). Note the two observations from January were not used in the mapping, so no rotational phase is listed.

Date	HJD (245 0000+)	UT (h:m:s)	$T_{exp}$ (s)	SNR	Cycle	$\phi_{rot}$	RV (km s <sup>-1</sup> )	Detection
2017-Jan-04	7757.74861	05:59:42	4 × 600	1319	1300.1699	-	-16.410	N
2017-Jan-07	7760.73668	05:42:10	4 × 600	1246	1301.0719	-	-16.580	M
2017-Feb-15	7799.71525	05:06:44	4 × 600	1302	1312.8392	-1.1608	-17.236	D
2017-Feb-16	7800.71449	05:05:31	4 × 600	1181	1313.1409	-0.8591	-16.458	D
2017-Feb-17	7801.64833	03:30:10	4 × 600	1364	1313.4228	-0.5772	-16.648	M
2017-Feb-18	7802.64306	03:22:28	4 × 600	1337	1313.7231	-0.2769	-17.282	D
2017-Feb-19	7803.64089	03:19:15	4 × 600	1355	1314.0243	0.0243	-16.749	D
2017-Feb-20	7804.66448	03:53:07	4 × 600	1170	1314.3333	0.3333	-16.529	N
2017-Feb-22	7806.66228	03:49:44	4 × 600	1231	1314.9364	0.9364	-17.052	M

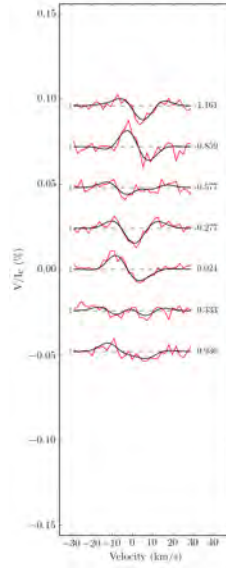


**Figure 4.1:** Stokes  $V$  parameters for  $\tau$  Boötis from February 2017. The observed profiles are shown in red, while synthetic profiles are shown in black. On the left of each profile we show a  $\pm 1\sigma$  error bar. The rotational cycle of each observation is indicated on the right of each profile.

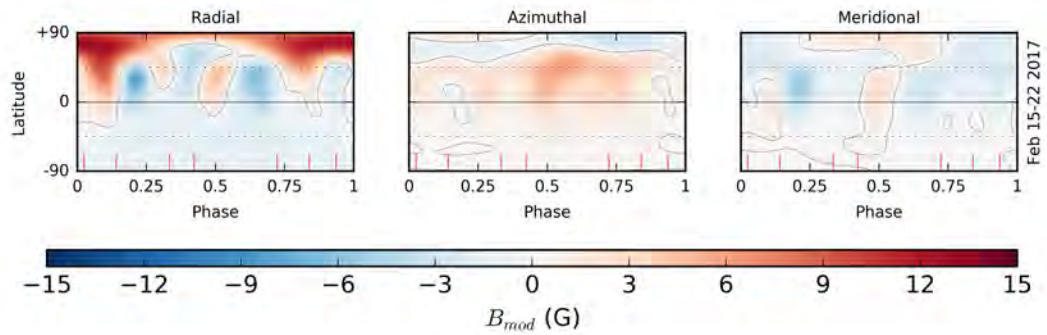


**Figure 4.2:** Magnetic topology of Boötis reconstructed from profiles in Fig. 4.1. The radial, azimuthal and meridional components of the field (with magnetic field strength labelled in G) are depicted for February 2017 from TBL/NARVAL. The contour line indicates where  $B_{mod}$  is zero. The red ticks along the lower x-axes indicate the observational phases for each epoch.

maps are shown in Figure 4.2.

Finally, the longitudinal magnetic field and the S-index was calculated for each observation, and these are shown in Figure 4.3. Figure 4.3 is an extended version of [Mengel et al. \(2017a, Fig. 3\)](#).

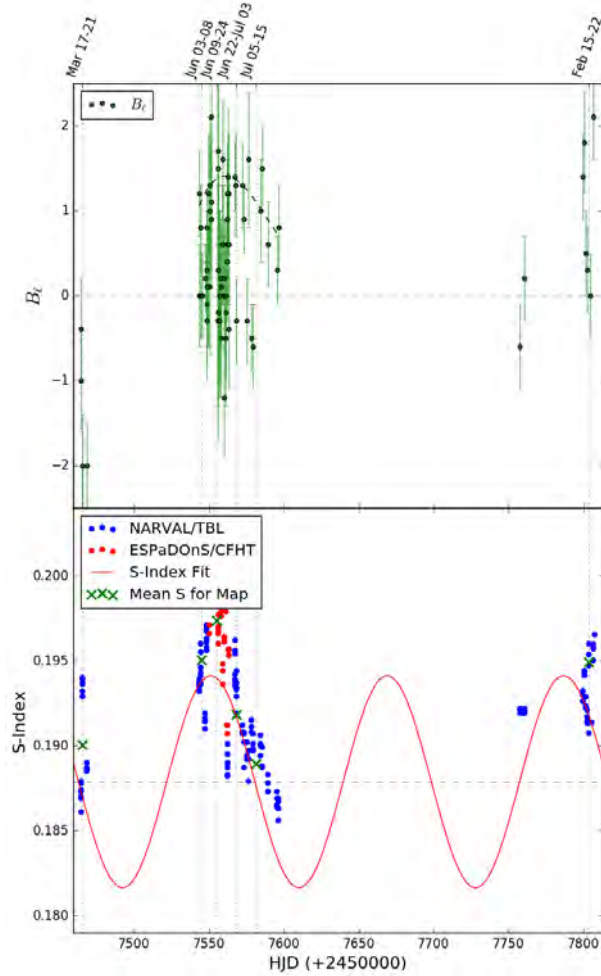


**Figure 4.3:** Longitudinal magnetic field ( $B_l$ ) of  $\tau$  Boötis over the epochs of observation from [Mengel et al. \(2017a\)](#) and January-February 2017 (upper panel) and corresponding S-Index (lower panel). In the lower panel, the red points indicate observations taken from ESPaDOnS, blue from NARVAL. The green cross indicates the mean S-Index for the map generated at that epoch. Note that the dominant polarity has changed from negative for the observations in March 2016 to positive for the June-July 2016. In January 2017, the polarity of the strongest measurement is negative, and in February the dominant polarity is positive. Note that cancellation effects lead to numerous results where  $B_l$  is close to zero. However, in the epochs in June-July 2016, the maximum value of the measured  $B_l$  declines as the S-index declines.

#### 4.2.1 DISCUSSION OF JANUARY-FEBRUARY 2017 OBSERVATIONS OF $\tau$ BOÖTIS

The observations of  $\tau$  Boötis from January and February 2017 confirm the magnetic cycle observed in the previous chapters. The observations in June and July 2016 are separated from those in February by two chromospheric activity cycles (see Fig. 4.3,

lower panel), and thus two reversals of the large-scale dipolar field should result in the same polarity (positive, as indicated by red in the maps) in the radial field for these epochs. This is what is observed. The maximum longitudinal magnetic field measured for the two observations in January, well before the chromospheric peak, is in the opposite polarity (negative), as expected. However given the uncertainties due to cancellation effects in measurements of the longitudinal field, this observation should be treated as tentative as more observations would be required for full coverage and mapping.

These observations, coupled with the observations from the [Mengel et al. \(2016\)](#) and [Mengel et al. \(2017a\)](#), serve to confirm that the magnetic cycle of  $\tau$  Boötis is indeed rapid ( $\sim 240$  d) and follows the chromospheric cycle.

#### 4.3 SUMMARY OF RESULTS

It is clear that the star  $\tau$  Boötis exhibits an extremely rapid magnetic cycle - the most rapid magnetic cycle observed on a solar-type star. It is confirmed that the large-scale radial field undergoes reversals every  $\sim 120$  d, thus confirming a magnetic cycle of  $\sim 240$  d. These reversals take place between the minimum and maximum of the chromospheric activity cycle, just as on the Sun and on 61 Cyg A. However, unlike these two stars, the azimuthal field component does not always undergo reversal. Additionally, it is not clear that the poloidal field components undergo significant variation, due to the fact that these reconstructed components are not well constrained. The relative amounts of toroidal and poloidal field does vary, and apparently in accordance with the chromospheric activity cycle.

[Mengel et al. \(2017a\)](#) also show that rotational modulation of both Ca II emission and the longitudinal magnetic field are apparent over short timescales.

This unusually rapid magnetic cycle, atypical for this type of star, raises the possibility that the massive planet orbiting close to the star is accelerating the magnetic cycle or otherwise affecting the magnetic field of the star.  $\tau$  Boötis thus remains an important target for future investigations into SPI.

*Eventually, we reach the utmost limits of our telescopes.  
There, we measure shadows and search among ghostly er-  
rors of measurement for landmarks that are scarcely more  
substantial.*

Edwin Hubble

# 5

## Discussion and Conclusions

### 5.1 THE MAGNETIC FIELDS OF PLANET-HOSTING SOLAR-TYPE STARS

Taken as a whole, the large-scale magnetic fields of planet-hosting solar-type stars appear similar to the overall population of solar-type stars. [Mengel et al. \(2017b\)](#) shows clearly that the relationships shown by [Marsden et al. \(2014\)](#) are followed, irrespective of the presence or otherwise of a planetary system. Magnetic field strength (and by implication, detectability) are strongly correlated with stellar age, chromospheric activity and spectral type (which may be used as a rough guide for the depth of the convective zone).

A small positive correlation between the strength of the measured longitudinal magnetic field was found. Apart from this tentative correlation, there are no other obvious effects of star-planet interaction on the observed longitudinal magnetic field for the overall sample. This does not necessarily rule out any such interaction, but may simply imply that any such effects are, in general, too subtle to discern using current

spectropolarimetric techniques. Additionally, the small sample size of [Mengel et al. \(2017b\)](#), particularly with regard to the small number of hot Jupiter systems, may mean that a larger sample of these systems would result in a clearer relationship becoming apparent.

Observational biases in planet-hunting programmes play a part in making the investigation of the magnetic fields of planet-hosting stars more difficult. Planet searches are focussed on stars that are relatively inactive, as stellar activity can mimic behaviour characteristic of the presence of planets. Consequently, the majority of the stars in [Mengel et al. \(2017b\)](#) are relatively inactive, meaning lower inherent magnetic field strength and lower rates of detection with current spectropolarimeters. Ongoing work that can resolve this degeneracy and allow the extension of the study to planet hosts with higher activity could assist with further investigations.

## 5.2 THE MAGNETIC CYCLE OF $\tau$ BOÖTIS

Despite the seeming absence of evidence of SPI in the survey performed in Chapter 2,  $\tau$  Boötis is a unique planet-hosting star whose regular reversals and chromospheric activity cycle is potentially caused by an interaction of its hot Jupiter planet with its shallow convective zone. This speculation is driven by the fact that stars with shallow convective zones and rotation rates similar to  $\tau$  Boötis typically do not exhibit these cyclic behaviours. Indeed, prior to the work presented in this thesis, the nature of the cyclic behaviour of the magnetic field of  $\tau$  Boötis was yet to be firmly established.

In [Mengel et al. \(2016\)](#), the rapid chromospheric activity cycle on the order of  $\sim 117$  d reported by the Mt. Wilson survey was independently confirmed using spectra from NARVAL observations over  $\sim 9$  yr. Given that the chromospheric activity cycle of the Sun and the K5 dwarf 61 Cyg A are correlated with a magnetic cycle, wherein both global large-scale reversals and evolution of the topology occur, it would be tempting to draw the conclusion that a magnetic cycle should be present on  $\tau$  Boötis in a similar manner. However, as stated previously,  $\tau$  Boötis is rotating much more rapidly than the Sun and 61 Cyg A and also has a significantly shallower convective zone. These

factors mean that the dynamo processes may operate differently from both the Sun and 61 Cyg A. Given that global polarity reversals were observed with a cycle period of  $\sim 720$  d, the interval between reversals would be three times longer than the chromospheric cycle, would give rise to speculation that indeed some unique behaviour is observed.

The work presented in Chapter 3 confirmed that the global polarity reversals were happening as expected. Of more significance, however, was the evidence obtained across the chromospheric activity minimum showing that the magnetic field intensity and topology were varying as one would expect with a magnetic cycle coincident with the chromospheric activity cycle. Given this evidence, coupled with a re-examination of previous epochs, a case could be made that observational biases caused by observing the star at predominantly the same time of year and the same location in the activity cycle may mask a shorter cycle of reversals. Further observations of  $\tau$  Boötis across the entire chromospheric activity cycle would confirm these speculations.

### 5.3 THE CONFIRMATION OF AN EXTREMELY RAPID MAGNETIC CYCLE ON $\tau$ BOÖTIS

Further observations of  $\tau$  Boötis (Chapter 4) confirmed the speculation from [Mengel et al. \(2016\)](#) that the global polarity reversals occur every  $\sim 120$  d (i.e a magnetic cycle with a length of  $\sim 240$  d). Additionally, the topology of the large-scale field was observed to change in configuration and intensity, following the chromospheric activity cycle. While not strictly “solar-type” as with 61 Cyg A (as the azimuthal field does not reverse every half-cycle), this shows that  $\tau$  Boötis exhibits a very rapid magnetic cycle that is synchronised with the chromospheric activity cycle, similar to the Sun (and 61 Cyg A).

This cycle is by far the fastest yet observed. Both the Sun and 61 Cyg A each exhibit a cycle on the order of several years in length, whereas that of  $\tau$  Boötis is on the order of months. This presents a challenge to existing models of shallow convective envelope stars. To date, other stars such as  $\tau$  Boötis, with thin convective zones and rapid rotation do not exhibit this type of cycle ([Schröder et al., 2013](#)). Field reversals have

been shown (e.g. [Morgenthaler et al., 2011](#)) on one or two other shallow convective zone stars, but have not been demonstrated to show stable cyclic behaviour (more observations of these stars may yet yield definitive evidence of cycles). This leads to the question of whether this rapid cycle is unique to  $\tau$  Boötis amongst this type of star. Further, if so, is the presence of the cycle due to interaction between the star and the hot Jupiter accelerating or sustaining the dynamo? As [Wolk et al. \(2015\)](#) shows, there may be a “Goldilocks zone” for SPI, where some planetary arrangements may enhance activity, others have no effect, while others may disrupt the dynamo.

It could be further speculated that as stars spin down, chaotic variation in the magnetic activity begins to settle into stable cycles. For example, the star HD 190771 has shown reversals of the radial field, but not also of the azimuthal field. HD 190771 has a rotation period of 8.8 d with convective zone somewhat larger than that of  $\tau$  Boötis. Observations of stars of similar ages or rotation rates may illustrate a common stage of evolution as the stars spin down, eventually the toroidal field becoming weak enough to undergo reversal every half cycle. Further observations of F-type stars, with and without hot Jupiters would be required to settle the question of whether hot Jupiters can sustain, accelerate or otherwise affect the magnetic field and magnetic cycle of their host star.

Of additional interest, the rotational modulation of the longitudinal magnetic field of  $\tau$  Boötis was shown to be anti-correlated with the rotational modulation of the chromospheric activity (Ca II H&K emission). As this emission is correlated with small-scale features, this can be interpreted as the associated small-scale magnetic features cancelling each other, resulting in lower magnetic flux integrated over the disc when the S-index is high. On longer time-scales, the maximum intensity of the longitudinal magnetic field was shown to broadly follow the chromospheric cycle.

#### 5.4 CONCLUSIONS

In this thesis, it was shown that there are indications of a small positive relationship between the tidal effects of massive, close-in planets on their host star and the star’s

magnetic field strength. For the peculiar case of  $\tau$  Boötis, this work confirms the presence of an extremely rapid magnetic cycle, atypical for this type of star, suggesting that the massive hot Jupiter  $\tau$  Boötis b may play a part in accelerating the magnetic cycle. Further, this work shows that the magnetic cycle of  $\tau$  Boötis is synchronised with its chromospheric activity cycle, like the Sun and 61 Cyg A.

## 5.5 THE FUTURE

$\tau$  Boötis provides several opportunities for further study of its cycles. No observations have yet taken place in the part of the chromospheric cycle between its activity minimum and activity maximum. This is the point in the cycle where the global polarity change takes place. Close observation of this part of the cycle should show how the opposite polarity emerges and become dominant, perhaps providing further insight into the dynamo process during reversal. A compelling case could be made to dedicate a spectropolarimetric observing campaign to cover an entire chromospheric cycle period, although this may be difficult to achieve.

$\tau$  Boötis also remains a key target of interest in ongoing monitoring of its magnetic field to better understand its origins and future. Magnetic maps from  $\tau$  Boötis can be used as empirical inputs for modelling its stellar winds (Nicholson et al., 2016), its interactions with any putative planetary magnetic field and the dynamo process in its interior.

In the larger context of the magnetic fields of planet-hosting stars, more targets, both planet- and non-planet-hosting need to be observed over extended periods to ascertain whether cycles exist and whether or not the establishment of cycles is inherent across the entire population or whether, in some cases, hot Jupiters in particular may facilitate the establishment of cycles. This is challenging, as in the case of slower rotators, the magnetic fields are weak and the cycles may extend to several years.

Future instruments, particularly near-infrared spectropolarimeters in development, such as SPIRou<sup>2</sup> (Thibault et al., 2012) will be of importance in these investigations,

---

<sup>2</sup><http://spirou.irap.omp.eu>

especially for cooler solar-type stars. Spectral lines in the near-infrared are much more Zeeman-sensitive, and the contrast between spot regions and the photosphere is lower. These factors will allow for more detailed investigation of magnetic fields on solar-type stars, particularly older stars with weaker magnetic fields. Increased sensitivity may also reveal possible SPI due to persistent active magnetic regions on stars hosting hot Jupiters.

The work presented here shows that of the population of stars broadly classified as solar-type - having a convective zone, yet not being fully convective; broadly speaking F, G and K type stars - a range from K<sub>5</sub> (61 Cyg A) through F7 ( $\tau$  Boötis) *can* exhibit stable magnetic cycles that follow the cycles of magnetic activity proxies such as chromospheric activity. More observations of stars with shallow convective zones are required to determine whether  $\tau$  Boötis is unusual in this respect or typical. Should  $\tau$  Boötis turn out to be atypical, then suspicions must grow as to the effect the hot Jupiter may have.

Given our incomplete understanding of stellar magnetic fields and their role in stellar and planetary evolution, studies of magnetic fields and cycles and the potential interactions between planets and their host stars promises to remain an area of intense interest for the future.

## References

Note that the references presented here are for Chapters 1 and 5, Section 4.2, and in introductory sections of the remaining chapters. References for the papers included in Chapters 2 - 4 are included in the references sections of the papers.

Adams, W. S. & Nicholson, S. B. (1933). IV. The Nature of the Solar Cycle. *Proceedings of the National Academy of Science*, 19, 371–375.

Augustson, K. C., Brun, A. S., & Toomre, J. (2013). Dynamo Action and Magnetic Cycles in F-Type Stars. *Ap.J.*, 777(2), 153.

Aurière, M. (2003). Magnetism and activity of the sun and stars. In J. Arnaud & N. Meunier (Eds.), *Magnetism and Activity of the Sun and Stars*, volume 9 of *EAS Pub. Ser.* (pp. 105).

Babcock, H. W. (1947). Zeeman effect in stellar spectra. *Ap. J.*, 105, 105–119.

Babcock, H. W. (1961). The topology of the Sun's magnetic field and the 22-year cycle. *Ap. J.*, 133, 572–587.

Bagnulo, S., Landolfi, M., Landstreet, J. D., Landi Degl'Innocenti, E., Fosfati, L., & Sterzik, M. (2009). *PASP*, 121(883), 993–1015.

Baliunas, S. L., Donahue, R. A., Soon, W. H., & Henry, G. W. (1998). Activity Cycles in Lower Main Sequence and Post Main Sequence Stars: The HK Project. In R. A. Donahue & J. A. Bookbinder (Eds.), *Cool Stars, Stellar Systems and the Sun*, volume 154 (pp. 153–172).: Ast. Soc. Pac.

- Barabash, S., Fedorov, A., Lundlin, R., & Sauvaud, J.-A. (2007). Martian atmospheric erosion rates. *Science*, 315, 501–503.
- Bell, S. J. & Hewish, A. (1967). *Nature*, 215(July 1.), 25 – 30.
- Boro Saikia, S., Jeffers, S. V., Morin, J., Petit, P., Folsom, C. P., Marsden, S. C., Donati, J.-F., Cameron, R., Hall, J. C., Perdelwitz, V., Reiners, A., & Vidotto, A. A. (2016). A solar-like magnetic cycle on the mature K-dwarf 61 Cygni A (HD 201091). *Astron. Astrophys.*, 594, A29.
- Brown, S. F., Donati, J.-F., Rees, D. E., & Semel, M. (1991). Zeeman-Doppler imaging of solar-type and Ap stars. IV. Maximum entropy reconstruction of 2D magnetic topologies. *Astron. Astrophys.*, 250, 463–474.
- Butler, R. P. & Marcy, G. W. (1996). A planet orbiting 47 Ursae Majoris. *Ap. J.*, 464, L153–L156.
- Cameron, A. C. & Donati, J.-F. (2002). Doin’ the twist: secular changes in the surface differential rotation on AB Doradus. *MNRAS*, 329, L23–L27.
- Carter, B., Brown, S., Donati, J.-F., Rees, D., & Semel, M. (1996). Zeeman Doppler imaging of stars with the AAT. *PASA*, 13, 150.
- Catala, C., Donati, J.-F., Shkolnik, E., Bohlender, D., & Alecian, E. (2007). The magnetic field of the planet-hosting star  $\tau$  Bootis. *MNRAS*, 374, L42–L46.
- Collett, E. (2005). *Field Guide to Polarization*. 1000 20th Street, Bellingham, WA 98227-0010 USA: SPIE.
- Cuntz, M., Saar, S. H., & Musielak, Z. E. (2000). On stellar activity enhancement due to interactions with extrasolar giant planets. *Ap. J.*, 533, L151–154.
- DeRosa, M. L., Brun, A. S., & Hoeksema, J. T. (2012). Solar Magnetic Field Reversals and the Role of Dynamo Families. *Ap. J.*, 757(1), 96.
- Dikpati, M. & Charbonneau, P. (1999). A Babcock-Leighton flux transport dynamo with solar-like differential rotation. *Ap. J.*, 518, 508–520.

- Donati, J.-F. & Brown, S. F. (1997). Zeeman-Doppler imaging of active stars V. Sensitivity of maximum entropy magnetic maps to field orientation. *Astron. Astrophys.*, 326, 1135–1142.
- Donati, J.-F. & Cameron, A. C. (1997). Differential rotation and magnetic polarity patterns on AB Doradus. *MNRAS*, 291, 1–19.
- Donati, J.-F., Cameron, A. C., & Petit, P. (2003). Temporal fluctuations in the differential rotation of cool active stars. *MNRAS*, 345, 1187–1199.
- Donati, J.-F., Howarth, I., Jardine, M. M., Petit, P., Catala, C., Landstreet, J. D., Bouret, J.-C., Alecian, E., Barnes, J. R., Forveille, T., Paletou, F., & Manset, N. (2006). The surprising magnetic topology of  $\tau$  Sco: fossil remnant or dynamo output? *MNRAS*, 370, 629–644.
- Donati, J.-F. & Landstreet, J. D. (2009). Magnetic fields of nondegenerate stars. *Annu. Rev. Astron. Astrophys.*, 47, 333–370.
- Donati, J.-F., Moutou, C., Farès, R., Bohlender, D., Catala, C., Deleuil, M., Shkolnik, E., Cameron, A. C., Jardine, M. M., & Walker, G. A. H. (2008). Magnetic cycles of the planet-hosting star  $\tau$  Bootis. *MNRAS*, 385, 1179–1185.
- Donati, J.-F., Semel, M., Carter, B. D., Rees, D. E., & Cameron, A. C. (1997). Spectropolarimetric observations of active stars. *MNRAS*, 291, 658–682.
- Donati, J. F., Yu, L., Moutou, C., Cameron, A. C., Malo, L., Grankin, K., Hébrard, E., Hussain, G. A., Vidotto, A. A., Alencar, S. H., Haywood, R. D., Bouvier, J., Petit, P., Takami, M., Herczeg, G. J., Gregory, S. G., Jardine, M. M., & Morin, J. (2017). *MNRAS*, 465(3), 3343–3360.
- Fares, R., Donati, J.-F., Moutou, C., Bohlender, D., Catala, C., Deleuil, M., Shkolnik, E., Cameron, A. C., Jardine, M. M., & Walker, G. A. H. (2009). Magnetic cycles of the planet-hosting star  $\tau$  Bootis – II. A second magnetic polarity reversal. *MNRAS*, 398, 1383–1391.
- Fares, R. et al. (2017). in preparation.

- Fares, R., Moutou, C., Donati, J.-F., Catala, C., Shkolnik, E. L., Jardine, M. M., Cameron, A. C., & Deleuil, M. (2013). A small survey of the magnetic fields of planet-host stars. *MNRAS*, 435, 1451–1462.
- Folsom, C. P. (2013). *Chemical abundances of very young intermediate mass stars*. Phd, The Queen’s University, Belfast and Armagh Observatory.
- Fossati, L., Bagnulo, S., Elmasli, A., Haswell, C. A., Holmes, S., Kochukhov, O., Shkolnik, E. L., Shulyak, D. V., Bohlender, D., Albayrak, B., Froning, C., & Hebb, L. (2010). A Detailed Spectropolarimetric Analysis of the Planet-Hosting Star WASP-12 ,. *Ap. J.*, 720(1), 872–886.
- Gleissberg, W. (1939). A long-periodic fluctuation of the sun-spot numbers. *The Observatory*, 62, 158–159.
- Hale, G. E. (1908). On the probable existence of a magnetic field in Sun-spots. *Ap. J.*, 28, 315–343.
- Hale, G. E., Ellerman, F., Nicholson, S. B., & Joy, A. H. (1919). The magnetic polarity of sun-spots. *Ap. J.*, 49, 153–178.
- Hathaway, D. H. (2010). The solar cycle. *Living Rev. Sol. Phys.*, 7, 1–65.
- Jeffers, S. V., Donati, J.-F., Alecian, E., & Marsden, S. C. (2011). Observations of non-solar-type dynamo processes in stars with shallow convective zones. *MNRAS*, 411(2), 1301–1312.
- Johansson, E. P. G., Müller, J., & Motschmann, U. (2011). Quasiparallel and parallel stellar wind interaction and the magnetospheres of close-in exoplanets. *Astro. Nachr.*, 332(9/10), 1062–1067.
- Kemp, J. C., Swedlund, J. B., Landstreet, J. D., & Angel, J. R. P. (1970). *Ap. J.*, 161, L77–L79.
- Kochukhov, O., Lueftinger, T., Neiner, C., & Alecian, E. (2014). *Astron. Astrophys.*, 565, 1–14.
- Kochukhov, O. & Wade, G. A. (2016). *Astron. Astrophys.*, 586, A30.

- Kretke, K. A., Lin, D. N. C., Garaud, P., & Turner, N. J. (2009). Assembling the building blocks of giant planets around intermediate-mass stars. *Ap. J.*, 690, 407–415.
- L. Rosén & O. Kochukhov (2012). *Astron. Astrophys.*, 8, 1–12.
- Lai, D., Foucart, F., & Lin, D. N. C. (2011). Evolution of accreting magnetic protostars and spin-orbit misalignment in exoplanetary systems. *MNRAS*, 412, 2790–2798.
- Landi Degl’Innocenti, E. (1976). *Astron. Astrophys. Supplement Series*, 25, 379.
- Landi Degl’Innocenti, E. & Landolfi, M., Eds. (2004). *Polarization in Spectral Lines*, volume 307 of *Astrophysics and Space Science Library*.
- Lanza, A. F. (2012). Star-planet magnetic interaction and activity in late-type stars with close-in planets. *Astron. Astrophys.*, 544, A23–A39.
- Leighton, R. B. (1969). A magneto-kinematic model of the solar cycle. *Ap. J.*, 156, 1–26.
- Lopez, E. D. & Fortney, J. J. (2013). the Role of Core Mass in Controlling Evaporation: the Kepler Radius Distribution and the Kepler-36 Density Dichotomy. *Ap. J.*, 776(1), 2.
- Maggio, A., Pillitteri, I., Scandariato, G., Lanza, A. F., Sciortino, S., Borsa, F., Bonomo, A. S., Claudi, R., Covino, E., Desidera, S., Gratton, R., Micela, G., Pagano, I., Piotto, G., Sozzetti, A., Cosentino, R., & Maldonado, J. (2015). Coordinated X-Ray and Optical Observations of Star–Planet Interaction in HD 17156. *Ap. J.*, 811(1), L2.
- Marcy, G. W. & Butler, R. P. (1996). A planetary companion to 70 Virginis. *Ap. J.*, 464, L147–L151.
- Marsden, S. C., Petit, P., Jeffers, S. V., Morin, J., Fares, R., Reiners, A., do Nascimento Jr, J.-D., Aurière, M., Bouvier, J., Carter, B. D., Catala,

- C., Dintrans, B., Donati, J.-F., Gastine, T., Jardine, M., Konstantinova-Antova, R., Lanoux, J., Lignières, F., Morgenthaler, A., Ramírez-Vélez, J. C., Théado, S., Grootel, V. V., & the BCool Collaboration (2014). A BCool magnetic snapshot survey of solar-type stars. *MNRAS*, 444, 3517–3536.
- Mathys, G. (1989). The Observation of Magnetic Fields in Nondegenerate Stars. *Fundamentals of Cosmic Physics*, 13, 143–308.
- Matt, S. P., Pinzón, G., Greene, T. P., & Pudritz, R. E. (2012). Spin evolution of accreting young stars. II. Effect of accretion-powered stellar winds. *Ap. J.*, 725, 101–113.
- Maunder, E. W. (1904). Note on the distribution of sun-spots in heliographic latitude, 1874 to 1902. *MNRAS*, 64, 747–761.
- Mayor, M. & Queloz, D. (1995). A Jupiter-mass companion to a solar-type star. *Nature*, 378, 355–359.
- McMaster, W. H. (1961). *Rev. Modern Phys.*, 33(1), 8–28.
- Mengel, M. W., Fares, R., Marsden, S. C., Carter, B. D., Jeffers, S. V., Petit, P., Donati, J.-F., & Folsom, C. P. (2016). The evolving magnetic topology of  $\tau$  Boötis. *MNRAS*, 459(4), 4325–4342.
- Mengel, M. W., Jeffers, S. V., Moutou, C., Marsden, S. C., Fares, R., & Carter, B. D. (2017a). A rapid magnetic cycle on  $\tau$  Boötis. in preparation.
- Mengel, M. W., Marsden, S. C., Carter, B. D., Horner, J., King, R., Fares, R., Jeffers, S. V., Petit, P., Vidotto, A. A., & Morin, J. (2017b). A BCool survey of the magnetic fields of planet-hosting solar-type stars. *MNRAS*, 465(3), 2734–2747.
- Miller, B. P., Gallo, E., Wright, J. T., & Pearson, E. G. (2015). A Comprehensive Statistical Assessment of Star-Planet Interaction. *Ap. J.*, 799(2), 163.
- Morgenthaler, A., Petit, P., Morin, J., Aurière, M., Dintrans, B., Konstantinova-Antova, R., & Marsden, S. (2011). Direct observation of magnetic cycles in Sun-like stars. *Astron. Nachr.*, 332(9-10), 866–871.

Morin, J., Donati, J.-F., Forveille, T., Delfosse, X., Dobler, W., Petit, P., Jardine, M. M., Cameron, A. C., Albert, L., Manset, N., Dintrans, B., Chabrier, G., & Valenti, J. A. (2008). The stable magnetic field of the fully convective star V374 Peg. *MNRAS*, 384, 77–86.

Moss, D. (2001). Magnetic Fields in the Ap and Bp Stars: a Theoretical Overview. In G. Mathys, S. K. Solanki, & D. T. Wickramasinghe (Eds.), *Magnetic Fields Across the Hertzsprung-Russell Diagram*, volume 248 of *Astronomical Society of the Pacific Conference Series* (pp. 305).

Muto, T., Masahiro, M. N., & Inutsuka, S. (2008). The effect of poloidal magnetic field on type i planetary migration: significance of magnetic resonance. *Ap. J.*, 679, 813–826.

Nicholson, B. A., Vidotto, A. A., Mengel, M., Brookshaw, L., Carter, B., Petit, P., Marsden, S. C., Jeffers, S. V., & Fares, R. (2016). Temporal variability of the wind from the star  $\tau$  Boötis. *MNRAS*, 459(2), 1907–1915.

Pacini, F. (1967). *Nature*, 216(5115), 567–568.

Pagano, I., Lanza, A. F., Leto, G., Messina, S., Barge, P., & Baglin, A. (2009). CoRoT-2a magnetic activity: Hints for possible star–planet interaction. *Earth Moon Planets*, 105, 373–378.

Parker, E. N. (1955). Hydromagnetic dynamo models. *Ap. J.*, 122, 293–314.

Parker, E. N. (1977). The origin of solar activity. *Annu. Rev. Astron. Astrophys.*, 15, 45–68.

Penz, T. & Micela, G. (2008). X-ray induced mass loss effects on exoplanets orbiting dM stars. *Astron. Astrophys.*, 479(2), 579–584.

Petit, P., Dintrans, B., Morgenthaler, A., Van Grootel, V., Morin, J., Lanoux, J., Aurière, M., & Konstantinova-Antova, R. (2009). A polarity reversal in the large-scale magnetic field of the rapidly rotating sun HD 190771. *Astron. Astrophys.*, 508(1), L9–L12.

- Petit, P., Dintrans, B., Solanki, S. K., Donati, J.-F., Aurire, M., Lignires, F., Morin, J., Paletou, F., Ramirez, J., Catala, C., & Fares, R. (2008). Toroidal versus poloidal magnetic fields in Sun-like stars: a rotation threshold. *MNRAS*, 388(1), 80–88.
- Petit, P., Donati, J.-F., & Cameron, A. C. (2002). Differential rotation of cool active stars: the case of intermediate rotators. *MNRAS*, 334, 374–382.
- Petit, P., Donati, J.-F., & the ESPaDOnS Project Team (2003). Magnetism and activity of the sun and stars. In J. Arnaud & N. Meunier (Eds.), *Magnetism and Activity of the Sun and Stars*, volume 9 of *EAS Pub. Ser.* (pp.97).
- Pillitteri, I., Wolk, S. J., Lopez-Santiago, J., Günther, H. M., Sciortino, S., Cohen, O., Kashyap, V., & Drake, J. J. (2014). The Corona of HD 189733 and its X-ray Activity. *Ap. J.*, 785(2), 145.
- Piskunov, N. & Kochukhov, O. (2002). *Astron. Astrophys.*, 381(2), 736–756.
- Poppenhaeger, K., Schmitt, J. H. M. M., & Wolk, S. J. (2013). Transit Observations of the Hot Jupiter HD 189733b at X-ray Wavelengths. *Ap. J.*, 773(1), 62.
- Rachkovsky, D. N. (1962). *Izv. Krymskoj Astrofiz. Obs.*, 28, 259–270.
- Rees, D. E., Durrant, C. J., & Murphy, G. A. (1989). *Ap. J.*, 339, 1093.
- Reiners, A. (2010). Magnetic Fields on Cool Stars. *arXiv:1012.1183v1 [astro-ph.SR]*, (pp.12).
- Reiners, A. & Schmitt, J. H. M. M. (2003). Rotation and differential rotation in field F- and G-type stars. *Astron. Astrophys.*, 398, 647–661.
- Rice, J. B. (1991). *Astron. Astrophys.*, 245, 561–566.
- Rice, J. B. & Strassmeier, K. G. (2000). *Astron. Astrophys. Supplement Series*, 147(1), 151–168.

- Rieger, E., Share, G. H., Forrest, D. J., Kanbach, G., Reppin, C., & Chupp, E. L. (1984). A 154-day periodicity in the occurrence of hard solar flares? *Nature*, 312, 623–625.
- Robinson, R. D., Worden, S. P., & Harvey, J. W. (1980). Observations of magnetic fields on two late-type dwarf stars. *Ap. J.*, 236, L155.
- Romanova, M. M. & Lovelace, R. V. E. (2006). The magnetospheric gap and the accumulation of giant planets close to a star. *Ap. J.*, 645, L73–L76.
- Rosén, L., Kochukhov, O., Hackman, T., & Lehtinen, J. (2016). Magnetic fields of young solar twins. *Astron. Astrophys.*, 593, A35.
- Rosén, L., Kochukhov, O., & Wade, G. A. (2013). Strong variable linear polarization in the cool active star II Peg. *MNRAS*, 436, L10–L14.
- Rosén, L., Kochukhov, O., & Wade, G. A. (2014). Zeeman Doppler imaging of a cool star using line profiles in all four Stokes parameters for the first time. *arXiv:1408.4035 [astro-ph.SR]*.
- Saar, S. H., Cuntz, M., & Shkolnik, E. (2004). Stellar Activity Enhancement by Planets: Theory and Observations. In A. K. Dupree & A. O. Benz (Eds.), *Stars as Suns : Activity, Evolution and Planets*, volume 219 of *IAU Symposium* (pp. 355).
- Sanderson, T. R., Appourchaux, T., Hoeksema, J. T., & Harvey, K. L. (2003). Observations of the Sun’s magnetic field during the recent solar maximum. *Journal of Geophysical Research: Space Physics*, 108(A1), 1–10.
- Schatzman, E. (1962). A theory of the role of magnetic activity during star formation. *Ann. d’Astro.*, 25, 18.
- Schrijver, C. J. & Zwaan, C. (2000). *Solar and stellar magnetic activity*. Cambridge Astrophysics Series. Cambridge University Press.
- Schröder, K.-P. K.-P., Mittag, M., Hempelmann, A., González-Pérez, J. N., & Schmitt, J. H. M. M. (2013). What do the Mt. Wilson stars tell us about solar activity? *Astron. Astrophys.*, 554, A50.

- See, V., Jardine, M., Vidotto, A. A., Donati, J.-F., Boro Saikia, S., Bouvier, J., Fares, R., Folsom, C. P., Gregory, S. G., Hussain, G., Jeffers, S. V., Marsden, S. C., Morin, J., Moutou, C., do Nascimento, J. D., Petit, P., & Waite, I. A. (2016). The connection between stellar activity cycles and magnetic field topology. *MNRAS*, 462, 4442–4450.
- Semel, M. (1989). Zeeman-Doppler imaging of active stars. I – Basic principles. *Astron. Astrophys.*, 225, 456–466.
- Shkolnik, E., Walker, G. A. H., Bohlender, D. A., Gu, P.-G., & Kürster, M. (2005). Hot jupiters and hot spots: the short- and long-term chromospheric activity on stars with giant planets. *Ap. J.*, 622, 1075–1090.
- Skilling, J. & Bryan, R. K. (1984). Maximum entropy image reconstruction – General algorithm. *MNRAS*, 211, 111–124.
- Stenflo, J. O. (2013). *Astron. Astrophys. Rev.*, 21(1), 66.
- Thibault, S., Rabou, P., Donati, J.-F., Desaulniers, P., Dallaire, X., Artigau, E., Pepe, F., Micheau, Y., Vallée, P., Pepe, F., Barrick, G., Reshetov, V., Hernandez, O., Saddlemyer, L., Pazder, J., Parès, L. P., Doyon, R., Delfosse, X., Kouach, D., & Loop, D. (2012). SPIRou @ CFHT: spectrograph optical design. In *Ground-based and Airborne Instrumentation for Astronomy IV*, volume 8446 of *Proceedings of the SPIE* (pp. 844630).
- Thompson, M. J., Christensen-Dalsgaard, J., Miesch, J., & Toomre, J. (2003). The internal rotation of the sun. *Annu. Rev. Astron. Astrophys.*, 41, 599.
- Tobias, S. M. (2002). The solar dynamo. *Phil. Trans. R. Soc. Lond. A*, 360, 2741–2756.
- Unno, W. (1956). *PASJ*, 8, 108–125.
- Vidotto, A. A., Fares, R., Jardine, M., Donati, J.-F., Opher, M., Moutou, C., Catala, C., & Gombosi, T. I. (2012). The stellar wind cycles and planetary radio emission of the  $\tau$  Boo system. *MNRAS*, 423, 3285–3298.

- Vogt, S. S., Penrod, G. D., & Hatzes, A. P. (1987). Doppler images of rotating stars using maximum entropy image reconstruction. *Ap. J.*, 321, 496–515.
- Wade, G. A., Donati, J.-F., Landstreet, J. D., & Shorlin, S. L. S. (2000). *MNRAS*, 313(4), 823–850.
- Walker, G. A. H., Croll, B., Matthews, J. M., Kusching, R., Huber, D., Weiss, W. W., Shkolnik, E., Rucinski, S. M., Guenther, D. B., Moffatt, A. F., & Sasselov, D. (2008). MOST detects variability on  $\tau$  Bootis A possibly induced by its planetary companion. *Astron. Astrophys.*, 482, 691–697.
- Wehlau, W. & Rice, J. (1993). Zeeman doppler imaging. In M. M. Dworetzky, F. Castelli, & R. Faraggiana (Eds.), *IAU Colloq. 138: Peculiar versus Normal Phenomena in A-type and Related Stars*, volume 44 of *Astronomical Society of the Pacific Conference Series* (pp. 247).
- Wilson, O. C. (1968). Flux measurements at the centers of stellar H and K lines. *Ap. J.*, 153, 221.
- Wilson, O. C. (1978). Chromospheric variations in main-sequence stars. *Ap. J.*, 226, 379.
- Wittenmyer, R. A., Horner, J., Mengel, M. W., Butler, R. P., Wright, D. J., Tinney, C. G., Carter, B. D., Jones, H. R. A., Anglada-Escudé, G., Bailey, J., & O’Toole, S. J. (2017). The Anglo-Australian Planet Search. XXV. A Candidate Massive Saturn Analog Orbiting HD 30177. *A. J.*, 153, 167.
- Wittenmyer, R. A., Johnson, J. A., Butler, R. P., Horner, J., Wang, L., Robertson, P., Jones, M. I., Jenkins, J. S., Brahm, R., Tinney, C. G., Mengel, M. W., & Clark, J. (2016). The Pan-Pacific Planet Search. IV. Two Super-Jupiters in a 3:5 Resonance Orbiting the Giant Star HD 33844. *Ap. J.*, 818, 35.
- Wolk, S. J., Pillitteri, I., & Poppenhaeger, K. (2015). Observed effects of star-planet interaction. *Proceedings of the International Astronomical Union*, 11(S320), 382–387.

Wright, J. T., Marcy, G. W., Butler, R. P., & Vogt, S. S. (2004). Chromospheric Ca II Emission in Nearby F, G, K, and M Stars. *Ap. J. Supp. Ser.*, 152(2), 261–295.

Zuluaga, J. I., Mason, P. A., & Cuartas-Restrepo, P. A. (2016). Constraining the Radiation and Plasma Environment of the Kepler Circumbinary Habitable-Zone Planets. *Ap. J.*, 818(2), 160.



# Temporal variation of the wind from the star $\tau$ Boötis

THE RADIAL FIELD MAPS OF THE MAGNETIC field of  $\tau$  Boötis were used as boundary condition inputs for MHD modelling of the winds of the star.

A.1 NICHOLSON ET AL. (2016) “TEMPORAL VARIATION OF THE WIND FROM THE STAR  $\tau$  BOÖTIS”

The published paper [Nicholson et al. \(2016\)](#), “Temporal variation of the wind from the star  $\tau$  Boötis” follows.



## Temporal variability of the wind from the star $\tau$ Boötis

B. A. Nicholson,<sup>1,2\*</sup> A. A. Vidotto,<sup>3,4</sup> M. Mengel,<sup>1</sup> L. Brookshaw,<sup>1</sup> B. Carter,<sup>1</sup>  
P. Petit,<sup>5,6</sup> S. C. Marsden,<sup>1</sup> S. V. Jeffers,<sup>7</sup> R. Fares<sup>8</sup> and the BCOOL Collaboration

<sup>1</sup>Computational Engineering and Science Research Centre, University of Southern Queensland, Toowoomba, Australia

<sup>2</sup>European Southern Observatory, Karl Schwarzschild Str. 2, D-85748 Garching, Germany

<sup>3</sup>Observatoire de l'Université de Genève, Chemin des Maillettes 51, Versoix CH-1290, Switzerland

<sup>4</sup>School of Physics, Trinity College Dublin, The University of Dublin, Dublin-2, Ireland

<sup>5</sup>CNRS, Institut de Recherche en Astrophysique et Planétologie, 14 Avenue Edouard Belin, F-31400 Toulouse, France

<sup>6</sup>Université de Toulouse, UPS-OMP, Institut de Recherche en Astrophysique et Planétologie, Toulouse, France

<sup>7</sup>Institut für Astrophysik, Universität Göttingen, Friedrich Hund Platz 1, D-37077 Göttingen, Germany

<sup>8</sup>INAF - Osservatorio Astrofisico di Catania, Via Santa Sofia, 78, I-95123 Catania, Italy

Accepted 2016 March 24. Received 2016 March 24; in original form 2016 January 14

### ABSTRACT

We present new wind models for  $\tau$  Boötis ( $\tau$  Boo), a hot-Jupiter-host-star whose observable magnetic cycles makes it a uniquely useful target for our goal of monitoring the temporal variability of stellar winds and their exoplanetary impacts. Using spectropolarimetric observations from May 2009 to January 2015, the most extensive information of this type yet available, to reconstruct the stellar magnetic field, we produce multiple 3D magnetohydrodynamic stellar wind models. Our results show that characteristic changes in the large-scale magnetic field as the star undergoes magnetic cycles produce changes in the wind properties, both globally and locally at the position of the orbiting planet. Whilst the mass loss rate of the star varies by only a minimal amount ( $\sim 4$  per cent), the rates of angular momentum loss and associated spin-down time-scales are seen to vary widely (up to  $\sim 140$  per cent), findings consistent with and extending previous research. In addition, we find that temporal variation in the global wind is governed mainly by changes in total magnetic flux rather than changes in wind plasma properties. The magnetic pressure varies with time and location and dominates the stellar wind pressure at the planetary orbit. By assuming a Jovian planetary magnetic field for  $\tau$  Boo b, we nevertheless conclude that the planetary magnetosphere can remain stable in size for all observed stellar cycle epochs, despite significant changes in the stellar field and the resulting local space weather environment.

**Key words:** MHD – methods: numerical – stars: individual:  $\tau$  Boötis – stars: magnetic field – stars: winds, outflows.

### 1 INTRODUCTION

The study of stellar winds gives insight into the evolution of stars and the planets that orbit them. The wind affects the stellar rotation rate through mass loss and magnetic braking (Schatzman 1962; Weber & Davis 1967; Bouvier 2013), and can also impact the atmospheres of orbiting planets (Adams 2011; Lammer et al. 2012), with potential implications on planet habitability (Horner & Jones 2010; Vidotto et al. 2013). An example of this impact is seen in our own Solar system with the stripping of Mars' atmosphere by the young Sun (Lundin, Lammer & Ribas 2007). However, studying stellar winds is problematic, as winds of stars like our Sun are too diffuse to observe directly (Wood, Linsky & Güdel 2015). Investigation of these stars therefore requires a combination of observation and

magnetohydrodynamic (MHD) simulation in order to estimate the properties of these winds.

The star  $\tau$  Boötis ( $\tau$  Boo, spectral type F7V) is an ideal candidate for a study of the temporal variability of stellar winds, and their potential impacts on orbiting planets. It is the only star to date, other than our Sun, observed to have a magnetic field cycle, with multiple field reversals observed (Catala et al. 2007; Donati et al. 2008; Fares et al. 2009; Fares et al. 2013; Mengel et al. 2016). These observations reveal that the star has a magnetic cyclic period estimated to be a rapid 740 d (Fares et al. 2013). The availability of multiple epochs of magnetic field observations allows us to make observationally informed MHD models of  $\tau$  Boo's wind, such as those detailed by Vidotto et al. (2012) (4 epochs observed between June 2006 and July 2008).

In this paper, we present an additional eight MHD simulations of the winds of  $\tau$  Boo from magnetic field observations taken between

\* E-mail: belinda.nicholson@usq.edu.au

May 2009 and January 2015. Our aim is to examine the changes in the wind behaviour due to the variations in the magnetic field over the observed epochs, which include multiple polarity reversals, and to demonstrate how these changes could impact the planet  $\tau$  Boo b.

In Section 2, we detail the wind model and magnetic field input. The results of our simulations are presented in two parts: Section 3 presents the global wind properties over the eight epochs, and in Section 4 we investigate the properties of the wind around  $\tau$  Boo b and the potential impact of the wind on the planet. We discuss these results in Section 5 and make conclusions based on our findings in Section 6.

## 2 STELLAR WIND MODEL

### 2.1 The BATS-R-US code

The stellar wind model used here is the same as used in Vidotto et al. (2012), but with higher resolution (as in Vidotto et al. 2014). For simulating the winds we use the BATS-R-US code (Powell et al. 1999; Tóth et al. 2012); a three-dimensional code that solves the ideal MHD equations

$$\frac{\partial \rho}{\partial t} + \nabla \cdot (\rho \mathbf{u}) = 0, \quad (1)$$

$$\frac{\partial (\rho \mathbf{u})}{\partial t} + \nabla \cdot \left[ \rho \mathbf{u} \otimes \mathbf{u} + \left( P + \frac{B^2}{8\pi} \right) \mathbf{I} - \frac{\mathbf{B} \otimes \mathbf{B}}{4\pi} \right] = \rho \mathbf{g}, \quad (2)$$

$$\frac{\partial \mathbf{B}}{\partial t} + \nabla \cdot (\mathbf{u} \otimes \mathbf{B} - \mathbf{B}) = 0, \quad (3)$$

$$\frac{\partial \epsilon}{\partial t} + \nabla \cdot \left[ \mathbf{u} \left( \epsilon + P + \frac{B^2}{8\pi} \right) - \frac{(\mathbf{u} \cdot \mathbf{B}) \mathbf{B}}{4\pi} \right] = \rho \mathbf{g} \cdot \mathbf{u}, \quad (4)$$

where  $\rho$  and  $\mathbf{u}$  are the plasma mass density and velocity,  $P$  is the gas pressure,  $\mathbf{B}$  the magnetic flux, and  $\mathbf{g}$  is the gravitational acceleration due to a star of mass  $M_*$ . The total energy density,  $\epsilon$ , is given by

$$\epsilon = \frac{\rho u^2}{2} + \frac{P}{\gamma - 1} + \frac{B^2}{8\pi}. \quad (5)$$

The polytropic index,  $\gamma$ , is defined such that

$$P \propto \rho^\gamma. \quad (6)$$

Table 1 lists the stellar and wind values used for this simulation. The values of  $\tau$  Boo's mass and radius,  $M_*$  and  $R_*$ , are taken from Takeda et al. (2007), and the rotation period,  $t_{\text{rot}}$ , is taken from Fares et al. (2009). The wind mean particle mass,  $\mu$ , is chosen on the assumption that the wind is only composed of protons and electrons. Each simulation is initialized using a polytropic wind solution and the magnetic field information from observations of a given epoch. It is then iterated forward around 30 000 time steps. This ensures that a steady state is achieved. Each simulation, therefore, is a snapshot of the wind at each epoch.

**Table 1.** Adopted stellar parameters for  $\tau$  Boo used in the wind model.

$M_*$ ( $M_\odot$ )	1.34
$R_*$ ( $R_\odot$ )	1.46
Rotation period, $t_{\text{rot}}$ (days)	3.0
Base wind temperature (K)	$2 \times 10^6$
Base wind density ( $\text{g cm}^{-3}$ )	$8.36 \times 10^{-16}$
Wind mean particle mass, $\mu$	0.5
Polytropic index, $\gamma$	1.1

### 2.2 Adopted surface magnetic fields

The BATS-R-US code uses a star's surface magnetic field as input to the inner boundary conditions. The magnetic field information for  $\tau$  Boo comes from spectropolarimetric observations with the NARVAL instrument at T el escope Bernard Lyot in the Midi Pyr en ees, accessed through the BCool collaboration (Marsden et al. 2014). The polarization information in the spectra observed at different stellar rotation phases are used to reconstruct the surface magnetic field topologies using Zeeman–Doppler imaging (ZDI, Donati & Landstreet 2009). The reconstruction of the magnetic field maps used in this work is presented in Mengel et al. (2016). The radial field topologies are of sole interest for the stellar wind modelling as the other, non-potential field components have been shown to have a negligible effect on the wind solution (Jardine et al. 2013).

Fig. 1 shows the reconstructed radial magnetic fields, in units of Gauss (G), for eight sets of observations (epochs): May 2009, January 2010, January 2011, May 2011, May 2013, December 2013, May 2014 and January 2015. The grey lines here are contours at 0 G. The first three of these epochs were published by Fares et al. (2013); however, for consistency the maps presented here are an updated version using the same methodology as used with the other five epochs, the details of which are presented in Mengel et al. (2016). Due to the inclination of the star, the area below  $-40^\circ$  is not observable. The field in this area of the stellar surface is solved for by enforcing  $\nabla \cdot \mathbf{B} = 0$ . Vidotto et al. (2012) showed that choosing this constraint, versus explicitly forcing a symmetric or antisymmetric solution to the large-scale field topology has little impact on the wind solution, especially in the visible hemisphere.

Table 2 shows a summary of the global magnetic field properties over the observed epochs. The magnetic cycle phase is calculated based on a 740-day cycle found by Fares et al. (2013), with the cycle zero phase chosen to be 2453818 Heliocentric Julian Date (HJD) to align with the magnetic cycle zero-point of Vidotto et al. (2012). The complexity of the field topology can be quantified by examining the amounts of energy in the different set spherical harmonics that are used to describe the field (Donati et al. 2006). The modes of these coefficients where  $l \leq 2$  give the dipolar and quadrupolar field configurations. The complexity of the large-scale field is quantified by the percentage of magnetic energy present in the modes where  $l > 2$  over the total energy. A lower percentage indicates a simpler field configuration, whereas a higher percentage means that a larger amount of energy is present in more complicated, smaller scale features.

The field remains dominantly poloidal throughout all observations, with most of the magnetic energy being contained in more complex field components and the complexity varying from 45 per cent to 83 per cent over the cycle. The star is observed to undergo three polarity reversals, with two reversals assumed to have occurred between the May 2011 and May 2013 observations. The absolute surface radial magnetic flux (see Section 3.2) ranges from  $1.53 \times 10^{23}$  Maxwells (Mx) to a peak of  $3.28 \times 10^{23}$  Mx before the polarity reversal that was then seen in the May 2014 observations. This same peak and fall in magnetic flux is not observed in the previous polarity reversals probably due to the timing of the observation, and the length of time between observed epochs.

## 3 WIND SIMULATION RESULTS: GLOBAL WIND PROPERTIES

### 3.1 Magnetic field

The behaviour of the stellar wind is dependent on the geometry and strength of the global stellar magnetic field. Here we examine the

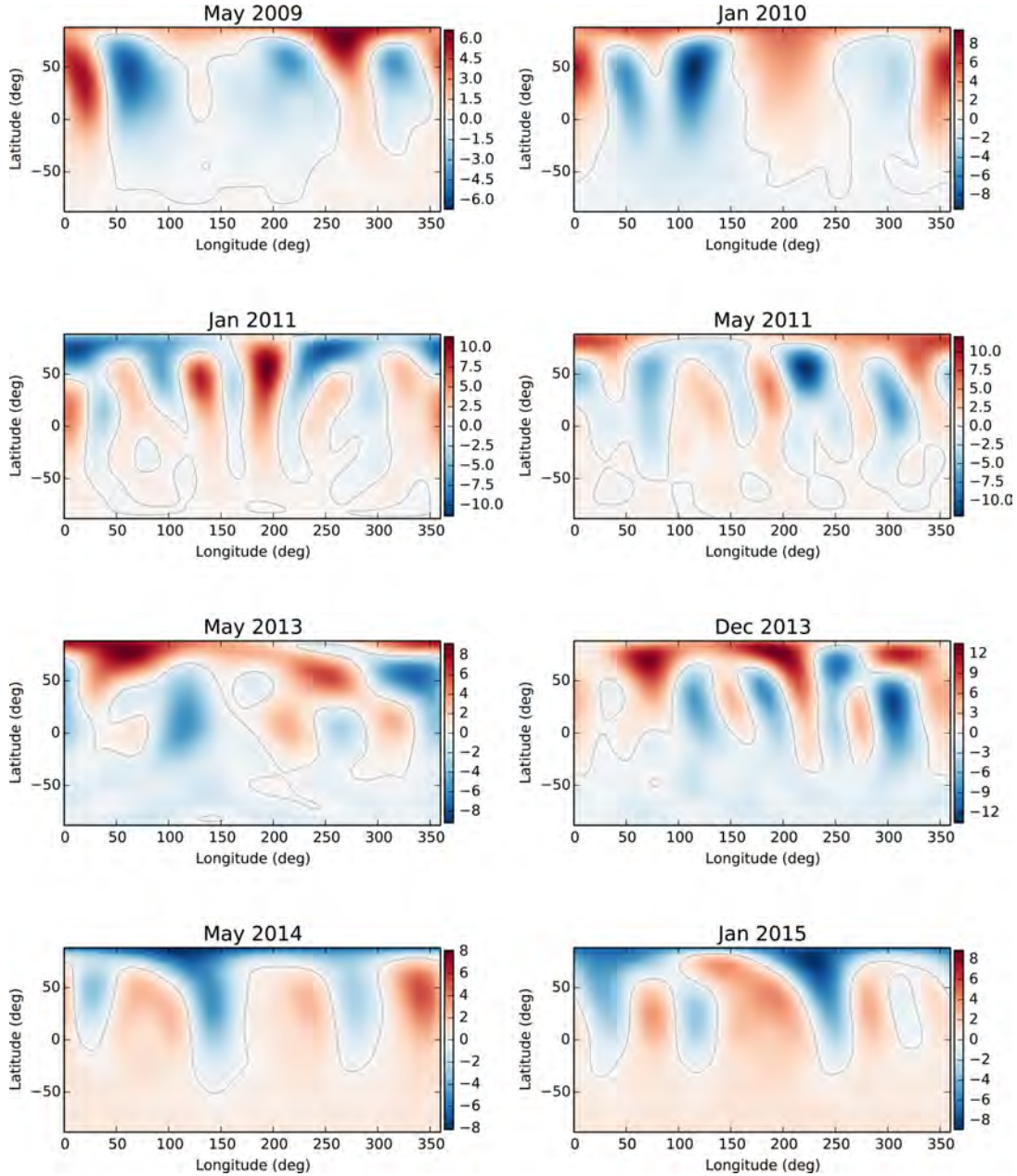


**Figure 1.** Radial magnetic field maps for the eight observed epochs, measured in Gauss (G), with the grey line indicating  $B_r = 0$  G. The May 2009 to January 2011 maps come from Fares et al. (2013), and the May 2011 to January 2015 maps from Mengel et al. (2016). The Fares et al. epochs have been reanalysed for consistency with the Mengel et al. maps. The field remains dominantly poloidal across the eight observations, and three polarity reversals are observed. It is believed that two polarity reversals have occurred between May 2011 and May 2013.

behaviour of the wind at intervals of five months to one year, over a total period of five years and seven months. It is expected that the wind will vary little over the time it takes to observe one epoch ( $\sim 14$  d; Vidotto et al. 2012).

As the magnetic field extends outward from the stellar surface, it will be influenced by the presence of the stellar wind. Fig. 2 shows the magnetic field lines (grey lines) outwards from the surface of the star. The colour contours on the surface represent radial magnetic

**Table 2.** Summary of the radial magnetic field polarity and complexity of  $\tau$  Boo for observations from May 2009 to January 2015. The magnetic cycle period is taken to be 740 d from Fares et al. (2013), with the phase zero-point at 2453818 HJD.

Date	Magnetic cycle phase	Visible pole polarity	Radial field complexity (per cent of $l > 2$ )
May 2009	0.57	Positive	77
Jan 2010	0.91	Positive	45
Jan 2011	0.38	Negative	73
May 2011	0.54	Positive	83
May 2013	0.51	Positive	62
Dec 2013	0.81	Positive	65
May 2014	0.02	Negative	58
Jan 2015	0.34	Negative	62

flux. The lines are seen to twist along the rotation axis ( $z$ -axis) of the star. The number of large closed loops is notable compared to similar plots produced by Vidotto et al. (2012), which is due to a difference in simulation resolution and different reconstruction process to create the magnetic maps. The impact of grid resolution on results is explored in more detail in Appendix A.

This proportion of open to closed magnetic flux can be quantified by examining magnetic flux at different points in the simulation. The unsigned radial flux,  $\Pi$ , is given by

$$\Pi = \oint_{S_R} |B_r| dS_R, \quad (7)$$

where  $S_R$  is a spherical surface of radius  $R$ . The unsigned surface radial magnetic flux,  $\Pi_0$ , can be calculated from equation (7) at the surface  $R = R_*$ . At  $R \geq 10R_*$  the magnetic flux is contained solely within open field lines, and equation (7) integrated over a sphere  $S_{R \geq 10}$  in this region then represents the absolute open magnetic flux,  $\Pi_{\text{open}}$ . The fraction of open flux,  $f_{\text{open}}$  is then defined as

$$f_{\text{open}} = \frac{\Pi_{\text{open}}}{\Pi_0}. \quad (8)$$

These values are given in Table 3. The proportion of open to closed flux is seen to be low, with a majority of the flux from the surface being contained within closed field lines.

### 3.2 Derived wind properties

Quantities of interest to the study of stellar rotation evolution, such as mass loss, angular momentum loss and spin-down time-scale, can be calculated from the output of the wind simulation. Table 3 summarizes the properties of the wind derived from our simulation. The mass loss rate,

$$\dot{M} = \oint_{S_{R \geq 10}} \rho \mathbf{u} \cdot dS_{R \geq 10}, \quad (9)$$

and angular momentum loss rate

$$\dot{J} = \oint_{S_{R \geq 10}} \left[ \frac{-B_\phi B_r \sqrt{x^2 + y^2}}{4\pi} + u_\phi \rho u_r \sqrt{x^2 + y^2} \right] dS_{R \geq 10} \quad (10)$$

(Mestel 1999; Vidotto et al. 2014) are also evaluated over  $S_{R \geq 10}$ , where these quantities reach a constant value. The angular momentum loss is used to infer the time-scale of magnetic braking,  $\tau$ , defined as  $\tau = J/\dot{J}$ , measured in Gyr, where  $J$  is the angular momentum of the star given by  $J = (I_{\text{core}} + I_{\text{envelope}})\Omega_*$ , with  $\Omega_*$  being the stellar angular velocity. We estimate the spin-down time of  $\tau$  Boo by using stellar evolution models to estimate the moment of

inertia of the core,  $I_{\text{core}}$ , and convective envelope,  $I_{\text{envelope}}$ , separately. This spin-down time-scale,  $\tau$ , is given by

$$\tau = \frac{2\pi(I_{\text{core}} + I_{\text{envelope}})}{I_{\text{rot}}\dot{J}}. \quad (11)$$

Table 3 gives these spin-down times using  $I_{\text{core}} = 1.05 \times 10^{54}$  g cm<sup>2</sup> and  $I_{\text{envelope}} = 4.53 \times 10^{51}$  g cm<sup>2</sup>, calculated from the model of Baraffe et al. (1998) (Gallet, private communication).

The mass loss rates show little variation over the eight epochs, ranging between  $2.29 \times 10^{-12}$  and  $2.38 \times 10^{-12}$   $M_\odot$  yr<sup>-1</sup>, approximately 100 times the Solar mass loss rate. This level of variation ( $\sim 4$  per cent) is in agreement with the epoch-to-epoch mass loss rate variability found by Vidotto et al. (2012) ( $\sim 3$  per cent).

We calculate a lower limit on the X-ray luminosity, as in Llama et al. (2013), assuming that the quiescent X-ray emission of the coronal wind is caused by free-free radiation. We find little variation ( $\sim 2$  per cent) over the observed epochs. This is in agreement with the previous wind model results of Vidotto et al. (2012), and the X-ray observations of  $\tau$  Boo by Poppenhaeger, Günther & Schmitt (2012) and Poppenhaeger & Wolk (2014).

The angular momentum loss rate values are seen to vary by  $\sim 140$  per cent over the eight epochs, with a peak at December 2013, corresponding to a peak in the observed radial surface flux,  $\Pi_0$ , as do the spin-down time-scales,  $\tau$ . Our values of spin-down time differ by 1 order of magnitude than those derived by Vidotto et al. (2012). This is due to different assumptions in the moment of inertia of the star (Vidotto et al. (2012) assumed that of a solid sphere, while we use a more sophisticated approach).

## 4 WIND ENVIRONMENT AROUND THE PLANET

### 4.1 Wind properties at $\tau$ Boo b

Since the planet  $\tau$  Boo b is tidally locked to its star in a 1:1 resonance, the location of the planet with respect to the surface of the star does not change. The planet's orbit lies in the equatorial ( $x$ - $y$ ) plane of the star (Brogi et al. 2012) on the negative  $x$ -axis at  $x = -6.8R_*$ . Table 4 gives the properties of the environment surrounding the planet. The total pressure,  $P_{\text{tot}}$ , is the sum of the thermal, ram and magnetic pressures. The thermal pressure due to the wind,  $P$ , is an output of the simulation. The ram pressure,  $P_{\text{ram}}$ , is given by:

$$P_{\text{ram}} = \rho |\Delta \mathbf{u}|^2 \quad (12)$$

where  $|\Delta \mathbf{u}| = |\mathbf{u} - \mathbf{v}_k|$  is the relative velocity between the planet and the wind, with  $\mathbf{v}_k$  being the planet's Keplerian velocity. The magnetic pressure,  $P_{\text{mag}}$  is given by:

$$P_{\text{mag}} = \frac{|\mathbf{B}|^2}{8\pi}. \quad (13)$$

The variation in surface absolute magnetic flux shown in Table 3 is reflected in the variation in level of absolute magnetic flux,  $|\mathbf{B}|$ , at the position of the planet. In contrast to this, the wind velocity,  $|\mathbf{u}|$ , and particle density,  $\Gamma$ , vary only a small amount ( $\sim 17$  per cent and  $\sim 14$  per cent, respectively) over the observed epochs. The temperature, however, is seen to change by nearly approximately 46 per cent, and total pressure,  $P_{\text{tot}}$ , varies between maxima and minima by  $\sim 94$  per cent.

Fig. 3 shows the total, ram, magnetic and thermal pressure measurement for each observed epoch. The magnetic pressure varies by up to 48 per cent, whereas the ram and thermal pressures vary minimally ( $\sim 5$  per cent) over the eight epochs, indicating that

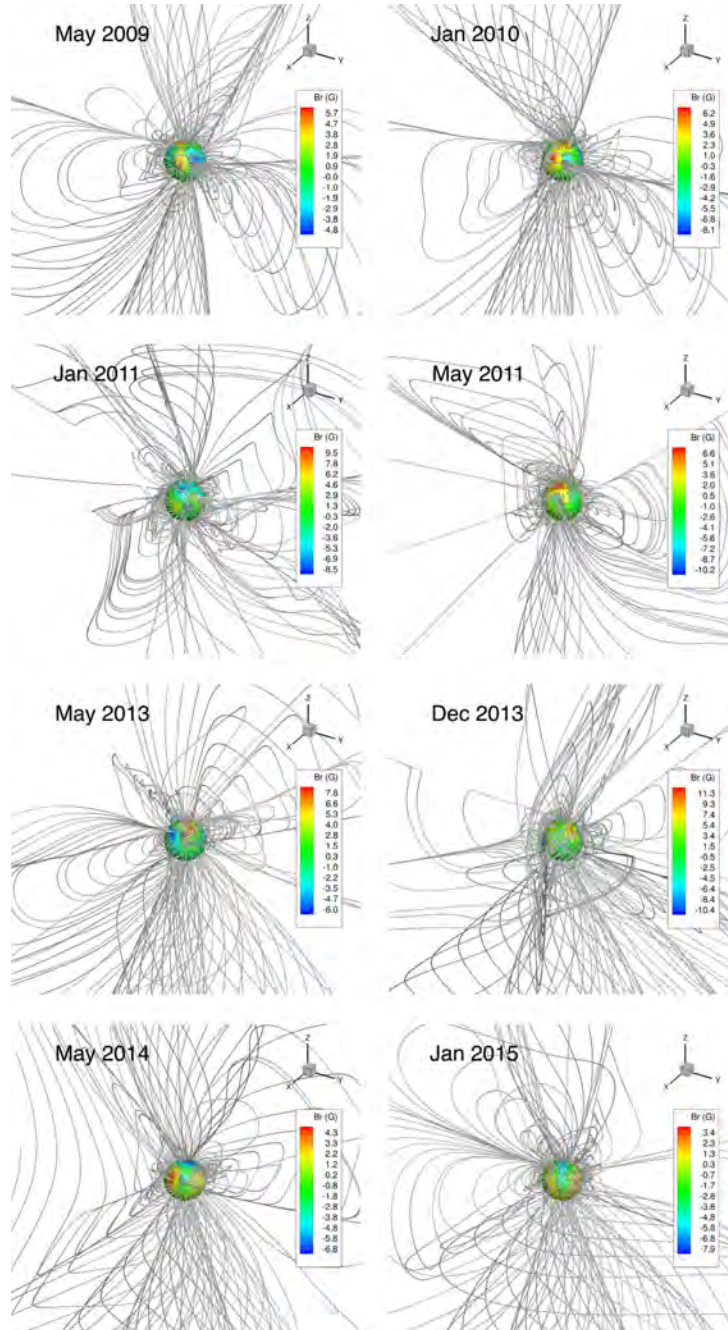


**Figure 2.** These plots show the simulation results of the large-scale magnetic field lines surrounding  $\tau$  Boo. The sphere in the centre represents the stellar surface, with the colour contours indicating the radial magnetic field strength at the surface. The rotational axis of the star is along the  $z$ -axis, with the equator lying in the  $xy$ -plane. It can be seen that the field lines become twisted around the axis of rotation ( $z$ -axis) due to the presence of the wind.

**Table 3.** Summary of the simulated global wind properties of  $\tau$  Boo based on observations from May 2009 to January 2015. The behaviour of the magnetic field is described by the unsigned surface flux,  $\Pi_0$ , the open flux beyond 10 stellar radii,  $\Pi_{\text{open}}$ , and the ratio of these quantities,  $f_{\text{open}}$ . These values indicate a significant variation in magnetic field behaviour between epochs. The stellar mass loss rate,  $\dot{M}$ , varies an insignificant amount over the observed epochs. The angular momentum loss rate,  $\dot{J}$ , however, and associated spin-down time-scales,  $\tau$ , are observed to vary significantly over the eight epochs, correlating with the observed changes in the magnetic field.

Date	$\Pi_0$ ( $10^{22}$ Mx)	$\Pi_{\text{open}}$ ( $10^{22}$ Mx)	$f_{\text{open}}$	$\dot{M}$ ( $10^{-12} M_{\odot} \text{ yr}^{-1}$ )	$\dot{J}$ ( $10^{32}$ erg)	$\tau$ (Gyr)
May 2009	15.3	4.5	0.29	2.34	1.3	6.5
Jan 2010	22.3	7.6	0.34	2.31	2.0	4.1
Jan 2011	22.3	5.6	0.25	2.34	1.6	5.0
May 2011	20.0	4.4	0.22	2.31	1.3	6.1
May 2013	21.4	7.1	0.33	2.29	1.7	4.7
Dec 2013	32.8	10.5	0.32	2.38	3.0	2.7
May 2014	18.7	8.0	0.43	2.30	1.6	5.2
Jan 2015	21.6	8.2	0.38	2.28	1.7	4.5

**Table 4.** Summary of the wind properties at the position of the planet  $\tau$  Boo b. The variations in absolute magnetic field,  $|\mathbf{B}|$ , reflects the variation in the observed field. The influence of the magnetic flux changes are seen in variations of the total pressure experienced by the planet.

Date	$ \mathbf{B} $ ( $\times 10^{-2}$ G)	$ \mathbf{u} $ ( $\text{km s}^{-1}$ )	$T$ ( $\times 10^6$ K)	$\Gamma$ ( $\times 10^6$ Particles $\text{cm}^{-3}$ )	$P_{\text{tot}}$ ( $\times 10^{-3}$ dyn $\text{cm}^{-2}$ )
May 2009	0.41	209	1.05	1.46	0.81
Jan 2010	3.12	245	1.04	1.33	1.28
Jan 2011	3.65	229	1.07	1.43	1.44
May 2011	2.46	215	1.05	1.42	1.06
May 2013	3.06	226	1.05	1.40	1.19
Dec 2013	4.10	232	1.52	1.52	1.57
May 2014	2.82	216	1.11	1.41	1.16
Jan 2015	2.10	224	1.05	1.36	1.02

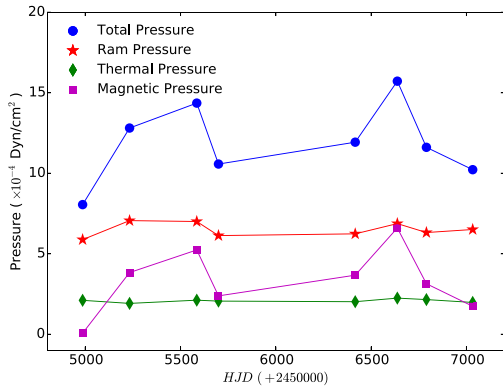


**Figure 3.** Pressure values at the orbit of the planet  $\tau$  Boo b for each observed epoch. The total pressure is the sum of the ram, thermal and magnetic pressures. The ram and thermal pressures vary only slightly over the observed epochs, whereas the magnetic pressure varies more significantly. The lines between points are to guide the eye, and do not represent a fit to the data.

the changes in total pressure are due to changes in the magnetic pressure.

#### 4.2 Planetary magnetospheric behaviour

The external pressure around the planet can be used to infer possible behaviours of the planet's magnetosphere. The ratio of the planetary

magnetospheric radius,  $R_m$ , to the planetary radius,  $R_p$ , is derived from the equilibrium between the pressure from the wind and the outward force of the planetary magnetosphere. This can be written as

$$\frac{R_m}{R_p} = \left( \frac{(B_p/2)^2}{8\pi P_{\text{tot}}} \right)^{\frac{1}{6}} \quad (14)$$

(Vidotto et al. 2012), where  $B_p$  is the strength of the planetary magnetic field at the pole. Since there have been no measurements of the magnetic field strength of hot Jupiters to date, we have assumed a planetary magnetic field strength similar to that of Jupiter, which is a maximum of  $\sim 14$  G (Bagenal 1992). The values of  $R_m/R_p$  evaluated over the eight epochs are shown in Table 5.

The behaviour of the planetary magnetosphere can also be described in terms of the auroral ring: the area around the poles of the planet over which the planetary magnetic flux is open, allowing the flow of particles to and from the planetary atmosphere. This can be described in terms of the percentage of the planet's surface area:

$$A_{\text{open}} = (1 - \cos(\alpha)) \times 100, \quad (15)$$

where  $\alpha$  is the auroral angular aperture, defined as

$$\alpha = \arcsin \left( \left( \frac{R_m}{R_p} \right)^{-\frac{1}{2}} \right) \quad (16)$$

Vidotto et al. (in preparation).

Despite notable changes in the total pressure exerted in the planet by the star, the planet's magnetosphere remains around 3.6 times the planet's radius, varying by only  $\sim 3$  per cent over the observed epochs. This is due to the relative insensitivity of  $R_m/R_p$  to changes

**Table 5.** Values for the ratio of planet magnetospheric radius to planet radius,  $R_m/R_p$ , auroral aperture  $\alpha$  and the percentage coverage of the polar cap,  $A_{\text{open}}$ , for the planet  $\tau$  Boo b. These have been calculated assuming magnetic field strength at the pole of 14 G. Despite notable changes in the behaviour of the star’s magnetic field and in the total pressure exerted on the planet by the stellar wind, these values remain quite stable over the observed epochs.

Date	$R_m/R_p$	$\alpha$ (degrees)	$A_{\text{open}}$ (per cent)
May 2009	3.67	31.5	14.7
Jan 2010	3.57	31.9	15.1
Jan 2011	3.56	32.0	15.2
May 2011	3.64	31.6	14.8
May 2013	3.62	31.7	14.9
Dec 2013	3.55	32.1	15.3
May 2014	3.61	31.7	15.0
Jan 2015	3.62	31.7	14.9

in  $P_{\text{tot}}$  (due to the  $-1/6$  power dependence). As with the planetary magnetospheric radius, there are minimal changes in the auroral aperture and polar surface area, which remain around  $32^\circ$  and 15 per cent, respectively. From this we can infer that despite considerable changes in the behaviour of  $\tau$  Boo’s magnetic field,  $\tau$  Boo b’s magnetosphere remains relatively stable.

## 5 DISCUSSION

### 5.1 Global wind properties

The wind simulations presented here are an advance on models that do not use observationally reconstructed magnetic fields as input, or that assume a simplified stellar magnetic field topology. The coronal base temperature and density are poorly constrained by observations, and are free parameters of our model. We chose a wind base temperature that is typical of stellar coronae, and the same base density as adopted in Vidotto et al. (2012). Our estimated mass loss rate ( $\sim 2.3 \times 10^{-12} M_\odot \text{ yr}^{-1}$ ) is within the range of previous estimates of  $1.67 \times 10^{-12}$  (Stevens 2005) to  $6.6 \times 10^{-12} M_\odot \text{ yr}^{-1}$  (Cranmer & Saar 2011). Given that Sun’s corona is adequately described by the adiabatic process given by equation (6), with the index  $\gamma = 1.1$  (Van Doorselaere et al. 2011), we assume the same for this star.

The behaviour of the angular momentum loss rate and associated spin-down time-scales found here agree with the predictions of Gallet & Bouvier (2013), who computed rotational evolution models based on wind-breaking laws derived for magnetised Solar-type stars. They find that the spin-down time-scales of stars at 1 Gyr old, which is the approximate age of  $\tau$  Boo (Borsa et al. 2015), should converge to the length of a few Gyrs, the same as presented in the results here. This further strengthens our choice of model parameters.

The lifetime of a main-sequence star,  $\tau_{\text{MS}}$ , with the mass of  $\tau$  Boo ( $1.34 M_\odot$ ) is expected to be  $\sim 4.8$  Gyr ( $\tau_{\text{MS}} = 10(M_*/M_\odot)^{-2.5}$ ). Given  $\tau$  Boo’s estimated age of 1 Gyr and our calculated mean spin-down time of  $\sim 4.9$  Gyr, this implies that Tau Boo will remain a rapid rotator throughout its main sequence lifetime, provided that only the stellar wind is affecting its rotational evolution.

The changing stellar magnetic field polarity of the poles does not have an effect on the wind solution. This is because there is no preferred up or down orientation of the star, and the global wind

properties are calculated as surface integrals around the star. Instead, it is the changing field strength as the star undergoes its reversals that drives changes in the wind behaviour.

Over the cycle there is a change in field complexity, and this is anti-correlated with the fraction of open flux  $f_{\text{open}}$  (linear correlation coefficient =  $-0.72$ ). As the field becomes more complex, the amount of flux contained in closed lines increases and the fraction of open flux decreases (see also Lang et al. 2012). No correlation is found, however, between changes in field complexity and changes, or lack thereof, in the angular momentum or mass loss rates.

### 5.2 Wind–planet interaction

Wind simulations can give insight into the potential behaviour of the planetary magnetosphere in the presence of the stellar wind. Since there have been no observations of magnetic fields of exoplanets to date, assumptions must be made as to what magnetic field can be expected from  $\tau$  Boo b. There is much discussion over the possible magnetic fields of exoplanets. It has been theorized that close in hot-Jupiters such as  $\tau$  Boo b are thought to have a weaker magnetic field than similar planets further away from the host star due to the tidal locking slowing the planet’s rotation, and hence reducing its magnetic field (Grießmeier et al. 2004). However, there are some studies that indicate that planetary rotation does not directly influence the strength of a planet’s magnetic field (Christensen, Holzwarth & Reiners 2009), but plays a role in the field geometry (Zuluaga & Cuartas 2012). Given the uncertainty in hot-Jupiters magnetic fields and the similar nature of this planet to Jupiter, we have assumed a Jovian planetary magnetic field strength for this work. The resulting magnetosphere suggests the planet is protected from the stellar wind, despite large changes in the magnetic field and wind strengths over the cycle.

The minimum field strength required to sustain a magnetosphere above the surface of  $\tau$  Boo b (i.e.  $R_m > R_p$ ) can be estimated by examining the condition of the space weather environment during at the most extreme part of the magnetic cycle (i.e., when  $P_{\text{tot}}$  is at a maximum). This is calculated to be  $\sim 0.4$  G. This does not mean, however, that the planet is protected at this point, as at this limit the Auroral aperture reaches 90 degrees, exposing 100 per cent of the planets surface area to particle inflow and outflow. If we were to call a planet ‘protected’ provided less than 25 per cent of its surface area was contained within the auroral aperture, then the minimum magnetic field strength to achieve this is  $\sim 4.7$  G for the  $\tau$  Boo system.

## 6 SUMMARY AND CONCLUSIONS

This study examines the variability in the wind behaviour of the star  $\tau$  Boo over eight epochs from May 2009 to January 2015 - the most extensive monitoring of the wind behaviour of a single object to date (apart from the Sun). The winds are examined globally to study the star’s rotational evolution, and locally around  $\tau$  Boo b for the possible impacts the wind might have on the planet’s magnetosphere.

Despite significant changes in the magnetic field behaviour, the mass loss rates do not significantly vary from epoch to epoch ( $\sim 4$  per cent), remaining around  $2.3 \times 10^{-12} M_\odot \text{ yr}^{-1}$ . However, the angular momentum loss rate is observed to change considerably over the eight observations, ranging from  $1.3 \times 10^{32}$  to  $3.0 \times 10^{32}$  erg. These findings are consistent with angular momentum loss rates and associated spin-down time-scales predicted by stellar evolution models.

Examining the wind environment of the planet shows that variations in the absolute flux due to changes in the magnetic field behaviour of the star are reflected in changes in the local space weather of  $\tau$  Boo b. Despite these changes, the magnetosphere from an assumed Jupiter-like planetary magnetic field is relatively invariant over the observed epochs, with the magnetospheric radius remaining around 3.6 times the size of the planetary radius.

#### ACKNOWLEDGEMENTS

This work was partly funded through the University of Southern Queensland Strategic Research Fund Starwinds Project. Some of the simulations presented in this paper were computed on the University of Southern Queensland's High Performance Computer. This research has made use of NASA's Astrophysics Data System. This work was carried out using the BATS-R-US tools developed at The University of Michigan Center for Space Environment Modeling (CSEM) and made available through the NASA Community Coordinated Modeling Center (CCMC). This work was supported by a grant from the Swiss National Supercomputing Centre (CSCS) under project ID s516. AAV acknowledges support from the Swiss National Science Foundation through an Ambizione Fellowship. Many thanks to Florian Gallet for providing the moment of inertia values for this work, and many thanks also to Colin Folsom for his help and advice.

#### REFERENCES

- Adams F. C., 2011, *ApJ*, 730, 27  
 Bagenal F., 1992, *Annu. Rev. Earth Planet. Sci.*, 20, 289  
 Baraffe I., Chabrier G., Allard F., Hauschildt P. H., 1998, *A&A*, 337, 403  
 Borsari F. et al., 2015, *A&A*, 578, A64  
 Bouvier J., 2013, *EAS Publ. Ser.*, 62, 143  
 Brogi M., Snellen I. A. G., de Kok R. J., Albrecht S., Birkby J., de Mooij E. J. W., 2012, *Nature*, 486, 502  
 Catala C., Donati J. F., Shkolnik E., Bohlender D., Alecian E., 2007, *MNRAS*, 374, L42  
 Christensen U. R., Holzwarth V., Reiners A., 2009, *Nature*, 457, 167  
 Cranmer S. R., Saar S. H., 2011, *ApJ*, 741, 54  
 Donati J. F., Landstreet J. D., 2009, *ARA&A*, 47, 333  
 Donati J. F. et al., 2006, *MNRAS*, 370, 629  
 Donati J. F. et al., 2008, *MNRAS*, 385, 1179  
 Fares R. et al., 2009, *MNRAS*, 398, 1383  
 Fares R., Moutou C., Donati J.-F., Catala C., Shkolnik E. L., Jardine M. M., Cameron A. C., Deleuil M., 2013, *MNRAS*, 435, 1451  
 Gallet F., Bouvier J., 2013, *A&A*, 556, A36  
 Grieblmeier J. M. et al., 2004, *A&A*, 425, 753  
 Horner J., Jones B. W., 2010, *Int. J. Astrobiol.*, 9, 273  
 Jardine M., Vidotto A. A., van Ballegoijen A., Donati J. F., Morin J., Fares R., Gombosi T. I., 2013, *MNRAS*, 431, 528  
 Lammer H. et al., 2012, *Earth Planets Space*, 64, 179  
 Lang P., Jardine M., Donati J.-F., Morin J., Vidotto A., 2012, *MNRAS*, 424, 1077

- Llama J., Vidotto A. A., Jardine M., Wood K., Fares R., Gombosi T. I., 2013, *MNRAS*, 436, 2179  
 Lundin R., Lammer H., Ribas I., 2007, *Space Sci. Rev.*, 129, 245  
 Marsden S. C. et al., 2014, *MNRAS*, 444, 3517  
 Mengel M. W., Fares R., Marsden S. C., Carter B. D., Jeffers S. V., Folsom C. P., 2016, *MNRAS*, in press  
 Mestel L., 1999, *Stellar Magnetism*, Oxford Univ. Press, Oxford  
 Poppenhaeager K., Wolk S. J., 2014, *A&A*, 565, L1  
 Poppenhaeager K., Günther H. M., Schmitt J. H. M. M., 2012, *Astron. Nachr.*, 333, 26  
 Powell K. G., Roe P. L., Linde T. J., Gombosi T. I., De Zeeuw D. L., 1999, *J. Comput. Phys.*, 154, 284  
 Schatzman E., 1962, *Annales d'Astrophysique*, 25, 18  
 Stevens I. R., 2005, *MNRAS*, 356, 1053  
 Takeda G., Ford E. B., Sills A., Rasio F. A., Fischer D. A., Valenti J. A., 2007, *ApJS*, 168, 297  
 Tóth G. et al., 2012, *J. Comput. Phys.*, 231, 870  
 Van Doorselaere T., Wardle N., Del Zanna G., Jansari K., Verwichte E., Nakariakov V. M., 2011, *ApJ*, 727, L32  
 Vidotto A. A., Fares R., Jardine M., Donati J. F., Opher M., Moutou C., Catala C., Gombosi T. I., 2012, *MNRAS*, 423, 3285  
 Vidotto A. A., Jardine M., Morin J., Donati J. F., Lang P., Russell A. J. B., 2013, *A&A*, 557, 67  
 Vidotto A. A., Jardine M., Morin J., Donati J. F., Opher M., Gombosi T. I., 2014, *MNRAS*, 438, 1162  
 Weber E. J., Davis L., Jr, 1967, *ApJ*, 148, 217  
 Wood B. E., Linsky J. L., Güdel M., 2015, in Lammer H., Khodachenko M., eds, *Astrophysics and Space Science Library* Vol. 411, Astrophysics and Space Science Library, p. 19  
 Zuluaga J. I., Cuartas P. A., 2012, *Icarus*, 217, 88

#### APPENDIX A: SENSITIVITY OF RESULTS TO GRID REFINEMENT LEVEL

The design of the BATS-R-US code allows the simulation grid to be constructed so that areas of interest can be studied in greater detail by local grid refinement. This means that the region closest to the surface of the star that is changing the greatest can be simulated at a much finer resolution, but leaving the outer regions of the simulation with a much coarser grid structure to save on computing resources.

This section examines how the level of refinement of the grid, that is, the number of times the grid in the region close to the star is subdivided into smaller cells, affects the simulation outcomes. Using the May 2011 data, we examined  $\dot{M}$ ,  $\dot{J}$  and  $f_{\text{open}}$  (as calculated in Section 3.2) for three different refinement levels. Table A1 shows these global wind parameters, along with the total number of computational cells and smallest cell size for each refinement level. In our grid design, the grid refinement changes occur in the simulation region close to the surface of the star, so that the grid size out beyond  $10R_*$  remains the same.

The values of the wind parameters are seen to vary across refinement levels, and these variations are on the same order as the variations observed across epochs, or greater as in the case of mass loss rate. However, these variations are much smaller than the

**Table A1.** This table shows the changes in the May 2011 global wind parameters with differing grid refinement levels. These variations are on similar to or greater than the variation between epochs. As such it is important to ensure that the grid levels are the same when comparing global wind properties between simulations.

Grid refinement level	Total number of cells	Smallest cell ( $\times 10^{-2} R_*$ )	$\dot{M}$ ( $10^{-12} M_{\odot} \text{ yr}^{-1}$ )	$\dot{J}$ ( $10^{32} \text{ erg}$ )	$f_{\text{open}}$
8	$2.78 \times 10^6$	5.7	2.9	1.8	0.35
9	$7.10 \times 10^6$	2.9	2.5	1.5	0.23
10	$3.92 \times 10^7$	1.4	2.3	1.3	0.22

**Table A2.** This table shows the changes in the May 2011 local wind environment around  $\tau$  Boo b with differing grid refinement levels. The variation in due to grid refinement level is on the same level or greater than the variation epoch to epoch. As such it is important to ensure that the grid levels are the same when comparing wind models across epochs.

Grid refinement level	$ \mathbf{u} $ (km s <sup>-1</sup> )	$ \mathbf{B} $ ( $\times 10^{-2}$ G)	$P_{\text{tot}}$ ( $\times 10^{-3}$ dyn cm <sup>-2</sup> )	$R_m/R_p$
8	230	1.46	1.18	3.47
9	221	2.15	1.08	3.58
10	215	2.46	1.06	3.64

observational uncertainties and theoretical limits of both  $\dot{M}$  and  $\dot{J}$ . The changes in  $f_{\text{open}}$  are not unexpected as the finer cell structure means that more of the magnetic field structure is being resolved, and field lines that could be taken to be open in a coarser grid structure are found to be closed at a higher refinement level.

Table A2 shows the changes in the simulation results at the position of  $\tau$  Boo b due to changes in grid refinement. As with the global wind properties, the local wind properties at the planet vary between grid sizes on the same scale as variations between epochs. Even though it might appear that an under-resolved grid overestimates the impact of the wind on the planet, these variations are smaller than the observational uncertainties on these parameters.

Given the variations seen due to different grid sizes it is important to use the same grid refinement level to compare simulations of different epochs. Using a higher resolution would give marginally more accurate results, but given the unreasonable amount for computation requires to reach refinement level 11 (total number of cells  $\sim 2.86 \times 10^8$ ), we conclude that refinement level 10 is the most appropriate for the current study.

This paper has been typeset from a  $\text{\LaTeX}$  file prepared by the author.

# B

## The Pan-Pacific Planet Search. IV. Two Super-Jupiters in a 3:5 Resonance Orbiting the Giant Star HD 33844

A SMALL CONTRIBUTION WAS MADE TO THE FOLLOWING paper. Provided code to allow running of simulations on various high-performance computing systems.

B.1 WITTENMYER ET AL. (2016B) THE PAN-PACIFIC PLANET SEARCH. IV. TWO SUPER-JUPITERS IN A 3:5 RESONANCE ORBITING THE GIANT STAR HD 33844

The published paper [Wittenmyer et al. \(2016\)](#), “The Pan-Pacific Planet Search. IV. Two Super-Jupiters in a 3:5 Resonance Orbiting the Giant Star HD 33844” follows.



## THE PAN-PACIFIC PLANET SEARCH. IV. TWO SUPER-JUPITERS IN A 3:5 RESONANCE ORBITING THE GIANT STAR HD 33844

ROBERT A. WITTENMYER<sup>1,2,3</sup>, JOHN ASHER JOHNSON<sup>4</sup>, R. P. BUTLER<sup>5</sup>, JONATHAN HORNER<sup>2,3</sup>, LIANG WANG<sup>6</sup>,  
PAUL ROBERTSON<sup>7,8,13</sup>, M. I. JONES<sup>9</sup>, J. S. JENKINS<sup>10</sup>, R. BRAHM<sup>11</sup>, C. G. TINNEY<sup>1,2</sup>, M. W. MENGEL<sup>3</sup>, AND J. CLARK<sup>12</sup>

<sup>1</sup>School of Physics, University of New South Wales, Sydney 2052, Australia; [rob@unsw.edu.au](mailto:rob@unsw.edu.au)

<sup>2</sup>Australian Centre for Astrobiology, University of New South Wales, Sydney 2052, Australia

<sup>3</sup>Computational Engineering and Science Research Centre, University of Southern Queensland, Toowoomba, Queensland 4350, Australia

<sup>4</sup>Harvard-Smithsonian Center for Astrophysics, Cambridge, MA 02138, USA

<sup>5</sup>Department of Terrestrial Magnetism, Carnegie Institution of Washington, 5241 Broad Branch Road, NW, Washington, DC 20015-1305, USA

<sup>6</sup>Key Laboratory of Optical Astronomy, National Astronomical Observatories, Chinese Academy of Sciences,

A20 Datun Road, Chaoyang District, Beijing 100012, China

<sup>7</sup>Department of Astronomy and Astrophysics, The Pennsylvania State University, USA

<sup>8</sup>Center for Exoplanets & Habitable Worlds, The Pennsylvania State University, USA

<sup>9</sup>Department of Electrical Engineering and Center of Astro-Engineering UC, Pontificia Universidad Católica de Chile,

Av. Vicua Mackenna 4860, 782-0436 Macul, Santiago, Chile

<sup>10</sup>Departamento de Astronomía, Universidad de Chile, Camino El Observatorio 1515, Las Condes, Santiago, Chile

<sup>11</sup>Instituto de Astrofísica, Facultad de Física, Pontificia Universidad Católica de Chile and Millennium Institute of Astrophysics,

Av. Vicuña Mackenna 4860, 7820436 Macul, Santiago, Chile

<sup>12</sup>School of Physical Sciences, University of Adelaide, Adelaide SA 5005, Australia

Received 2015 October 8; accepted 2015 December 22; published 2016 February 4

### ABSTRACT

We report the discovery of two giant planets orbiting the K giant HD 33844 based on radial velocity data from three independent campaigns. The planets move on nearly circular orbits with semimajor axes  $a_b = 1.60 \pm 0.02$  AU and  $a_c = 2.24 \pm 0.05$  AU, and have minimum masses ( $m \sin i$ ) of  $M_b = 1.96 \pm 0.12 M_{\text{Jup}}$  and  $M_c = 1.76 \pm 0.18 M_{\text{Jup}}$ . Detailed  $N$ -body dynamical simulations show that the two planets have remained on stable orbits for more than  $10^6$  years for low eccentricities and are most likely trapped in a mutual 3:5 mean motion resonance.

*Key words:* planetary systems – stars: individual (HD 33844) – techniques: radial velocities

### 1. INTRODUCTION

Surveys for planets orbiting evolved stars more massive than the Sun are well into their second decade. The longest-running surveys (e.g., Sato et al. 2005; Reffert et al. 2015) have been monitoring several hundred such stars for  $\sim 15$  years. The combined efforts of these and other surveys have amassed enough data to begin making quantitative statements about the frequency and detailed properties of planetary systems beyond solar-type main-sequence stars.

An early prediction from formation models proposed that higher-mass stars should host higher-mass planets (Ida & Lin 2005), a prediction that is being borne out by observation (Bowler et al. 2010). Giant planet frequency has also been shown to increase with host star mass (Fischer & Valenti 2005; Bowler et al. 2010; Johnson et al. 2010), though with a drop-off for hosts with  $M_* > 2.5 - 3.0 M_{\odot}$  (Omiya et al. 2009; Kunitomo et al. 2011; Reffert et al. 2015). Kretke et al. (2009) proposed a mechanism to explain the efficient formation of gas giant planets at orbital distances  $a \gtrsim 1$  AU. For intermediate-mass stars, the inner edge of the magneto-rotational instability (MRI) dead zone lies far enough from the star to permit cores to accrete gas rapidly and produce gas giants at a higher rate than for solar-mass stars. An interesting consequence of their models is that the frequency of giant planets would have little dependence on stellar metallicity, in contrast to the well-known planet-metallicity correlation for dwarf stars (Fischer & Valenti 2005). However, recent results from Reffert et al. (2015) with a sufficiently large and self-consistent sample of

intermediate-mass stars and their planets in hand, show that planet occurrence remains positively correlated with metallicity for these stars.

The Pan-Pacific Planet Search (PPPS—Wittenmyer et al. 2011a) was a radial velocity survey of 170 southern giant stars using the 3.9 m Anglo-Australian Telescope (AAT) and its UCLES high-resolution spectrograph (Diego et al. 1990). It was originally conceived of as a southern hemisphere extension of the Lick and Keck Observatory survey for planets orbiting northern “retired A stars” (Johnson et al. 2006). The targets were selected to be redder ( $1.0 < (B - V) < 1.2$ ) than the northern hemisphere sample to select for more metal-rich stars (Girardi et al. 2002). The PPPS operated from 2009 to 2014; papers detailing the spectroscopic stellar parameters and new planet detections are now in preparation (Wittenmyer et al. 2015b, 2016). This paper is organized as follows: Section 2 details the AAT and Keck observations of HD 33844 and gives the stellar parameters. Section 3 describes the orbit-fitting procedures and gives the parameters of the two planets in the HD 33844 system. In Section 4 we discuss the evidence for a planetary interpretation of the observed radial velocity variations, including dynamical stability simulations. We give our conclusions in Section 5.

### 2. OBSERVATIONS AND STELLAR PROPERTIES

HD 33844 is common to the AAT, Keck, and FEROS evolved-star surveys. Precision Doppler measurements for the PPPS are obtained with the UCLES echelle spectrograph at the AAT. The observing procedure is identical to that used by the long-running Anglo-Australian Planet Search (e.g., Butler et al.

<sup>13</sup> NASA Sagan Fellow.

**Table 1**  
AAT Radial Velocities for HD 33844

BJD-2400000	Velocity (m s <sup>-1</sup> )	Uncertainty (m s <sup>-1</sup> )
54867.00962	-14.89	1.63
55139.20744	-35.49	2.00
55525.14921	-2.27	1.97
55580.04370	-36.05	1.83
55601.94622	-51.59	1.79
55879.18697	4.37	2.28
55880.14794	3.28	1.75
55881.12234	-1.95	1.93
55906.00994	13.02	2.06
55968.97219	13.41	1.53
55993.93352	8.92	3.17
56051.85691	8.61	3.18
56343.96912	-1.05	2.30
56374.91336	3.36	1.82
56376.92296	3.92	1.79
56377.91375	0.00	1.44
56399.92598	16.56	2.37
56530.28448	8.68	2.28
56685.94081	-57.81	2.34
56747.87554	-64.48	2.16

2001; Tinney et al. 2001; Jones et al. 2010; Wittenmyer et al. 2012c); a 1 arcsec slit delivers a resolving power of  $R \sim 45,000$ . Calibration of the spectrograph point-spread function is achieved using an iodine absorption cell temperature-controlled at  $60.0 \pm 0.1^\circ\text{C}$ . The iodine cell superimposes a forest of narrow absorption lines from 5000 to 6200 Å, allowing simultaneous calibration of instrumental drifts as well as a precise wavelength reference (Valenti et al. 1995; Butler et al. 1996).

We have obtained 20 AAT observations of HD 33844 since 2009 February 4 and an iodine-free template spectrum was obtained on 2011 January 19. With  $V = 7.29$ , exposure times are typically 900–1200 s with a resulting S/N of  $\sim 100$ –200 per pixel each epoch. The data given in Table 1 span a total of 1880 days (5.5 years) and have a mean internal velocity uncertainty of  $2.1 \text{ m s}^{-1}$ .

HD 33844 was also observed with the High Resolution Echelle Spectrometer (HIRES) on the 10 m Keck I telescope. A total of 36 epochs have been obtained spanning 2190 days (6 years). Radial velocities were computed using the iodine cell method as described above; the data are given in Table 2 and have a mean internal uncertainty of  $1.3 \text{ m s}^{-1}$ .

We also include 11 radial velocity observations from the FEROS spectrograph (Kaufer et al. 1999) on the 2.2 m telescope at La Silla Observatory. Those data are part of the EXPRESS (EXoPlanets aRound Evolved StarS) survey (Jones et al. 2011, 2015) for planets orbiting evolved stars. The PPPS and EXPRESS surveys have 37 targets in common; further papers are in preparation detailing joint planet discoveries made possible by the combination of the two data sets. The FEROS data for HD 33844 are given in Table 3; they cover a span of 1108 days and have a mean internal uncertainty of  $3.9 \text{ m s}^{-1}$ . The typical observing time was 250 s, leading to a S/N of 200 per pixel. The spectra were reduced using a flexible pipeline for echelle spectra (Jordan et al. 2014; R. Brahm et al. 2015, in preparation). The radial velocities were computed using the simultaneous calibration technique according to the method described in Jones et al. (2013) and Jones & Jenkins (2014).

**Table 2**  
Keck Radial Velocities for HD 33844

BJD-2400000	Velocity (m s <sup>-1</sup> )	Uncertainty (m s <sup>-1</sup> )
54340.13214	29.1	1.2
54400.03609	20.0	1.2
54461.88282	3.4	1.4
54718.14825	-19.7	1.3
54791.07499	-10.8	1.4
54809.92924	-1.6	1.3
54839.01997	-0.4	1.4
54846.97020	-0.7	1.5
54864.91819	4.6	1.4
54929.72286	-11.5	1.5
55079.13055	-43.3	1.3
55109.10676	-31.3	1.3
55173.05357	-22.4	1.2
55187.90328	-13.5	1.3
55197.97134	-12.3	1.4
55229.77649	0.2	1.3
55255.74938	20.3	1.3
55285.78110	47.9	1.3
55312.72317	52.1	1.4
55428.13474	9.6	1.2
55456.04501	22.6	1.2
55490.96109	12.7	1.4
55521.97151	-3.1	1.4
55546.07504	-13.0	1.4
55584.91662	-35.2	1.3
55633.81481	-58.0	1.4
55791.13774	-33.8	1.2
55810.13994	-19.4	1.1
55902.01080	9.5	1.2
55904.86470	10.1	1.4
55931.98977	9.7	1.3
55960.77092	26.9	1.3
55972.77806	10.9	1.3
56197.06671	-18.9	1.3
56319.74545	7.3	1.4
56530.11001	14.2	1.3

**Table 3**  
FEROS Radial Velocities for HD 33844

BJD-2400000	Velocity (m s <sup>-1</sup> )	Uncertainty (m s <sup>-1</sup> )
55457.83090	39.0	5.2
55612.57290	-55.3	3.8
56160.93800	-1.4	4.0
56230.78520	-10.3	3.9
56241.78170	-7.2	4.5
56251.83720	-23.6	2.6
56321.60110	15.8	3.7
56331.62140	24.1	3.9
56342.58360	23.9	3.5
56412.47550	8.8	4.6
56565.79190	-13.7	3.3

### 2.1. Stellar Properties

We have used our iodine-free template spectrum ( $R \sim 60,000$ , S/N  $\sim 200$ ) to derive spectroscopic stellar parameters. In brief, the iron abundance [Fe/H] was determined from the equivalent widths of 32 unblended Fe lines and the LTE model atmospheres adopted in this work were interpolated from the ODFNEW grid of ATLAS9 (Castelli & Kurucz 2004). The effective temperature ( $T_{\text{eff}}$ ) and bolometric correction (BC)

**Table 4**  
Stellar Parameters for HD 33844

Parameter	Value	References
Spec. Type	K0 III	Houk & Smith-Moore (1988)
Distance (pc)	$100.9 \pm 6.5$	van Leeuwen (2007)
$(B - V)$	$1.040 \pm 0.009$	Perryman et al. (1997)
$E(B - V)$	0.0290	...
$A_V$	0.0903	...
Mass ( $M_\odot$ )	$1.78 \pm 0.18$	This work
	$1.74 \pm 0.18$	Jones et al. (2011)
$V \sin i$ (km s <sup>-1</sup> )	<1	This work
	1.65	Jones et al. (2011)
[Fe/H]	$+0.27 \pm 0.09$	This work
	$+0.17 \pm 0.10$	Jones et al. (2011)
	$+0.19 \pm 0.12$	Luck & Heiter (2007)
$T_{\text{eff}}$ (K)	$4861 \pm 100$	This work
	4890	Jones et al. (2011)
	4710	Massarotti et al. (2008)
	4886	Luck & Heiter (2007)
log $g$	$3.24 \pm 0.08$	This work
	3.05	Jones et al. (2011)
	3.1	Massarotti et al. (2008)
$v_r$ (km s <sup>-1</sup> )	$1.00 \pm 0.15$	This work
	1.17	Jones et al. (2011)
	1.42	Luck & Heiter (2007)
Radius ( $R_\odot$ )	$5.29 \pm 0.41$	This work
	$5.33 \pm 0.51$	Jones et al. (2011)
Luminosity ( $L_\odot$ )	$14.1 \pm 1.8$	This work
	14.4	Jones et al. (2011)
	12.6	Massarotti et al. (2008)
Age (Gyr)	$1.88^{+0.76}_{-0.48}$	This work

were derived from the color index  $B - V$  and the estimated metallicity using the empirical calibration of Alonso et al. (1999, 2001). Since the color- $T_{\text{eff}}$  method is not extinction-free, we corrected for reddening using  $E(B - V) = 0.0290$  (Schlegel et al. 1998). The stellar mass and age were estimated from the interpolation of Yonsei-Yale ( $Y^2$ ) stellar evolution tracks (Yi et al. 2003). The resulting stellar mass of  $1.78 \pm 0.18 M_\odot$  was adopted for calculating the planet masses. Our derived stellar parameters are given in Table 4 and are in excellent agreement with the results of Jones et al. (2011) who found a mass of  $1.74 \pm 0.18 M_\odot$  and a radius of  $5.33 \pm 0.51 R_\odot$ .

### 3. ORBIT FITTING AND PLANETARY PARAMETERS

Early AAT data for HD 33844 exhibited a periodicity of  $\sim 510$  days, but the one-planet fit worsened with time until it could be tentatively fit with a second planet near  $\sim 900$  days. Preliminary analysis of the AAT and Keck data together corroborated the two candidate periodicities. We first explored a wide range of parameter space by fitting the two data sets with a two-Keplerian model within a genetic algorithm (e.g., Horner et al. 2012; Wittenmyer et al. 2012a, 2013c). In brief, the genetic algorithm works on principles of evolutionary biology, producing an initially random population of planetary system parameters and then selecting the best-fit (lowest  $\chi^2$ ) models for “reproduction.” The next generation is then generated by perturbing the best-fit models (“mutation”) and repeating the process. The two planets were allowed to take on orbital periods in the range  $P_1$ : 400–600 day and  $P_2$ : 700–1200 day and eccentricities  $e < 0.3$ . A total of about  $10^7$  possible system configurations were tested in this manner. The best two-

planet solution was then used as a starting point for the generalized least-squares program *GaussFit* (Jefferys et al. 1988), which is used here to solve a Keplerian radial velocity orbit model as in our previous work (Tinney et al. 2011; Wittenmyer et al. 2011a, 2015c). As a further check, we performed a Keplerian fit optimized with a simplex algorithm using version 2.1730 of the *Systemic Console* (Meschiari et al. 2009) and estimated parameter uncertainties using the bootstrap routine therein on 100,000 synthetic data set realizations. We added  $7 \text{ m s}^{-1}$  of jitter in quadrature to the uncertainties of each of the three data sets. This jitter estimate is derived from 37 stable stars in the PPPS (334 measurements); their velocity distribution can be fit with a Gaussian of width  $\sigma = 7 \text{ m s}^{-1}$ . Since the planets are massive and move on orbits relatively close to each other (such that interactions can be expected), we also performed a dynamical fit using the Runge–Kutta integration method within *Systemic*. Table 5 gives the planetary system parameters resulting from both the Keplerian and dynamical fits; the results are indistinguishable and hence neither technique is clearly favored. The parameters given represent the mean of the posterior distribution and the 68.7% confidence interval. Using the host star mass of  $1.78 M_\odot$  in Table 4, we derive planetary minimum masses of  $1.96 \pm 0.12 M_{\text{Jup}}$  (HD 33844b) and  $1.76 \pm 0.18 M_{\text{Jup}}$  (HD 33844c). The data and model fits for each planet are plotted in Figures 1–2.

## 4. DISCUSSION

### 4.1. Evidence for Orbiting Planets

Particularly for giant stars, where spots and pulsations can induce spurious radial velocity shifts with periods of hundreds of days, any claim of orbiting planets must be carefully examined to rule out intrinsic stellar signals (e.g., Hatzes & Cochran 2000; Reffert et al. 2015; Trifonov et al. 2015). For HD 33844, the periods of the two signals (551 and 916 days) are nowhere near the window function peaks at 384 and 8.1 days (AAT) or 30 and 364 days (Keck). Spurious periods in observational data commonly arise at those periods due to sampling (imposed by bright-time scheduling and the yearly observability of a given target).

To check whether the observed velocity variations could be due to intrinsic stellar processes, we examined the All-Sky Automated Survey (ASAS)  $V$  band photometric data for HD 33844 (Pojmanski & Maciejewski 2004). A total of 596 epochs were obtained from the ASAS All Star Catalog.<sup>14</sup> We computed the mean magnitude per epoch over the five apertures then subjected the time series to an iterative sigma-clipping process. We removed points more than  $3\sigma$  from the grand mean then recalculated the mean and its standard deviation. This process was performed three times, after which 511 epochs remained with a mean value of  $7.28 \pm 0.02$ . The generalized Lomb–Scargle periodogram (Zechmeister & Kürster 2009) is shown in Figure 3 with the periods of the planets marked as dashed lines. While there are significant periodicities at 730 and 1250 days, there is little power near the periods of the candidate planets (551 and 916 days).

We also checked for correlation between the radial velocities and the equivalent width of the  $H\alpha$  absorption line, which has been used as an activity indicator for giants (Hatzes et al. 2015)

<sup>14</sup> <http://www.astrouw.edu.pl/asas>

**Table 5**  
HD 33844 Planetary System Parameters

Parameter	Keplerian Fit		Dynamical Fit	
	HD 33844b	HD 33844c	HD 33844b	HD 33844c
Period (days)	$551.4 \pm 7.8$	$916.0 \pm 29.5$	$547.9 \pm 6.4$	$924.3 \pm 32.5$
Eccentricity	$0.15 \pm 0.07$	$0.13 \pm 0.10$	$0.16 \pm 0.07$	$0.09 \pm 0.08$
$\omega$ (degrees)	$211 \pm 28$	$71 \pm 67$	$190 \pm 62$	$5 \pm 30$
$K$ ( $\text{m s}^{-1}$ )	$33.5 \pm 2.0$	$25.4 \pm 2.9$	$32.9 \pm 2.2$	$24.0 \pm 2.2$
$T_0$ (BJD-2400000)	$54609 \pm 41$	$54544 \pm 164$	$54578 \pm 50$	$54356 \pm 281$
$m \sin i$ ( $M_{\text{Jup}}$ )	$1.96 \pm 0.12$	$1.75 \pm 0.18$	$1.92 \pm 0.11$	$1.68 \pm 0.16$
$a$ (AU)	$1.60 \pm 0.02$	$2.24 \pm 0.05$	$1.59 \pm 0.01$	$2.25 \pm 0.03$
rms of fit—AAT ( $\text{m s}^{-1}$ )	5.9		9.4	
rms of fit—Keck ( $\text{m s}^{-1}$ )	7.2		7.2	
rms of fit—FEROS ( $\text{m s}^{-1}$ )	10.7		11.6	
Total $\chi^2$ (54 dof)	65.7		66.4	

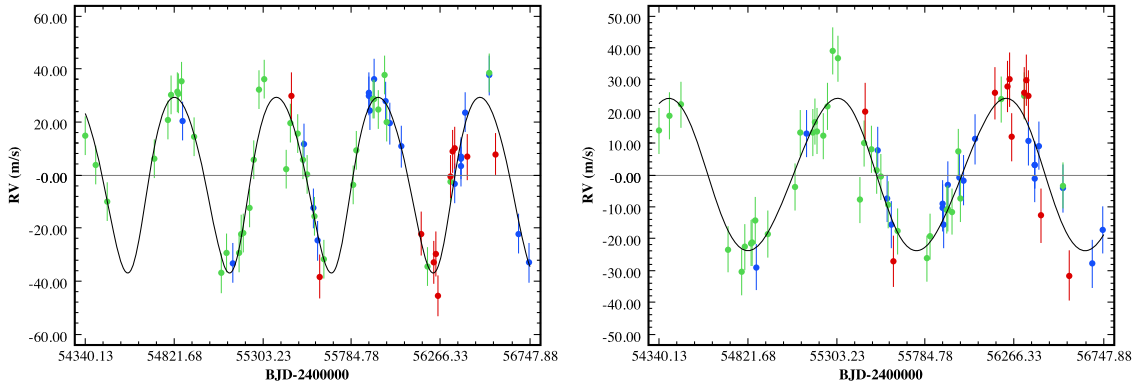


**Figure 1.** Left panel: data and Keplerian model fit for the inner planet HD 33844b, with the outer planet removed. Error bars are the quadrature sum of the internal uncertainties and  $5 \text{ m s}^{-1}$  of jitter. Right panel: same, but for the outer planet HD 33844c with the inner planet removed. The total rms about the two-planet Keplerian fit is  $7.3 \text{ m s}^{-1}$ . AAT—blue, Keck—green, FEROS—red.

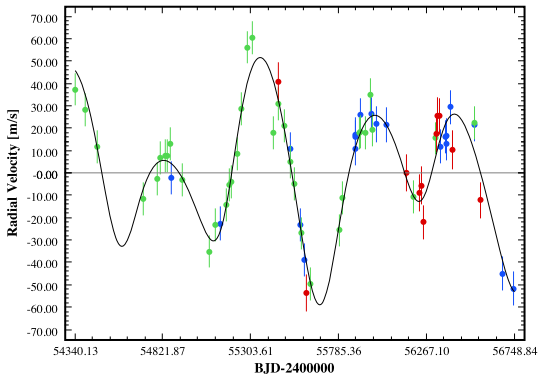


**Figure 2.** Two-planet Keplerian fit for the HD 33844 system. The symbols have the same meaning as in Figure 1.

as well as for M dwarfs (Robertson et al. 2013). The equivalent widths were measured in a  $2 \text{ \AA}$  window centered on  $\text{H}\alpha$  to avoid contamination by telluric lines. A generalized Lomb–Scargle periodogram of the  $\text{H}\alpha$  equivalent widths from the AAT spectra (Figure 4) shows no significant periodicities and

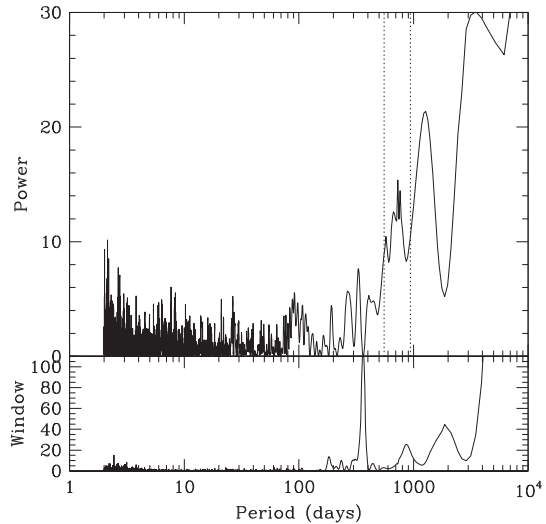


**Figure 3.** Generalized Lomb–Scargle periodogram of ASAS photometry for HD 33844. A total of 511 epochs spanning 8.8 years reveal no periodicities commensurate with the orbital periods of the planets (vertical dashed lines).

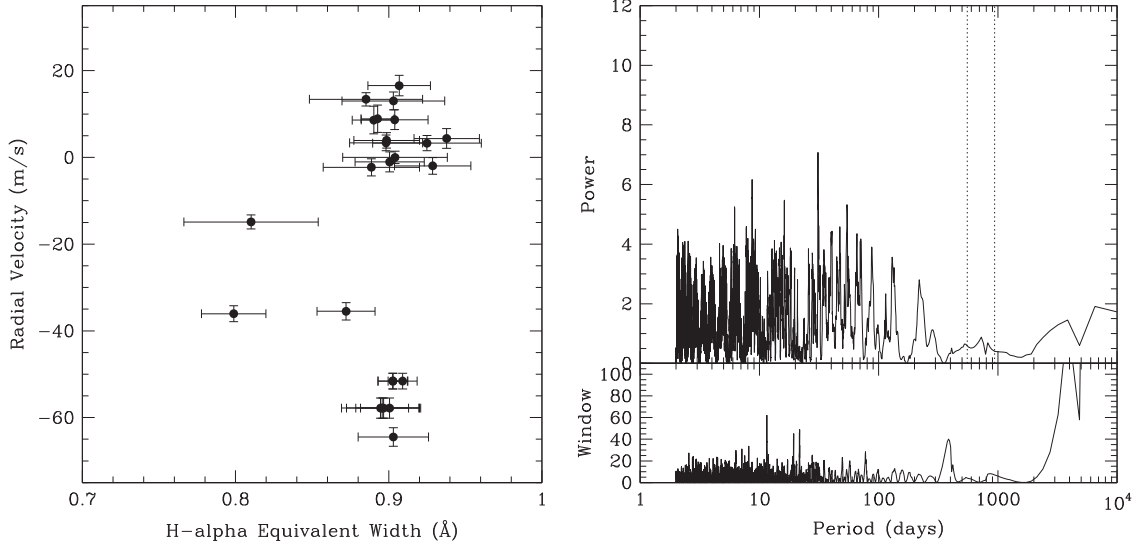


**Figure 4.** Left panel: AAT radial velocities and their H $\alpha$  equivalent widths. No correlations are evident. Right panel: generalized Lomb–Scargle periodogram of the H $\alpha$  measurements, again revealing no significant periodicities. The orbital periods of the planets are marked as vertical dashed lines.

there are no correlations with the velocities. Furthermore, the bisector velocity spans (defined as the velocity difference between line bisectors from the upper and lower part of an absorption line) computed from the FEROS spectra show no correlation with the radial velocities.

#### 4.2. Dynamical Stability

The HD 33844 system appears to contain two super-Jupiter planets in orbits relatively close to each other. Given their mass and proximity, it is clearly important to consider whether the planets are dynamically feasible. That is, could planets on such tightly packed orbits be dynamically stable on timescales comparable to the lifetime of the system? A first estimate of the system’s stability can be garnered by simply assessing the dynamical separation of the two planets, considering the separation of their orbits compared to their mutual Hill radius. Following Gladman (1993), we can calculate the mutual Hill radius of the two planets as follows:

$$R_H = \left[ \frac{(m_1 + m_2)}{3M_\odot} \right]^{1/3} \left[ \frac{(a_1 + a_2)}{2} \right], \quad (1)$$

where the symbols have their usual meaning and the subscripts refer to the inner (1) and outer (2) planets respectively. Following this formulism, we find that the best-fit orbits for the two candidate planets are separated by 3.8 times their mutual Hill radius ( $R_H = 0.167$  AU). For low-eccentricity orbits Gladman (1993) found that orbits became unstable at separations smaller than  $\sim 2\sqrt{3} = 3.46 R_H$ . The HD 33844 system is therefore close to this critical separation and as the proposed orbits are somewhat eccentric, it is clearly important to subject the proposed planets to further scrutiny. In contrast to widely separated systems such as HD 121056, (where the planets orbit at 0.4 and 3.0 AU—more than 9 mutual Hill radii apart), for which  $N$ -body simulations were not necessary, here

we must rigorously test the HD 33844 system stability as in our previous work (e.g., Marshall et al. 2010; Horner et al. 2013; Wittenmyer et al. 2013a).

Most interesting are those systems (e.g., Robertson et al. 2012a, 2012b; Wittenmyer et al. 2012b) for which the planets prove stable and dynamically feasible across just a small fraction of the potential orbital solutions. In these cases, which typically feature planets moving on or close to mutually resonant orbits, dynamical simulations serve a dual purpose. First, they provide evidence that supports the existence of the planets and secondly, they provide a strong additional constraint on the potential orbits followed by those planets, helping us to better tie down their true orbits than can be achieved on the basis of the observations alone.

Here, we study the stability of the candidate planets orbiting HD 33844 following a now well-established route. We created a suite of 126,075 copies of the HD 33844 system. In each of these cloned systems, the initial orbit of HD 33844b was the same, located at its nominal best-fit values (Table 5). For each system, we systematically varied the initial semimajor axis ( $a$ ), eccentricity ( $e$ ), argument of periastron ( $\omega$ ), and mean anomaly ( $M$ ) of HD 33844c. The masses of the planets were held fixed at their minimum values ( $m \sin i$ , Table 5). We note that changing the mass of the planets could alter the stability of the system. This can be illustrated by examination of Equation (1): it is immediately apparent that if the masses of the planets are increased, so too is the size of their mutual Hill radius and thereby the strength of their mutual interaction. However, the effect is actually relatively small when compared with the influence of their orbital elements. As such, in this work we solely explore the influence of “element space” and leave the exploration of “mass space” for future work, once the orbital elements of the planets have been better constrained through followup observations. Once the uncertainties in those elements are sufficiently small, it might be possible to use “mass space” to constrain the maximum masses of the planets and thereby

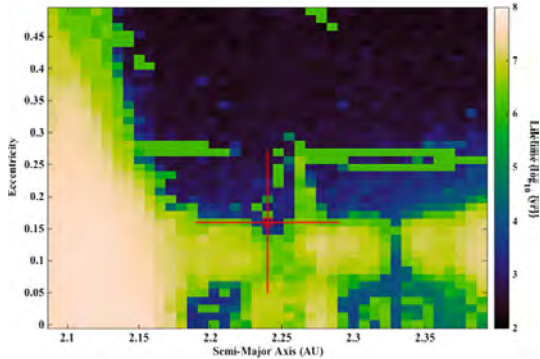


**Figure 5.** Dynamical stability for the HD 33844 system as a function of the initial semimajor axis and eccentricity of the outer planet. The best-fit orbit for that planet is marked by the open square and the crosshairs show the  $1\sigma$  uncertainties. Configurations featuring eccentricities  $1\sigma$  smaller than the nominal best fit generally remained stable for more than  $10^6$  years.

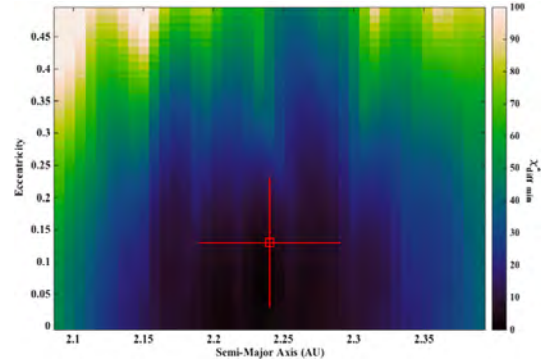


**Figure 6.**  $\chi^2$  difference compared with the best fit for the 126,075 system configurations tested in Figure 5 as a function of the initial semimajor axis and eccentricity of HD 33844c. At each  $a - e$  location we show the minimum value of total  $\chi^2$  from the 75  $\omega$ -mean anomaly combinations tested therein (54 degrees of freedom).

obtain some constraints on the inclination of the system to our line of sight, but such calculations are beyond the scope of this work. We do, however, note that a tentative upper limit on the masses of the planets can be obtained using the resonance overlap criterion (e.g., Wisdom 1980; Deck et al. 2013). This analytic estimate sets an upper bound of  $\sim 10 M_{\text{Jup}}$  for each planet. As such, we can be fairly confident that the two bodies are planetary in nature rather than being brown dwarfs.

Since previous studies have shown that the stability of a system is most strongly dependent on semimajor axis and eccentricity, we tested 41 discrete values of each of these variables spanning the full  $\pm 3\sigma$  uncertainty ranges. At each of the 1681  $a - e$  pairs created in this way, we tested 15 unique values of the argument of periastron and five of the mean anomaly, distributed in each case evenly across the  $1\sigma$  uncertainty ranges in these variables. This gave us a total of 126,075 unique potential orbits for HD 33844c.

We then used the Hybrid integrator within the  $n$ -body dynamics package MERCURY (Chambers 1999) to follow the evolution of each of the test planetary systems for a period of 100 Myr. Simulations were stopped early if either of the planets were ejected from the system (upon reaching a barycentric distance of 5 AU, which would require significant strong instability between the two planets). They were also halted if either of the planets fell into the central star whose mass was set at  $1.78 M_{\odot}$  or if they collided with one another. If any of these events happened, the time of collision/ejection was recorded and the simulation was brought to a close.

As a result of these simulations, we are able to examine the dynamical stability of the HD 33844 system as a function of the initial orbit on which HD 33844c was placed. Figure 5 shows the stability of the system as a function of the initial semimajor axis and eccentricity of that planet's orbit. In Figure 6 we show how the orbital solutions tested in our dynamical simulations fit to the observed data, expressed in terms of the difference in total  $\chi^2$  relative to the best fit.

It is immediately clear from Figure 5 that the proposed orbital solution for the system lies in a region of complex dynamical behavior with both extremely stable and unstable solutions being possible. It is reassuring, however, to note that broad regions of dynamical stability lie comfortably within the

$1\sigma$  uncertainties on the proposed solution, particularly toward lower eccentricities. We note that least-squares radial velocity fitting routines are well-known to inflate eccentricities (e.g., Shen & Turner 2008; O'Toole et al. 2009; Wittenmyer et al. 2013c). That stability is due to orbits in that region being trapped in mutual 3:5 mean motion resonance with the orbit of HD 33844b. From Table 5 the Keplerian solution gives a period ratio of 1.661 and 1.687 for the dynamical fit. Within their uncertainties these solutions agree with each other and are wholly consistent with the 3:5 resonance (period ratio 1.667).

In addition to the central region of stability, orbits at smaller semimajor axes fall into a broad region of stability that extends across the full span of tested orbital eccentricities. This feature is the result of the mutual 2:3 mean motion resonance between HD 33844c and HD 33844b which is centered on 2.102 AU.

We can also see evidence of unstable resonant behavior through the plot. Most strikingly, there is a band of unstable solutions centered at 2.33 AU. This band is the result of the 4:7 mean motion resonance between the two planets. A further unstable resonant region can be seen around 2.195 AU, associated with the 5:8 resonance between the planets. Finally, the 5:9 resonance can be found at 2.375 AU, which is likely the cause of the sculpting of the stability of the system in that region.

As such, we can conclude that the candidate planets orbiting HD 33844 are dynamically feasible but that they most likely move on mutually resonant, low-eccentricity orbits. As a further check, we investigated the behavior of the resonant angles for a number of key resonances in the vicinity of the complicated "stability terrain" around the best-fit orbit. We found that the best-fit orbital solution is strongly influenced by its proximity to the 3:5 resonance. In particular, we found that the resonant angle  $\phi = 5\lambda_2 - 3\lambda_1 - \omega_1 + \omega_2$  alternates between libration and circulation in a regular manner, completing three full cycles (one libration + one circulation) per 500 years of integration. A similar but noisier behavior was observed for a scenario in which the planets were located on orbits whose periods were in 5:8 commensurability. Here the resonant angle for the 5:8 mean motion resonance switched chaotically between periods of libration (lasting up to 1000 years) and period of smooth, slow circulation. The influence of

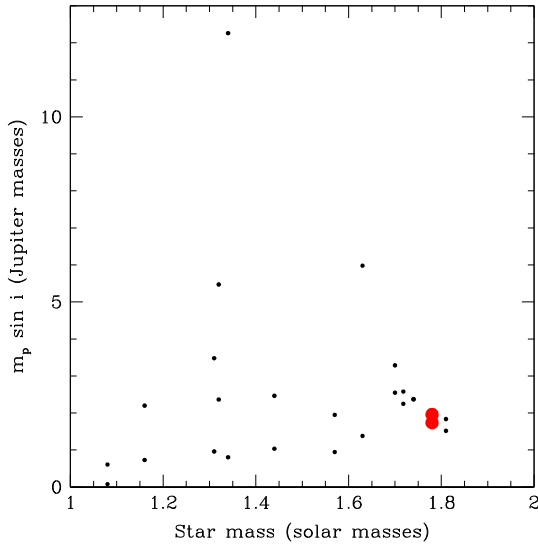


**Figure 7.** Minimum masses ( $m \sin i$ ) of planets in multiple systems orbiting evolved stars ( $\log g < 4.0$ ) as a function of stellar mass. Only 12 such systems are known; HD 33844 is shown as large red filled circles.

resonant interaction for these solutions was unmistakable, and given the proximity of the best-fit solution to the location of the 3:5 resonance, it seems most likely that the planets are trapped within it (although we note that the 5:8 and 7:12 mean motion resonances also fall within the  $1\sigma$  uncertainty in semimajor axis) together with an abundance of higher-order weaker resonances.

## 5. CONCLUSIONS

We have given evidence for two super-Jovian mass planets orbiting the metal-rich ( $[\text{Fe}/\text{H}] = +0.27 \pm 0.09$ ) giant, HD 33844. This result is consistent with findings from Reffert et al. (2015) and Maldonado et al. (2013) demonstrating that metal-rich stars with masses greater than  $1.5 M_{\odot}$  are more likely to host planets. To date, relatively few systems of multiple giant planets are known to orbit evolved stars. Figure 7 shows the 12 previously known multiple-planet systems orbiting evolved stars ( $\log g < 4.0$ ). The HD 33844 system is included as large red circles. HD 33844 is also a multiple-Jovian planet system in which all of the gas giants ( $m \sin i > 0.2 M_{\text{Jup}}$ ) have low eccentricities ( $e < 0.2$ ). Such a configuration is relatively uncommon (Harakawa et al. 2015), with only 15 systems known to date. Jones et al. (2015) noted that of the multiple-planet systems known to orbit evolved stars all but one of the host stars were first-ascent giants; HD 33844 adds to this count as it is near the base of the red giant branch. This is relevant because although the inner planet has a large orbital distance ( $a \sim 1.6$  AU), it might eventually be engulfed in a distant future due to tidal interaction with the host star while the outer planet ( $a \sim 2.3$  AU) might eventually survive such a process (e.g., Villaver & Livio 2007; Kunitomo et al. 2011; Mustill & Villaver 2012). As a result, in a distant future this system might evolve to a single-planet system, which is what we typically find around post-RGB stars as suggested by Jones et al. (2015).

It has been noted by Ghezzi et al. (2010) and Sousa et al. (2008) that there may be a correlation between the stellar metallicity and the masses of the planets, i.e., stars hosting only  $\sim$  Neptune-mass planets tend to have lower metallicity than stars hosting Jupiter-mass planets. In particular, Ghezzi et al. (2010) remarked that it is possible that “metallicity plays an important role in setting the mass of the most massive planet.” We have checked for the possibility of additional undetected planets using our well-established detection-limit methods (e.g., Wittenmyer et al. 2006, 2011b, 2013b). For our data on HD 33844, with a total residual rms of  $7.3 \text{ m s}^{-1}$  we can rule out the presence of additional planets with  $m \sin i > 0.3 M_{\text{Jup}}$  interior to HD 33844b at 99% confidence. To push this limit down to the Neptune-mass regime, one must observe at higher cadence (Wittenmyer et al. 2015a) or adopt observing strategies specifically intended to mitigate stellar oscillation noise (O’Toole et al. 2008; Dumusque et al. 2011).

J.H. is supported by USQ’s Strategic Research Fund: the STARWINDS project. C.G.T. is supported by Australian Research Council grants DP0774000 and DP130102695. We gratefully acknowledge the efforts of PPPS guest observers Brad Carter, Hugh Jones, and Simon O’Toole. This research has made use of NASA’s Astrophysics Data System (ADS) and the SIMBAD database operated at CDS, Strasbourg, France. This research has also made use of the Exoplanet Orbit Database and the Exoplanet Data Explorer at exoplanets.org (Wright et al. 2011).

## REFERENCES

- Alonso, A., Arribas, S., & Martínez-Roger, C. 1999, *A&AS*, **140**, 261  
 Alonso, A., Arribas, S., & Martínez-Roger, C. 2001, *A&A*, **376**, 1039  
 Bowler, B. P., Johnson, J. A., Marcy, G. W., et al. 2010, *ApJ*, **709**, 396  
 Butler, R. P., Marcy, G. W., Williams, E., et al. 1996, *PASP*, **108**, 500  
 Butler, R. P., Tinney, C. G., Marcy, G. W., et al. 2001, *ApJ*, **555**, 410  
 Castelli, F., & Kurucz, R. L. 2004, in Proc. IAU Symp. 210, Modelling of Stellar Atmospheres, ed. N. Piskunov et al. (Dordrecht: Kluwer)  
 Chambers, J. E. 1999, *MNRAS*, **304**, 793  
 Deck, K. M., Payne, M., & Holman, M. J. 2013, *ApJ*, **774**, 129  
 Diego, F., Charalambous, A., Fish, A. C., & Walker, D. D. 1990, Proc. SPIE, **1235**, 562  
 Dumusque, X., Udry, S., Lovis, C., Santos, N. C., & Monteiro, M. J. P. F. G. 2011, *A&A*, **525**, A140  
 Fischer, D. A., & Valenti, J. 2005, *ApJ*, **622**, 1102  
 Ghezzi, L., Cunha, K., Smith, V. V., et al. 2010, *ApJ*, **720**, 1290  
 Girardi, L., Bertelli, G., Bressan, A., et al. 2002, *A&A*, **391**, 195  
 Gladman, B. 1993, *Icar*, **106**, 247  
 Harakawa, H., Sato, B., Omiya, M., et al. 2015, *ApJ*, **806**, 5  
 Hatzes, A. P., & Cochran, W. D. 2000, *AJ*, **120**, 979  
 Hatzes, A. P., Cochran, W. D., Endl, M., et al. 2015, *A&A*, **580**, A31  
 Horner, J., Wittenmyer, R. A., Hinse, T. C., et al. 2013, *MNRAS*, **435**, 2033  
 Horner, J., Wittenmyer, R. A., Hinse, T. C., & Tinney, C. G. 2012, *MNRAS*, **425**, 749  
 Houk, N., & Smith-Moore, M. 1988, in Michigan Catalogue of Two-dimensional Spectral Types for the HD Stars, Vol. 4, ed. N. Houk, & M. Smith-Moore (Ann Arbor, MI: Univ. Michigan) 14+505  
 Ida, S., & Lin, D. N. C. 2005, *ApJ*, **626**, 1045  
 Jefferys, W. H., Fitzpatrick, M. J., & McArthur, B. E. 1988, *CeMec*, **41**, 39  
 Johnson, J. A., Aller, K. M., Howard, A. W., & Crepp, J. R. 2010, *PASP*, **122**, 905  
 Johnson, J. A., Marcy, G. W., Fischer, D. A., et al. 2006, *ApJ*, **652**, 1724  
 Jones, H. R. A., Butler, R. P., Tinney, C. G., et al. 2010, *MNRAS*, **403**, 1703  
 Jones, M. I., & Jenkins, J. S. 2014, *A&A*, **562**, A129  
 Jones, M. I., Jenkins, J. S., Rojo, P., & Melo, C. H. F. 2011, *A&A*, **536**, A71  
 Jones, M. I., Jenkins, J. S., Rojo, P., Melo, C. H. F., & Bluhm, P. 2013, *A&A*, **556**, A78  
 Jones, M. I., Jenkins, J. S., Rojo, P., Melo, C. H. F., & Bluhm, P. 2015, *A&A*, **573**, A3  
 Jordan, A., Brahm, R., Bakos, G. A., et al. 2014, *AJ*, **148**, 29

- Kaufer, A., Stahl, O., Tubbesing, S., et al. 1999, *Msngr*, **95**, 8
- Kretke, K. A., Lin, D. N. C., Garaud, P., & Turner, N. J. 2009, *ApJ*, **690**, 407
- Kunitomo, M., Ikoma, M., Sato, B., Katsuta, Y., & Ida, S. 2011, *ApJ*, **737**, 66
- Luck, R. E., & Heiter, U. 2007, *AJ*, **133**, 2464
- Maldonado, J., Villaver, E., & Eiroa, C. 2013, *A&A*, **554**, A84
- Marshall, J., Horner, J., & Carter, A. 2010, *IJAsB*, **9**, 259
- Massarotti, A., Latham, D. W., Stefanik, R. P., & Fogel, J. 2008, *AJ*, **135**, 209
- Meschiari, S., Wolf, A. S., Rivera, E., et al. 2009, *PASP*, **121**, 1016
- Mustill, A. J., & Villaver, E. 2012, *ApJ*, **761**, 121
- Omiya, M., Izumiura, H., Han, I., et al. 2009, *PASJ*, **61**, 825
- O'Toole, S. J., Tinney, C. G., & Jones, H. R. A. 2008, *MNRAS*, **386**, 516
- O'Toole, S. J., Tinney, C. G., Jones, H. R. A., et al. 2009, *MNRAS*, **392**, 641
- Perryman, M. A. C., Lindegren, L., Kovalevsky, J., et al. 1997, *A&A*, **323**, L49
- Pojmanski, G., & Maciejewski, G. 2004, *AcA*, **54**, 153
- Reffert, S., Bergmann, C., Quirrenbach, A., Trifonov, T., & Künstler, A. 2015, *A&A*, **574**, A116
- Robertson, P., Endl, M., Cochran, W. D., et al. 2012a, *ApJ*, **749**, 39
- Robertson, P., Endl, M., Cochran, W. D., & Dodson-Robinson, S. E. 2013, *ApJ*, **764**, 3
- Robertson, P., Horner, J., Wittenmyer, R. A., et al. 2012b, *ApJ*, **754**, 50
- Sato, B., Kambe, E., Takeda, Y., et al. 2005, *PASJ*, **57**, 97
- Schlegel, D. J., Finkbeiner, D. P., & Davis, M. 1998, *ApJ*, **500**, 525
- Shen, Y., & Turner, E. L. 2008, *ApJ*, **685**, 553
- Sousa, S. G., Santos, N. C., Mayor, M., et al. 2008, *A&A*, **487**, 373
- Tinney, C. G., Butler, R. P., Marcy, G. W., et al. 2001, *ApJ*, **551**, 507
- Tinney, C. G., Wittenmyer, R. A., Butler, R. P., et al. 2011, *ApJ*, **732**, 31
- Trifonov, T., Reffert, S., Zechmeister, M., et al. 2015, *A&A*, **582**, A54
- Valenti, J. A., Butler, R. P., & Marcy, G. W. 1995, *PASP*, **107**, 966
- van Leeuwen, F. 2007, *A&A*, **474**, 653
- Villaver, E., & Livio, M. 2007, *ApJ*, **661**, 1192
- Wisdom, J. 1980, *AJ*, **85**, 1122
- Wittenmyer, R. A., Butler, R. P., Wang, L., et al. 2016, *MNRAS*, **455**, 1398
- Wittenmyer, R. A., Endl, M., Cochran, W. D., et al. 2006, *AJ*, **132**, 177
- Wittenmyer, R. A., Endl, M., Wang, L., et al. 2011a, *ApJ*, **743**, 184
- Wittenmyer, R. A., Gao, D., Hu, S. M., et al. 2015a, *PASP*, **127**, 1021
- Wittenmyer, R. A., Horner, J., & Marshall, J. P. 2013a, *MNRAS*, **431**, 2150
- Wittenmyer, R. A., Horner, J., Marshall, J. P., Butters, O. W., & Tinney, C. G. 2012a, *MNRAS*, **419**, 3258
- Wittenmyer, R. A., Horner, J., & Tinney, C. G. 2012b, *ApJ*, **761**, 165
- Wittenmyer, R. A., Horner, J., Tuomi, M., et al. 2012c, *ApJ*, **753**, 169
- Wittenmyer, R. A., Liu, F., Wang, L., et al. 2015b, *AJ*, submitted
- Wittenmyer, R. A., Tinney, C. G., Horner, J., et al. 2013b, *PASP*, **125**, 351
- Wittenmyer, R. A., Tinney, C. G., O'Toole, S. J., et al. 2011b, *ApJ*, **727**, 102
- Wittenmyer, R. A., Wang, L., Liu, F., et al. 2015c, *ApJ*, **800**, 74
- Wittenmyer, R. A., Wang, S., Horner, J., et al. 2013c, *ApJS*, **208**, 2
- Wright, J. T., Fakhouri, O., Marcy, G. W., et al. 2011, *PASP*, **123**, 412
- Yi, S. K., Kim, Y.-C., & Demarque, P. 2003, *ApJS*, **144**, 259
- Zechmeister, M., & Kürster, M. 2009, *A&A*, **496**, 577



# The Anglo-Australian Planet Search XXV: A Candidate Massive Saturn Analog Orbiting HD 30177

A SMALL CONTRIBUTION WAS MADE TO THE FOLLOWING paper. Provided plots for Figures 7-8 and 10-13 analysing statistical significance of relationships of orbital solutions.

C.1 WITTENMYER ET AL. (2017) THE ANGLO-AUSTRALIAN PLANET SEARCH XXV: A CANDIDATE MASSIVE SATURN ANALOG ORBITING HD 30177

The accepted paper [Wittenmyer et al. \(2017\)](#), “The Anglo-Australian Planet Search XXV: A Candidate Massive Saturn Analog Orbiting HD 30177” follows.



## The Anglo-Australian Planet Search. XXV. A Candidate Massive Saturn Analog Orbiting HD 30177

Robert A. Wittenmyer<sup>1,2</sup>, Jonathan Horner<sup>1,2</sup>, M. W. Mangel<sup>1</sup>, R. P. Butler<sup>3</sup>, D. J. Wright<sup>2</sup>, C. G. Tinney<sup>2</sup>,  
B. D. Carter<sup>1</sup>, H. R. A. Jones<sup>4</sup>, G. Anglada-Escudé<sup>5</sup>, J. Bailey<sup>2</sup>, and Simon J. O’Toole<sup>6</sup>

<sup>1</sup>Computational Engineering and Science Research Centre, University of Southern Queensland, Toowoomba, Queensland 4350, Australia; [rob.w@usq.edu.au](mailto:rob.w@usq.edu.au)

<sup>2</sup>School of Physics and Australian Centre for Astrobiology, University of New South Wales, Sydney 2052, Australia

<sup>3</sup>Department of Terrestrial Magnetism, Carnegie Institution of Washington, 5241 Broad Branch Road, NW, Washington, DC 20015-1305, USA

<sup>4</sup>Centre for Astrophysics Research, University of Hertfordshire, College Lane, Hatfield, Herts AL10 9AB, UK

<sup>5</sup>School of Physics and Astronomy, Queen Mary University of London, 327 Mile End Road, London E1 4NS, UK

<sup>6</sup>Australian Astronomical Observatory, P.O. Box 915, North Ryde, NSW 1670, Australia

Received 2016 September 19; revised 2016 November 22; accepted 2016 December 5; published 2017 March 20

### Abstract

We report the discovery of a second long-period giant planet orbiting HD 30177, a star previously known to host a massive Jupiter analog (HD 30177b:  $a = 3.8 \pm 0.1$  au,  $m \sin i = 9.7 \pm 0.5 M_{\text{Jup}}$ ). HD 30177c can be regarded as a massive Saturn analog in this system, with  $a = 9.9 \pm 1.0$  au and  $m \sin i = 7.6 \pm 3.1 M_{\text{Jup}}$ . The formal best-fit solution slightly favors a closer-in planet at  $a \sim 7$  au, but detailed  $n$ -body dynamical simulations show that configuration to be unstable. A shallow local minimum of longer period, lower eccentricity solutions was found to be dynamically stable, and hence we adopt the longer period in this work. The proposed  $\sim 32$  year orbit remains incomplete; further monitoring of this and other stars is necessary to reveal the population of distant gas giant planets with orbital separations  $a \sim 10$  au, analogous to that of Saturn.

**Key words:** planetary systems – stars: individual (HD 30177) – techniques: radial velocities

**Supporting material:** animations

### 1. Introduction

Prior to the dawn of the exoplanet era, it was thought that planetary systems around other stars would likely resemble our own—with small, rocky planets close to their host stars, and the more massive, giant planets at greater distances. With the discovery of the first exoplanets, however, that paradigm was shattered—and it rapidly became clear that many planetary systems are dramatically different to our own. However, to truly understand how unusual (or typical) the solar system is, we must find true Jupiter and Saturn analogs: massive planets on decade-long orbits around their hosts. The only way to find such planets is to monitor stars on decade-long timescales, searching for the telltale motion that might reveal such distant neighbors.

Nearly three decades of planet search have resulted in a great unveiling, at every stage of which we are finding our expectations consistently upturned as the true diversity of worlds becomes ever more apparent. Much progress has been made in understanding the occurrence rates and properties of planets orbiting within  $\sim 1$  au of their stars, brought on by the *Kepler* revolution (e.g., Borucki et al. 2011; Rowe et al. 2014; Coughlin et al. 2016) and the advent of Doppler velocimetry at precisions of  $1 \text{ m s}^{-1}$  (Fischer et al. 2016). While *Kepler* has been hugely successful in exploring the frequency of planets close to their stars, such transit surveys are not suited to search for planetary systems like our own—with giant planets moving on orbits that take decades to complete. To understand the occurrence of such systems requires a different approach—radial velocity monitoring of individual stars on decadal timescales.

Sometimes overshadowed by the *Kepler* discoveries, but equally important for a complete picture of planetary system properties, are the results from ongoing “legacy” Doppler

surveys, which are now sensitive to giant planets in orbits approaching 20 years. Those surveys include, for example, the McDonald Observatory Planet Search (Robertson et al. 2012a; Endl et al. 2016), the California Planet Search (Howard et al. 2010; Feng et al. 2015), the Anglo-Australian Planet Search (Tinney et al. 2001; Wittenmyer et al. 2011, 2014c), and the Geneva Planet Search (Marmier et al. 2013; Moutou et al. 2015).

The emerging picture is that the solar system is not typical of planetary systems in the solar neighborhood. For example, super-Earths, planets with masses of  $\sim 3\text{--}10 M_{\oplus}$ , are extremely common yet are completely absent from our solar system. Jupiter-like planets in Jupiter-like orbits appear to be relatively uncommon, orbiting only about 6% of solar-type stars (Wittenmyer et al. 2016a).

Such a low incidence of true solar system analogs is of particular interest in the context of astrobiology and the search for truly Earth-like planets beyond the solar system. In the solar system, Jupiter has played a key role in the formation and evolution of the planetary system—variously corralling, sculpting, and destabilizing the system’s smaller bodies (and thereby likely contributing significantly to the introduction of volatiles, including water, to the early Earth). Over the system’s more recent history, Jupiter has managed the flux of smaller objects toward the Earth, influencing (but not necessarily reducing) the frequency of impacts on the terrestrial planets. It has long been argued that the presence of a true Jupiter analog would be an important selection factor for an Earth-like planet to be truly habitable—though many recent studies have suggested that this might not be the case (e.g., Horner & Jones 2008; Horner et al. 2010; Horner & Jones 2010; Lewis et al. 2013).

The Anglo-Australian Planet Search (AAPS) monitored  $\sim 250$  solar-type stars for 14 years. Of these, a subset of  $\sim 120$

**Table 1**  
Stellar Parameters for HD 30177

Parameter	Value	References
Spec. Type	G8 V	Houk & Cowley (1975)
Distance (pc)	$54.7 \pm 2.3$	van Leeuwen (2007)
Mass ( $M_{\odot}$ )	$0.951^{+0.093}_{-0.053}$	Takeda et al. (2007)
	$1.05 \pm 0.08$	Santos et al. (2013)
	$0.988 \pm 0.033$	Sousa et al. (2011)
$V \sin i$ (km s <sup>-1</sup> )	$2.96 \pm 0.50$	Butler et al. (2006)
[Fe/H]	$+0.33 \pm 0.05$	Franchini et al. (2014)
	$0.37 \pm 0.06$	Adibekyan et al. (2012)
	$0.39 \pm 0.05$	Ghezzi et al. (2010)
	$0.394 \pm 0.030$	Butler et al. (2006)
$T_{\text{eff}}$ (K)	$5580 \pm 12$	Franchini et al. (2014)
	$5601 \pm 73$	Adibekyan et al. (2012)
	$5595 \pm 50$	Ghezzi et al. (2010)
	$5607 \pm 44$	Butler et al. (2006)
log $g$	$4.41 \pm 0.12$	Franchini et al. (2014)
	$4.34 \pm 0.05$	Sousa et al. (2011)
	$4.15 \pm 0.13$	Ghezzi et al. (2010)
	$4.31 \pm 0.06$	Butler et al. (2006)
Age (Gyr)	$11.6^{+1.8}_{-2.2}$	Takeda et al. (2007)

stars continued to be observed for a further three years, with the primary aim of detecting Jupiter-mass planets in orbits of  $P > 10$  year (Wittenmyer et al. 2016a). The AAPS has delivered a consistent  $3 \text{ m s}^{-1}$  velocity precision since its inception, enabling the discovery of several Jupiter analogs (e.g., Jones et al. 2010; Wittenmyer et al. 2012c, 2014a).

This paper is organized as follows. Section 2 outlines the AAT and HARPS observations of HD 30177 and gives the stellar parameters. Section 3 describes the orbit-fitting procedures and gives the resulting planetary parameters for the HD 30177 system. In Section 4, we perform a detailed dynamical stability analysis of this system of massive planets. Then we give our conclusions in Section 5.

## 2. Observational Data and Stellar Properties

HD 30177 is an old, Sun-like star, with a mass within 5% of solar. It lies approximately 54.7 pc from the Sun and has approximately twice solar metallicity. The stellar parameters for HD 30177 can be found in Table 1. We have observed HD 30177 since the inception of the AAPS, gathering a total of 43 epochs spanning 17 years (Table 2). Precise radial velocities are derived using the standard iodine-cell technique to calibrate the instrumental point-spread function (Valenti et al. 1995; Butler et al. 1996). The velocities have a mean internal uncertainty of  $3.9 \pm 1.2 \text{ m s}^{-1}$ .

HD 30177 has also been observed with the HARPS spectrograph on the ESO 3.6 m telescope in La Silla. At this writing, 20 epochs spanning 11 years are publicly available at the ESO Archive. Velocities were derived using the HARPS-TERRA technique (Anglada-Escudé & Butler 2012) and are given in Table 3.

## 3. Orbit Fitting and Results

The inner planet, HD 30177b, was first announced in Tinney et al. (2003), with a relatively unconstrained period of  $1620 \pm 800$  days and  $m \sin i = 7.7 \pm 1.5 M_{\text{Jup}}$ . Its orbit was updated in Butler et al. (2006) on the basis of observations that clearly spanned one full orbital period, to  $P = 2770 \pm 100$

**Table 2**  
AAT Radial Velocities for HD 30177

BJD-2400000	Velocity (m s <sup>-1</sup> )	Uncertainty (m s <sup>-1</sup> )
51118.09737	227.2	4.5
51119.19240	188.6	6.9
51121.15141	210.7	6.1
51157.10219	223.5	4.5
51211.98344	234.6	5.0
51212.96597	235.8	4.2
51213.99955	245.4	4.0
51214.95065	237.3	3.6
51525.99718	177.1	3.4
51630.91556	144.9	4.6
51768.32960	73.4	4.2
51921.10749	14.8	4.6
52127.32049	-9.2	8.5
52188.25324	-41.3	3.6
52358.91806	-45.6	3.8
52598.18750	-49.8	2.0
52655.02431	-57.6	4.4
52747.84861	-49.0	2.2
52945.18132	-12.7	2.6
53044.03464	8.2	3.6
53282.26188	58.2	2.8
53400.99440	91.4	2.5
54010.25007	137.4	1.8
54038.21420	126.4	3.4
54549.93698	-47.3	2.2
54751.25707	-83.8	3.8
54776.17955	-79.6	2.2
54900.95132	-78.0	3.4
55109.18072	-77.0	3.2
55457.26529	-32.2	3.9
55461.28586	-25.3	4.3
55519.17942	-2.1	3.3
55845.21616	82.2	4.7
55899.10987	79.0	3.2
56555.28257	149.0	4.1
56556.25219	152.0	3.6
56746.90702	97.7	5.1
56766.86295	66.2	4.0
56935.25257	10.2	4.0
56970.23271	5.6	3.0
57052.02821	-2.2	3.0
57094.90039	-28.0	4.6
57349.14648	-34.5	3.1

days and  $m \sin i = 10.5 \pm 0.9 M_{\text{Jup}}$ . We now present a further 10 years of AAT data, along with 11 years of concurrent HARPS data, to refine the orbit of this planet. As a result of this additional data, we now find that the single-planet fit exhibits significant residuals, suggesting the presence of a second, very long-period object in this system. We have added  $6 \text{ m s}^{-1}$  of jitter in quadrature to both data sets; this brings the reduced  $\chi^2$  close to 1 for two-planet models. A single-planet model now has a reduced  $\chi^2$  of 7.1 and an rms of  $17.3 \text{ m s}^{-1}$ . As in our previous work (e.g., Tinney et al. 2011; Wittenmyer et al. 2013; Horner et al. 2014; Wittenmyer et al. 2016b), we have used a genetic algorithm to explore the parameter space for the outer planet, fitting a simultaneous two-Keplerian model that allows the outer planet to take on periods of 4000–8000 days and eccentricities of  $e < 0.3$ . The best fit from the genetic algorithm results was then used as a starting point for a two-Keplerian fit (downhill simplex minimization) within the *Systemic Console* (Meschiari et al. 2009).

**Table 3**  
HARPS-TERRA Radial Velocities for HD 30177

BJD-2400000	Velocity (m s <sup>-1</sup> )	Uncertainty (m s <sup>-1</sup> )
52947.76453	-70.7	1.6
53273.88347	0.0	1.9
53274.88548	4.6	1.9
53288.84830	4.6	1.5
53367.68146	21.6	1.8
53410.60057	32.3	1.5
53669.80849	95.9	2.0
54137.58873	31.0	1.5
54143.51190	28.9	1.4
54194.47989	8.6	1.5
54315.91894	-38.8	2.3
54384.87123	-60.3	3.2
54431.68520	-75.4	1.9
55563.54385	-63.1	1.0
55564.57743	-66.2	0.8
55903.70118	30.9	2.2
56953.81794	-43.4	0.7
56955.78182	-45.2	0.7
56957.88054	-46.5	1.1
56959.68147	-47.8	0.8

The results of these fits are given in Table 4. The precision with which the parameters for the inner planet are known are now improved by a factor of 10, or more, over the previously published values (Butler et al. 2006). The model fit for the inner planet is shown in Figure 1. The nominal best-fit solution features a second planet, HD 30177c, with a period of  $6921 \pm 621$  days and  $m \sin i = 3.0 \pm 0.3 M_{\text{Jup}}$ . We present both a “best fit” and a “long-period” solution in recognition of the fact that for an incomplete orbit, the period can be wildly unconstrained and allow for solutions with ever-longer periods by adjusting the eccentricity. Figure 2 shows the  $\chi^2$  contours as a function of the outer planet’s period and eccentricity, based on the results from the best-fit solution given in the left columns of Table 4. The best-fit solution appears to be a shallow minimum in the  $\chi^2$  space, with a secondary minimum at lower eccentricity and longer period ( $P \sim 10,000$  days). We thus attempted a second fit, starting the orbital period of the outer planet at 10,000 days to guide the *Systemic* simplex algorithm into the apparent secondary  $\chi^2$  minimum seen in Figure 2. The results are given in the right columns of Table 4, labelled “long period.” This fit results in an outer planet with period  $11640 \pm 2432$  days and  $m \sin i = 6.4 \pm 3.3 M_{\text{Jup}}$ ; the uncertainties are of course much larger since the available data

only cover  $\sim 60\%$  of the orbital period. The best-fit and long-period solutions are plotted in Figure 3.

One might argue that the outer planet hypothesis relies heavily on the presumption of a velocity turnover in the first few epochs, in particular, the point at BJD 2451119, which lies about  $30 \text{ m s}^{-1}$  below the previous night’s velocity. To check the effect of this potentially bad observation, we repeated the orbit fitting described above after removing that point. The results are given in Table 5, again expressed as a “best fit” and a “long-period” solution. We now find a best fit at a period of  $7601 \pm 1134$  days and  $m \sin i = 3.3 \pm 0.5 M_{\text{Jup}}$ . Removing the suspected outlier resulted in a slightly longer period that remains in formal agreement with the original solution in Table 4. For the long-period solution, we again started the *Systemic* fitting routine at a period of 10,000 days for the outer planet. This results again in a long period consistent with the long-period solution obtained from the full set of velocities: we obtain a period of  $11613 \pm 1837$  days and  $m \sin i = 7.6 \pm 3.1 M_{\text{Jup}}$ . We thus have two possible solutions for the HD 30177 two-planet system, which are virtually indistinguishable in terms of the rms about the model fit or the  $\chi^2$ , due to the shallow minima and complex  $\chi^2$  space (Figure 4).

For the old, solar-type stars generally targeted by radial velocity surveys, stellar magnetic cycles like the Sun’s 11-year cycle are a concern when claiming detection of planets with orbital periods  $\sim 10$  years and longer. While our AAT/UCLES spectra do not include the Ca II H and K lines most commonly used as activity proxies, the HARPS spectra used in this work do (e.g., Dumusque et al. 2011; Lovis et al. 2011; Hébrard et al. 2014). Figure 5 shows the Ca II activity  $\log R'_{HK}$  versus the HARPS radial velocities. No correlation is evident. Clearly, a long-period body is present, but a longer time baseline is necessary to observe a complete orbit and better constrain its true nature. In the next section, we explore the dynamical stability of the two candidate orbital solutions.

#### 4. Dynamical Stability Simulations

In order to understand the dynamical context of the two distinct orbital solutions presented above, and to see whether they yield planetary systems that are dynamically feasible, we followed a now well-established route (e.g., Marshall et al. 2010; Robertson et al. 2012b; Horner et al. 2013). For each solution, we performed 126,075 unique integrations of the system using the Hybrid integrator within the *n*-body dynamics package, MERCURY (Chambers 1999). In each of those simulations, we held the initial orbit of the innermost planet

**Table 4**  
HD 30177 Planetary System Parameters (All Data)

Parameter	Nominal Best Fit		Long-period Solution	
	HD 30177b	HD 30177c	HD 30177b	HD 30177c
Period (days)	$2532.5 \pm 10.6$	$6921 \pm 621$	$2520.6 \pm 8.9$	$11640 \pm 2432$
Eccentricity	$0.189 \pm 0.014$	$0.35 \pm 0.10$	$0.188 \pm 0.014$	$0.14 \pm 0.11$
$\omega$ (degrees)	$32 \pm 4$	$11 \pm 13$	$30 \pm 4$	$32 \pm 48$
$K$ (m s <sup>-1</sup> )	$126.1 \pm 1.9$	$35.8 \pm 3.4$	$126.9 \pm 1.7$	$59.4 \pm 27.6$
$T_0$ (BJD-2400000)	$51428 \pm 26$	$51661 \pm 573$	$51434 \pm 24$	$48426 \pm 2978$
$m \sin i$ ( $M_{\text{Jup}}$ )	$8.07 \pm 0.12$	$3.0 \pm 0.3$	$8.11 \pm 0.11$	$6.4 \pm 3.3$
$a$ (au)	$3.58 \pm 0.01$	$6.99 \pm 0.42$	$3.57 \pm 0.01$	$9.9 \pm 1.4$
rms of fit (m s <sup>-1</sup> )	7.04		7.17	
$\chi^2_r$ (51 d.o.f.)	0.98		1.01	

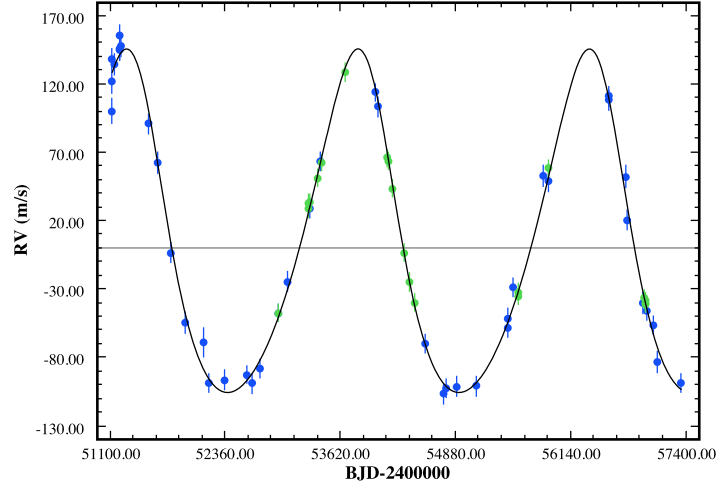


**Figure 1.** Data and Keplerian model fit for the inner planet HD 30177b. AAT—blue; HARPS—green. The orbit of the outer planet has been removed. We have added  $6 \text{ m s}^{-1}$  of jitter in quadrature to the uncertainties, and this fit has an rms of  $7.07 \text{ m s}^{-1}$ .

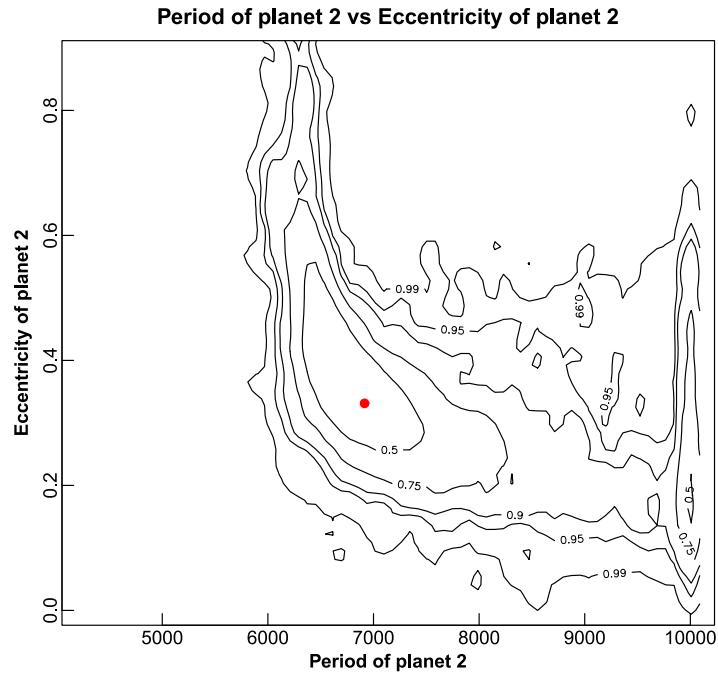


**Figure 2.** Contours of  $\chi^2$  as a function of the outer planet's eccentricity and orbital period. Contours are labeled with confidence intervals around the best fit (red dot). Hints of a second local  $\chi^2$  minimum can be seen in the lower right, at long periods and low eccentricities.

fixed at its nominal best-fit values (as detailed in Table 4). We then proceeded to systematically move the orbit of the outermost planet through the full  $\pm 3\sigma$  uncertainty ranges for the semimajor axis,  $a$ , eccentricity,  $e$ , argument of periastron,  $\omega$ , and mean anomaly,  $M$ . In this manner, we created a regular grid of solutions, testing 41 unique values of  $a$  and  $e$ , 15 unique values of  $\omega$ , and 5 unique values of  $M$ .

These simulations make two assumptions: first, that the two planets move on coplanar orbits (as is essentially the case in the solar system), and, second, we assign the planets their minimum masses ( $m \sin i$ ) as derived from the radial velocity data. In a number of previous studies (e.g., Horner et al. 2011, 2014; Hinse et al. 2014), we have examined the impact of mutual inclination on system stability. However, for

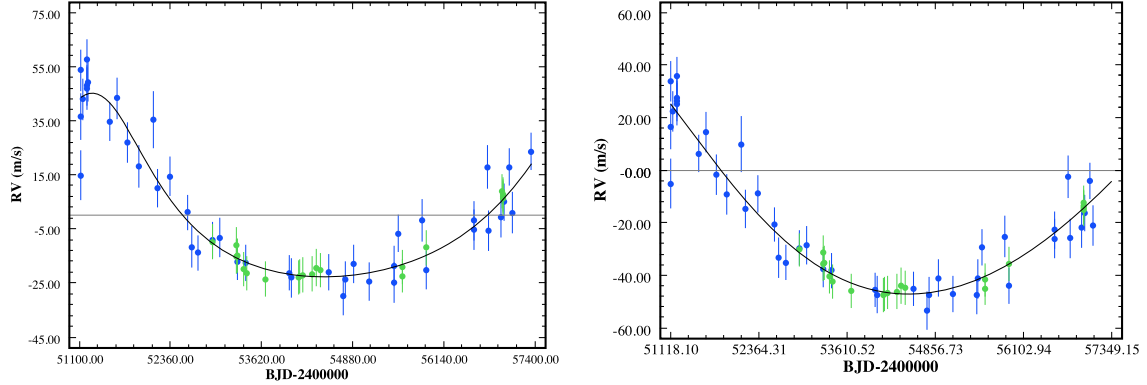


**Figure 3.** Data and Keplerian model fit for the outer planet HD 30177c. AAT—blue; HARPS—green. The orbit of the inner planet has been removed. We have added  $6 \text{ m s}^{-1}$  of jitter in quadrature to the uncertainties. Left panel: nominal best fit, with  $P = 6921$  days. Right panel: long-period solution, with  $P = 11640$  days.

**Table 5**  
HD 30177 Planetary System Parameters (Outlier Removed)

Parameter	Nominal Best Fit		Long-period Solution	
	HD 30177b	HD 30177c	HD 30177b	HD 30177c
Period (days)	$2531.3 \pm 11.3$	$7601 \pm 1134$	$2524.4 \pm 9.8$	$11613 \pm 1837$
Eccentricity	$0.185 \pm 0.012$	$0.31 \pm 0.11$	$0.184 \pm 0.012$	$0.22 \pm 0.14$
$\omega$ (degrees)	$32 \pm 4$	$13 \pm 16$	$31 \pm 3$	$19 \pm 30$
$K$ ( $\text{m s}^{-1}$ )	$125.8 \pm 1.7$	$37.9 \pm 3.8$	$126.3 \pm 1.5$	$70.8 \pm 29.5$
$T_0$ (BJD-2400000)	$51430 \pm 27$	$52154 \pm 2009$	$51434 \pm 29$	$48973 \pm 1211$
$m \sin i$ ( $M_{\text{Jup}}$ )	$8.06 \pm 0.11$	$3.32 \pm 0.45$	$8.08 \pm 0.10$	$7.6 \pm 3.1$
$a$ (au)	$3.58 \pm 0.01$	$7.45 \pm 0.75$	$3.58 \pm 0.01$	$9.89 \pm 1.04$
Rms of fit ( $\text{m s}^{-1}$ )	5.98		6.01	
$\chi_r^2$ (50 d.o.f.)	0.76		0.77	

widely separated planets, the inclination between the two orbits seems to play a minimal role in their stability. It seems most likely that there would not be large mutual inclination between the orbits of the planets; from a dynamical point of view, given the assumption that the two planets formed in a dynamically cool disk, it is challenging to imagine how they could achieve significant mutual inclination without invoking the presence of a highly inclined distant perturber (i.e., an undetected binary companion, driving excitation through the Kozai mechanism). It is certainly reasonable to assume that the orbits are most likely relatively coplanar, as is seen in the solar system giant planets, and also in those multiple exoplanet systems with orbital inclinations constrained by transits (Fang & Margot 2012) or by resolved debris disk observations (Kennedy et al. 2013).

Regarding the use of minimum masses, one would expect increased planetary masses to destabilize the systems. The reason for this can be seen when one considers the “gravitational reach” of a planet, which can be defined in terms of its Hill radius. The Hill radius is proportional to the semimajor axis of the planet’s orbit, but only increases as the cube root of the planet’s mass. As a result, doubling the mass of a planet only increases its gravitational reach, and therefore its Hill radius, by a factor of  $2^{(1/3)} = 1.26$ —a relatively minor change.

The simulations were set to run for a maximum of 100 million years, but were brought to a premature end if one or other of the planets were ejected from the system or collided

with the central body. Simulations were also curtailed if the two planets collided with one another. For each of these conditions, the time at which the simulation finished was recorded, allowing us to create dynamical maps of the system to examine the dynamical context of the orbits presented above, and to see whether the system was dynamically feasible. Such maps have, in the past, revealed certain systems to be dynamically unfeasible (e.g., Horner et al. 2011; Wittenmyer et al. 2012a; Horner et al. 2013, 2014). In other cases, dynamical mappings have resulted in stronger constraints for a given system’s orbits than was possible solely on the grounds of the observational data (e.g., Robertson et al. 2012a; Wittenmyer et al. 2012b, 2014b). Dynamical simulations therefore offer the potential to help distinguish between different solutions with a similar goodness of fit, such as those proposed in this work, as well as yielding an important dynamical “sanity check.”

To complement these dynamical simulations, we also chose to trial a new technique for the dynamical analysis of newly discovered systems. Rather than populate regular grids in element space, while holding the better constrained planet’s initial orbit fixed, we instead performed repeated fits to the observational data. In our fitting, we required solely that the solutions produced lie within  $3\sigma$  of the best-fit solution, allowing all parameters to vary freely. This created clouds of “potential solutions” distributed around the best fit out to a

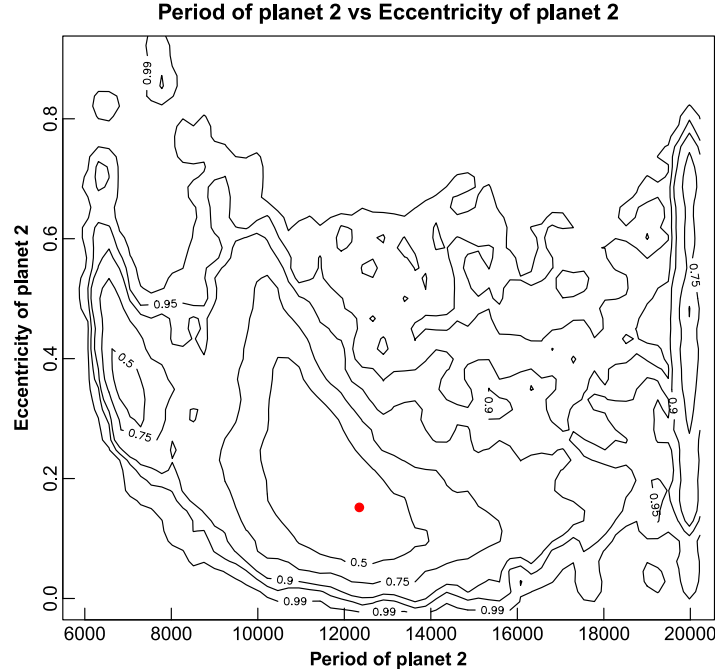


**Figure 4.** Same as Figure 2, but for the long-period solution where one outlier data point has been removed. Two local  $\chi^2$  minima are evident, with the longer period solution at lower eccentricity (red dot).

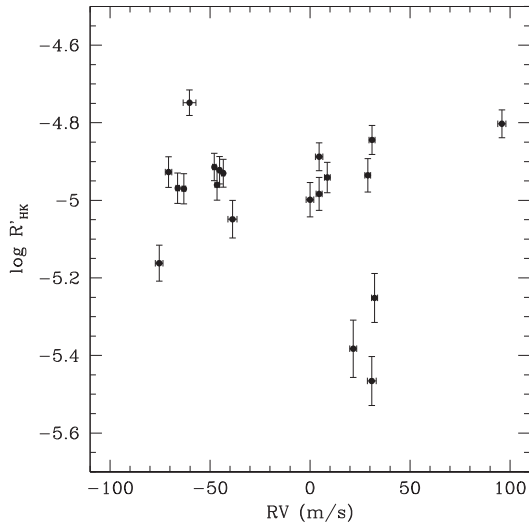


**Figure 5.** Ca II activity index  $\log R'_{HK}$  as a function of radial velocity for the HARPS spectra of HD 30177. No correlation is evident from the 11 years of data, and hence we conclude that a stellar magnetic cycle is not responsible for the observed radial velocity variations.

range of  $\chi^2_{\text{best}} + 9$ . We then randomly selected solutions to evenly sample the phase space between the best-fit solution (at  $\chi^2_{\text{best}}$ ) and  $\chi^2_{\text{best}} + 9$ . As before, we generated 126,075 unique solutions for each of the two scenarios presented above.

Where our traditional dynamical maps explore the dynamical context of the solutions in a readily apparent fashion, these new simulations are designed to instead examine the stability of the system as a function of the goodness of fit of the orbital solution. In addition, they allow us to explore the stability as a function of the masses assigned to the two planets in question. As such, they provide a natural complement to the traditional maps, as can be seen below.

### 5. Dynamical Stability Results

Figure 6 shows the dynamical context of the short-period solution for the two-planet HD 30177 system, as described in Table 4. The best-fit solution lies in an area of strong dynamical instability, with the majority of locations within the  $1\sigma$  uncertainty range being similarly unstable. There is, however, a small subset of solutions in that range that are stable, marking the inner edge of a broad stable region seen toward larger semimajor axes and smaller eccentricities. The small island of stability at  $a \sim 5.687$  au is the result of the planets becoming trapped in mutual 2:1 mean-motion resonance, while the narrow curved region of moderate stability at high eccentricities is caused by orbits for HD 30177c with periastron located at the semimajor axis of HD 30177b. Dynamical stability for the system on near-circular, non-resonant orbits is only seen in these simulations exterior to the planet's mutual 3:1 mean-motion resonance, located at  $a \sim 7.453$  au (and the cause of the small island of stability at non-zero eccentricities at that semimajor axis). As a result, these simulations suggest that the short-period solution is not dynamically favored, unless the orbital period for HD 30177c is significantly longer than

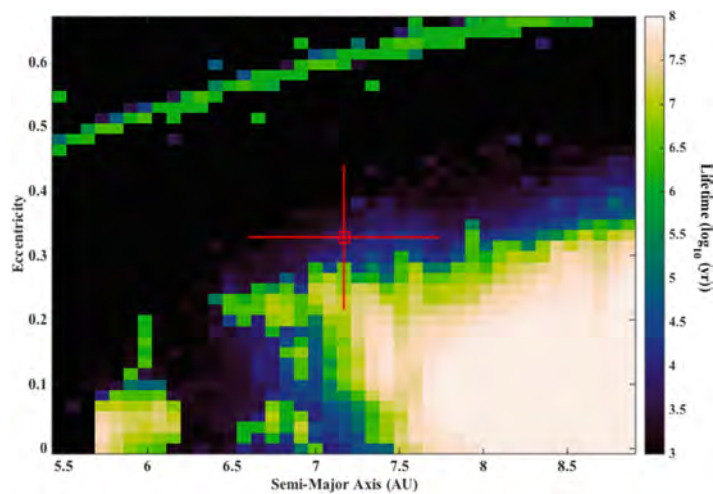


**Figure 6.** Dynamical stability of the short-period solution for the orbit of HD 30177c, as a function of semimajor axis and eccentricity. The red box toward the center of the plot denotes the location of the best-fit solution, while the lines radiating from that point show the  $1 - \sigma$  uncertainties. It is immediately apparent that the best-fit solution lies in a region of significant dynamical instability.

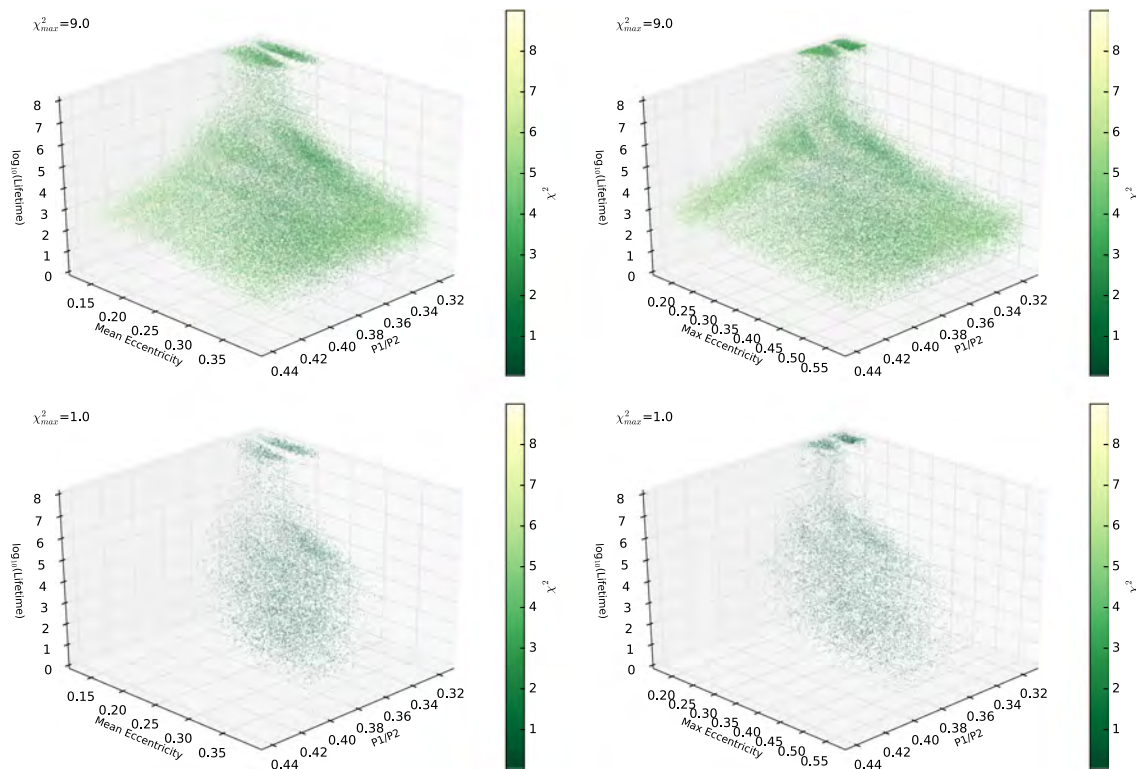


**Figure 7.** Stability of the short-period solution for HD30177, as a function of the mean (left) and maximum (right) eccentricity of the two planets in the system. The color axis shows the goodness of fit for each of the solutions tested, with the vertical axis showing the lifetime, and the y-axis showing the ratio of the two planetary orbital periods. The upper plots show the results for solutions within  $3\sigma$  of the best fit, while the lower show only those simulations within  $1\sigma$  of that solution. We note that animated versions of the figures are available, which may help the reader to fully visualize the relationship between the stability and the various variables considered.

(Animations (a and b) of this figure are available.)

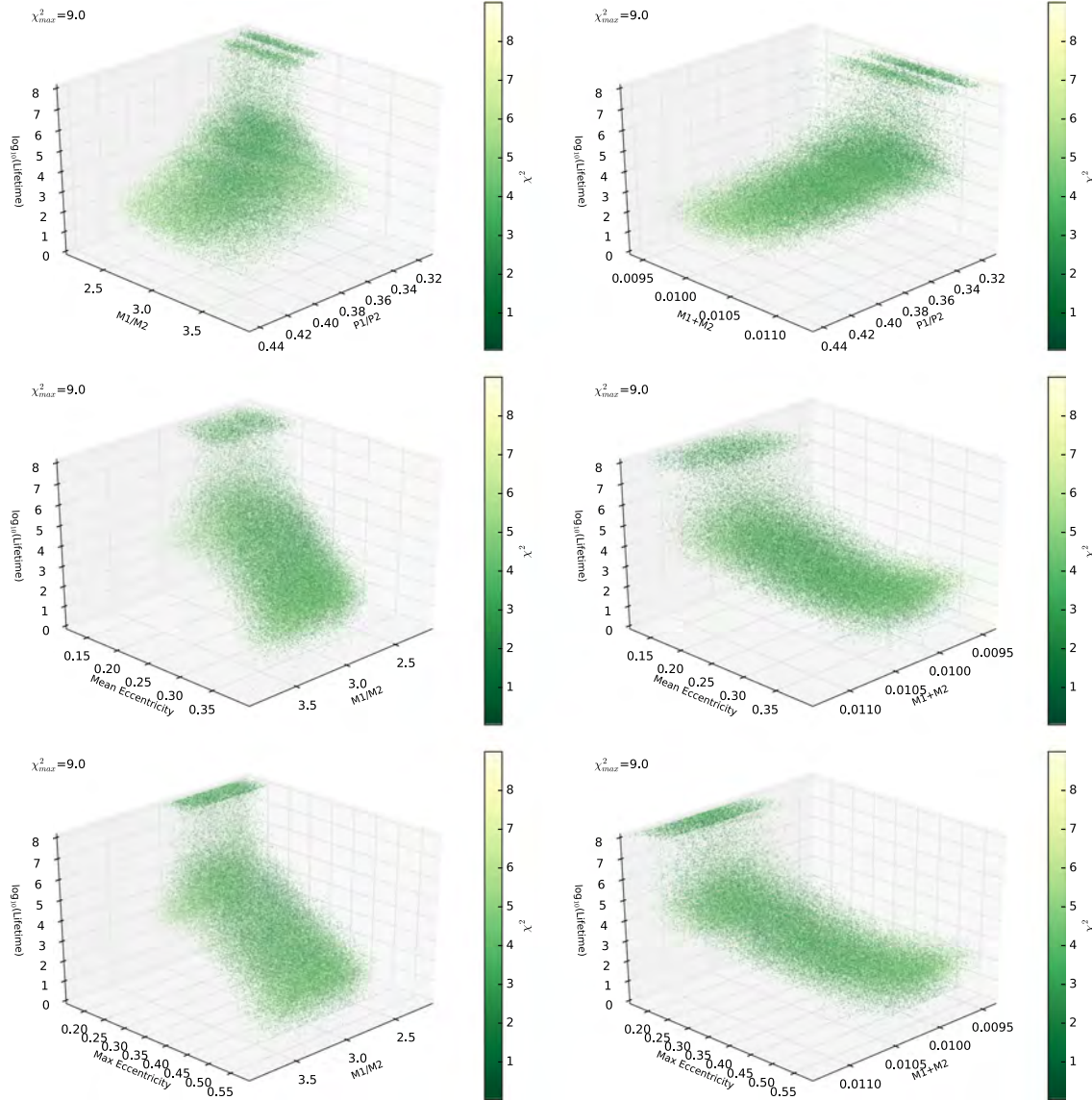


**Figure 8.** Upper row: the stability of the short-period solution for HD 30177c, as a function of the mass ratio (left) and total mass (right) of the two planets in the system. The color scale shows the goodness of fit for each of the solutions tested, with the vertical axis showing the lifetime, and the y-axis showing the ratio of the two planetary orbital periods. Results for solutions within  $3\sigma$  of the best fit are shown. Middle row: same, but the x-axis now denotes the mean eccentricity of the planetary orbits. Bottom row: same, but the x-axis now denotes the maximum eccentricity of the planetary orbits.

(Animations (a, b, c, d, e and f) of this figure are available.)

the best fit, the orbit markedly less eccentric, or if the two planets are trapped in mutual 3:1 mean-motion resonance.

These results are strongly supported by our subsidiary integrations—the results of which are shown in Figures 7–8. Figure 7 shows the stability of the candidate HD 30177 planetary systems as a function of the eccentricities of the two planets, their period ratio, and the goodness of the fit of the solution tested. In Figure 7, the upper plots show all solutions

within  $3\sigma$  of the best fit, while the lower show only those solutions within  $1\sigma$  of the best fit. It is immediately apparent that truly stable solutions are limited to only a very narrow range of the plots—namely two narrow regions with low eccentricities, and widely separated orbits. In fact, these solutions all lie at, or somewhat outside of, the location of the 3:1 mean-motion resonance between the two planets ( $P1/P2 \sim 0.33$ ). The inner of the two stable patches are those

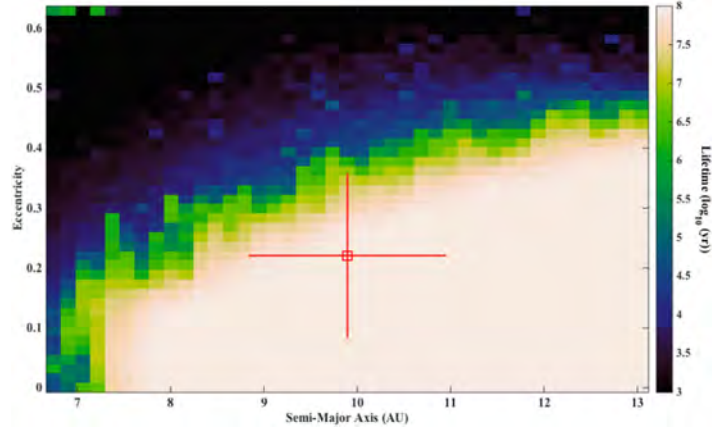


**Figure 9.** Stability of the long-period solution for the orbit of HD 30177c, as a function of semimajor axis and eccentricity. As with Figure 6, the red box marks the location of the best-fit solution, with the red lines radiating showing the  $1 - \sigma$  uncertainties. Unlike the short-period solution, the best-fit orbit now lies in a broad region of dynamical stability, with most solutions within  $1 - \sigma$  proving stable for the full 100 Myr of our integrations.

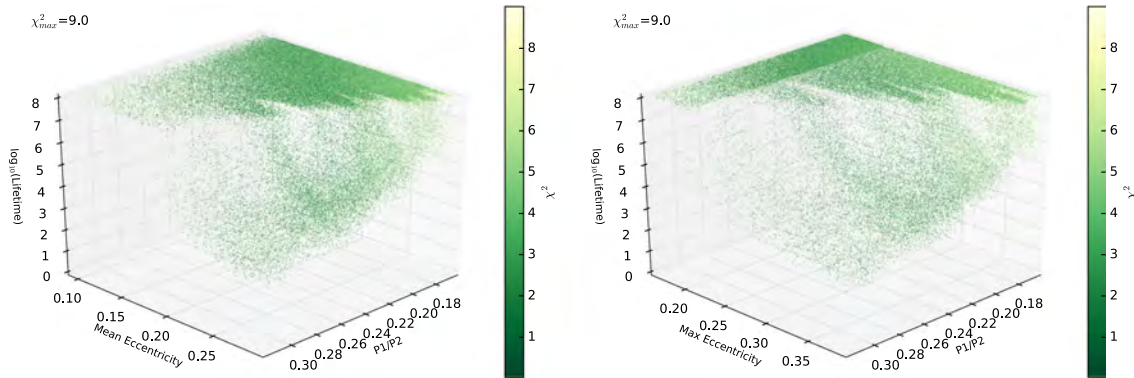


**Figure 10.** Stability of the long-period solution for HD 30177, as a function of the mean (left) and maximum (right) eccentricity of the two planets in the system. The color scale and axes have the same meaning as in Figure 7. The upper plots show the results for solutions within  $3\sigma$  of the best fit, while the lower show only those simulations within  $1\sigma$  of that solution.

(Animations (a and b) of this figure are available.)

orbits that are resonant, while the outermost are those sufficiently separated to be exterior to that resonance. Even at these stable separations, the system is only feasible for low-to-moderate planetary eccentricities—solutions that ascribe an eccentricity of  $\sim 0.25$  or greater to either planet prove strongly unstable.

Figure 8 shows the influence of the mass of the two planets on the stability of the solution. The resonant and extra-resonant stable regions are again clearly visible, and it is apparent that the masses of the two planets seem to have little influence on the stability of the solution. A slight influence from the planetary mass can be seen in the middle row of Figure 8, which shows that stable solutions with the lowest cumulative planet mass (i.e.,  $M_b + M_c$ ) have slightly higher mean eccentricities than those for larger cumulative masses. This effect is only weak, and is the result of the least massive solutions veering away from lower eccentricities. Given that the eccentricities of planetary orbits tend to be somewhat overestimated when fitting radial velocity data (O’Toole

et al. 2009), this may be an indication that the lower-mass solutions are slightly less favorable than their higher mass counterparts.

Finally, the bottom row of Figure 8 shows the stability of the solution clouds as a function of the maximum eccentricity between the two planets (i.e., the value plotted on the y-axis is whichever is greater between  $e_b$  and  $e_c$ ). This reinforces the result from Figure 7 that solutions with either of the two planets moving on orbits with  $e \geq 0.25$  are unstable regardless of their separation, or the mass of the planets involved.

Taken in concert, our results show that, while short-period solutions for the HD 30177 system can prove dynamically stable, they require the two planets to either be trapped in mutual 3:1 mean-motion resonance, or to be more widely spaced, and further require that neither planet move on an orbit with eccentricity greater than 0.25.

However, what of our alternative, longer period solution for the planetary system? Figure 9 shows the dynamical context of that solution. Unlike the short-period solution, the two planets

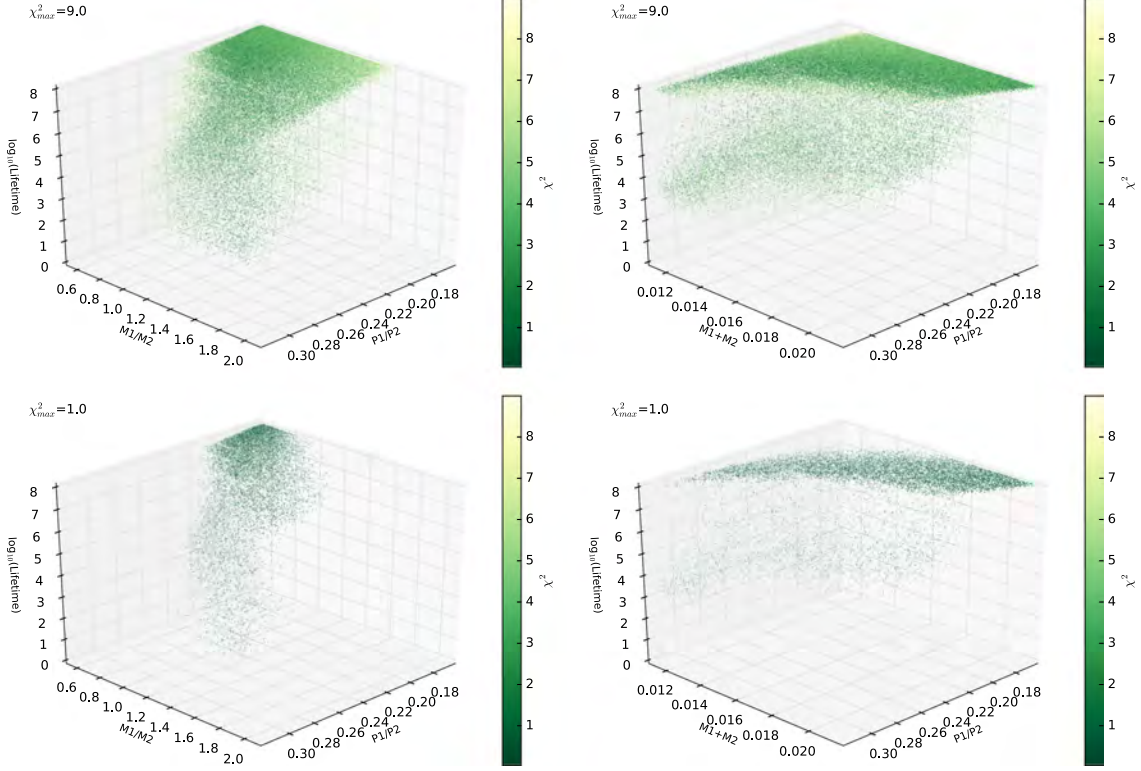


**Figure 11.** Stability of the long-period solution for HD 30177, as a function of the mass ratio (left) and total mass (right) of the two planets in the system. As before, the color axis shows the goodness of fit for each of the solutions tested, with the vertical axis showing the lifetime, and the y-axis showing the ratio of the two planetary orbital periods. Solutions within  $3\sigma$  of the best fit are shown in the upper panels, and only those within  $1\sigma$  are shown in the lower panels. (Animations (a) and (b) of this figure are available.)

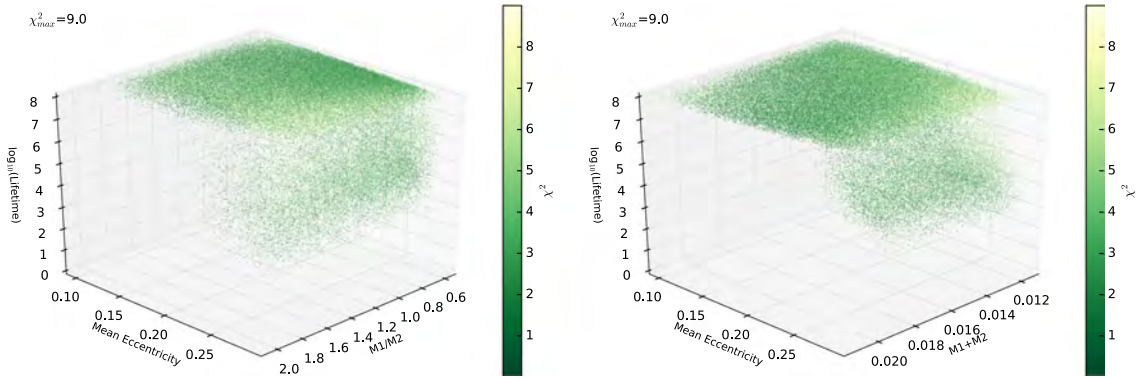


**Figure 12.** Stability of the long-period solution for HD 30177, again as a function of the mass ratio (left) and total mass (right) of the two planets in the system. Again, the color axis shows the goodness of fit for each of the solutions tested, with the vertical axis showing the lifetime, and the x-axis showing the mean eccentricity of the planetary orbits. Results for solutions within  $3\sigma$  of the best fit are shown. (Animations (a) and (b) of this figure are available.)

are now sufficiently widely separated that the great majority of orbits around the best-fit solution are now dynamically stable for the full 100 Myr of our simulations. At the very inner edge of the plot, the cliff of the instability exterior to the planet's

mutual 3:1 mean-motion resonance can again be seen, as can hints of the moderate stability afforded by the periastron of HD 30177c falling at the semimajor axis of HD 30177b (top left of the plot). Purely on the basis of this plot, the longer

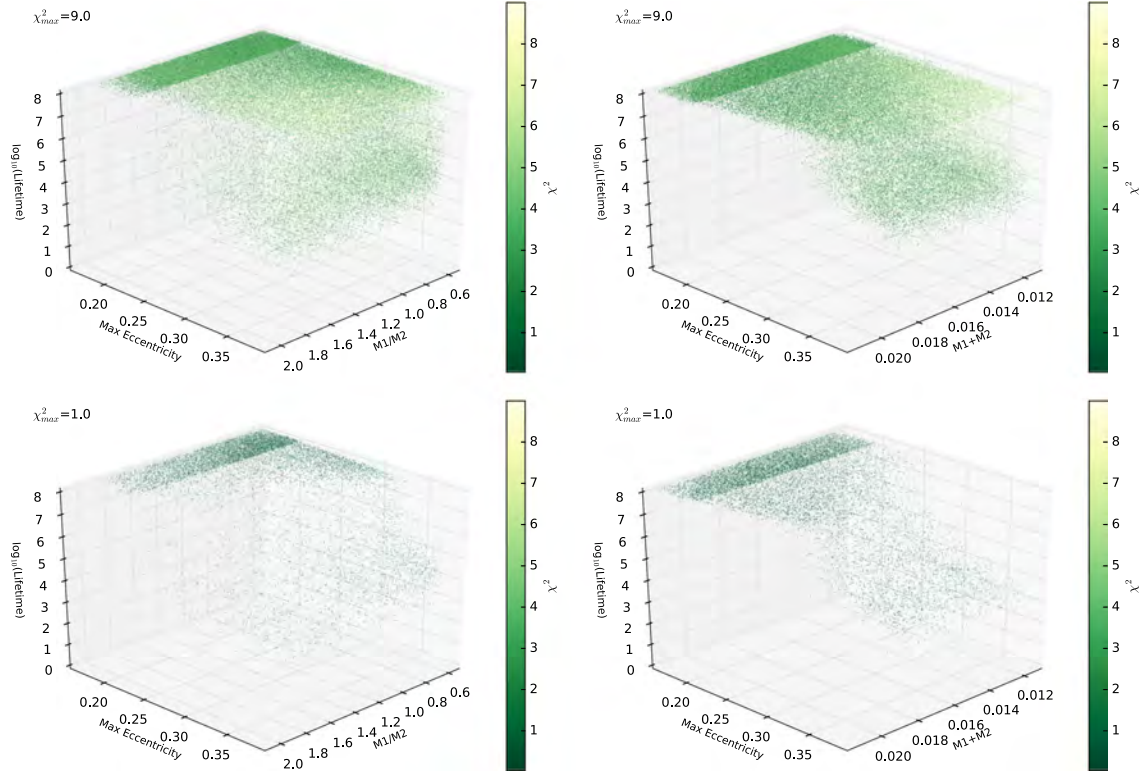


**Figure 13.** Stability of the long-period solution for HD 30177, again as a function of the mass ratio (left) and total mass (right) of the two planets in the system. The color axis shows the goodness of fit for each of the solutions tested, with the vertical axis showing the lifetime, and the  $x$ -axis the maximum eccentricity of the planetary orbits. The upper plots show the results for solutions within  $3\sigma$  of the best fit, while the lower show only those simulations within  $1\sigma$  of that solution. (Animations (a) and (b) of this figure are available.)

period solution seems markedly more dynamically feasible, a result once again borne out by the plots of our subsidiary simulations of the long-period solution (Figures 10–13).

Figure 10 reveals many of the same features as Figure 9—a significant proportion of the solutions are dynamically stable—particularly those within  $1\sigma$  of the best fit (lower panels). The greater the orbital separation of the two planets, the greater their orbital eccentricities can be before destabilising the system. In addition, however, the destabilizing influence of distant mean-motion resonances is revealed in these plots, as the notches of instability carved into the distribution at specific period ratios. Aside from these few unstable regions, however, the great majority of solutions within  $1\sigma$  of the best fit are stable.

Figure 11 shows that the mass ratio of the planets (left-hand plots) has little or no influence on their stability. Interestingly, though, the lower right hand panel reveals an apparent relationship in the fitting between the cumulative mass of the planets and their mutual separation. The more widely separated the two planets (and hence the more distant HD 30177c is), the greater their cumulative mass. This is not at all surprising: the more distant HD 30177c is, the greater its mass would have to be to achieve a radial velocity signal of a given amplitude. This feature is therefore entirely expected, but nevertheless serves to nicely illustrate the relationship between different parameters in the radial velocity fitting process.

Figure 12 again reveals that the more eccentric the orbits of the planets, the more likely they are to prove unstable—though, once again, the great majority of the sampled phase space proves dynamically stable. More interesting, however, are the results shown in Figure 13. The left-hand panels of that plot, which show the stability of the solutions as a function of the maximum eccentricity between the two planets ( $y$ -axis) and the mass ratio of the two planets ( $x$ -axis) suggest that, the closer the two planetary masses are to parity, the more likely eccentric orbits are to be stable. By contrast, the lower right hand plot suggests that the greater the sum of the planetary masses, the more likely solutions with high eccentricities are to be stable. Taken in concert, these results are once again a reflection of the relationship between cumulative mass and orbital separation. That is, the greater the orbital separation of the two planets, the greater their cumulative mass, and the closer to parity their masses become (since our fits suggest that HD 30177c is the less massive of the two). At the same time, we saw from Figure 10 that the greater the separation of the two planets, the more stable those orbital solutions are at higher eccentricity. So, once again, we are looking at the same thing—these two apparent trends are the result of the requirement that a more distant HD 30177c must be more massive in order to generate the observed radial velocity amplitude.

## 6. Conclusions

We present the results of new radial velocity observations of HD 30177, which reveal for the first time the presence of a second, long-period planet in that system. Two possible orbital solutions for the planetary system are presented—one with a shorter-period orbit for HD 30177c, and one with the two planets more widely spaced, and HD 30177c on a longer period orbit. The two solutions are virtually indistinguishable from one another in terms of the quality of fit that they provide to the data. However, the short-period solution placed the two planets on orbits sufficiently compact that they lie closer than their mutual 3:1 mean-motion resonance.

Although several highly compact multi-planet systems have been discovered in recent years, it has become apparent that such compact systems rely on dynamical stability conferred by mutual resonant planetary orbits. As such, it seemed prudent to build on our earlier work and to carry out detailed  $n$ -body simulations of the two potential solutions for the HD 30177 system to see whether it was possible to rule either out on dynamical stability grounds.

Our results reveal that, although some stable solutions can be found for the short-period variant of the HD 30177 system, those solutions require orbital eccentricities for the planets that are typically smaller than that given by the best-fit solution, and require HD 30177c to be somewhat more distant than the best fit. In other words, they require relatively low-eccentricity orbits for that planet exterior to its mutual 3:1 mean-motion resonance with HD 30177b. By contrast, the great majority of the longer period solutions tested proved dynamically stable—and across a much greater range of potential semimajor axes and orbital eccentricities.

As a result, we consider that the most likely solution for the orbit of HD 30177c is the longer period option: an  $m \sin i = 7.6 \pm 3.1 M_{\text{Jup}}$  planet with  $a = 9.89 \pm 1.04$  au,  $e = 0.22 \pm 0.14$ , and an orbital period of  $P = 11613 \pm 1837$  days. We note that for inclinations of  $i \lesssim 30^\circ$ , the two orbiting bodies in the HD 30177 system fall into the brown dwarf regime. With an orbital separation of  $a \sim 10$  au, one can consider HD 30177c to be one of the first members of an emerging class of “Saturn analogs,” referring to planets with orbital separations similar to Saturn. Just as long-term radial velocity surveys have begun to characterize “Jupiter analogs” (Wittenmyer et al. 2011; Rowan et al. 2016; Wittenmyer et al. 2016a), the continuation of legacy surveys such as the AAPS will enable us to probe the population of planets in Saturn-like orbits in the coming decade.

J.H. is supported by USQ’s Strategic Research Fund: the STARWINDS project. C.G.T. is supported by Australian Research Council grants DP0774000 and DP130102695. This research has made use of NASA’s Astrophysics Data System (ADS), and the SIMBAD database, operated at CDS, Strasbourg, France. This research has also made use of the Exoplanet Orbit Database and the Exoplanet Data Explorer at exoplanets.org (Wright et al. 2011; Han et al. 2014).

## References

- Adibekyan, V. Z., Sousa, S. G., Santos, N. C., et al. 2012, *A&A*, 545, A32  
 Anglada-Escudé, G., & Butler, R. P. 2012, *ApJS*, 200, 15  
 Borucki, W. J., Koch, D. G., Basri, G., et al. 2011, *ApJ*, 736, 19  
 Butler, R. P., Marcy, G. W., Williams, E., et al. 1996, *PASP*, 108, 500  
 Butler, R. P., Wright, J. T., Marcy, G. W., et al. 2006, *ApJ*, 646, 505  
 Chambers, J. E. 1999, *MNRAS*, 304, 793  
 Coughlin, J. L., Mullally, F., Thompson, S. E., et al. 2016, *ApJS*, 224, 12  
 Dumusque, X., Lovis, C., Ségransan, D., et al. 2011, *A&A*, 535, A55  
 Endl, M., Brugamyer, E. J., Cochran, W. D., et al. 2016, *ApJ*, 818, 34  
 Fang, J., & Margot, J.-L. 2012, *ApJ*, 761, 92  
 Feng, Y. K., Wright, J. T., Nelson, B., et al. 2015, *ApJ*, 800, 22  
 Fischer, D., Anglada-Escudé, G., Arriagada, P., et al. 2016, arXiv:1602.07939  
 Franchini, M., Morossi, C., Marcantonio, P. D., Malagnini, M. L., & Chavez, M. 2014, *MNRAS*, 442, 220  
 Ghezzi, L., Cunha, K., Smith, V. V., et al. 2010, *ApJ*, 720, 1290  
 Han, E., Wang, S. X., Wright, J. T., et al. 2014, *PASP*, 126, 827  
 Hébrard, E. M., Donati, J.-F., Delfosse, X., et al. 2014, *MNRAS*, 443, 2599  
 Hinse, T. C., Horner, J., & Wittenmyer, R. A. 2014, *JASS*, 31, 187  
 Horner, J., & Jones, B. W. 2008, *IJAsB*, 7, 251  
 Horner, J., & Jones, B. W. 2010, *IJAsB*, 9, 273  
 Horner, J., Jones, B. W., & Chambers, J. 2010, *IJAsB*, 9, 1  
 Horner, J., Marshall, J. P., Wittenmyer, R. A., & Tinney, C. G. 2011, *MNRAS*, 416, L11  
 Horner, J., Wittenmyer, R. A., Hinse, T. C., et al. 2013, *MNRAS*, 435, 2033  
 Horner, J., Wittenmyer, R. A., Hinse, T. C., & Marshall, J. P. 2014, *MNRAS*, 439, 1176  
 Houk, N., & Cowley, A. P. 1975, University of Michigan Catalogue of Two-dimensional Spectral Types for the HD stars. Vol. I (Ann Arbor, MI: Univ. Michigan Press)  
 Howard, A. W., Johnson, J. A., Marcy, G. W., et al. 2010, *ApJ*, 721, 1467  
 Jones, H. R. A., Butler, R. P., Tinney, C. G., et al. 2010, *MNRAS*, 403, 1703  
 Kennedy, G. M., Wyatt, M. C., Bryden, G., Wittenmyer, R., & Sibthorpe, B. 2013, *MNRAS*, 436, 898  
 Lewis, A. R., Quinn, T., & Kaib, N. A. 2013, *AJ*, 146, 16  
 Lovis, C., Dumusque, X., Santos, N. C., et al. 2011, arXiv:1107.5325  
 Marmier, M., Ségransan, D., Udry, S., et al. 2013, *A&A*, 551, A90  
 Marshall, J., Horner, J., & Carter, A. 2010, *IJAsB*, 9, 259  
 Meschiari, S., Wolf, A. S., Rivera, E., et al. 2009, *PASP*, 121, 1016  
 Moutou, C., Lo Curto, G., Mayor, M., et al. 2015, *A&A*, 576, A48  
 O’Toole, S. J., Tinney, C. G., Jones, H. R. A., et al. 2009, *MNRAS*, 392, 641  
 Robertson, P., Endl, M., Cochran, W. D., et al. 2012a, *ApJ*, 749, 39  
 Robertson, P., Horner, J., Wittenmyer, R. A., et al. 2012b, *ApJ*, 754, 50  
 Rowan, D., Meschiari, S., Laughlin, G., et al. 2016, *ApJ*, 817, 104  
 Rowe, J. F., Bryson, S. T., Marcy, G. W., et al. 2014, *ApJ*, 784, 45  
 Santos, N. C., Sousa, S. G., Mortier, A., et al. 2013, *A&A*, 556, A150  
 Sousa, S. G., Santos, N. C., Israelian, G., Mayor, M., & Udry, S. 2011, *A&A*, 533, A141  
 Takeda, G., Ford, E. B., Sills, A., et al. 2007, *ApJS*, 168, 297  
 Tinney, C. G., Butler, R. P., Marcy, G. W., et al. 2001, *ApJ*, 551, 507  
 Tinney, C. G., Butler, R. P., Marcy, G. W., et al. 2003, *ApJ*, 587, 423  
 Tinney, C. G., Wittenmyer, R. A., Butler, R. P., et al. 2011, *ApJ*, 732, 31  
 Valenti, J. A., Butler, R. P., & Marcy, G. W. 1995, *PASP*, 107, 966  
 van Leeuwen, F. 2007, *A&A*, 474, 653  
 Wittenmyer, R. A., Butler, R. P., Tinney, C. G., et al. 2016a, *ApJ*, 819, 28  
 Wittenmyer, R. A., Butler, R. P., Wang, L., et al. 2016b, *MNRAS*, 455, 1398  
 Wittenmyer, R. A., Horner, J., Marshall, J. P., Butters, O. W., & Tinney, C. G. 2012a, *MNRAS*, 419, 3258  
 Wittenmyer, R. A., Horner, J., & Tinney, C. G. 2012b, *ApJ*, 761, 165  
 Wittenmyer, R. A., Horner, J., Tinney, C. G., et al. 2014a, *ApJ*, 783, 103  
 Wittenmyer, R. A., Horner, J., Tuomi, M., et al. 2012c, *ApJ*, 753, 169  
 Wittenmyer, R. A., Tan, X., Lee, M. H., et al. 2014b, *ApJ*, 780, 140  
 Wittenmyer, R. A., Tinney, C. G., O’Toole, S. J., et al. 2011, *ApJ*, 727, 102  
 Wittenmyer, R. A., Tuomi, M., Butler, R. P., et al. 2014c, *ApJ*, 791, 114  
 Wittenmyer, R. A., Wang, S., Horner, J., et al. 2013, *ApJS*, 208, 2  
 Wright, J. T., Fakhouri, O., Marcy, G. W., et al. 2011, *PASP*, 123, 412

This page intentionally left blank.